Novel Cellulose Nanoparticles for Potential Cosmetic and Pharmaceutical Applications

by

Neha Dhar

A thesis

presented to the University of Waterloo

in fulfilment of the

thesis requirement for the degree of

Master of Applied Science

in

Chemical Engineering

Waterloo, Ontario, Canada, 2010

AUTHOR'S DECLARATION

I hereby declare that I am the sole author of this thesis. This is a true copy of the thesis, including any required final revisions, as accepted by my examiners. I understand that my thesis may be made electronically available to the public.

ABSTRACT

Cellulose is one of the most abundant biopolymers found in nature. Cellulose based derivatives have a number of advantages including recyclability, reproducibility, biocompatibility, biodegradability, cost effectiveness and availability in a wide variety of forms. Due to the benefits of cellulose based systems, this research study was aimed at developing novel cellulosic nanoparticles with potential pharmaceutical and personal care applications. Two different cellulosic systems were evaluated, each with its own benefits and proposed applications.

The first project involves the synthesis and characterization of polyampholyte nanoparticles composed of chitosan and carboxymethyl cellulose (CMC), a cellulosic ether. EDC carbodiimide chemistry and inverse microemulsion technique was used to produce crosslinked nanoparticles. Chitosan and carboxymethyl cellulose provide amine and carboxylic acid functionality to the nanoparticles thereby making them pH responsive. Chitosan and carboxymethyl cellulose also make the nanoparticles biodegradable and biocompatible, making them suitable candidates for pharmaceutical applications. The synthesis was then extended to chitosan and modified methyl cellulose microgel system. The prime reason for using methyl cellulose was to introduce thermo-responsive characteristics to the microgel system. Methyl cellulose was modified by carboxymethylation to introduce carboxylic acid functionality, and the chitosan-modified methyl cellulose microgel system was found to be pH as well as temperature responsive.

Several techniques were used to characterize the two microgel systems, for e.g. potentiometric and conductometric titrations, dynamic light scattering and zeta potential measurements. FTIR along with potentiometric and conductometric titration was used to confirm the carboxymethylation of methyl cellulose. For both systems, polyampholytic behaviour was observed in a pH range of 4-9. The microgels showed swelling at low and high pH values and deswelling at isoelectric point (IEP). Zeta potential values confirmed the presence of positive charges on the microgel at low pH, negative charges at high pH and neutral charge at the IEP. For chitosan-modified methyl cellulose microgel system, temperature dependent behaviour was observed with dynamic light scattering.

The second research project involved the study of binding interaction between nanocrystalline cellulose (NCC) and an oppositely charged surfactant tetradecyl trimethyl ammonium bromide (TTAB). NCC is a crystalline form of cellulose obtained from natural sources like wood, cotton or animal sources. These rodlike nanocrystals prepared by acid hydrolysis of native cellulose possess negatively charged surface. The interaction between negatively charged NCC and cationic TTAB surfactant was examined and it was observed that in the presence of TTAB, aqueous suspensions of NCC became unstable and phase separated. A study of this kind is imperative since NCC suspensions are proposed to be used in personal care applications (such as shampoos and conditioners) which also consist of surfactant formulations. Therefore, NCC suspensions would not be useful for applications that employ an oppositely charged surfactant. In order to prevent destabilization, poly (ethylene glycol) methacrylate (PEGMA) chains were grafted on the NCC surface to prevent the phase separation in presence of a cationic surfactant. Grafting was carried out using the free radical approach.

The NCC-TTAB polymer surfactant interactions were studied via isothermal titration calorimetry (ITC), surface tensiometry, conductivity measurements, phase separation and zeta potential measurements. The major forces involve in these systems are electrostatic and hydrophobic interactions. ITC and surface tension results confirmed two kinds of interactions: (i) *electrostatically driven* NCC-TTAB complexes formed in the bulk and at the interface and (ii) *hydrophobically driven* TTAB micellization on the NCC rods. Conductivity and surface tension results confirmed that the critical micelle concentration of TTAB (CMC_{TTAB}) shifted to higher values in the presence of NCC. Phase separation measurements allowed us to identify the formation of large aggregates or hydrophobic flocs depending on the TTAB concentration. Formation of NCC-TTAB complexes in aqueous solutions was confirmed by a charge reversal from negative to positive charge on the NCC rods. The effect of electrolyte in shielding the negative charges on the NCC was observed from ITC, surface tensiometry and phase separation experiments. Several mechanisms have been proposed to explain the above results. Grafting of PEGMA on the NCC surface was confirmed using FTIR and ITC experiments. In phase separation experiments NCC-g-PEGMA samples showed greater stability in the presence of TTAB compared to unmodified NCC. By comparing ITC and phase separation results, an optimum grafting ratio (PEGMA : NCC) for steric stabilization was also proposed.

ACKNOWLEDGEMENTS

I would like to express my deepest gratitude to my supervisor, Dr. K.C. Tam for his constant guidance, support and encouragement throughout my master's studies. I would also like to extend my gratitude to several undergraduate research assistants, Nate Grishkewich, Diana Chan & Daniel Au, who helped me in bringing this thesis to fruition. I would like to thank all the members of the Tam research group for their valuable insights and constant motivation. I wish to thank the University of Waterloo for providing me the opportunity to conduct meaningful research during my graduate studies. Last but not the least, I wish to express my immense gratitude to my loving family and friends for their patience and moral support.

TABLE OF CONTENTS

LIST OF FIGURES

uranyl acetate as a continuous stained background (b)

oxidation

LIST OF TABLES

LIST OF EQUATIONS

LIST OF ABBREVIATIONS

FTIR   : Fourier Transform IR spectroscopy

DLS   : Dynamic Light Scattering

SANS   : Small Angle Neutron Scattering

AFM   : Atomic Force Microscopy

ITC   : Isothermal Titration Calorimetry

DSC   : Dynamic Light Scattering

MC   : Methyl Cellulose

CMC   : Carboxymethyl Cellulose

CS   : Chitosan

ModMC   : Modified methyl cellulose

NCC   : Nanocrystalline cellulose

TTAB   : Tetradecyl trimethyl ammonium bromide

PEGMA   : Poly (ethylene glycol) methacrylate

CHAPTER 1

INTRODUCTION

1.1 CELLULOSE

One of the most abundant organic polymers known to mankind is cellulose, a biopolymer and a primary constituent of cell walls in plants. While cellulose can be obtained from wood, cotton and other plant fibres, wood pulp is the most common source for cellulose processing. The molecular structure of cellulose is shown in Figure 1.1. As seen from the structure, cellulose is a carbohydrate polymer made up of repeating β-d-glucopyranose and consists of three hydroxyl groups per anhydroglucose unit (AGU) giving the cellulose molecule high functionality. [1]
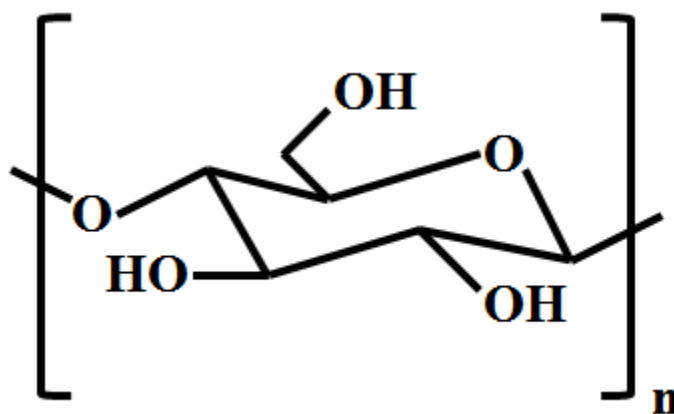
Figure 1.1 Structure of Cellulose [1]

The degree of polymerization (DP) of cellulose varies depending on the source and the kind of treatment rendered to the cellulose. For instance, DP of wood pulp is around 300-1700 and that of cotton is around 800-10000. Acid treatment of cellulose leads to DP values of 150-300

1

producing microcrystalline cellulose (MCC). The molecular structure of cellulose is of prime importance as it explains the characteristic properties of cellulose like hydrophilicity, chirality, biodegradability and high functionality. The hydroxyl groups of cellulose introduce partially crystalline (high order) regions interspersed with amorphous regions (low order); this is because of the extensive network of hydrogen bonds between the hydroxyl groups on the cellulosic chains. The morphology of cellulose can be described by three distinct fibre structures: elementary fibrils, microfibrils and microfibrillar bands. The lengths are of the order of a few hundred nanometres and the diameters are in the range of 1.5-3.5 nm, 10-30 nm and around 100 nm respectively. Cellulose also exhibits different properties in solution state depending upon the degree of substitution, concentration, solvent type and chain length distribution. [1]

Since it is derived from natural sources, cellulose and its derivatives have a number of advantages over their inorganic or synthetic counterparts, some of which are: [2]

- renewable in nature
- wide variety of cellulose forms available depending on the origin
- high functionality due to high surface coverage of hydroxyl groups
- biodegradable
- cheap and readily available

1.2 MOTIVATION AND RESEARCH OBJECTIVES

Due to the beneficial properties of cellulose, the focus of this thesis is the study of novel cellulosic structures at the nano-scale. The research work aims to study the properties of different cellulosic systems for their potential applications in cosmetic and pharmaceutical industry. This thesis explores two different cellulose based systems: polyampholyte microgels and nanocrystalline cellulose.

1.2.1. Polyampholyte Microgels

Polyampholyte microgels are crosslinked systems and are typically based on synthetic polymers. In this work, cellulosic derivatives such as carboxymethyl cellulose (CMC) and methyl cellulose (MC) were used to synthesize polyampholyte microgels which would be biodegradable and biocompatible in nature thereby making them suitable for potential drug delivery applications.

1.2.2. Nanocrystalline Cellulose

Nanocrystalline cellulose (NCC) is a rod-like crystalline product obtained from cellulosic sources. Due to its benign properties, this unique product has many potential applications in personal care (cosmetics) and pharmaceutical industries. In order to utilize NCC in personal care applications like conditioners, this work studies the interaction of NCC with an oppositely charged surfactant. Furthermore, NCC was also chemically modified by grafting in order to explore their potential in personal care applications.

1.3 PROJECT 1: POLYAMPHOLYTE MICROGELS

1.3.1 POLYAMPHOLYTES

Polyampholytes are defined as polymers capable of possessing both positive and negative charges on their backbones. The properties of polyampholytes are dependent on intra-chain electrostatic interactions since both charges are present on the same backbone. Thus, the polyampholyte chain conformation would depend on two effects:

(1) *polyampholyte effect* which tends to attract the unlike charges on the same chain thereby causing chain compression

(2) *polyelectrolyte effect* which tends to repel the like charges on the same chain thereby causing chain elongation [3]

1.3.2 POLYAMPHOLYTE MICROGELS

Polyampholytes differ from polyelectrolytes in the sense that polyelectrolytes may possess *either* positive *or* negative charges on their backbones unlike polyampholytes which possess *both* charges on the same backbone. Microgels on the other hand are crosslinked polymer particles with sizes ranging from 100 nm to 1 μm that exhibit swelling in a good solvent. One of the most widely studied microgel systems is poly (N-isopropylacrylamide) or PNIPAM microgels which swell and de-swell in a solvent medium according to their LCST (lower critical solution temperature). [4] Microgels are extremely functional systems and depending on the constituent polymers, microgels exhibit a different stimuli responsive behaviour (swelling/de-swelling) in

response to different stimulus like pH, temperature, ionic strength, solvent and an external magnetic field (Figure 1.2). [5]
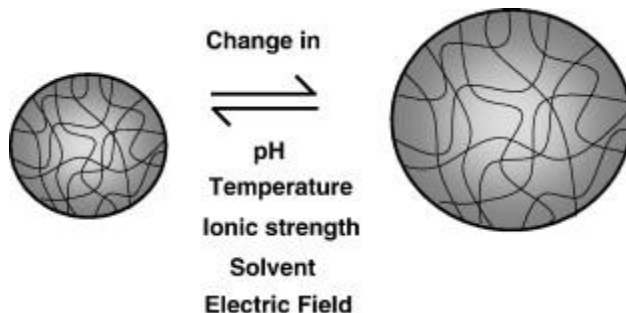
Figure 1.2 Microgel responsiveness (swelling/deswelling) in response to different external stimuli [5]

Thus, by combining the properties of *'polyampholyte'* and *'microgel'* we obtain *'polyampholyte microgels'* which are crosslinked polymer particles such that the constituent polymers are capable of possessing positive and negative charges on their backbones. Typically, the positive and negative charges come from pH-responsive functional groups like amino and carboxylic acid groups. At low pH, amino groups become protonated and exhibit positive charges while at high pH, carboxylic acid groups become deprotonated and exhibit negative charges.

1.3.3 pH-RESPOSNIVE BEHAVIOUR OF POLYAMPHOLYTE MICROGELS

At low pH, the amino groups in the polyampholyte microgel become protonated making the microgel chains positively charged. The positively charged chains within the microgel repel each other electrostatically which swells the microgels. The swelling of polyampholyte microgels at low pH is also explained by Ho et al.; the authors explain that due to trapping of counterions in

the microgel network, an increase in the osmotic pressure inside the microgel causes the microgel to swell in size. [6] Similarly, at high pH, the carboxylic acid groups in the polyampholyte microgel become deprotonated thereby imparting negative charges to the microgel. The negatively charged chains within the microgels repel each other, which causes the microgel particles to swell. However, in the neutral pH range, the microgel has an equal number of positive and negative charges resulting in an overall neutral environment within the microgel. Hence, the microgel particles tend to flocculate in neutral pH ranges and the pH at which this phenomenon occurs is called the isoelectric point (IEP). Grafting the microgel particles with a steric stabilizer prevents flocculation in neutral pH ranges. [6]

Figure 1.3 shows the pH-responsive behaviour of polyampholyte microgels composed of poly(methacrylic acid) (PMAA) and poly(2-(diethylamino)ethyl methacrylate) (PDEA) polymers. [7] Thus, polyampholyte microgels consisting of carboxylic acid and amino groups would typically show pH responsive behaviour i.e. swelling at high and low pH and deswelling at neutral pH.
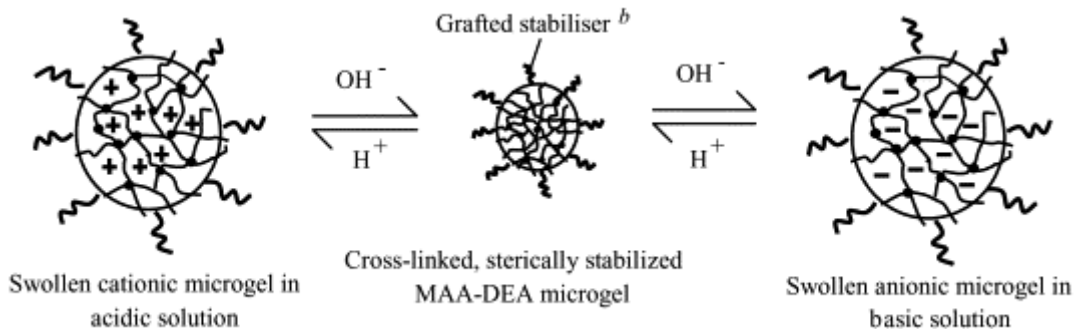
Figure 1.3 pH responsiveness of polyampholyte microgels [7]

1.3.4 SCOPE OF POLYAMPHOLYTE MICROGELS PROJECT

Due to the pH-responsive character of polyampholyte microgels, they have potential drug and protein delivery applications. [6] In this research project, polyampholyte microgels composed of biodegradable polymers like chitosan, carboxymethyl cellulose and methyl cellulose were synthesized. Chitosan (CS) is obtained by deacetylation of chitin [8], carboxymethyl cellulose (CMC) from carboxymethylation of cellulose [9] and methyl cellulose (MC) from methylation of alkali cellulose [10].

The advantages of using these biodegradable polymers in place of synthetic monomers for microgel synthesis are as follows:

1. The polymers are biodegradable and biocompatible [11] [8] [12]

2. They are non toxic and non allergenic [2]

3. They are readily available as they are obtained from natural sources hence they are recyclable and cost effective [2]

4. Using polymers as starting material instead of synthetic monomers would ensure that there are no toxic initiators after microgel synthesis, making them suitable for biomedical and pharmacological applications [13] [14]

Two different polyampholytic systems were synthesized: chitosan-carboxymethyl cellulose (CS-CMC) and chitosan-modified methyl cellulose (CS-ModMC). These systems were synthesized using inverse microemulsion technique and EDC carbodiimide chemistry (for crosslinking). For the first system, chitosan and carboxymethyl cellulose were chosen as they

would provide amine and carboxylic acid functionality to the microgels. As a further extension of the first system, chitosan-modified methyl cellulose system was also synthesized, wherein the methyl cellulose was modified by carboxymethylation [9] to incorporate the carboxylic acid functionality. Also, methyl cellulose contains methoxide groups which initiate hydrophobic interactions between the methyl cellulose chains causing them to aggregate at LCST. [15] Thus, combining the pH-responsive character of chitosan and the thermo-responsive character of methyl cellulose, a dually responsive system was synthesized from biodegradable and biocompatible polymers.

1.4 PROJECT 2: NANOCRYSTALLINE CELLULOSE

1.4.1 BACKGROUND ON NANOCRYSTALLINE CELLULOSE

Nanocrystalline cellulose (NCC) refers to rigid rod-like crystals produced by sulphuric acid treatment of native cellulose. The rod-like crystals have the following typical dimensions: diameter in the range of 10-20 nm and lengths in the range of a few hundred nanometres (Figure 1.4). Depending on the origin of the cellulose and the hydrolysis conditions, NCC possesses different morphologies, for e.g. crystallites from tunicates and green algae have lengths in the range of a few micrometers while crystallites from wood and cotton have lengths of the order of a few hundred nanometres. [16] [17]
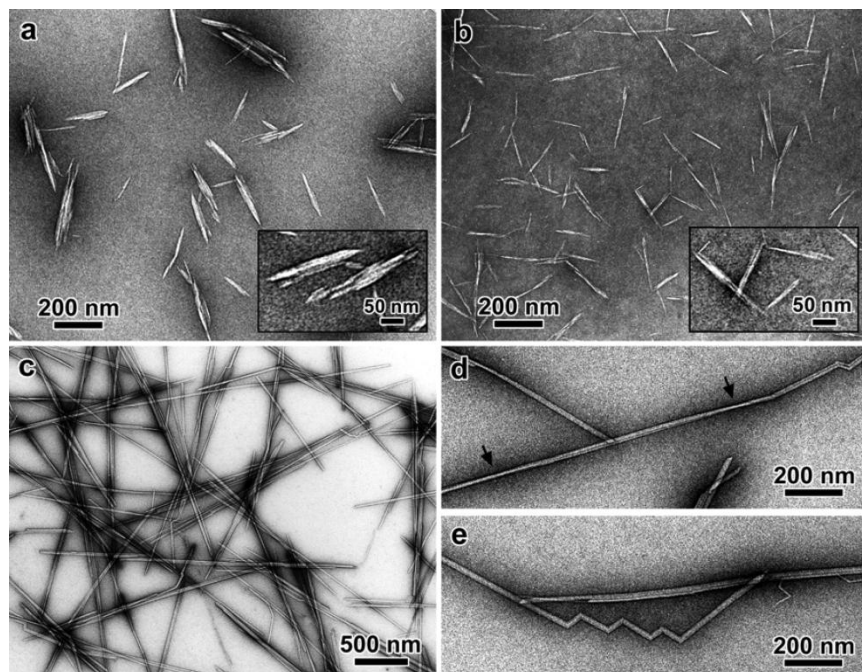
Figure 1.4 TEM micrographs of nanocrystals obtained from various sources (a) cotton (b) avicel (c-e) tunicate [16]

As was mentioned earlier, native cellulose consists of amorphous and crystalline regions. When native cellulose is subjected to harsh sulphuric acid treatment, the hydronium ions migrate to the amorphous regions since they have lower density compared to the crystalline regions. The hydronium ions cleave the glycosidic linkages hydrolytically thereby releasing the individual crystallites (Figure 1.5). Acid hydrolysis is dependent on different parameters, such as acid concentration, time of reaction, temperature of reaction and the specific acid used for the treatment. Another important characteristic of NCC is that the individual crystallites have negative charges on their surface due to the formation of sulphate ester groups during acid treatment. The negatively charged NCC forms stable aqueous suspensions due to the electrostatic repulsion between the individual crystallites. [17]
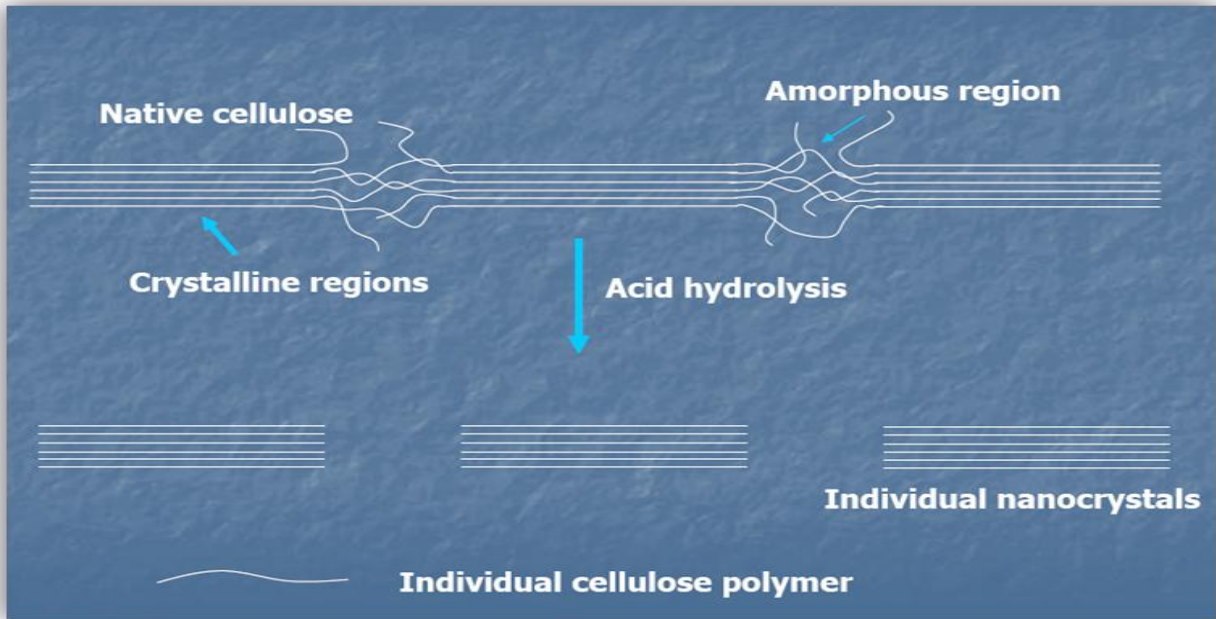
Figure 1.5 Sulphuric acid treatment of native cellulose [121]

1.4.2 SCOPE OF NANOCRYSTALLINE CELLULOSE PROJECT

Obtained from native cellulose (wood, cotton or plant fibres), nanocrystalline cellulose (NCC) possesses a number of advantages, such as biodegradability, recyclability, availability, non-toxicity etc. NCC can be used for various applications such as security paper, coloured pigments or as a filler material for nanocomposites. [17] Due to its polyelectrolyte characteristics, NCC can potentially be used in personal care applications such as conditioners. Personal care applications often employ surfactant formulations and studying the effect of surfactants on NCC suspensions would be imperative if NCC is to be used in personal care and cosmetics industry. Therefore, this research project involves the study of polymer-surfactant interactions between NCC and a cationic surfactant. The presence of a cationic surfactant would disrupt the

electrostatic repulsion between the NCC rods thereby destabilizing aqueous NCC suspensions (causing phase separation) and making NCC a poor candidate for cosmetic applications. Furthermore, the presence of electrolytes would shield the negative charges on the NCC, which introduces another parameter in the study of polymer-surfactant interactions. Consequently, poly (ethylene glycol) methacrylate (PEGMA) was grafted onto the NCC surface in order to prevent the destabilization of NCC suspensions in the presence of a cationic surfactant. Therefore, the scope of this research project is to understand the nature of binding and types of interactions between NCC and a cationic surfactant. This work also aims to study the effect of PEGylation (grafting PEGMA on the NCC surface) on the polymer-surfactant interactions and its effectiveness in preventing destabilization.

1.5 OVERVIEW OF THESIS

This thesis covers both research projects comprehensively. Chapter 2 discusses previously published literature on polyampholyte microgels and nanocrystalline cellulose. This chapter is divided into two subsections:

2.1 Polyampholyte microgels

2.2 Nanocrystalline cellulose (NCC)

Chapter 3 gives a brief theoretical background on various characterization techniques used to study the properties of polyampholyte microgels and the NCC system. In this thesis, the experimental results and discussions are collated into three chapters. Chapter 4 discusses the project on "Biodegradable and biocompatible polyampholyte microgels from chitosan, carboxymethyl cellulose and modified methyl cellulose". Chapters 5 and 6 focus on two different

NCC systems: NCC-TTAB and NCC-PEGMA. These chapters discuss two interrelated projects: "Interaction of nanocrystalline cellulose with an oppositely charged surfactant in an aqueous medium" and "Steric stabilization of nanocrystalline cellulose in the presence of an oppositely charged surfactant"

Chapter 7 lists the important inferences and conclusions drawn from experimental studies on polyampholyte microgels and nanocrystalline cellulose. Furthermore, this chapter also offers recommendations for future studies in both research projects. Chapter 7 is further divided into two subsections:

7.1 Project 1: Polyampholyte microgels

7.2 Project 2: Nanocrystalline cellulose

CHAPTER 2

LITERATURE REVIEW

2.1 POLYAMPHOLYTE MICROGELS

Numerous papers have been published on chitosan, carboxymethyl cellulose and methyl cellulose; researchers have also investigated various systems which are a combination of the three polymers. The literature review discussed below is divided into the following subsections sections:

2.1.1 Chitosan

2.1.2 Carboxymethyl Cellulose

2.1.3 Methyl Cellulose

2.1.4 Microgel synthesis techniques

2.1.5 Combined systems from CS, CMC and MC polymers

2.1.1 CHITOSAN

Chitosan is a derivative of chitin, a natural polysaccharide obtained from exoskeletons of arthropods or from cell walls of yeast and fungi. Partial deacetylation of chitin in solid state under alkaline conditions or enzymatic hydrolysis of chitin using chitin deacetylase produces chitosan. After about 50% deacetylation of chitin, the final product called chitosan solubilises in an acidic medium. Chitosan dissolves in an acidic aqueous medium due to the protonation of amino groups in the presence of H^+ ions. A number of papers state that chitosan is soluble below pH~6 and can be easily dissolved in 1% acetic acid. The chitosan solubility is a complex function of degree of deacetylation, pH and ionic strength of medium, the type of acid used, acetyl group distribution, intra-molecular hydrogen bonds between hydroxyl groups and final drying conditions for chitosan preparation. Chitosan exists in semicrystalline state when in a solid form while complete deacetylation produces single crystals of chitosan. [18]
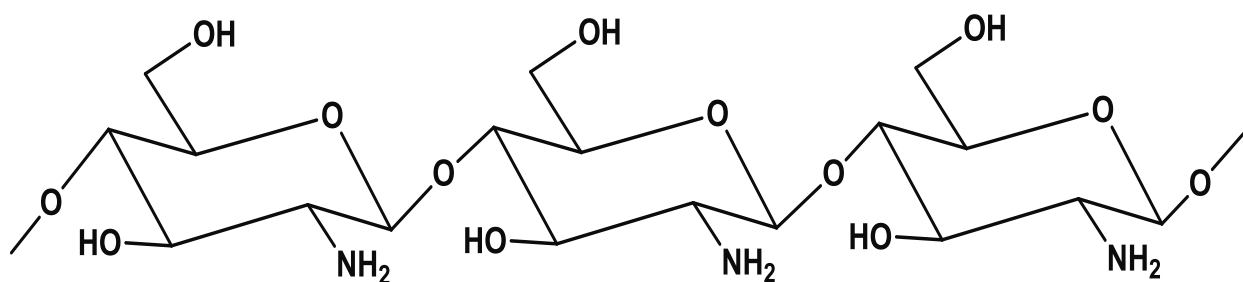
Figure 2.1 Structure of chitosan (CS)

Due to its polyelectrolyte nature at low pH, it has potential applications in aqueous solutions, films, hydrogels, sponges and fibres. Chitosan is used in a number of pharmaceutical and

biological applications due to its biodegradability, hydrophilicity and its anti-bacterial properties.

In a comprehensive review [18], Rinaudo summarized the properties and applications of chitosan.

Potential Biomedical Applications	Principal characteristics of Chitosan
Surgical sutures	Biocompatible
Dental implants	Biodegradable
Artificial skin	Renewable
Rebuilding of bone	Film-forming
Corneal contact lenses	Hydrating agent
Time release drugs for animals and humans	Non-toxic, biological tolerance
Encapsulating material	Hydrolyzed by lysozyme, wound healing properties,efficient against bacteria, viruses, fungi

Table 2.1 Properties and biomedical applications of chitosan [18]

Apart from complexing with copper and Fe^{+3} metal ions, chitosan also complexes electrostatically with anionic surfactants, such as sodium dodecyl sulphate (SDS). These interactions are said to be co-operative and surface tension curves (Figure 2.2) for chitosan-SDS clearly show CAC (critical aggregation concentration) and CMC (critical micelle concentration) transition points. Due to its cationic charge, chitosan also forms polyelectrolyte complexes with a number of oppositely charged anionic polyelectrolytes, such as polyacrylic acid, carboxymethyl cellulose, Xanthan, carrageenan, alginates, pectin, heparin hyaluronan, sulphated celluloses, dextran sulphate and chondroitin sulphate. [18]
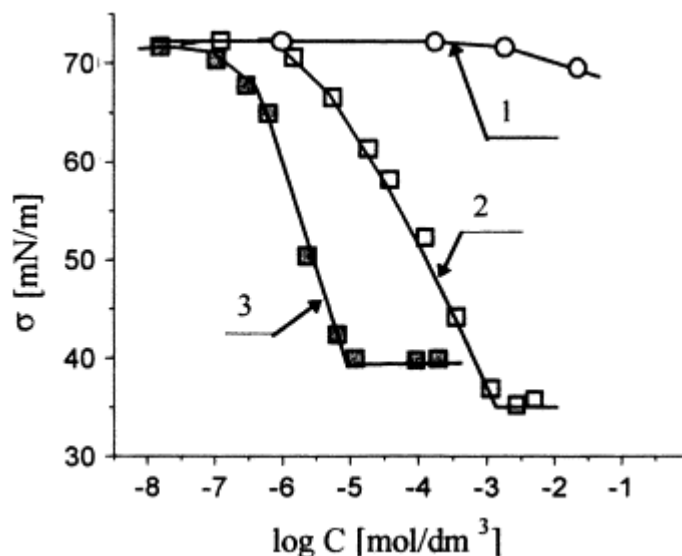
Figure 2.2 Surface tension curves for chitosan (o) SDS (□) and SDS into chitosan in

acetate buffer(■)[18]

Khor and Lim have also reported on the biocompatibility and biodegradability of chitosan for implantable applications. They summarize the laboratory results from various researchers who have previously shown that chitosan is degradable in vivo by lysozyme and that at least 50% deacetylated chitosan is easily degraded with no bioaccumulation. In some studies the researchers found that chitosan has an effect on cell proliferation and cell growth. Studies have also shown that chitosan facilitates cell migration for wound healing applications. [19]

2.1.2 CARBOXYMETHYL CELLULOSE

Carboxymethyl cellulose, popularly known as CMC, is a carboxymethyl ether of cellulose. Carboxymethylation is initiated using an alkali to activate the cellulosic chains and then reacted with monochloroacetic acid (or its sodium salt) to yield carboxymethyl groups through

Williamson ether synthesis. CMC is widely available in a number of grades for specific applications in the industry. For instance, extra pure CMC grade is used in food products, pharmaceuticals and toothpastes while semi purified and technical grades may be used for oil drilling muds, paper coatings, textile sizing, mining operations, detergents etc. [9]
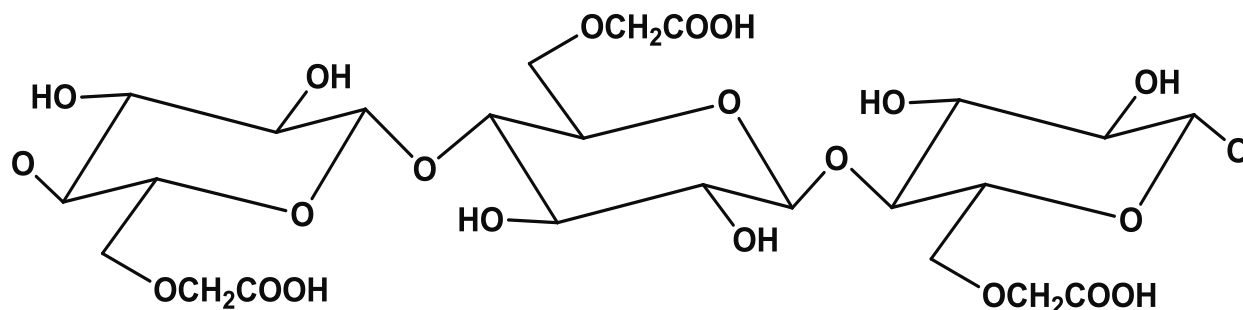
Figure 2.3 Structure of carboxymethyl cellulose (CMC)

One of the simplest methods of determining the number of carboxymethyl groups on carboxymethyl cellulose is the conductometric titration. [20] In this method, 0.1wt% of the CMC sample is typically used and the sample pH is increased to pH 11. This is done to ensure that the CMC is completely in its protonated form. Next the conductivity of the sample is measured while it is titrated with 0.1M HCl. Typical conductometric titration curve for sodium salt of CMC is shown below in Figure 2.4. The two transition points denote the initiation and completion of protonation of $-OCH_2COO^-$ groups on CMC. By calculating the volume of HCl reacted with the CMC (i.e. V_2-V_1), we can calculate the no. of milli equivalents of acid reacted. Finally dividing the no. of milli equivalents of HCl reacted by the wt. of CMC in the sample gives us the no. of milli equivalents of -COOH groups present per gram of the CMC sample (units: meq/g).
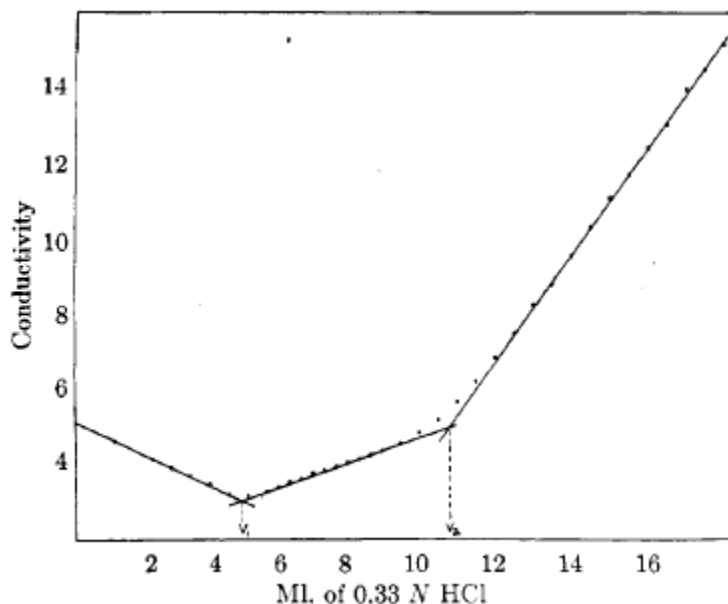
Figure 2.4 Conductometric titration of CMC-Na [20]

Commercial production of CMC involves swelling wood pulp or cotton linters in aqueous NaOH and then reacting the resulting alkali cellulose with monochloroacetic acid or its sodium salt. By manipulating the degree of polymerization of the starting materials, one can control the viscosity of the resulting CMC. Experimental studies have shown that carboxymethylation follows a nucleophilic mechanism; the reaction rate increases with temperature but decreases with increased substitution on the cellulosic chains. The maximum degree of substitution (DS) achievable from this slurry method is ~1.3-1.5. However, using multi-step carboxymethylation leads to higher DS values of ~2.3-2.6. Multistep carboxymethylation involves isolation of CMC and subsequent carboxymethylation to yield higher DS values. Some important derivatives of CMC have also been obtained by further derivatization. For e.g. partial hydrophobization produces polymeric surfactants from CMC and etherification with diethylaminoethyl (DEAE) produces a polyampholyte. [21] Formic acid is a derivatizing solvent for CMC such that CMC

18

formyl esters are soluble in dipolar aprotic solvents and can be regenerated to CMC-Na by reaction with NaOH. It has also been reported in literature that biodegradable CMC gels were formed using ferric ions as crosslinker. [9]

2.1.3 METHYL CELLULOSE

Due to strong intermolecular hydrogen bonding between the hydroxyl groups on the cellulosic chains, unmodified cellulose is insoluble in water. However, methylation of cellulose introduces hydrophobic groups on the cellulosic chains producing methyl cellulose which can be easily dissolved in cold water. [22]
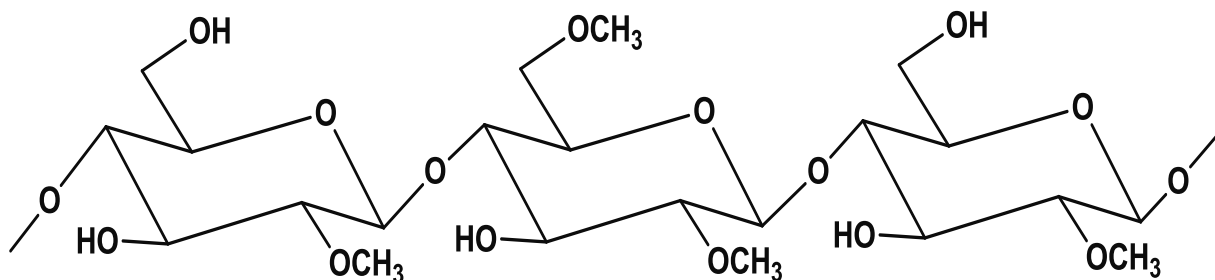
Figure 2.5 Structure of methyl cellulose (MC)

Mansour et al. have studied the effect of different variables on methylation reaction of cellulose. The methylation reactions are described as follows:

a. Production of alkali cellulose [23]

$$Cell\text{-}OH + NaOH \rightarrow Cell\text{-}ONa + H_2O$$

alkali cellulose I or II

19
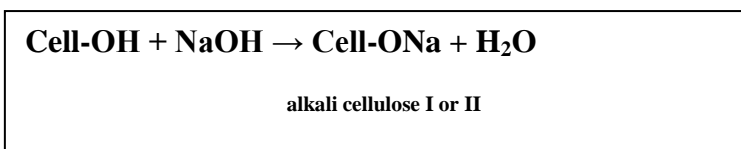
b. Methylation of alkali cellulose to produce methyl cellulose (MC) [23]
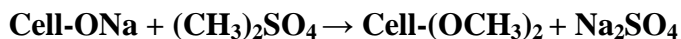
> **Cell-ONa + (CH$_3$)$_2$SO$_4$ → Cell-(OCH$_3$)$_2$ + Na$_2$SO$_4$**
>
> **alkali cellulose I or II**

Experimental results confirmed how different variables affect the methylation of cellulose and they are described as follows: [23]

1. Effect of NaOH concentration: Increasing the NaOH concentration beyond 25% lead to the formation of alkali cellulose II, which is more suitable for methylation than alkali cellulose I. Degree of substitution (DS) increased as the concentration of NaOH was increased up to 50%, primarily due to the formation of alkali cellulose II structures (beyond 25% NaOH) aiding methylation.

2. Effect of Methylating agent: Increasing the amount of methylating agent (DMS-dimethyl sulphate) decreased the DS values when all the other reaction conditions were kept constant.

3. Effect of liquor ratio: At 50% NaOH concentration and with the cellulose to DMS ratio set at 3, a liquor ratio (cellulose : alkali) of 1:5 was found to be optimum and gave higher DS values (up to 0.8) as the reaction time was increased. At higher liquor ratios, the DS decreased as reaction time was increased due to the formation of impenetrable gel networks; these gel networks make the active hydroxyl groups inaccessible to methylation.

Due to the presence of methoxide groups on their chains, methyl cellulose exhibits thermoreversible association and gelation on increasing temperature. There are three different forces acting in aqueous methyl cellulose solutions:

1. H-bonds between hydroxyl groups on the MC chains

2. H-bonds between hydroxyl groups on MC and the surrounding water molecules

3. Hydrophobic interactions between the methoxide groups on MC

At low temperatures, MC is soluble in water since the hydrogen bonding between MC and water molecules dominates all other interactions. Conversely, at elevated temperatures (~ 50-75°C), the hydrophobic interactions between methoxide groups dominate causing thermal gelation. [22]

Figure 2.6 shows heating and cooling curves for an aqueous MC solution. [24] At low temperatures, the water molecules surround the MC chains and form cage-like structures around thereby making MC soluble in water. As temperature is increased, the cage-like structure made by water molecules is broken down exposing the hydrophobic methoxide groups which begin to interact through intermolecular hydrophobic association. As temperature is further increased, hydrophobic associations take place throughout the solution and a sol-gel transition is observed. Figure 2.6 clearly shows that the cooling curve does not follow the heating curve and exhibits a peak at a much lower temperature with the appearance of a shoulder. This behaviour was explained by a delay in the gel-to-sol transition as the dissociation of MC gel takes place in two steps: disruption of intermolecular hydrophobic interactions and the formation of ordered cage-like water structures around the MC chains. [22]
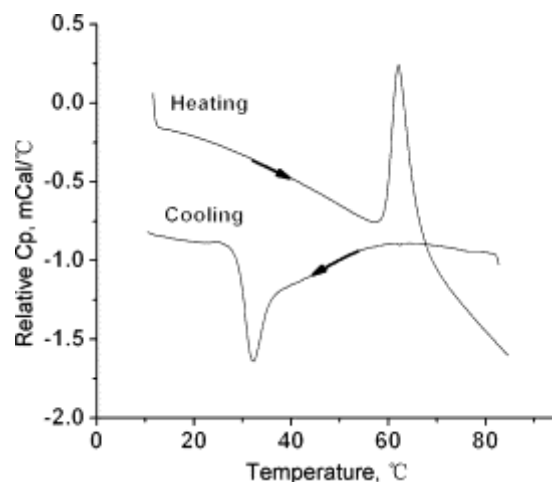
Figure 2.6 Calorimetric thermograms of MC for heating and cooling cycles at 1°C/min [24]

Li et al. also explained that molecular weight of MC does not have an effect on the shape of the thermograms or the peak positions. However, the amount of heat required for breaking the cage-like structures of water molecules was found to be greater for a higher M.W. MC than a lower M.W. MC sample. This is explained from the fact that a higher M.W. MC sample has lower solubility in water; hence more water molecules would be required to solubilize the chains. Additionally, a higher M.W. MC sample contains more flexible chains resulting in a larger fraction of intra-molecular coiled structures that require more water molecules to solubilize the chains. Experiments have also shown that addition of Cl⁻ ions decreases the sol-gel transition temperature and promotes the gelling behaviour in aqueous MC solutions. Cl⁻ ions are highly hydrated in water thereby breaking up the cage-like water structures surrounding MC chains. Since they compete with MC chains for water molecules, Cl⁻ ions make it harder for the MC chains to solubilise and easier to associate hydrophobically. On the other hand, I⁻ ions increase the sol-gel transition temperature and suppress the gelling behaviour. This is because I⁻ ions are

weakly hydrated and act as extra solvent molecules in the system thereby making it harder for the MC chains to associate hydrophobically. [22]

2.1.4 MICROGEL SYNTHESIS TECHNIQUES

Microgels/nanogels can be considered as micron/nano sized hydrogels with a number of advantages [25], such as high surface area for surface functionalization (high surface to volume ratio), porous network for incorporation of drugs, tunable/controlled size and water retention capability. Recently, a number of methods have been used to synthesize micro/nano gel systems and they are described as follows:

1. Photolithography techniques: For producing microgel particles, "Particle Replication In Nonwetting Templates" (PRINT) approach is used. A silicon master template is patterned using electron beam lithography; next, dimethyl acrylate functionalized oligomers of perfluoropolyether (PFPE) and a photoinitiator are poured on the master template and photocured to produce replica molds which are later used for microgel synthesis. [25] Figure 2.7 shows the difference between a PRINT process and a traditional lithography technique. While the lithography technique uses a wetting substrate for producing embossed films, a PRINT process uses non-wetting substrates for producing isolated microgel particles.
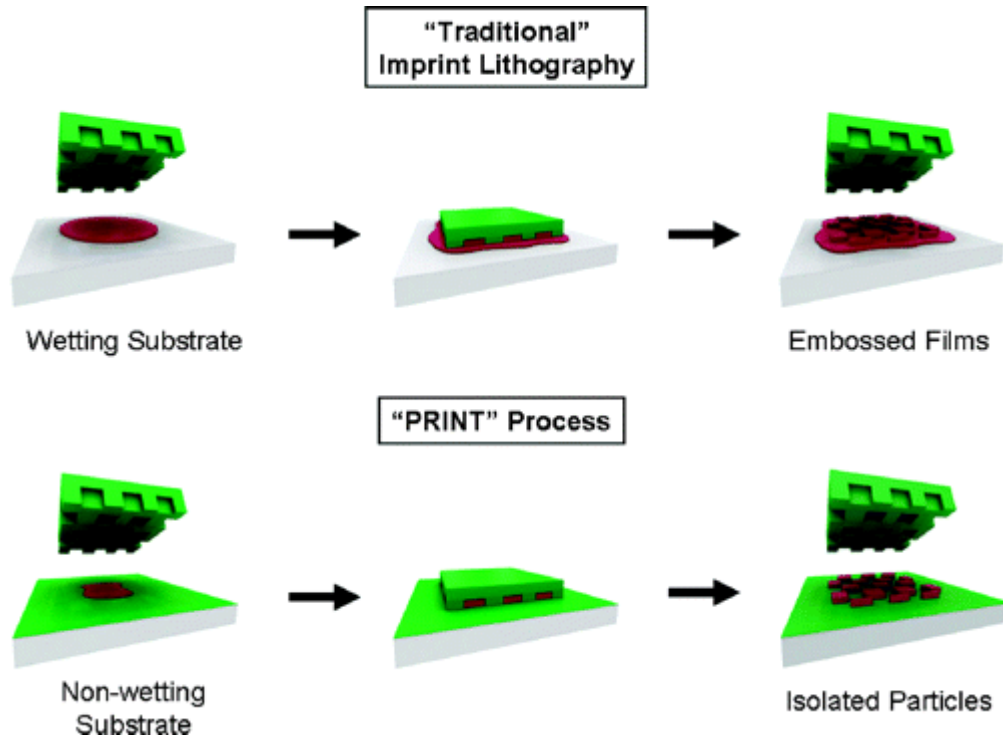
Figure 2.7 PRINT process for microgel synthesis [26]

2. <u>Microfluidics</u>: Microfluidic reactors (made from PDMS or polyurethane) are used to synthesize microgels. These reactors consist of microchannels for allowing flow of reactants to a tapered nozzle to produce droplets which can be either photo-crosslinked or chemically crosslinked. Figure 2.8 shows a schematic for producing alginate microgels by ionic gelation in a microfluidic reactor. [25]

3. <u>Inverse miniemulsion technique</u>: In this technique a water-in-oil (W/O) inverse emulsion is formed using water soluble polymers in aqueous droplets and an organic solvent, such as hexane as the continuous organic phase. Span 80 and Aerosol OT are used as oil-soluble surfactants to emulsify the aqueous and oil phases. [25]

a)

A: dispersion of CaCO₃ in aqueous alginate solution
B: solution of acetic acid in soyabean oil

• Calcium carbonate
∿ Sodium alginate

b)

C: aqueous alginate solution
D: mixture of soybean oil and (CH₃COO)₂Ca

• Calcium acetate
∿ Sodium alginate
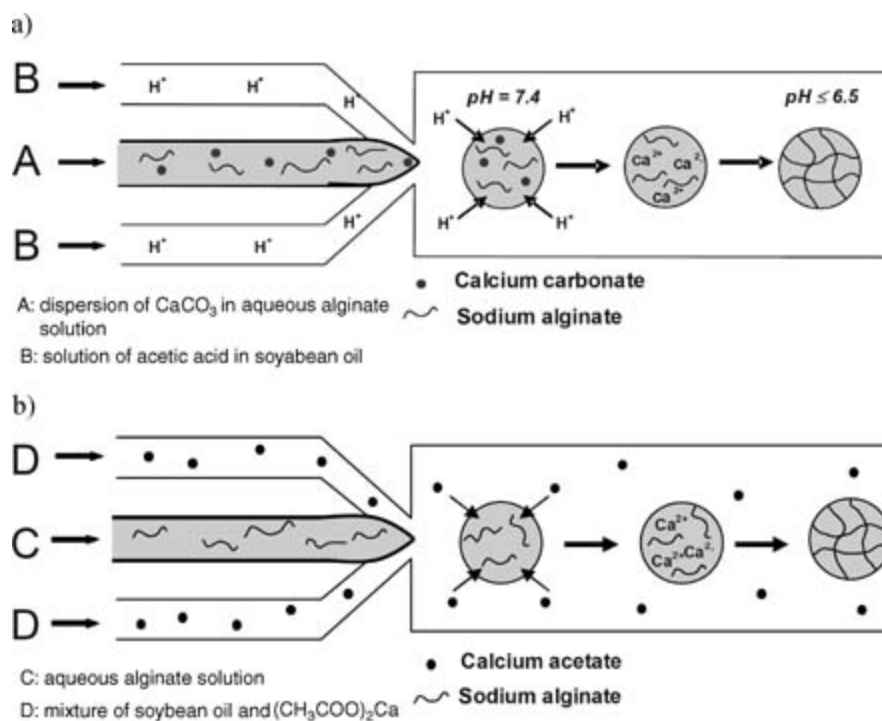
Figure 2.8 Production of alginate microgels using (a) internal gelation (b) external gelation [27]

4. <u>Reverse micellar method</u>: This approach is similar to that of the mini-inverse emulsion technique but it requires large amount of oil-soluble surfactants like Span 65, Span 80 and Tween 80 to produce thermodynamically stable inverse emulsions. [25] A water-soluble crosslinker can be used to crosslink the aqueous polymer droplets (see Figure 2.9).

5. <u>Membrane emulsification</u>: This method involves the use of Shirasu porous glass (SPG) membranes with uniform pore sizes (0.1-18μm) to produce different microgel morphologies like microspheres, hollow spheres, core-shell particles etc. The technique involves two steps: membrane emulsification and redispersion of formed droplets in a continuous phase to produce W/O, O/W, O/W/O or W/O/W (see Figure 2.10). [25]
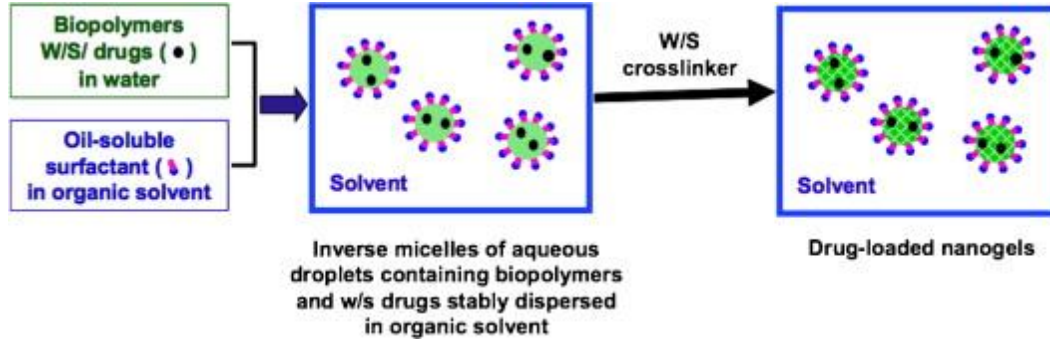
Figure 2.9 Reverse micellar method [25]
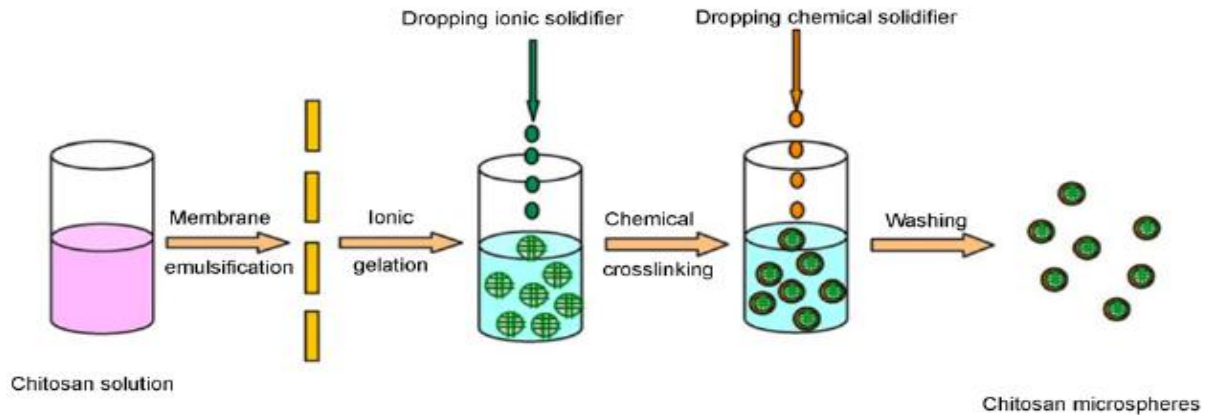
Figure 2.10 Chitosan microspheres from membrane emulsification [28]

6. Dispersion polymerization: In this method, all the reactants including monomers and initiators are dissolved in a continuous organic phase. When the polymerization begins, the polymers partition from the organic phase and form dispersed droplets in the organic phase stabilized by polymeric stabilizers. Precipitation polymerization is also similar to dispersion method where a crosslinker is used to form the microgel particles to precipitate them from an initially homogeneous solution. [25]

26

7. <u>Inverse micro emulsion polymerization (IMEP)</u>: While inverse mini emulsions in that mini emulsions are kinetically stable below, near or above the CMC, micro emulsions are thermodynamically stable only upon the addition of large amounts of surfactants. [25] Inverse microemulsion method is especially useful for water-soluble polymers that polymerize in bulk instead of forming microgel particles. [6] Ho et al. have synthesized polyampholyte microgels using a mixture of non ionic surfactants Brij 92 and Brij 96. Mixing non-ionic surfactants in different ratios produces different hydrophile-lipophile balance (HLB) values. HLB values in turn tune the phase inversion temperature (PIT) values for an inverse emulsion. Thus, non-ionic surfactants mixed in a certain ratio can be used to produce a W/O inverse emulsion when the temperature is increased beyond their PIT value. [29] After the phase inversion, water droplets contain the water soluble polymers and the water soluble crosslinker thereby producing crosslinked microgel particles.

2.1.5 COMBINED SYSTEMS FROM CS, CMC AND MC POLYMERS

This section describes other novel systems developed using chitosan (CS), carboxymethyl cellulose (CMC), methyl cellulose (MC) or combinations of them. A brief description of chitosan-carboxymethyl cellulose systems and chitosan-methyl cellulose systems is provided.

Chitosan-carboxymethyl cellulose systems

Chitosan-carboxymethyl cellulose microspheres were prepared using emulsion phase separation method and bovine serum albumin (BSA) was encapsulated in the microspheres to study their release kinetics. The microspheres were formed by the hydrogen bonding between the two polymers to produce insoluble polyelectrolyte complexes. BSA encapsulation efficiency was calculated around 75% and its release was controlled by the amount of chitosan in the microspheres (i.e. on account of more compact structure). It was also observed that at low pH (gastric juices), the microspheres had a lower swelling degree and lower BSA release as compared to pH 7.2 (intestinal fluids). The authors explained that at lower pH, chitosan is highly protonated and forms very compact/dense microspheres due to strong electrostatic interactions with the carboxylic acid groups on CMC. [30]

Enzymatic hydrolysates of chitosan and CMC have been used to produce biocompatible nanoparticles. Chitosanase and cellulase were used to enzymatically hydrolyze chitosan and CMC. The enzymatic hydrolysates were mixed at intermediate pH of 5.6 so that nanoparticles would form due to the electrostatic interaction between negatively charged carboxylic acid groups on CMC and positively charged amino groups on chitosan. It was shown that without subjecting the polymers to enzymatic hydrolysis, the molecular weight of the polymers was too high for nanoparticle formation. Upon hydrolysis, it was observed that increase in hydrolysis time reduced the M.W of chitosan and the nanoparticles became smaller in size. The nanoparticles also showed high stability under a variety of conditions, such as low pH (~3), high ionic strength (1M NaCl) and low temperature (4°C). [31]

The same research group also studied the entrapment and release of various compounds from the nanoparticles. Negatively charged compounds like Texas Red and DNA fragments, amphoteric molecules like OVA, and positively charged compounds like trypsin inhibitor could be easily entrapped due to formation of electrostatic complexes with the nanoparticles. However, non-ionic FITC-dextran could not be trapped as hydrophobic interactions with chitosan hydrolysates could not drive entrapment. In a 3 hour study, OVA and trypsin inhibitor showed a 50% release while Texas Red and DNA fragments showed less than 1% release since they interact very strongly with the nanoparticles. Addition of lysozyme to nanoparticles trapped with Texas Red and DNA fragments released most of the compounds within a day. [32]

Chitosan-methyl cellulose systems

Chitosan-methyl cellulose polymeric complexes have been prepared by Ioshchenko et al. by mixing the polymer solutions in a certain ratio and casting a film on a glass substrate; this was then followed by vacuum evaporation of the solvent. Various chitosan polymeric complexes were also shown to decontaminate water by removal of metal ions, petroleum products and phenols. The polymer complexes showed stability when examined under thin-layer chromatography and the polymers associated to form macromolecular cavities with dimension of ~ 130 nm. For CS-MC complex, the degree of decontamination of water to remove petroleum products was 42.1% and for removal of phenol the efficiency was 23.6%. Also, CS-MC complex showed high retention for Cu^{2+} and Cd^{2+} and moderate-to-low retention for Fe^{3+}, Zn^{2+}, Ni^{2+} ions. Due to the presence of hydrophilic groups on methyl cellulose, CS-MC film also showed a large degree of swelling in water. [33]

Lagaron et al. have studied the biodegradability properties of nanofilled films of chitosan and methyl cellulose. Digital photographic evidence showed that addition of nanofillers montmorillonite and mica did not decrease biodegradation of the films and all films degraded within a 60 day period (see Figure 2.11). The authors observed that in general chitosan films degraded faster than methyl cellulose films. [34]
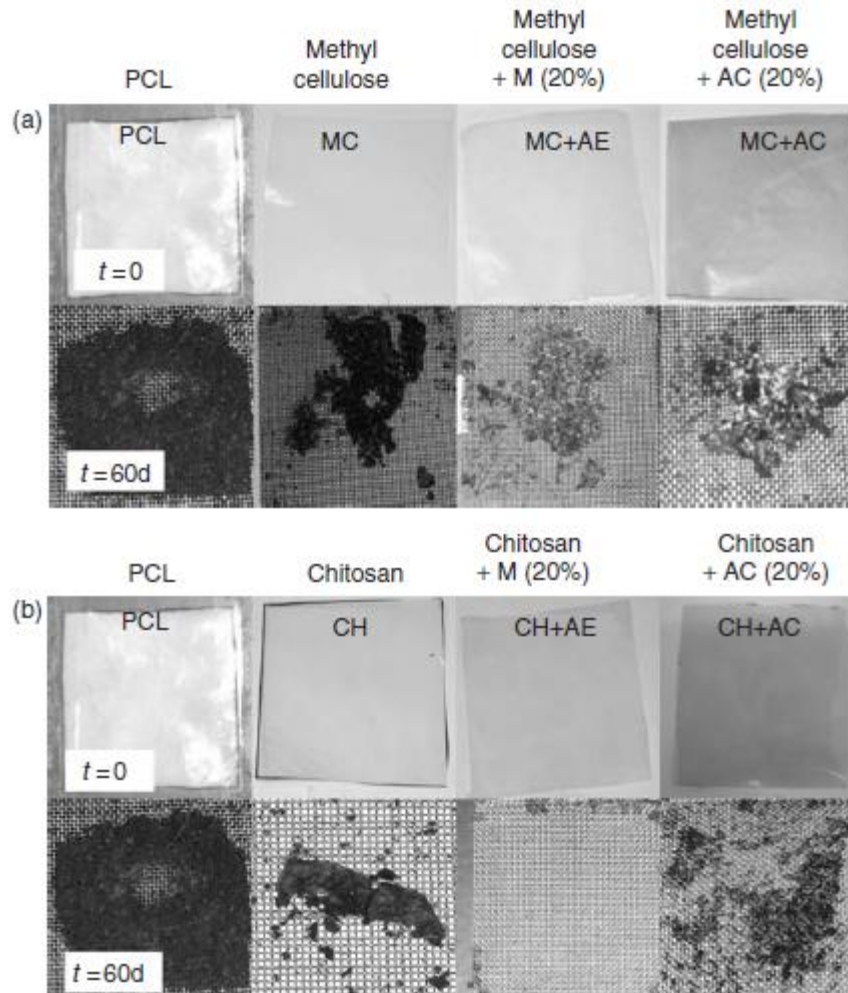
Figure 2.11 Biodegradation of chitosan (CS) & methyl cellulose (MC) films with nanofillers [34]

2.2 NANOCRYSTALLINE CELLULOSE

A review of recent literature indicates that there has been a rise in the number of publications related to the NCC system. NCC is a relatively new system and a number of research groups are involved in different aspects of NCC research. This literature review is divided into the following four sections:

2.2.1 NCC Synthesis

2.2.2 NCC Properties

2.2.3 NCC Characterization

2.2.4 NCC Modification

2.2.1 NCC SYNTHESIS

Acid treatment (acid hydrolysis) of native cellulose from a variety of sources like wood pulp, cotton, tunicate cellulose, bacterial cellulose, microcrystalline cellulose (MCC) produces nanocrystalline cellulose. The final properties of NCC depend on various factors like the cellulose source, reaction time and the type of acid used in the hydrolysis. Nanocrystals from tunicate and algae sources are several micrometers in length since the cellulose microfibrils in tunicate and algae sources are highly crystalline. Nanocrystals from bacterial cellulose also have dimensions similar to those obtained from tunicate and algal sources, while nanocrystals of smaller dimensions are obtained from cotton and wood microfibrils. When acid treatment is continued for a longer time period, shorter nanocrystals are produced. Moreover, acid hydrolysis

with sulphuric acid produces sulphate ester groups on the NCC surface due to the esterification of hydroxyl groups. These negatively charged sulphate ester groups produce very stable aqueous NCC suspensions due to electrostatic repulsion between the individual NCC crystallites. On the other hand, acid hydrolysis with hydrochloric acid does not produce as many negative surface charges on nanocrystalline cellulose, resulting in less stable NCC suspensions. [35]

Gray and co-workers synthesized and investigated the properties of *wood cellulose nanocrystals* produced from two wood sources: softwood (black spruce) and hardwood (eucalyptus). Keeping the reaction time, reaction temperature and acid-to-pulp ratio constant, the authors observed that the two wood cellulose suspensions possessed similar dimensions and surface charge. The critical concentration required to form anisotropic liquid phases was similar for both kinds of suspensions. Furthermore, it was observed that in the production of softwood suspensions, longer reaction times resulted in nanocrystals with shorter lengths, smaller diameters and lower polydispersity in the length of the nanocrystals. Larger acid-to-pulp ratio also produced shorter crystal length in the softwood suspensions with smaller PDIs. Combining both effects, higher acid-to-pulp ratio and longer reaction time, produced shorter length nanocrystals with narrow PDIs and increased critical concentration to form an anisotropic phase (confirmed by Onsager's phase separation theory). The authors also observed that surface charge and sulphur content of the nanocrystals can be decreased by the application of heat which de-esterifies the sulphate groups. [35]

Roman and Winter studied the thermal degradation and thermal stability of cellulose nanocrystals obtained from bacterial cellulose using thermal gravimetric analysis. With

increasing applications of NCC as fillers in nanocomposites, a study of this kind is important since processing temperatures in various composite applications is greater than 200°C. The authors observed that in the hydrolysis of bacterial cellulose, the number of sulphate groups on the nanocrystals produced could be increased by increasing the reaction time, reaction temperature, acid concentration and acid-to-pulp ratio. Increasing sulphate groups led to degradation at lower temperatures and a broader temperature range was observed as compared to unhydrolyzed samples. Also increasing the number of sulphate groups on nanocrystals increased the amount of charred residue indicating that sulphate groups are flame-retardant in nature. [36]

The authors of [36] describe the degradation as a two step process: low temperature process and high temperature process. The low temperature process involves the degradation of most accessible amorphous regions which are also highly sulphated. The high temperature process involves the degradation of less accessible interior crystalline regions that are less sulphated in comparison. For highly sulphated samples, an extra step involves the degradation of sulphated ends of crystalline regions. Using the Broido method, the authors calculated the activation energies of both degradation processes and concluded that more sulphate groups led to lower activation energies for degradation. It is also suggested that sulphuric acid may be instrumental in catalyzing the degradation process; direct catalysis by the acidic molecules could be a possible mechanism. Therefore, the authors concluded that using sulphuric acid produces sulphated nanocrystals which are susceptible to thermal degradation. At the cost of NCC aggregation, sulphation of nanocrystals can be reduced using shorter reaction times, lower acid-to-pulp ratio and lower acid concentrations. It is also suggested that hydrochloric acid be used for hydrolysis

since there is minimum sulphation during hydrolysis; however, such nanocrystals have higher aggregation tendencies without sufficient negative surface charges. [36]

Cellulose nanocrystals have also been produced from recycled pulp using microwave assisted enzymatic hydrolysis. Filson et al. synthesized cellulose nanocrystals using endoglucanase, a constituent of cellulases enzyme. Endoglucanase was used to selectively hydrolyze the amorphous regions in the recycled pulp and ultrasonication was further used to separate the individual crystallites. The authors observed that microwave heating produced NCC with greater yield compared to conventional heating since microwave heating is more selective and also reduces reaction time. After varying the reaction times, temperature, enzyme-to-pulp ratio and mode of heating, microwave-assisted reaction at $50^{o}C$ was suggested as an optimum condition for enzymatic hydrolysis of recycled pulp. [37]

Capadona et al. synthesized nanocrystals from microcrystalline cellulose (MCC) for use in nanocomposites applications. Partial hydrolysis of cellulosic sources with mineral acids produced microcrystalline cellulose particles with lengths in the range of 10-100 μm. [38] Cellulose nanocrystals were produced by the ultrasonication of commercially available MCC to produce dimensions similar to those obtained for cotton/wood cellulose nanocrystals [35]. In a slightly different approach, Bondeson et al. optimized the reaction conditions for sulphuric acid hydrolysis of MCC (Figure 2.12) to produce high yields of NCC with a short reaction time. The authors have considered five important parameters for optimizing the reaction conditions: starting concentration of MCC, concentration of sulphuric acid, reaction time, reaction temperature and sonication time. [39]
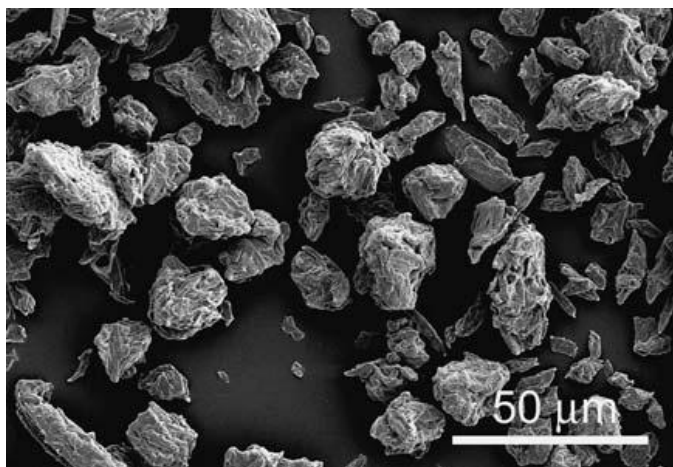
Figure 2.12 SEM image of MCC particles [39]

Response surface methodology was used to determine the effect of the five parameters in order to maximize yield and minimize reaction time. The model predicted that an increase in sulphuric acid concentration, reaction time and reaction temperature would decrease the size of MCC but not the NCC yield significantly. Neither the starting concentrations nor the sonication times have any significant effect on the MCC size or the NCC yield. However, the model predicted that sulphuric acid concentration and reaction time work synergistically in increasing the NCC yields. The optimum reaction conditions suggested by the model are as follows: sulphuric acid concentration - 63.5% (w/w); reaction time - 130.3 min; reaction temperature - 44∘C; MCC starting concentration - 10.2g/100mL; duration of sonication - 29.6 min. These optimal reaction conditions predicted by the model produced a low experimental yield of 30% which is attributed to the degradation of amorphous and crystalline regions during hydrolysis. [39]

Furthermore, NCC with a narrow size distribution was produced from MCC using differential centrifugation technique. MCC was hydrolyzed with sulphuric acid to produce NCC suspensions

35

which were further subjected to centrifugal treatment. Six different NCC fractions were produced by using differential angular velocities i.e. by creating relative centrifugal force (RCF) for each fraction at a constant centrifugation time. Initially the NCC suspension was subjected to 500 rpm for 10 minutes followed by rejection of the precipitate. Next the suspension left from the first centrifugation was subjected to 1000 rpm for 10 minutes. The precipitate obtained was identified as the 1st fraction. Next the suspension from 100 rpm centrifugation was subjected to 1500 rpm for 10 minutes. The precipitate obtained was identified as 2nd fraction. Again the resulting suspension was further subjected to centrifugation and the whole process was continued till six different fractions with different NCC yields were obtained. The authors also derived an inverse relation between the volume of NCC and the RCF applied as shown in Equation 2.1:

$$Log(V) = Log(Av) - Log(RCF)$$

Equation 2.1 Relation between vol. of NCC and RCF applied

Volume V is proportional to settling velocity v if the RCF is kept constant i.e. a larger NCC particle with more volume would settle with higher velocity as compared to a smaller NCC particle with lower volume. Considering one NCC particle, the settling velocity is proportional to RCF i.e. as the RCF is increased for an NCC particle, its settling velocity increases as well. Thus, the above equation indicates that increasing the RCF in multiple steps would separate NCC of different volumes if the centrifugation time is kept constant. On studying the volume and length distributions for all NCC fractions, the authors concluded that as RCF was increased the volume of the individual NCC fractions became smaller, the volume range was narrower, the lengths of

36

NCC particles in a certain fraction were smaller and the length distributions became narrower as well. [40]

Recently, Hirota et al. synthesized two types of cellulose nanocrystal samples: The first was TEMPO-mediated oxidation of mercerized cellulose and the second was TEMPO-mediated oxidation of acid hydrolyzed cellulose and mercerized cellulose. On comparing the light transmittance and rheological properties of both kinds of nanocrystals, the authors concluded that cellulose nanocrystals obtained from mercerized cellulose and TEMPO-mediated oxidation revealed greater water-dispersibility due to incorporation of highest number of carboxylate groups (during oxidation of C6 hydroxyl groups on the crystallite structures of mercerized cellulose). This sample also exhibited highest transmittance, shear stress and viscosity values as compared to the acid hydrolyzed sample due to higher carboxylate content on the nanocrystals thereby producing higher dispersibility and lesser number of bundles in water. [41]

It has been observed by several authors, that cellulose nanocrystals from tunicin and bacterial cellulose are larger in dimension compared to those obtained from wood and cotton. [42] This is because tunicin and bacterial cellulose are highly crystalline. Recently, Yun et al. synthesized cellulose nanocrystals by sulphuric acid hydrolysis of bacterial cellulose by varying the hydrolysis times. Bacterial cellulose produced by *Acetobacter xylinum* has a twisted ribbon-like cellulose structure. The authors conducted the acid hydrolysis with 65 wt% sulphuric acid at $70^{o}C$ and various hydrolysis times i.e. 1, 2 and 3 hours. Increasing the hydrolysis time decreased the aspect ratio of the resulting rods (since the rod length decreased and the width remained unaffected). Also, the sulphur content of the rods increased with increasing hydrolysis time. The

authors suggested that since bacterial cellulose is highly crystalline, the hydrolysis occurs due to surface reaction mechanism and the reduction in length after hydrolysis is not very drastic. [42] Apart from the sources discussed earlier, cellulose nanocrystals have also been produced from other miscellaneous sources, such as mulberry [43], *Syngonanthus nitens* (a polycarpic herb) [44] and coconut husk [45].

2.2.2 NCC PROPERTIES

Cellulose nanocrystals are cellulosic systems with unique properties. A number of research groups have synthesized and characterized cellulose nanocrystals in order to thoroughly study their unique properties and potential applications. The various properties of cellulose nanocrystals are described as follows:

Dispersibility of NCC in different media

Researchers have produced homogeneous dispersions of tunicate cellulose nanocrystals in an organic medium. Otto et al. produced tunicate cellulose nanocrystals with and without surface charge by hydrolyzing the tunicate with sulphuric acid and hydrochloric acid respectively. This is because hydrochloric acid does not impart any negative surface charge on the nanocrystals unlike sulphuric acid. The two samples prepared were identified as HCL-TW and SO_4-TW and were dispersed in a number of polar protic and aprotic solvents. Next, the authors conducted dispersibility studies of the prepared tunicate nanocrystals in various polar solvents such as water, N,N-dimethyl formamide (DMF), dimethyl sulfoxide (DMSO), N-methyl pyrrolidone (NMP),

formic acid and m-cresol. Freeze dried SO_4-TW re-dispersed easily in water, formic acid and m-cresol; while re-dispersion in DMF and DMSO took rigorous ultrasonication at 60^oC. As shown by FTIR, the use of formic acid led to the esterification of some hydroxyl groups thereby limiting the stability of SO_4-TW dispersions in formic acid. Moreover, the oxidative stability of m-cresol also places a limit on the stability of SO_4-TW dispersions in m-cresol. On the other hand, due to the absence of surface charge groups on HCL-TW sample, neither water nor aprotic solvents were able to produce homogeneous dispersions of HCL-TW sample. Thus, the HCL-TW samples tend to aggregate on account of strong hydrogen bonds and the absence of electrostatic repulsion between the crystallites. However, formic acid and m-cresol successfully re-dispersed the HCL-TW sample on account of their ability to break the hydrogen bonds between the crystallites. [46]

Viet et al. synthesized cellulose nanocrystals from cotton and studied their dispersibility in polar aprotic solvents like DMF, DMSO and formamide without the use of surfactants or chemical modification. The dispersibility was studied using crossed polarizers and shear birefringence was observed in samples that were re-dispersed in all three solvents. Moreover, the re-dispersed samples were stable in their respective solvents for months. However, DLS data suggested that some aggregation did occur in DMF and DMSO compared to water since the hydrodynamic radius measured in DMF and DMSO were higher. The authors also noted that addition of small amounts of water (0.2% w/v) was essential in dispersing the samples in polar aprotic solvents otherwise a gelatinous white precipitate was obtained. [47]

Chiral nematic behaviour of NCC suspensions

When the concentration of rod-like particles reaches a certain critical concentration, they form liquid crystalline phases like nematic, smectic or chiral nematic phases, depending on the type of rods and their external environment. Cellulose nanocrystals are negatively charged rods and expectantly, they show chiral nematic character beyond a critical concentration i.e. NCC suspensions transform from an isotropic phase to an anisotropic chiral nematic liquid crystal phase. [48]

According to Onsager's theory for perfect neutral rods, the critical concentration for formation of ordered phases depends on the aspect ratio L/D. Stroobants, Lekkerkerker, and Odijk (SLO) modified Onsager's theory for charged polyelectrolyte rods by including the effect of electrostatic repulsion on the phase separation. This is explained using two factors: increase in effective diameter and the twisting of rods due to the preferential perpendicular orientation. [48]
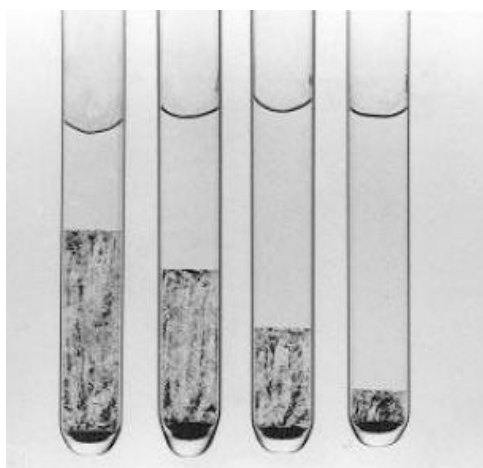
Figure 2.13 Phase separation of NCC at 8.78, 7.75, 6.85 and 5.78 wt % (left to right) [48]
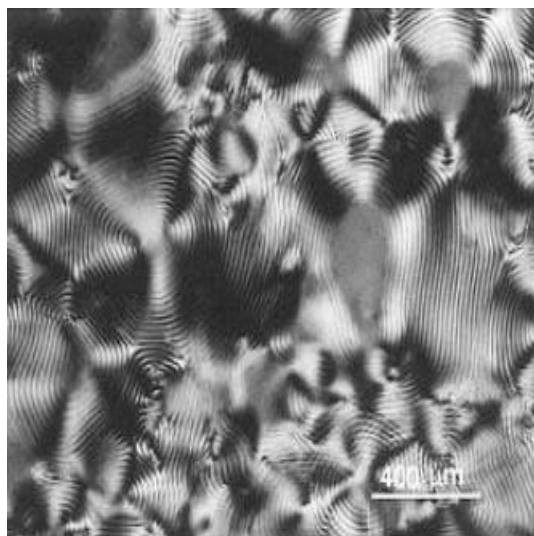
Figure 2.14 Anisotropic chiral nematic structure of NCC [48]

As explained by the SLO and Onsager's theories, cellulose nanocrystals exhibit phase separation from isotropic to anisotropic phase on increasing the concentration (typically above 5 wt %) and show chiral nematic character in their anisotropic phases (shown in Figure 2.13 and 2.14). [48] Apart from the visual observations, Dong et al. also plotted the volume fraction of the anisotropic phase (φ) vs. the total concentration for suspensions prepared in water and at a constant pH (Figure 2.15). The reason for considering constant pH was to maintain constant ionic strength. The phase diagrams clearly show the concentrations at which an isotropic → biphasic and biphasic → anisotropic transitions occur. Moreover, as the total concentrations of the suspensions increased, the coexisting concentrations of the anisotropic and isotropic phases also increased. [48]
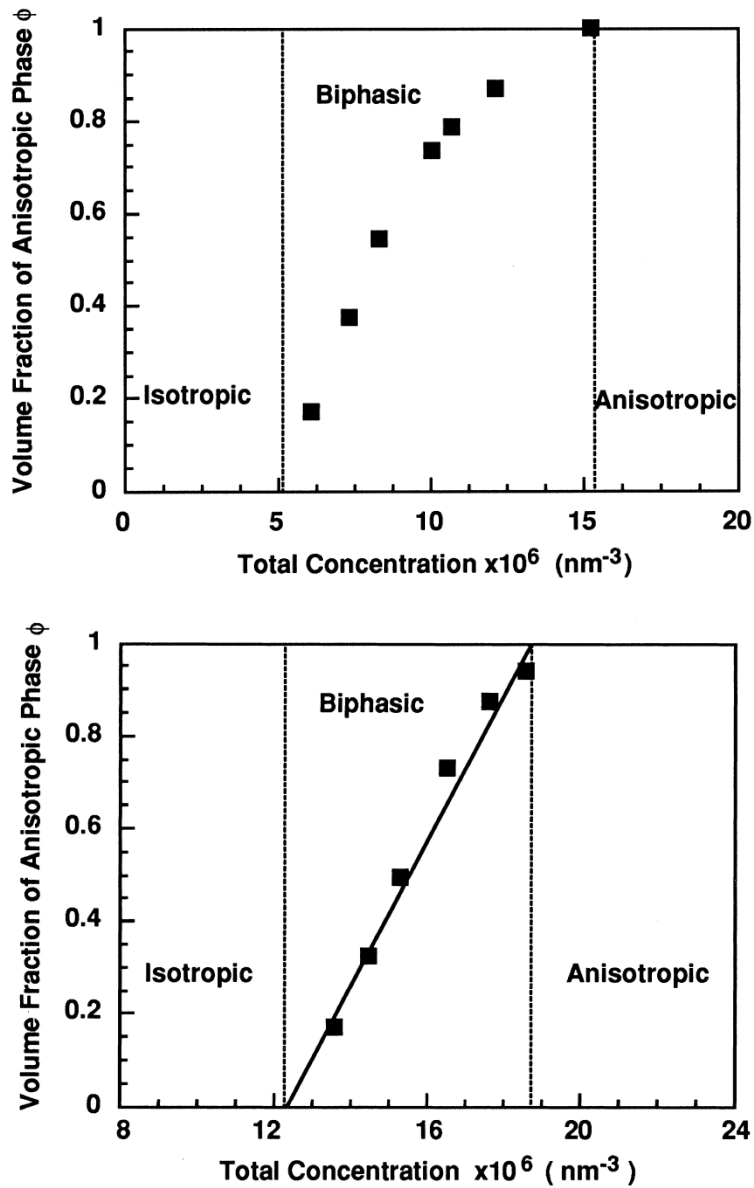
Figure 2.15 Volume fraction of anisotropic phase vs. total concentration for suspensions in water

(top) and at pH = 1.61(bottom) [48]

The effect of added electrolyte on the phase separation was also studied. Figure 2.16 shows how

the addition of electrolytes like HCl, NaCl and KCl decrease the volume fraction of the

anisotropic phase (φ) significantly, indicating that addition of electrolytes decreases the

anisotropic phase for a constant total concentration of suspension. Moreover, it was observed that the critical concentration required for isotropic $\rightarrow$ biphasic transition increased with the addition of salt   (Figure 2.17). The extent of chiral interactions in the ordered phase of the NCC suspensions was measured using the chiral nematic pitch. The chiral nematic pitch decreases on increasing the concentration of the NCC suspensions, indicating stronger interactions at higher concentrations. In addition, the presence of electrolytes also decreases the chiral nematic pitch suggesting stronger chiral interactions when electrolytes suppress the electrical double layer of the NCC molecules. [48]
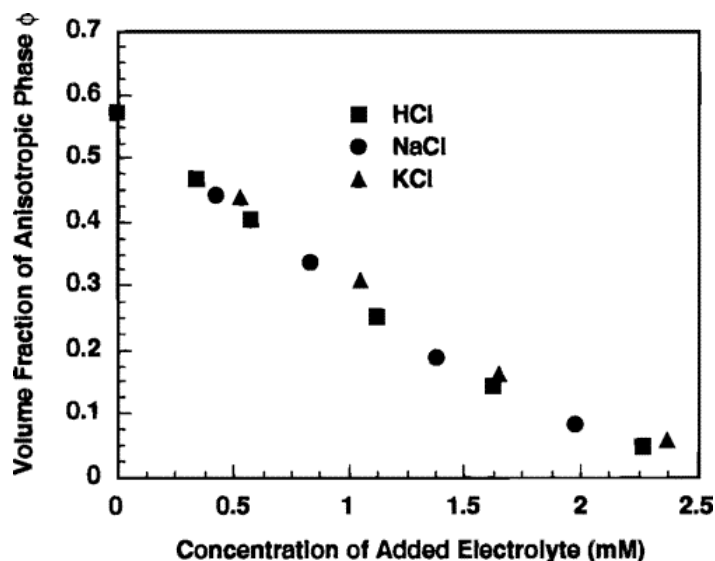
Figure 2.16 Effect of added electrolyte on volume fraction of anisotropic phase [48]
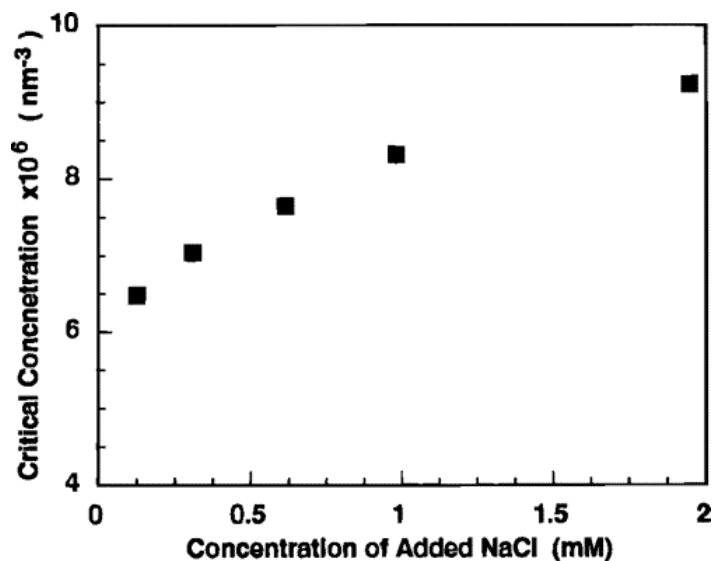
Figure 2.17 Increase in critical concentration with addition of salt [48]

Dong and Gray have also studied the effect of counter ions on the phase separation behaviour and stability of NCC suspensions. The counter-ions were divided into three groups: inorganic counter-ions, weakly basic organic counter-ions and highly basic organic tetraalkylammonium salts. It was observed that the type of counter ion had a significant effect on phase separation behavior of NCC suspensions. [49]

1. Inorganic counter-ions

For a given concentration of NCC suspension, the acid-form suspensions had the highest volume fraction of anisotropic phase (φ) and comparatively lower critical concentrations indicating that the acid-form of the suspensions have a higher tendency to form ordered phases in comparison to salt-form suspensions. The tendency to form ordered phases is expressed as:

S-H > S-Na > S-K > S-Cs (H_3O^+, sodium, potassium, cesium)
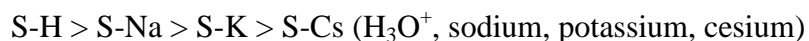
As the inorganic cations condense on the NCC surface, they decrease the hydrodynamic size of the crystallites thereby making it more difficult for the suspension to form ordered phases.

Increasing the atomic number decreases the size of the counter-ions and increases their mobility thereby making it harder for the counter-ion to reduce the hydrodynamic size of the crystallites.

2. Weakly basic organic counter-ions

Similar results were obtained with the acid-form suspensions having greater tendency to form ordered phases. The tendency to form ordered phases is expressed as:

S-NH$_4$ > S-Tri-MA > S-Tri-EA (ammonium, trimethylamine, triethylamine)

 2. Strongly basic organic counter-ions

It was observed that as the length of the alkyl chains on the counter-ions increased, the tendency to form ordered phase decreased. The tendency to form ordered phases is expressed as:

S-TMA > S-TEA = S-TBA > S-TPA (tetramethylammonium, tetraethylammonium, tetra-*n*-butylammonium, tetrapropylammonium)

As the organic counter-ions have alkyl chains, the authors suggest that there are two opposing forces, i.e. attractive hydrophobic interaction and repulsive steric interaction that control their behavior. As the size of the organic counter-ion increases for (S-NH$_4$ > S-Tri-MA > S-Tri-EA) series and (S-TMA > S-TEA > S-TPA) series, the hydrophobic interactions exceed the repulsive interactions, making it harder to form ordered phases thereby increasing the critical concentrations. For S-TBA counter-ion, the increase in alkyl chain length produces a balance between steric repulsion and hydrophobic attraction that results in a lower critical concentrations needed for the transition. [49]

Recently, Pan and co-workers studied various factors affecting the chiral nematic properties of NCC films. The authors observed that the inverse of chiral nematic pitch is proportional to the inverse of temperature according to the relation $1/P = C (T_N/T - 1)$, where C is a constant

dependent upon solution concentration and M.W. of the polymer and T_N is the temperature at which pitch becomes infinite. Previous studies [50] have also shown that NCC suspensions show negative diamagnetic susceptibility anisotropy as they dry under the influence of a magnetic field i.e. the crystallites align along their long-axes (perpendicular to the direction of the magnetic field) with their chiral nematic axis parallel to the applied magnetic field. The authors observed that for NCC films, the presence of magnetic field did not facilitate the formation of chiral nematic phase but only increased the chiral nematic pitch of the suspensions. An increase in magnetic field strength and increase in exposure time led to an increase in the chiral nematic pitch. These properties are probably due to alignment of NCC in magnetic fields, anisotropic shapes and non-zero magnetic susceptibilities of NCC rods. [51]

The effect of AC electric field on the alignment and orientation of NCC was investigated by Habibi et al. It was observed that application of an AC electric field to NCC suspensions deposited in between two metallic electrodes resulted in homogeneous alignment of NCC molecules. This behaviour is ascribed to the formation of an induced dipole moment on the NCC molecules in the presence of an electric field. Also, the presence of sulphate charges on the NCC surface allows the electric field to distort the counter-ion cloud thereby increasing the polarizability of the NCC molecules. Therefore, from the equation $\Gamma = \vec{\mu} \times \vec{E}$, the field induced torque for particles with anisotropic geometry (like NCC) is non-zero. It is this torque that aligns the NCC molecules in the direction of the applied electric field. The authors also observed that for tunicate whiskers alignment occurred after 2500 V/cm field was applied. The orientation was also highly sensitive to applied frequency of the electric field i.e. in the frequency range of $10^4 Hz < \upsilon < 10^6 Hz$, a maximum orientation was observed. It is suggested that for frequencies

below 10^4 Hz, NCC molecules show a tendency to aggregate while for frequencies above 10^6 Hz, the NCC molecules are attracted towards the electrodes. [52]

Rheological behaviour of NCC suspensions

A number of researchers have also focussed on alignment of NCC rods on application of shear. Lima and Borsali [17] studied the rheological characteristics of NCC suspensions from cotton linter source. The authors measured viscosity vs. shear rate values for different NCC concentrations (Figure 2.18) and the different regimes are explained as follows:

1. Regime 1: At low shear rates, shear thinning occurs due to the initial alignment of the NCC crystalline domains

2. Regime 2: At intermediate shear rates, a plateau occurs in the curve indicating the alignment of the NCC crystalline domains in the direction of flow

3. Regime 3: At high shear rates, another shear thinning region is observed; this occurs due to the breakup of the existing NCC crystalline domains into individual crystals which start to align under shear [17]
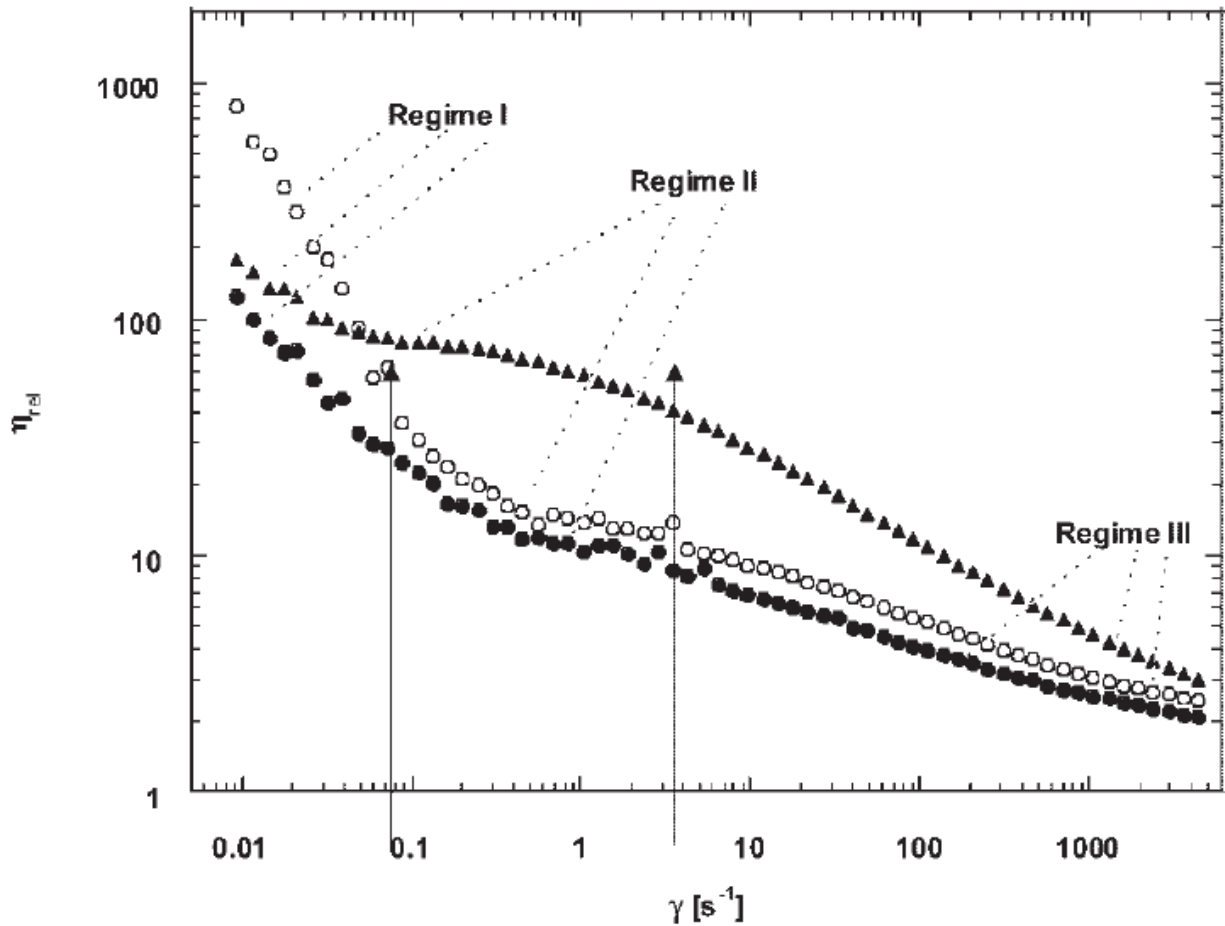
Figure 2.18 Viscosity vs. shear rate for different NCC concentrations (•) 1.2 wt%; (o)

1.7 wt% and (▲) 2.7 wt% [17]

Similar results were obtained by Orts et al. using SANS experiments. [53] As mentioned

previously, after a certain critical concentration, NCC suspensions phase separate into an

isotropic and an anisotropic phase. Based on this fact, Bercea and Navard [54] studied and

reported on the rheological properties of isotropic and anisotropic phases of NCC suspensions.

For the isotropic-at-rest (0-0.8 wt%), the authors explained that the two regimes were observed

for solutions below a concentration of 0.4 wt% and an isotropic → nematic transition occurred at

0.85 wt%. For isotropic-at-rest (below 0.4 wt%), two plateaus are observed at low and high shear rates. At low shear rates, the rods are randomly oriented due to which no change in viscosity is observed at low shear rates. At high shear rates, the rods become well oriented due to which viscosity becomes independent of shear rate (See Figure 2.19). This viscosity vs. shear rate relation at different shear rates is clarified further in Figure 2.20. On the other hand, for anisotropic-at-rest (1-3.5 wt%) a typical curve for liquid polymer solutions was observed, i.e. two shear thinning regions surrounding a plateau region. Shear thinning at low shear rates is attributed to defects in the texture and shear thinning at high shear rates is attributed to flow alignment of the suspensions.

Alignment of cellulose whiskers under the influence of shear was studied using SANS experiments. Ebeling et al. studied the rheological properties of 6.9 wt% suspensions composed of cotton microcrystals (aspect ratio ~ 10). [55] The experiments were conducted in two stages: radial scattering and tangential scattering patterns. Schematic of experimental setup is shown in Figure 2.21. The 2D scattering patterns obtained are shown in Figure 2.22. At low shear rates $(0.05s^{-1})$ the radial and tangential patterns possess isotropic rings and anisotropic peaks respectively, indicating that cellulose whiskers align themselves preferentially in the vertical direction. At high shear rates $(500s^{-1})$ the radial pattern shows anisotropic rings while the tangential pattern shows an isotropic ring, indicating that the cellulose whiskers change alignment from vertical direction to the direction of shear.
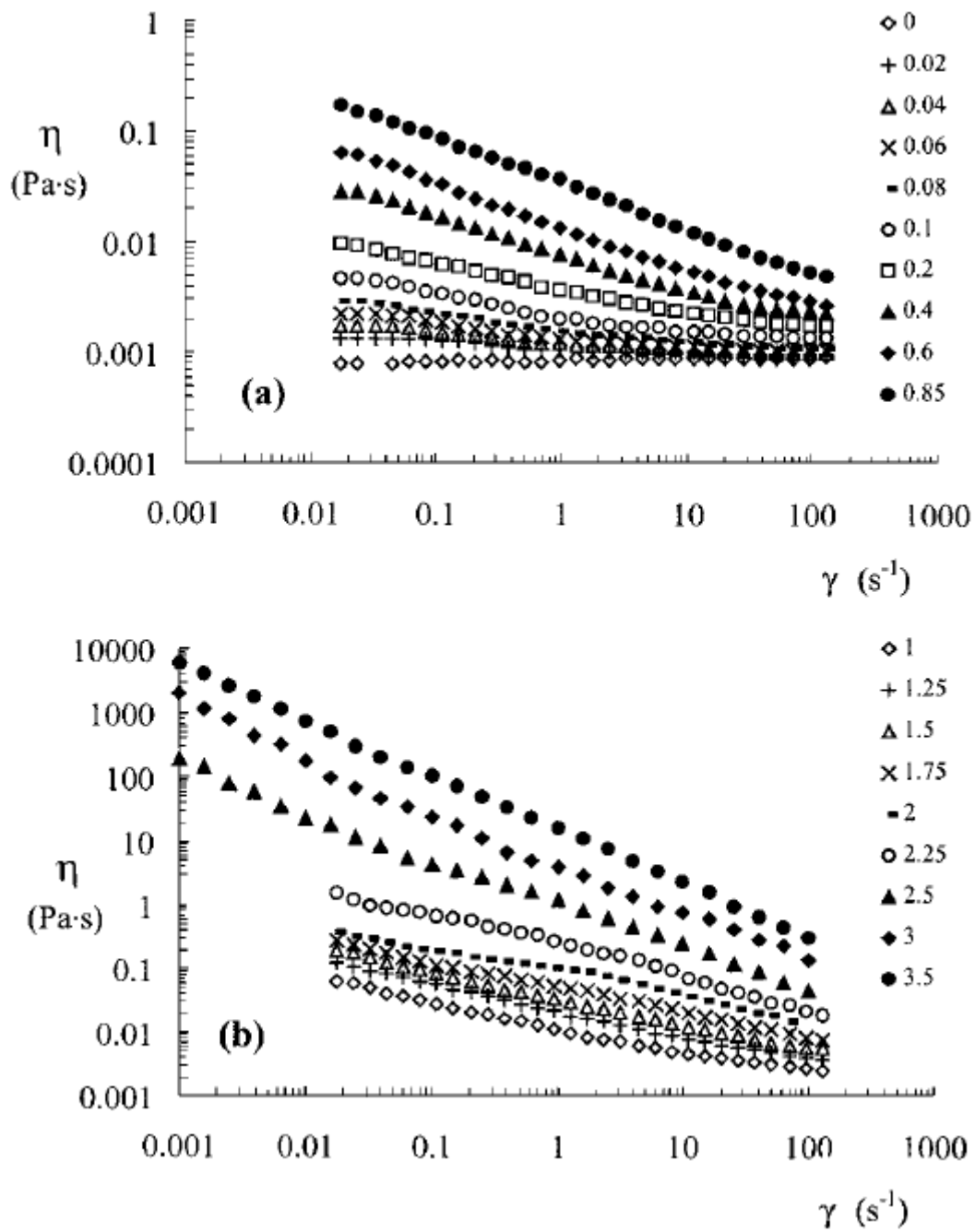
Figure 2.19 Viscosity vs. shear rate for different NCC concentration [54]
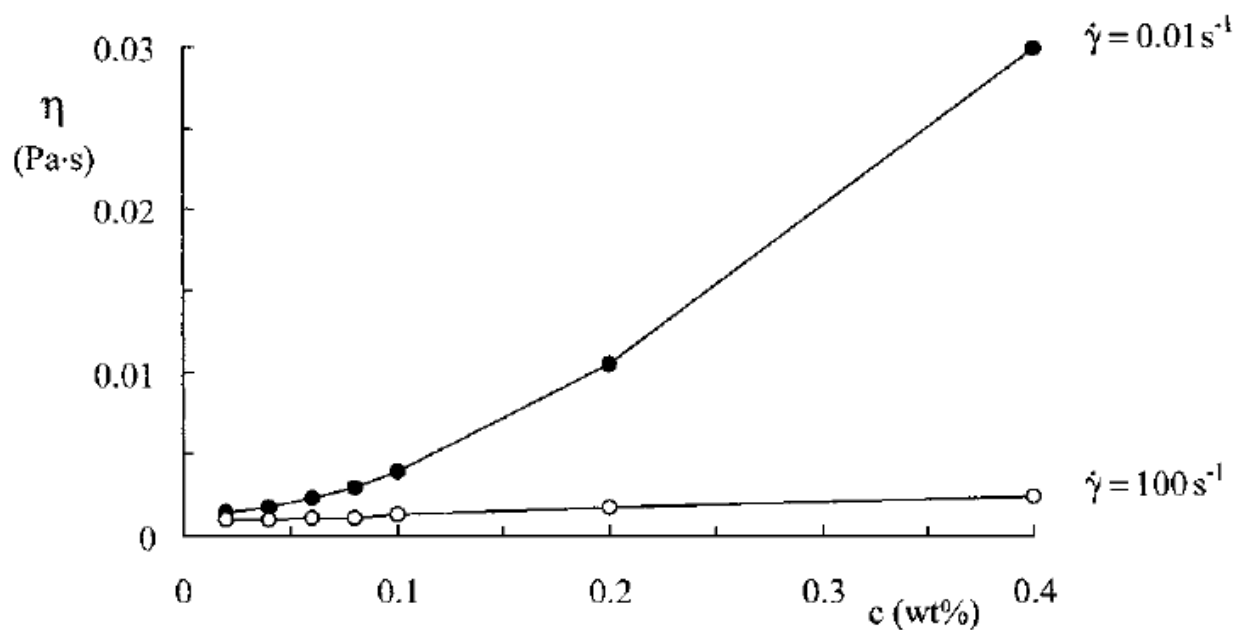
Figure 2.20 Viscosity vs. shear rate at different shear rates [54]
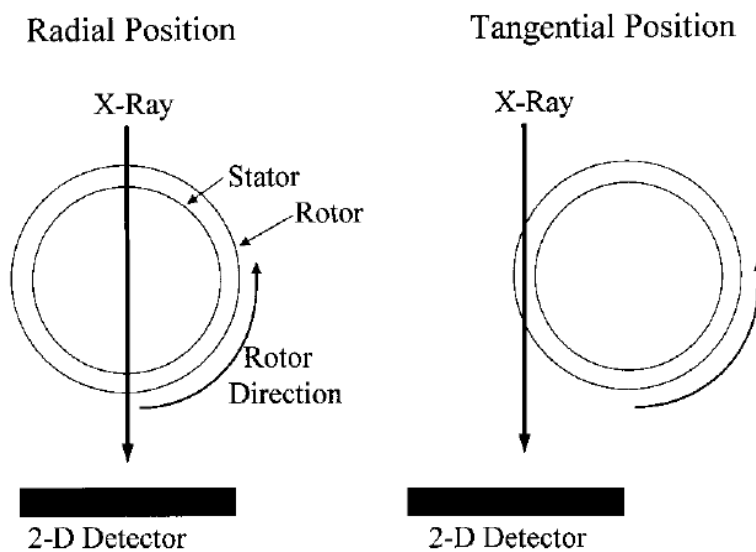
Figure 2.21Experimental setup [55]
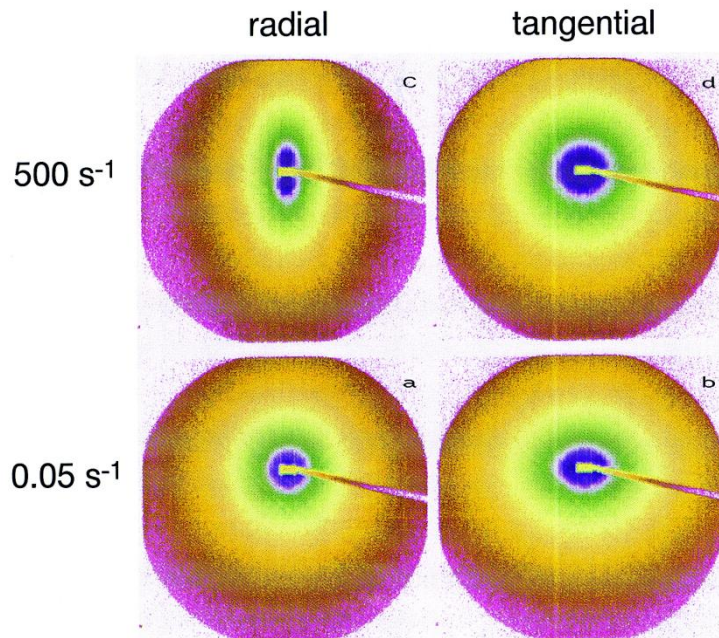
Figure 2.22 Two dimensional scattering patters at different shear rates [55]

Phase separation behaviour of NCC suspensions in the presence of macromolecules

Based on their concentrations, NCC suspensions exhibit three phases: isotropic phase, anisotropic phase and biphasic region, where the isotropic and the anisotropic phases coexist. Thus, addition of high-molecular weight dextrans to these solutions would lead to preferential partitioning of dextran into one or the other phase (Figure 2.23). [56]   The authors observed that dextran was absorbed into the isotropic phase and the dextran absorption increased with increasing cellulose concentration. On the other hand, dextran absorbance for the anisotropic phase was considerably lower due to the mutual exclusion of the NCC ordered domains and dextran molecules. A separation into dextran-rich and NCC-rod-rich phase was observed. Also, addition of dextran induced distortions in the liquid crystal structure of anisotropic NCC

suspensions. Similar results were obtained for the biphasic region; due to mutual exclusion dextran molecules migrate into the isotropic phase thereby increasing the osmotic pressure. The NCC rods move into the anisotropic phase (chiral nematic) in order to balance the osmotic pressure. This preferential migration in turn increases the width of the biphasic region.

Dye induced phase separation in anisotropic NCC suspensions were also studied by the Beck-Candanedo and co-workers using three different kinds of dyes: anionic, cationic and neutral. [57] Here phase separation refers to the separation of an anisotropic suspension into a biphasic region where both isotropic and chiral nematic phases coexist or increasing the critical NCC concentration to form anisotropic phase. It was observed that cationic dyes did not induce phase separation in anisotropic NCC suspensions since they interact with the negative surface charges on the NCC surface. Neutral dyes could not induce phase separation as well since they were incapable of changing the ionic strength of the NCC suspensions. However, direct dyes like Congo Red were unable to induce phase separation as they bind strongly to the NCC molecules therefore they are unable to compress the electrical double layer around the NCC and induce phase separation. One the other hand, anionic dyes were able to induce separation of the anisotropic NCC suspension into an isotropic and chiral nematic phase. The authors deduced that ionic strength or effect of size were not the cause for induced phase separation. Rather, it is explained that charge distribution, hydration radii and/or polyvalence of the anionic dyes themselves may be causing the phase separation.

Blue Dextran absorbed preferentially in the isotropic phase
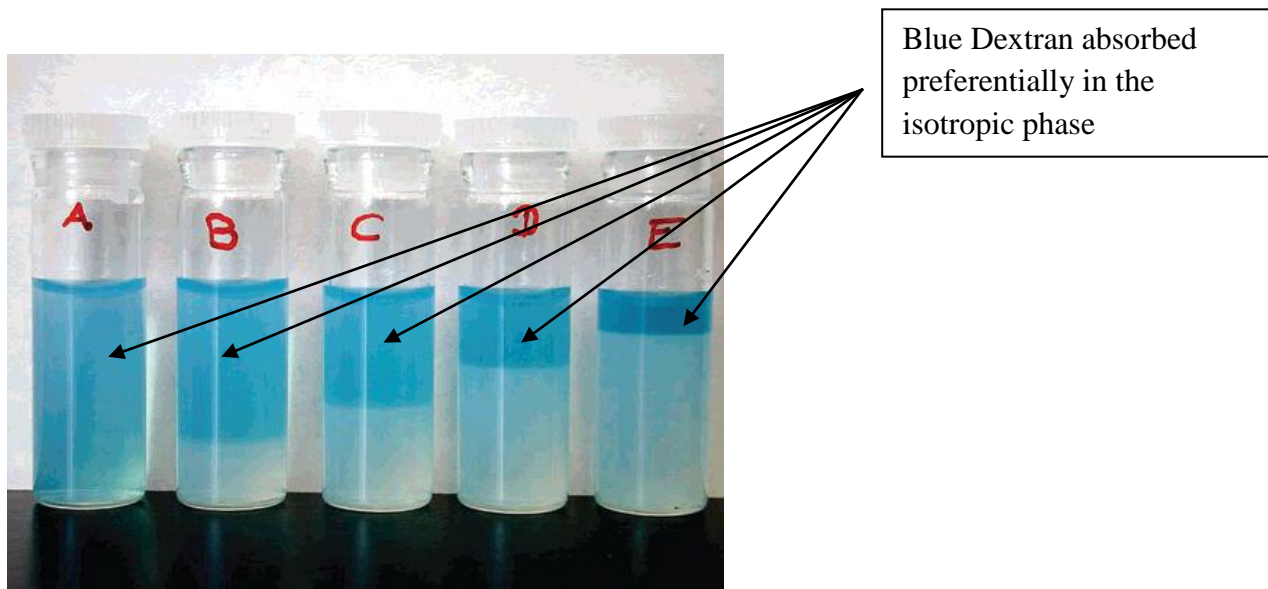
Figure 2.23 Preferential adsorption of blue dextran in the upper isotropic phase [56]

Beck-Candanedo et al. [58] have further studied the effect of molecular weight and dye content of blue dextrans on induced phase separation in highly anisotropic NCC suspensions (13.8 wt%). Cibacron blue 3G-A is used as the dye molecule and when it is conjugated with dextran, then the dextran-dye conjugate is referred to as ligand. By using blue dextrans of increasing number density (keeping the dye content constant) and increasing molecular weights, the authors observed that there was no appreciable effect on the phase separation suggesting that depletion attraction alone is not responsible for the induced phase separation. However on increasing the ligand density (i.e. increasing the dye-dextran conjugate), induced phase separation was observed; the authors suggested that the ionic strength of the suspensions arising from the ionic dye components in dextran contribute significantly to the induced phase separation behavior. The authors observed that the addition of the dye alone also induced phase separation while the addition of equivalent ionic strength of electrolyte was not able to induce phase separation. The phase separation of anisotropic NCC suspensions was attributed to ionic dye ligands, which may

screen out the electrostatic interactions between the NCC rods thereby facilitating depletion attraction.

In conclusion, induced phase separation in the presence of blue dextran is due to two factors: (i) increase in critical cellulose concentration (for formation of a completely anisotropic phase) and (ii) screening effect of the dye-ligands on the NCC. At low ligand concentrations, the increase in critical cellulose concentration comes into play while at high ligand concentrations increased depletion attraction due to the screening of ionic dyes. The same research group also studied the partitioning of neutral and charged dextrans in biphasic NCC suspensions [59] and the triphase equilibrium in mixtures of blue dextrans, un-dyed dextrans and NCC suspensions [60].

2.2.3 NCC CHARACTERIZATION

AFM studies

Apart from using the conventional bright field TEM imaging and field emission SEM, Kvien et al. also conducted AFM (atomic force microscopy) studies on NCC suspensions obtained from acid hydrolysis of MCC. Figure 2.24 shows the TEM images of the NCC on a porous carbon film and NCC with uranyl acetate as a continuous stained background respectively. Although the TEM analysis showed a little parallel agglomeration of NCC particles, the size of the NCC sample was determined as follows: length $L = 210\pm75$ nm and diameter $D = 5\pm2$ nm. [61]
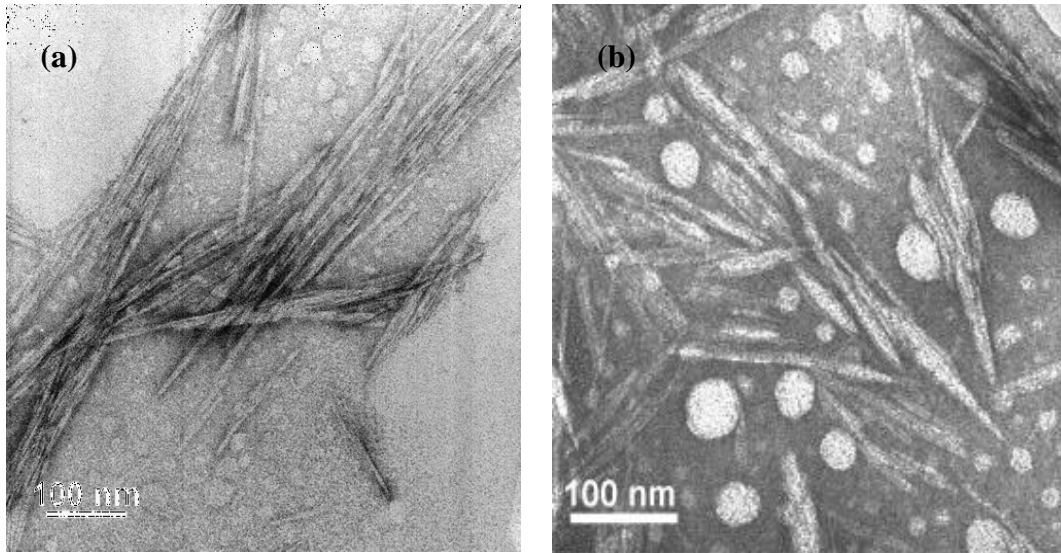
Figure 2.24 TEM images of the NCC on a porous carbon film (a) and NCC with uranyl acetate as a continuous stained background (b) [61]

Heavy element staining was used to characterize the NCC rods using backscattered electrons in field emission SEM imaging technique. It is clear from the backscattered images (Figure 2.25) that the identification of NCC particles was difficult with poor image resolution. Therefore, SEM analysis gave L = 475$\pm$285 nm indicating that SEM was able to identify the dimensions of NCC agglomerates better than individual NCC rods.
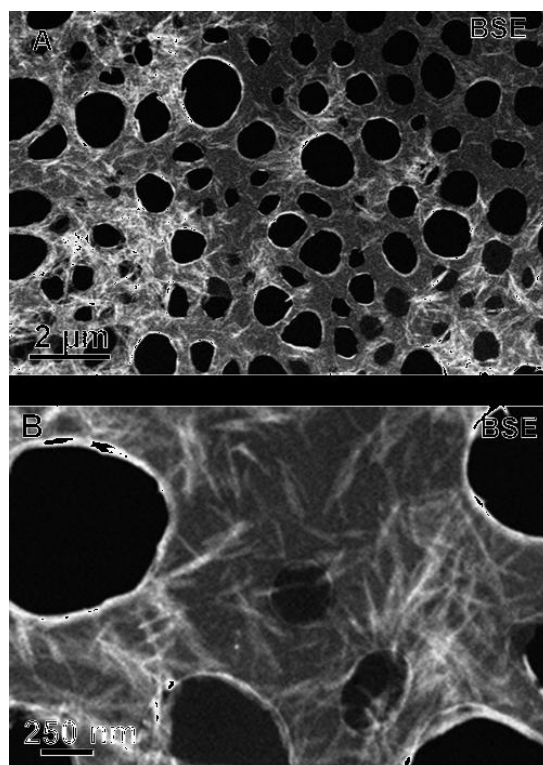
Figure 2.25 Back scattered image NCC on porous carbon film (top) and an image at

higher magnification (bottom) [61]

In comparison to TEM and SEM, the authors observed that AFM images were not plagued by

image resolution or contrast issues; however, the AFM images of NCC rods appeared broader

and more rounded at the ends compared to images obtained from TEM (see Figure 2.26). This

broadening effect is attributed to the finite shape and size of the AFM probe. The authors explain

that when the AFM tip encounters certain features on the surface, which have a size similar to

that of the AFM probe, then the probe shape and geometry contribute to the final image of the

surface thereby broadening the image of NCC rods. Similar to the length obtained from

SEM, AFM analysis gave a length, L of 420 ± 190 nm. By measuring the difference in height

between the NCC and the mica surface, the diameter of the NCC particles was obtained as $D = 10 \sim 15$ nm. [61]
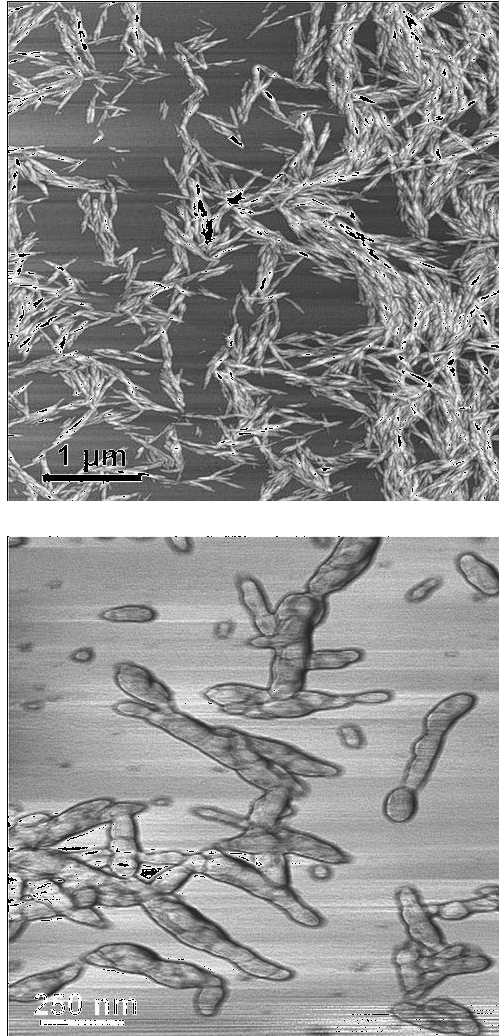
Figure 2.26 AFM image of NCC on mica (top) and broadened AFM image (bottom) [61]

Lahiji et al. used the AFM technique to characterize the material properties of NCC with regard to topography, adhesion and stiffness. Since NCC is widely used as reinforcing filler in nanocomposites, the authors studied two important mechanical characteristics of NCC applicable

to nanocomposites: the transverse elastic modulus (E_T) and the AFM manipulation of NCC to determine flexibility of the individual NCC rods.

1. AFM manipulation of NCC

   Firstly, dynamic mode AFM was used to locate an individual NCC rod, subsequently followed by contact mode AFM to apply a normal force to a specific NCC rod. Next dynamic mode AM-AFM imaging was used to determine whether the NCC rod slipped/rolled on the mica surface or was deformed/bent permanently on application of force. Bending was observed on application of 8-10 nN normal force. Bending of NCC rods without any fracture/failure is either due to the strong intermolecular hydrogen bonds which increase stiffness of the sample or aggregation of smaller NCC rods into a stiffer NCC crystallite. [62]

2. Transverse elastic modulus (E_T)

   The transverse elastic modulus (E_T) of NCC is determined from the force-indentation $F(\delta)$ curves. The indentation values or $F(\delta)$ curves were obtained by calculating the z-distance between the $F(z)$ curves for NCC and mica surface. By using 5 different locations on a certain NCC rod, a range of E_T values was obtained as 18-50GPa. The wide range of E_T values was attributed to uncertainty in indentation, location of indentation, tip roughness and dimension of each indentation. [62]
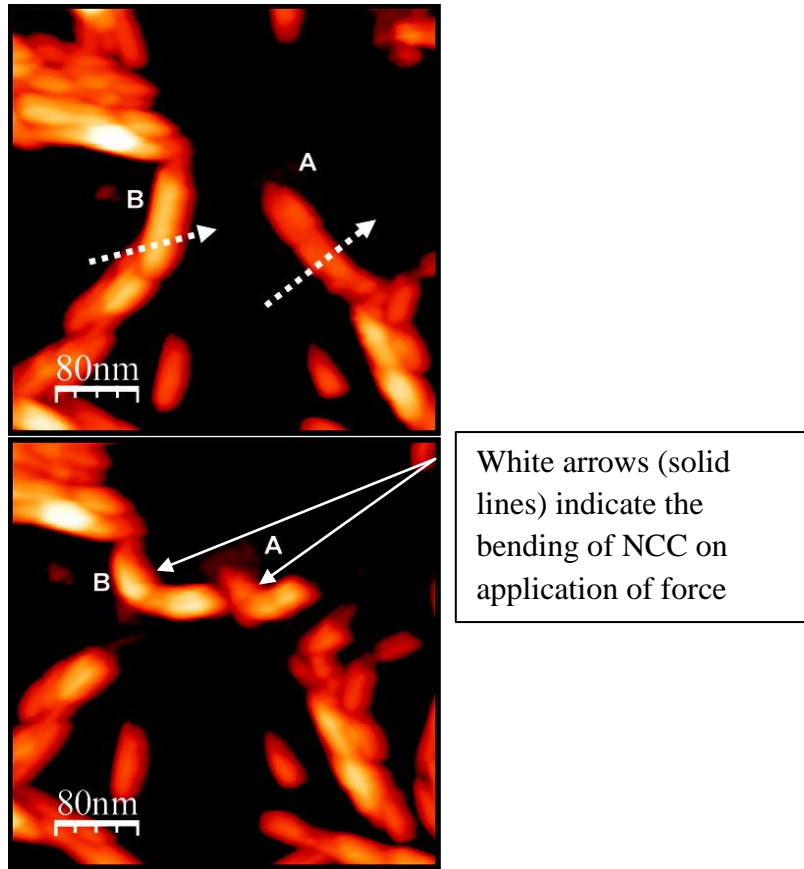
Figure 2.27 AFM Nanomanipulation (bending) of NCC on application of force [62]

Raman spectroscopy studies

Raman spectroscopy has been used to determine the stiffness of NCC nanowhiskers dispersed in an epoxy resin. Rusli and Eichhorn suggested that due to the method of sample preparation, the nanowhiskers in the sample are 2D and the stiffness was calculated to be 57GPa (2D). Figure 2.28 shows a typical Raman spectrum of the cotton nanowhiskers, clearly showing the carbonyl stretching band (C-O) at 1095cm^{-1}. Application of tensile or compressive stress shifted the value of C-O wave-number position to a lower or higher position respectively. The amount of shift indicated the amount of deformation at the molecular scale and the amount of stress transfer

60

from the epoxy matrix to the NCC reinforcement. From Figure 2.29a, the slope of the loading

data (under tension) gives the amount of stress transfer from the matrix to the reinforcement and

a plateau in the data indicates a breakdown of the matrix-reinforcement interface. Therefore, the

Unload1 and the Load2 data points fail to correspond to the Load1 data indicating some sort of

deformation (under tension) at the molecular scale. From Figure 2.29b, the variation in slope of

the loading data (under compression) indicates buckling of the NCC reinforcements under

compressive forces. [63]
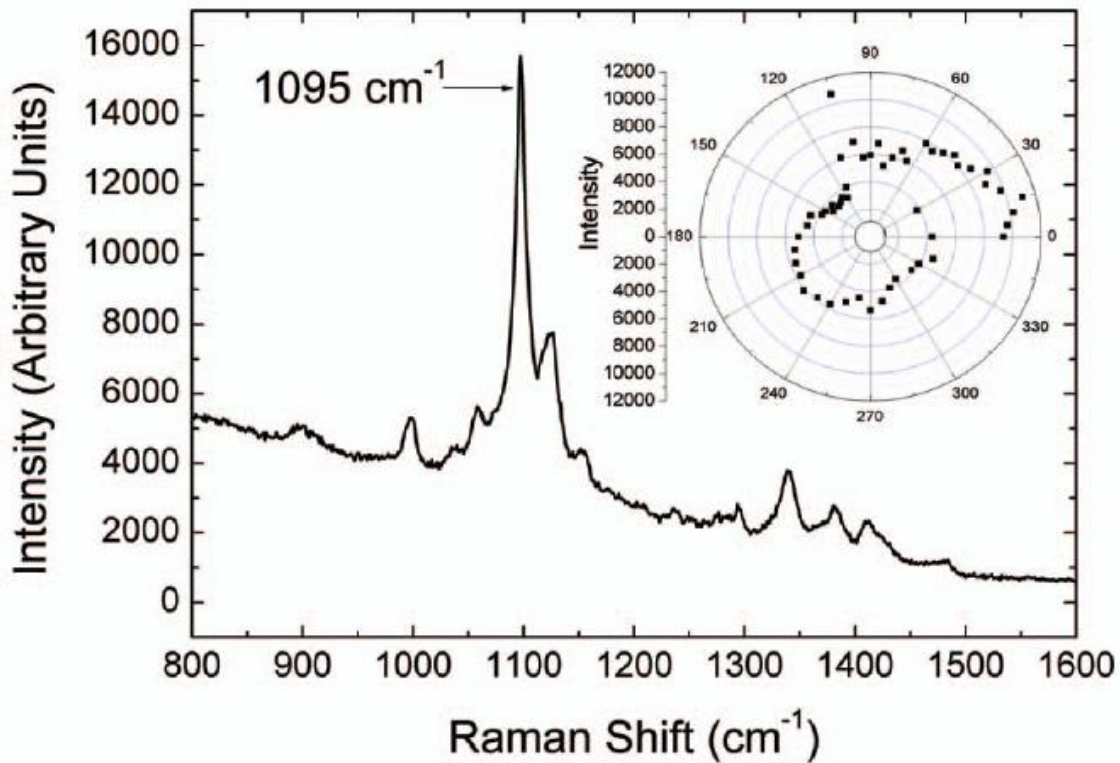
Figure 2.28 Typical Raman spectrum of cotton whiskers and orientation (of whiskers) as

function of specimen angle w.r.t polarization axis (inset) [63]
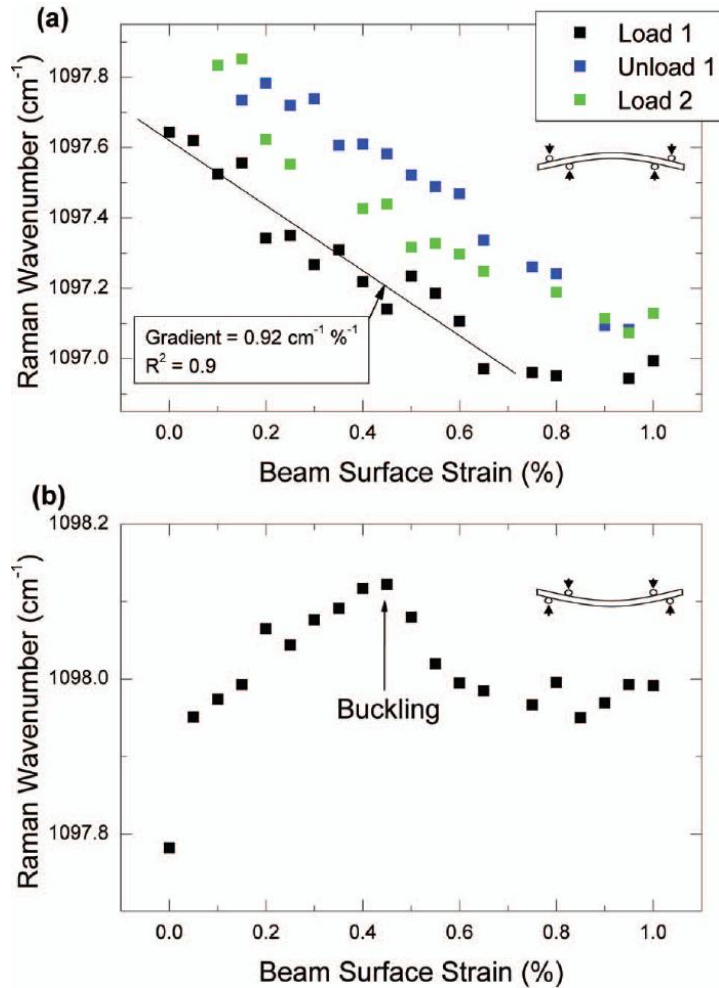
Figure 2.29 Loading data for matrix-reinforcement under tension and compression [63]

SANS studies

Small-angle neutron scattering experiments have been conducted by Terech et al. for NCC suspensions obtained from tunicate. Six samples at different concentrations were used i.e. 1.37, 0.91, 0.71, 0.35, 0.18 and 0.071 wt%. Figure 2.30a shows the neutron scattering data for all the concentrations and reveals that the scattering curves are independent of NCC concentration i.e. absence of aggregation on increasing NCC concentration. Scattering curves obtained also show

the characteristics of long rod-like particles with high aspect-ratio. The radius of the particles (R_o) was also calculated from the $\ln(QI)$ vs. Q^2 curve (see Figure 2.30b) using Equation 2.2:

$$QI(Q) = (QI)_O \exp(- Q^2 R_o^2 / 2) \text{ (Gaussian decay)}$$

Equation 2.2 Gaussian decay for calculating R_o

The weight per unit length of rods (M_1) was calculated from $(QI)_O$ values. The average R_o and M_1 values obtained were: 84 ± 1 Å and 1.45×10^{-20} g/Å. On extrapolation of M_1 value, R_o was calculated as 54 ± 2 Å. In order to explain this discrepancy, the authors used Porod analysis for a circular cross-section and the R_o value was calculated as 59 Å. However, the theoretical curve for 0.91 wt% sample did not exactly correspond to the calculated scattering curve. This made the authors consider a two-population model with radii 44 and 83 Å giving a better fit to the experimental data. This two-population model fitting further suggested that curve fitting using a single population model was possible by considering anisometric rectangular cross sectional for the NCC particles. Considering a rectangular cross-section (2a = 88 Å and 2b = 182 Å), the theoretical scattering curve showed an excellent fit with the experimental scattering curve for the 0.91 wt% sample. On considering effective area as = 88 X 182 = 16016 Å^2, the radius of the particle (R_o) was calculated as 71 Å. [64]
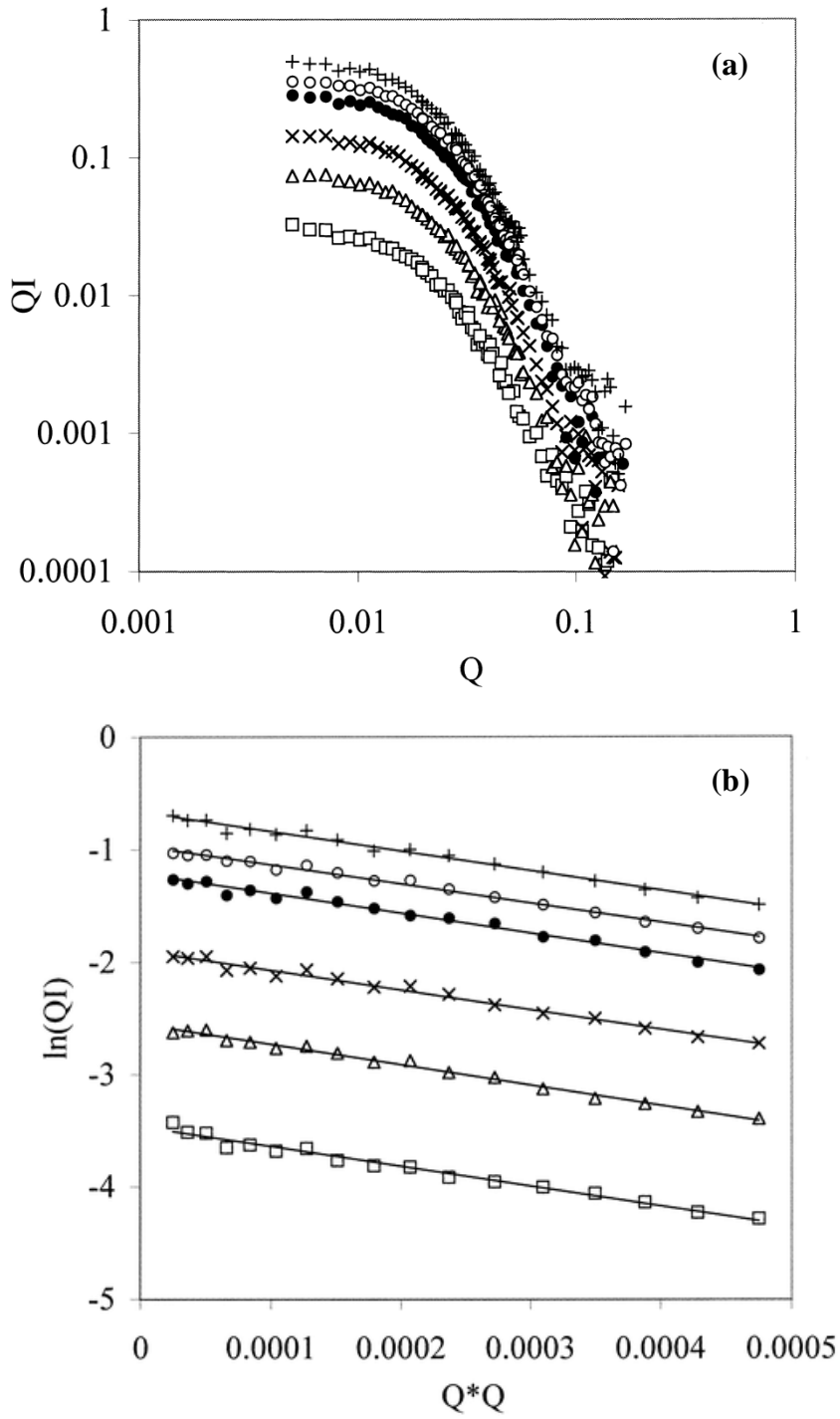
Figure 2.30 Neutron scattering data: QI vs. Q and ln(QI) vs. Q^2 [64]

WS01 (+), WS02 (O), WS03 (●), WS04 (x), WS05 (Δ), WS06 (□) Q is in Å^{-1}, I in cm^{-1}

Bonini and co-workers have also studied the dimensions of NCC suspensions coated with poly(ethylene oxide) nonyl phenyl (PEPNP) surfactant in an apolar organic medium using small angle neutron scattering experiments. The scattering experiments were conducted in water (0.45 wt%) and in toluene (1.5 wt%) as the organic solvent. PEPNP was used to study the effect of surfactants on NCC dimensions. Figure 2.31 shows QI vs. Q scattering curves for NCC particles in water and toluene; the sharper decay and the extra scattering observed for the toluene curve indicates that the surfactant has an effect on the NCC structure and dimensions. Next the authors modified equation(2) into equation(3) using a rectangular cross-section for analysis.

$$QI(Q) = (QI)_O \, \exp(- Q^2 r_c^2/2) \text{ (Gaussian decay)}$$

$$r_c = \text{cross-sectional radius of gyration}$$

Equation 2.3 Modification of Equation 2.2 to include the r_c term

Using $\ln(QI)$ vs. Q^2 (Figure 2.32), the slopes of the linear portions were used to calculate r_c according to Equation (2). The r_c values were calculated as 59Å for the NCC whiskers in water and 69 ± 1 Å in the presence of surfactants in toluene. The increase in cross-sectional radius of gyration indicates that the surfactants modify the NCC surface and increase the lateral dimensions of individual NCC whiskers. Using the theoretical expression of form factor for rods with rectangular cross-section, the calculated lateral dimensions of the NCC whiskers increased from 88 X 182 Å^2 (in water) to 120 X 210 Å^2 (in toluene) in the presence of surfactants. The calculations also confirmed that surfactants formed a shell of 15Å thickness around the NCC whiskers; since the extended length of the PEPNP surfactant is about 42 Å, the authors also deduced that the surfactant is adsorbed on the NCC surface in closed/folded conformation rather than an extended conformation. [65]
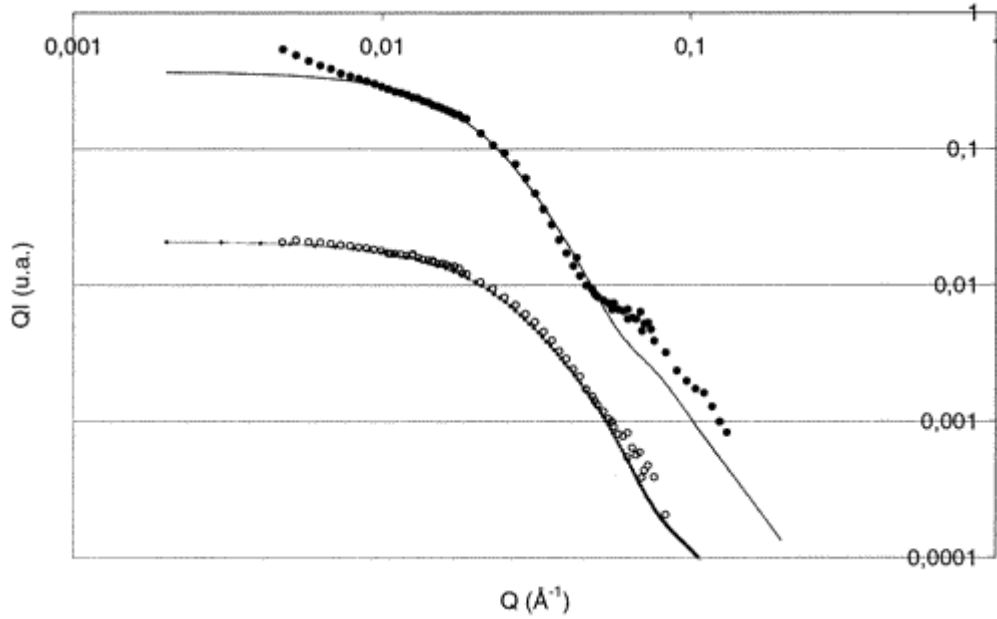
Figure 2.31 Neutron scattering data: QI vs. Q in toluene 1.5wt%(●) and in water 0.45wt%(O)

solid lines indicate theoretical curve fit [65]
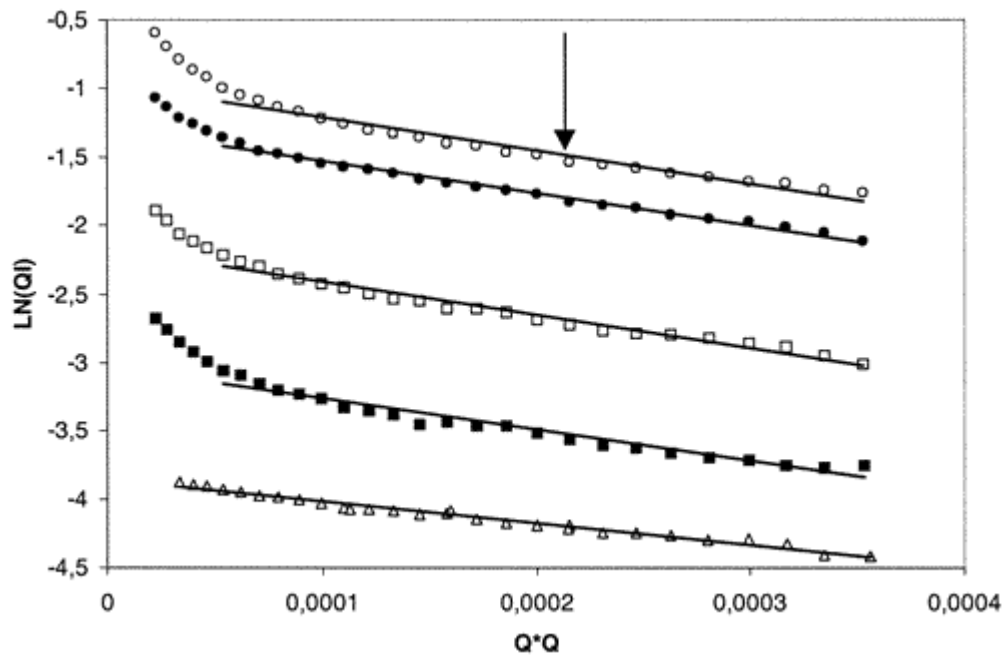
Figure 2.32 Neutron scattering data: ln(QI) vs. Q^2 in toluene 0.2wt%(■), 0.4 wt%(□), 0.8wt%(●),

1.5wt%(O) and in D_2O 0.45wt%(△) [65]

Light scattering studies

A review of literature on NCC reveals that there are a few publications on light scattering studies with aqueous NCC suspensions. Some research groups have studied NCC dimensions using light scattering, a very versatile technique for measuring dimensions and structure of nanosized particles. Static and dynamic light scattering experiments on NCC whiskers have been conducted by Lima and Borsali using NCC whiskers obtained from tunicate; the samples for this light scattering study were fractionated by ultracentrifugation aided by a saccharose gradient. Figure 2.33 shows the NCC samples before and after ultracentrifugation. As seen in the picture, before ultracentrifugation two phases exist (tube a): a clear phase representing NCC whiskers accumulated on the sucrose gradient and a black phase representing the NCC whiskers which did not accumulate on the sucrose gradient. After ultracentrifugation, the sample was fractioned into different bands (tube b) and TEM analysis (See Figure 2.34) on each fraction confirmed that the fractionated samples had narrow polydispersity and reduced whisker aggregation. [66]

(a)   **(b)**
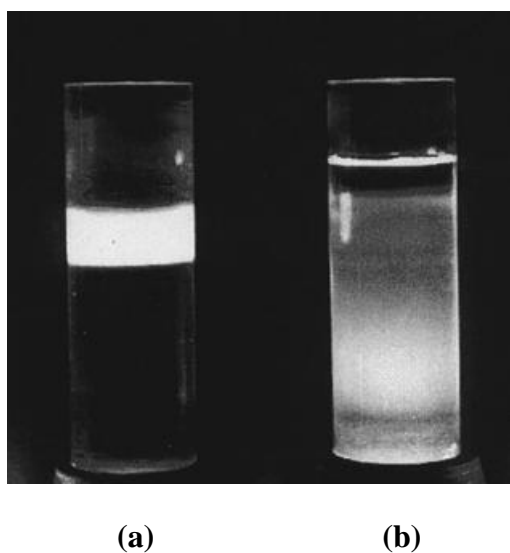
Figure 2.33Tunicate NCC whiskers before (tube a) & after ultracentrifugation (tube b) [66]
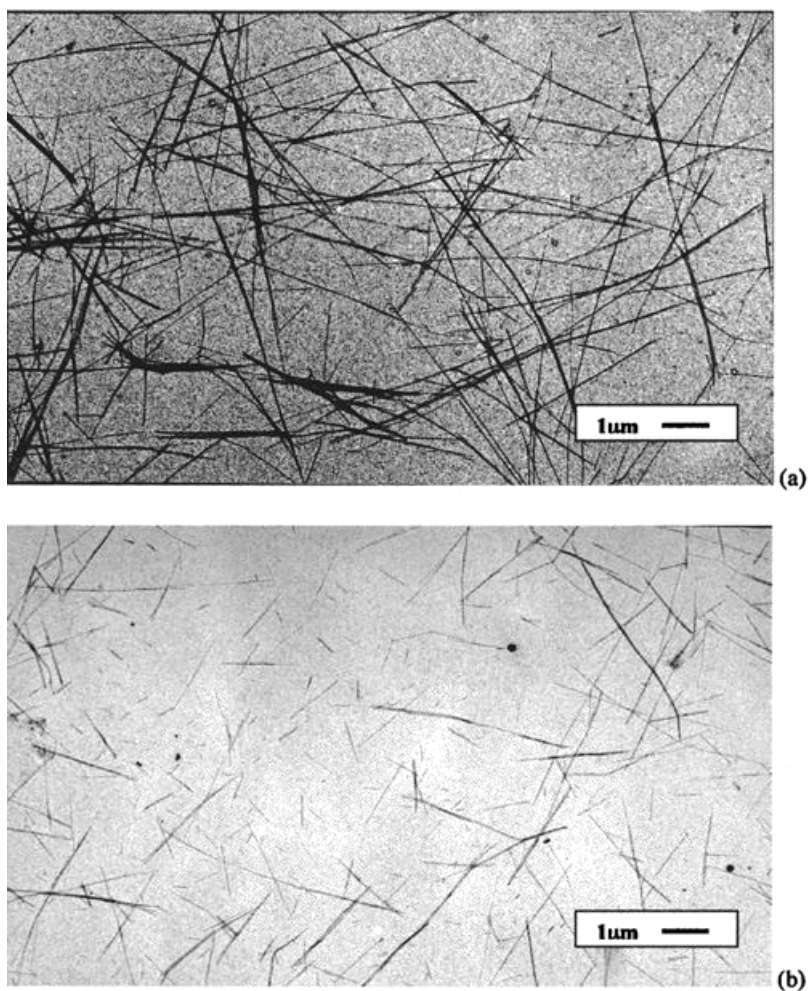
Figure 2.34 TEM images of NCC whiskers before (a) and after ultracentrifugation (b) [66]

For static light scattering studies, the authors measured reduced elastic scattering I(q)/kC vs. wave vector q and plotted them in a normalized form to obtain normalized scattering curves at different concentrations. Normalized scattering curves in the absence of salt (Figure 2.35) showed the presence of angular scattering peaks at q_{max} depending on the concentration of NCC suspensions. On conducting the same experiment before NCC fractionation (Figure 2.36), the peaks disappear due to formation of NCC aggregates and increased polydispersity. [66]
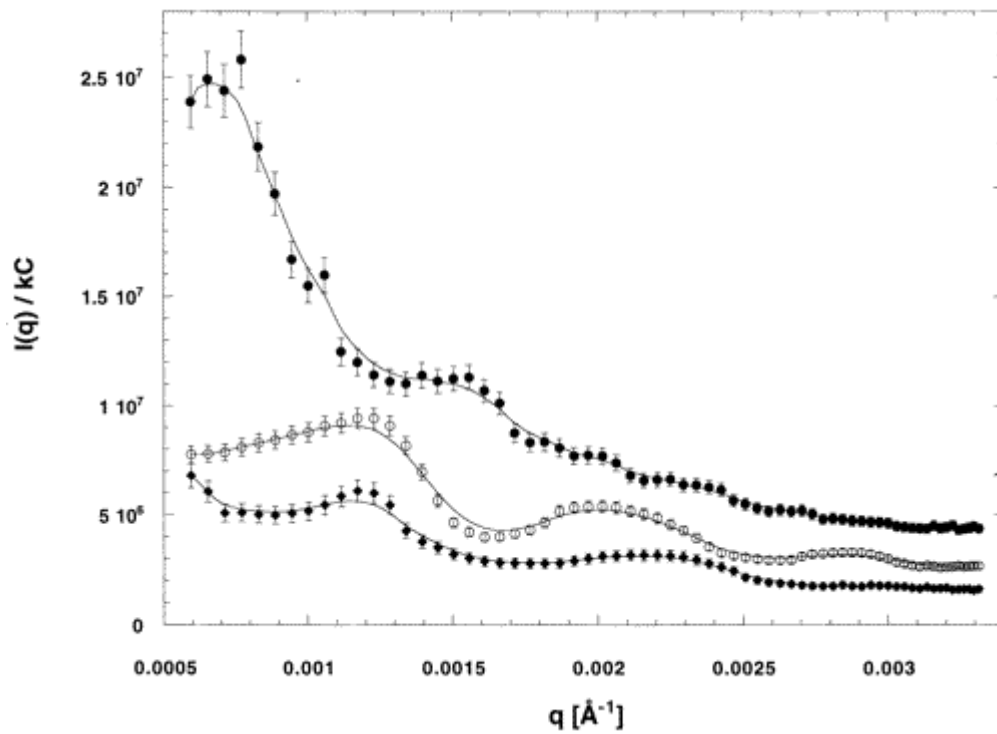
Figure 2.35 I(q)/kC vs. q (●) 0.37×10^{-2}g/cm^3(o) 0.87×10^{-2}g/cm^3 (♦) 1.04×10^{-2}g/cm^3 [66]
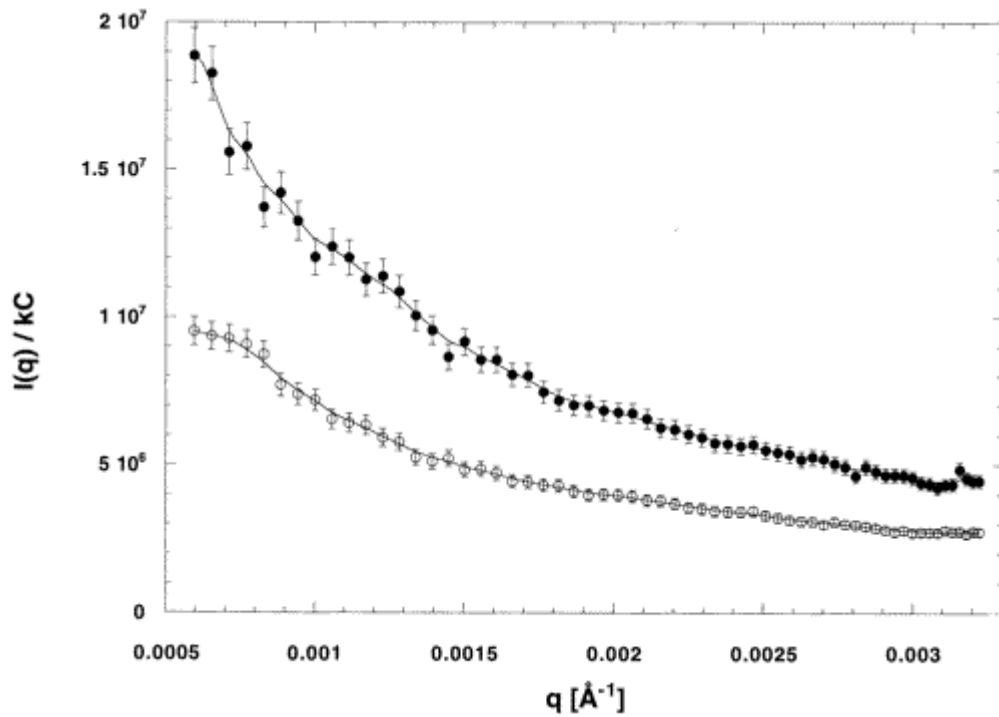
Figure 2.36 I(q)/kC vs. q before fractionation (●) 0.38×10^{-2}g/cm^3(o) 0.92×10^{-2}g/cm^3 [66]

It is a well known fact that for spherical particles, the scattered intensity I(q) can be correlated with structure factor S(q) and form factor P(q) by the relation:

$$I(q) \ = S(q) \, P(q)$$

Equation 2.4 Relation between structure factor and form factor

The above relation maybe valid for rod-like particles under two conditions:

1) When the concentration of the rods is sufficiently high the contributions from larger aggregates supersedes the contribution from smaller/pair aggregates.

2) When most rods are aligned perpendicular to the scattering vector q, these perpendicular rods have the maximum contribution to scattering making qL>>1. Therefore, P(q) becomes more-or-less constant and the above relation can be used to calculate the structure factor of rod-like particles.

For the tunicate system used, since qL is >>1, the above relation in combination with the equation for form factor of rigid rod-like particles, the structure factor S(q) was derived. The broad scattering peaks of S(q) (see Figure 2.37) with second and third maxima peaks indicate the presence of strong and long-range electrostatic interactions between the NCC rods. Figure 2.38 illustrates that in the presence of salt the scattering peaks disappear as salt screens out the electrostatic interactions between the NCC rods. [66]
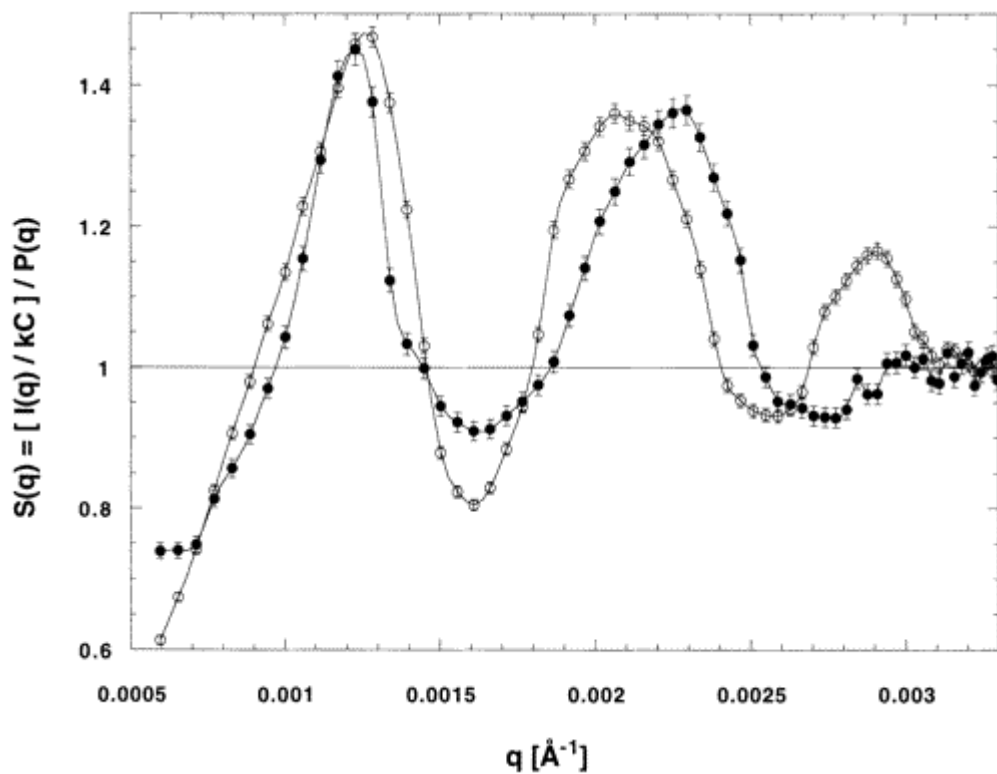
Figure 2.37 S(q) vs. q in the absence of salt (o) 0.87×10^{-2}g/cm^3($\blacklozenge$) 1.04×10^{-2}g/cm^3 [66]
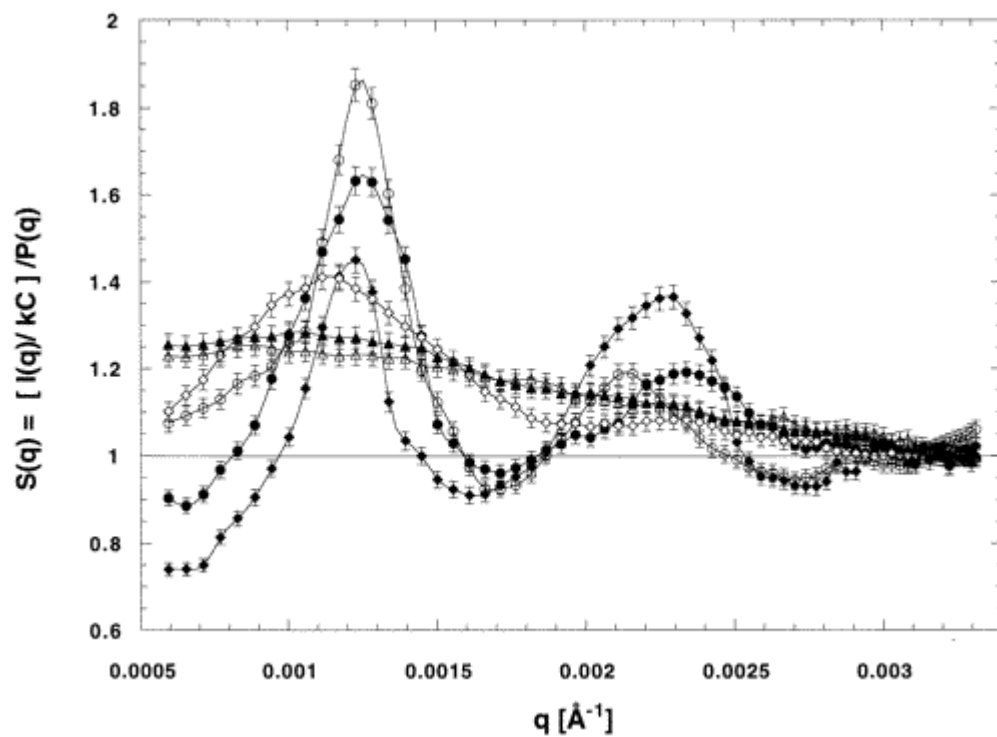
Figure 2.38 S(q) vs. q at C=1.04×10^{-2}g/cm^3 & diff. salt conc.($\blacklozenge$)0M (o)10^{-6}M ($\bullet$)3×10^{-6}M ($\lozenge$)6×10^{-6}M ($\triangle$) 8×10^{-6}M (filled) ($\triangle$) 10^{-5}M [66]

The authors also observed that the q_{max} peaks for S(q) varied with concentration (Figure 2.39) as follows: first maxima: C0.49±0.01; second maxima: C0.42±0.01; third maxima: C0.41±0.01
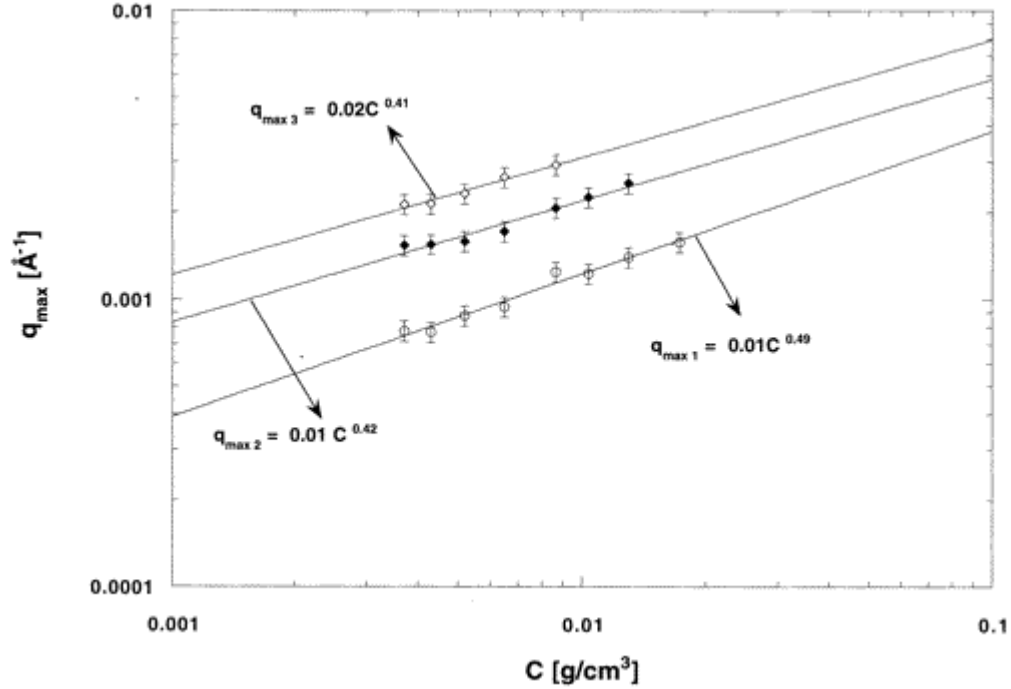
Figure 2.39 Logq_{max} vs. LogC for (o) first maxima (♦) second maxima (◊) third maxima [66]

Lima et al. [67] have also studied the translational and rotational dynamics of NCC whiskers using cotton and tunicate whiskers. For cylindrical rods, the translational and rotational diffusion coefficients can be determined from polarized I_{VV} and depolarized I_{VH} scattering intensities using Equations 2.5 and 2.6:

$$I_{VV}(q,t) = <N>\alpha_{iso}^2 \exp(-q^2 Dt) + 4/45 <N>\alpha_{aniso}^2 \exp[-(q^2 D+6\theta)t]$$

Equation 2.5 Polarized scattering intensities

$$I_{VH}(q,t) = 1/15 <N> \alpha_{aniso}^2 \exp[-(q^2 D + 6\theta)t]$$

Equation 2.6 Depolarized scattering intensities

$<N>$: avg. no. of particles in the scattering volume

α_{iso} : isotropic polarizability tensor

α_{aniso} : molecular optical anisotropy

Figure 2.40 shows the autocorrelation functions obtained at different angles for cotton whiskers at 0.1 wt% concentration for polarized scattered light (I_{VV}). When the frequency Γ was plotted against the square of scattering wave-vector q^2, the authors observed slow and fast relaxation modes for both cotton and tunicate whiskers with the slower mode contributing 90% of the scattered intensity. Moreover, frequency Γ varies with q^2 (Figure 2.41), hence all relaxation modes are said to be diffusive. Next, the values of translational (D) and diffusion (θ) coefficients were deduced from the slopes of Γ vs. q^2 curves (Figure 2.42, 2.43) from I_{VV} and I_{VH} measurements. Finally, the D and θ values obtained from DLS experiments were used in Broersma's equations (described below) to obtain the dimensions of cotton and tunicate whiskers. [67]

Translational diffusion coefficient	Rotational diffusion coefficient
$D = (k_b T/3\pi\eta L)[\delta-(1/2)(\gamma_{\parallel} + \gamma\perp)]$	$\theta = (3k_b T/\pi\eta L^3)(\delta-\xi)$
$\delta = \ln(2L/d)$	$\xi = 1.14+0.2/\delta+16/\delta^2-63/\delta^3+62/\delta^4$
$\gamma_{\parallel} = 0.807+0.15/\delta+13.5/\delta^2-37/\delta^3+22/\delta^4$	
$\gamma\perp = -0.193+0.15/\delta+8.1/\delta^2-18/\delta^3+9/\delta^4$	

Equations 2.7 Broersma's eqns for calculating translational and rotational diffusion coeff. [67]
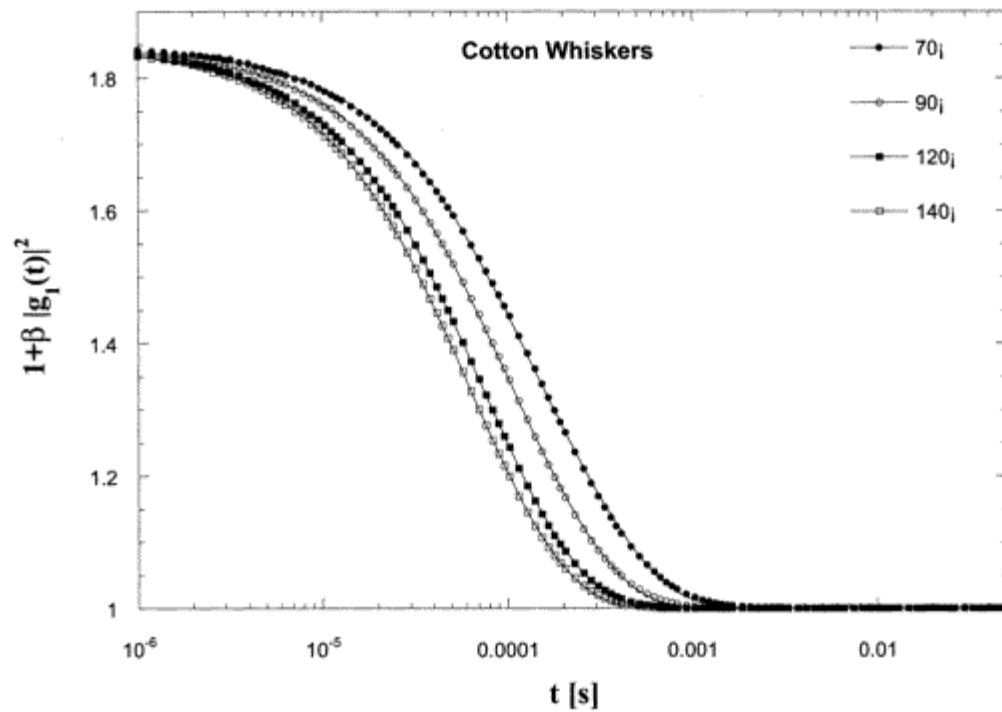
Figure 2.40 ACF obtained at 0.1 wt% concentration (I_{VV}) [67]
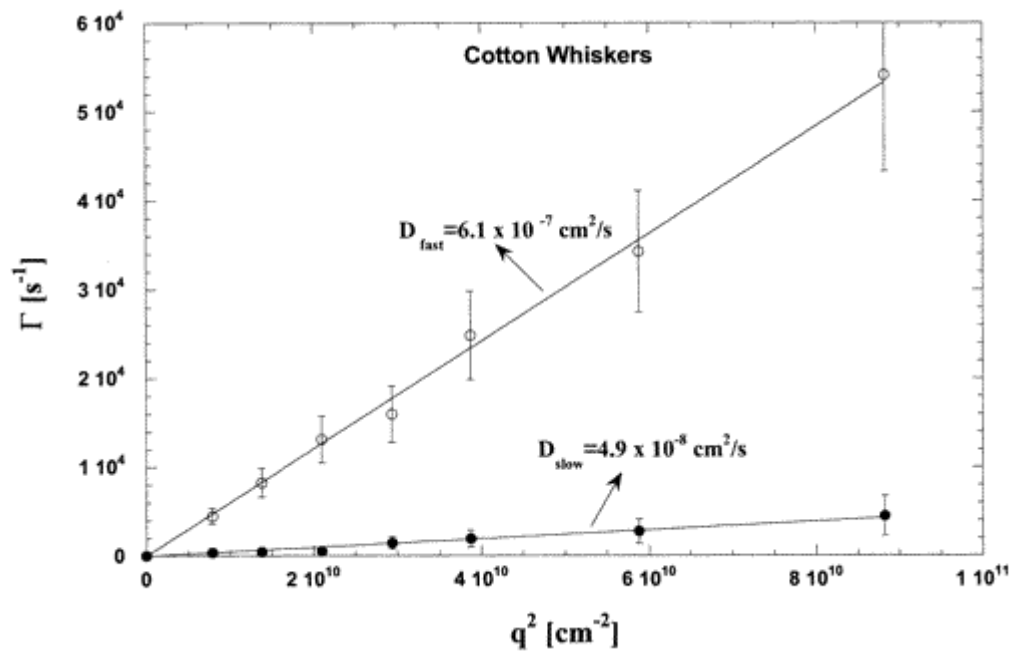
Figure 2.41 Γ vs. q^2 at 0.2 wt% (I_{VV}) [67]
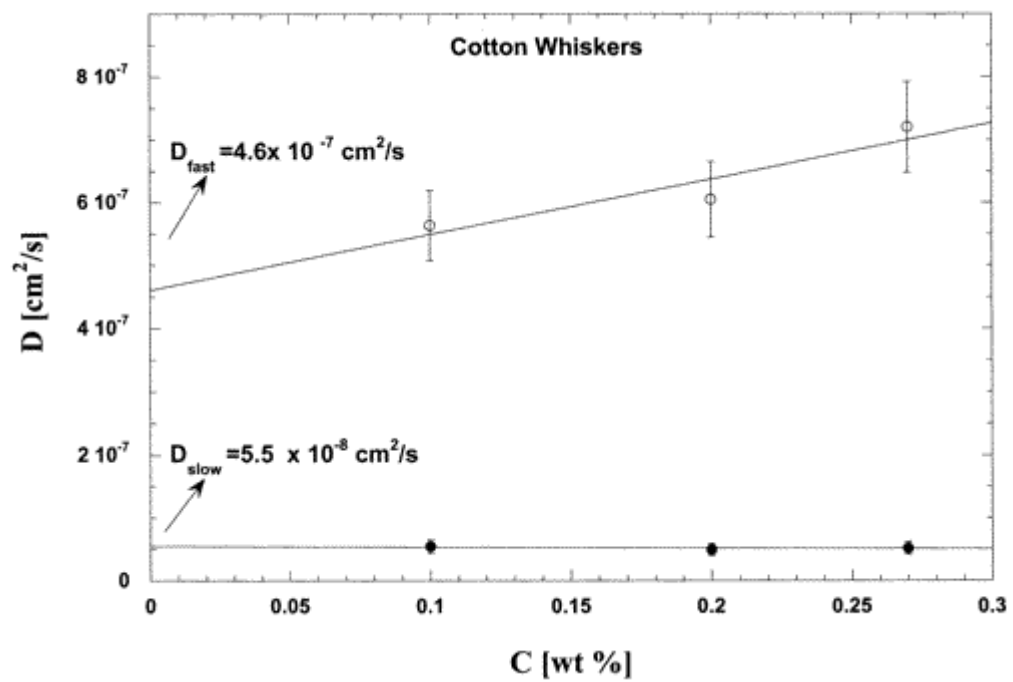
Figure 2.42 Translational diffusion coeff. D for slow($\bullet$) and fast(o) modes in I_{VV} detection [67]
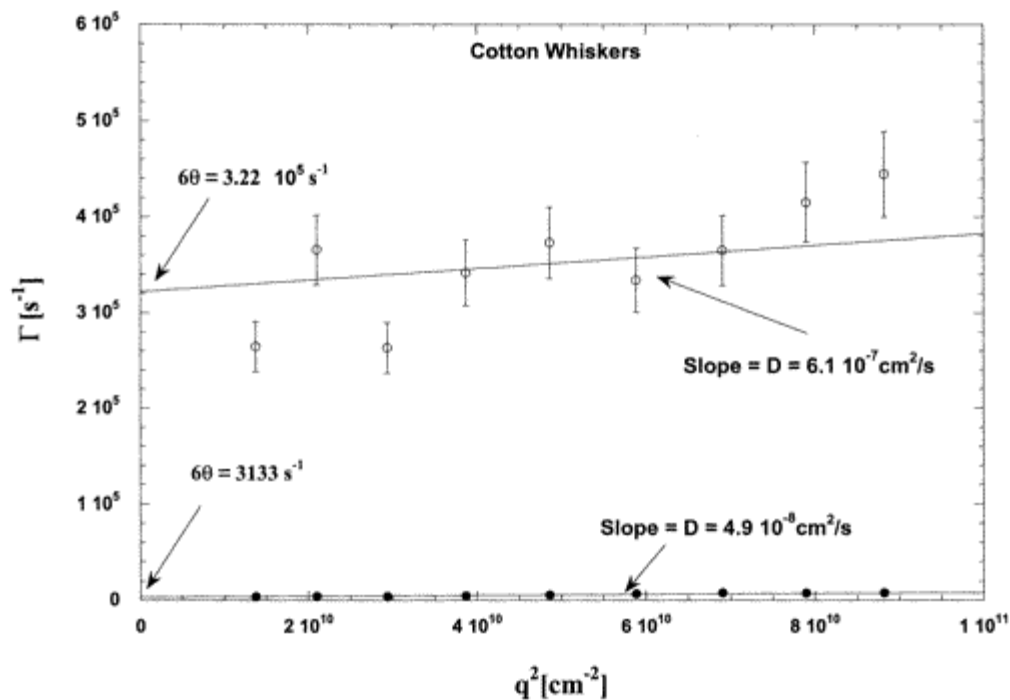
Figure 2.43 Rotational diffusion coeff. Θ for slow(•) and fast(o) modes in I_{VH} detection [67]

2.2.4 NCC MODIFICATION

Nanocrystalline cellulose has a highly functional surface due to the presence of large number of surface hydroxyl groups. Therefore, the NCC surface can be easily functionalized by simple reactions with the hydroxyl groups. These functionalized NCC can be tailored to specific applications like cosmetics, pharmaceuticals or nanocomposites. In 2001, Araki et al. synthesized NCC polymer brushes using HCl-hydrolyzed NCC as the starting material. Firstly, the HCl-hydrolyzed NCC was carboxylated using TEMPO catalyzed NaClO oxidation. Next the carboxylated NCC was grafted with an amino-terminated PEG (PEG-NH$_2$ M.W = 1000 Da) to produce NCC polymer brush-like structure. EDC/NHS carbodiimide chemistry was used to conduct a room temperature reaction between the -COOH groups of the carboxylated NCC and

76

the -NH$_2$ groups of the PEG-NH$_2$. Figure 2.44 shows a schematic of the synthesis of PEG-grafted NCC. [68]

Evidence of PEG-grafting on NCC was provided by thermogravimetric analysis (see Figure 2.45). The decomposition temperature of carboxylated NCC whiskers was around 200°C and the decomposition of PEG-NH$_2$ was around 340-360°C; combining both results, the decomposition curve of PEG-grafted NCC showed a two-step profile, one corresponding to the decomposition of carboxylated NCC and the other corresponding to the decomposition of the grafted PEG.
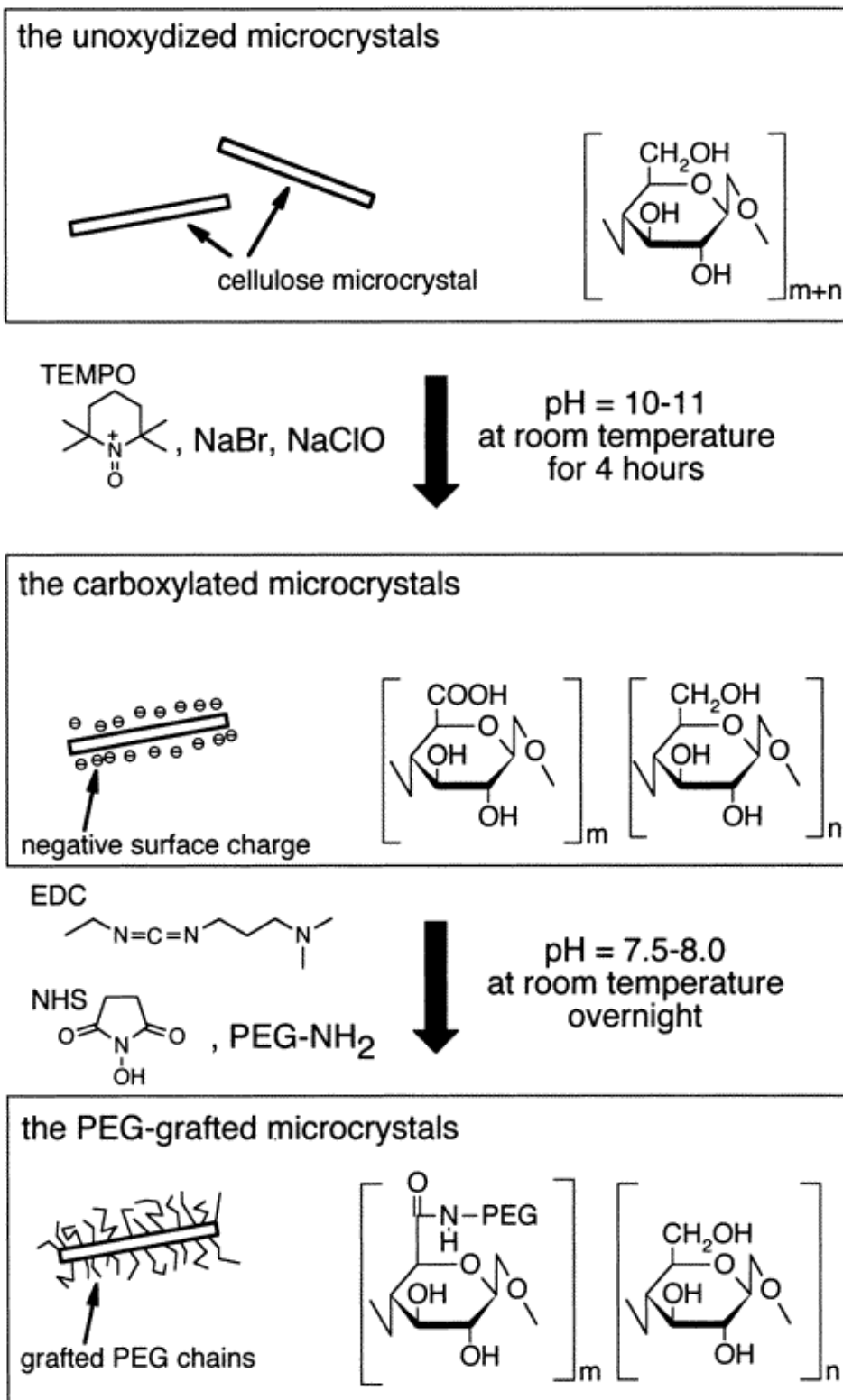
Figure 2.44 Schematic showing the synthesis of PEG-grafted NCC [68]

The X-ray diffraction profiles for carboxylated NCC and PEG grafted NCC are very similar; however, they fail to show the characteristic diffraction peaks for pure PEG most probably due to the inability of the grafted PEG chains to mobilize and crystallize. Also TEM images showed that carboxylated NCC whiskers and PEG grafted NCC whiskers were less aggregated and more disperse compared to the starting material (HCl-hydrolyzed NCC whiskers). Figure 2.46 clearly shows the characteristics peaks for free and salt forms of -COOH groups (1708 and 1640 cm^{-1}) in carboxylated NCC sample (b) while the PEG grafted NCC sample (a) showed amide I and amide II absorptions (1657 and 1544 cm^{-1}). Figure 2.47 shows that the PEG grafted NCC suspensions were stable and showed flow birefringence at low (left-0.5M) and high (right-2M) concentrations of salt. Also, 0.2% (w/v) freeze-dried and chloroform redispersed samples showed stability and flow birefringence (see Figure 24b). Figure 2.48 shows the fingerprint texture of carboxylated NCC whiskers (a) and PEG grafted NCC whiskers (b). The authors observed a decrease in fingerprint spacing in the PEG grafted NCC sample probably due to a decrease in the surface negative charge. Also the authors suggest that since the fingerprint textures of H_2SO_4 hydrolyzed NCC, carboxylated NCC and PEG grafted NCC show similar chiral nematic phases, the twisting of NCC whiskers along with the charged envelopes is the most probable mechanism of formation of liquid crystalline phases. [68]
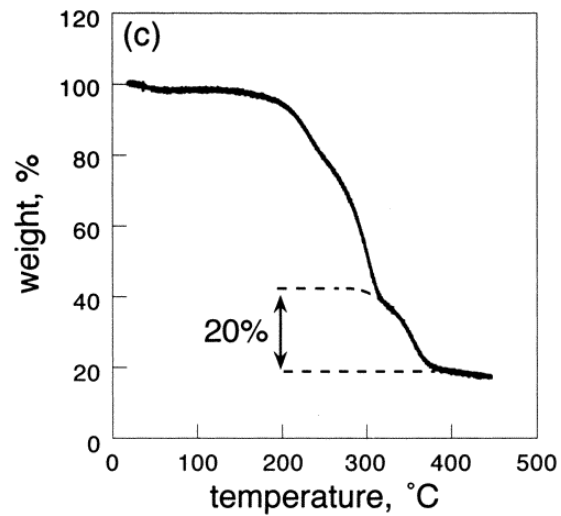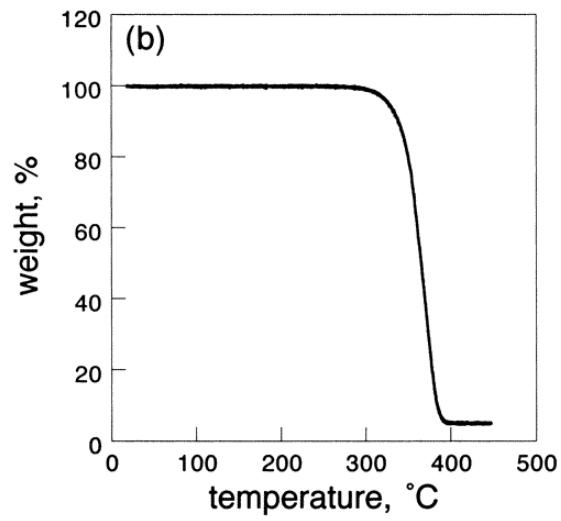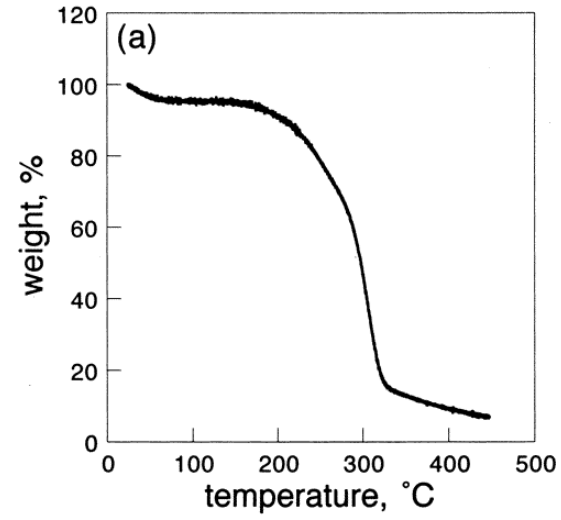
Figure 2.45 TGA curves for (a) carboxylated NCC (b) PEG-NH$_2$ (c) PEG-grafted NCC [68]
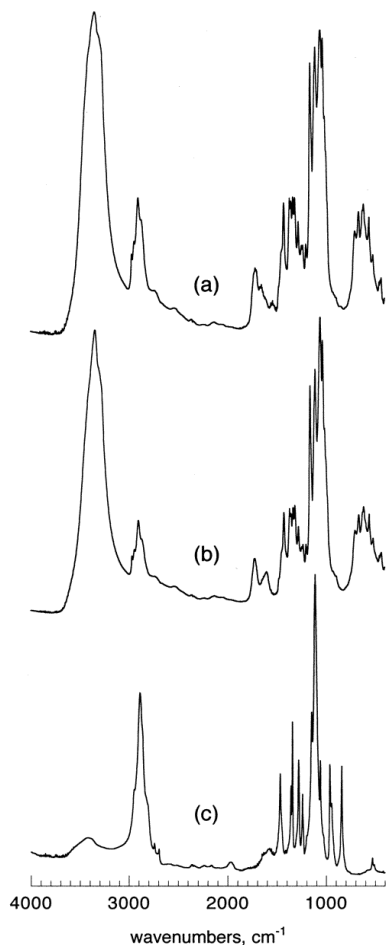
Figure 2.46 FTIR spectra
(a)PEG grafted NCC
(b)Carboxylated NCC
(c)PEG-NH$_2$ [68]
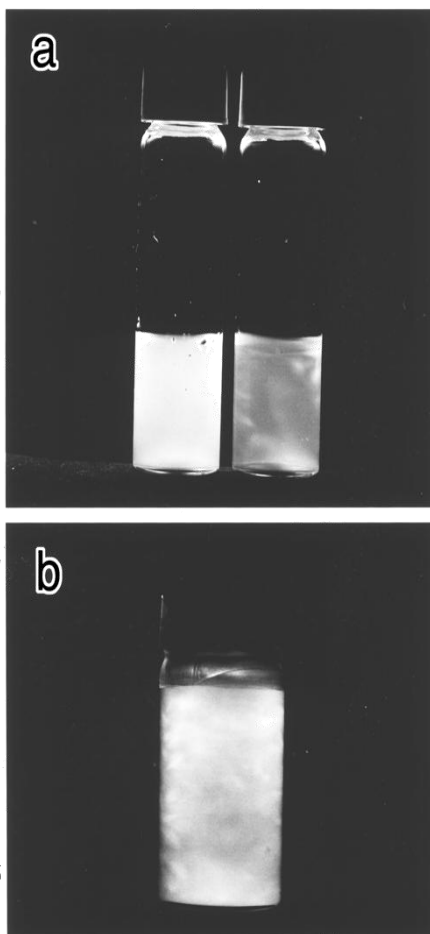
Figure 2.47 (a) PEG grafted
NCC at low and high salt
(b) PEG grafted NCC
redispersed in chloroform [68]
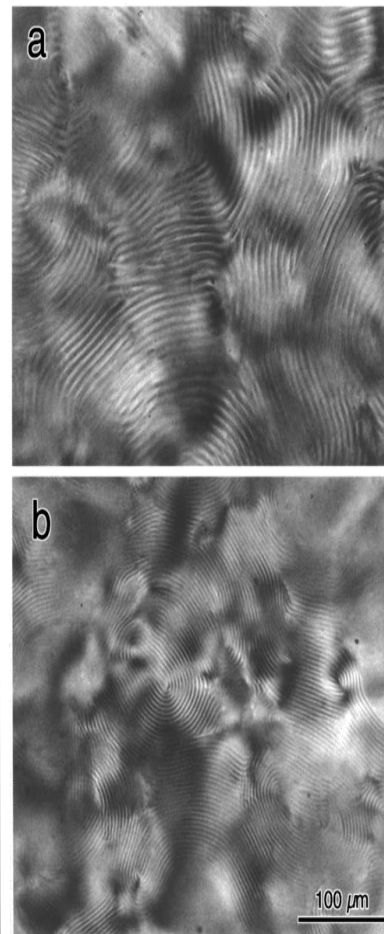
Figure 2.48 Fingerprint texture
(a) carboxylated NCC
(b) PEG grafted NCC [68]

Hasani and co-workers have also functionalized the surface of NCC whiskers produced from sulphuric acid hydrolysis. Epoxypropyltrimethylammonium chloride (EPTMAC) was used to produce cationic NCC functionalized with hydroxypropyltrimethylammonium chloride (HPTMAC) groups. Figure 2.49 shows the reaction scheme where the reaction between NCC (from sulphuric acid hydrolysis of cotton) and EPTMAC proceeded in the presence of 7% w/v

NaOH at 65°C for 5 hours. The no. of trimethylammonium groups per AGU unit were measured using conductometric titration with 0.01M $AgNO_3$. Zeta potential measurements also confirmed that the surface charge of the functionalized NCC converted to +30±5 mV from -39±3 mV for unfunctionalized NCC. The authors also observed shear birefringence through crossed polarizers for 1.9 wt% HPTMAC-NCC suspensions in water. However, for higher concentration of 3.5 wt%, isotropic gels were formed instead of the expected chiral nematic phases. Figure 2.51 shows the threadlike texture of the chiral nematic phase formed near the drying edge of the solidifying sample. [69]
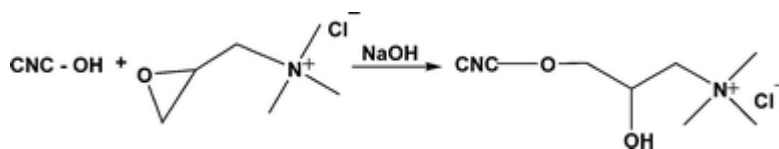
Figure 2.49 Reaction scheme to produce HPTMAC functionalized NCC [69]
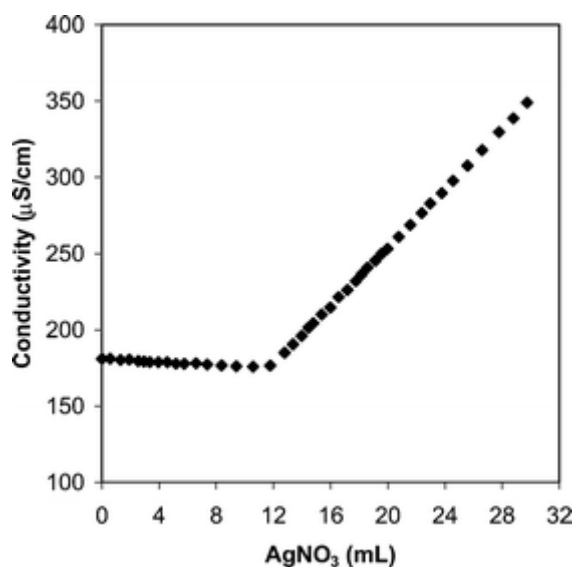
Figure 2.50 Conductometric titration of 1wt% HPTMAC-NCC with 0.01M $AgNO_3$[69]
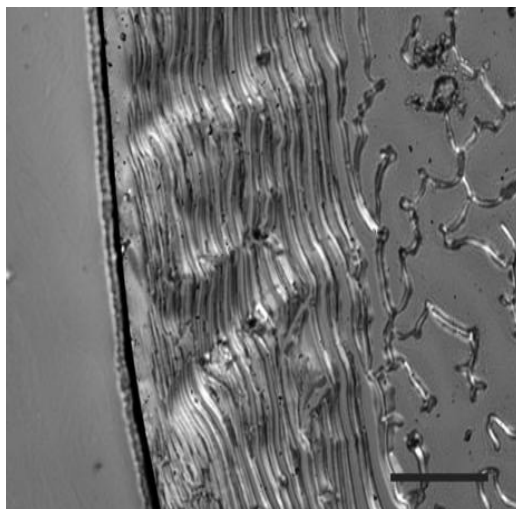
Figure 2.51 Threadlike texture of the chiral nematic phase formed near the drying edge [69]
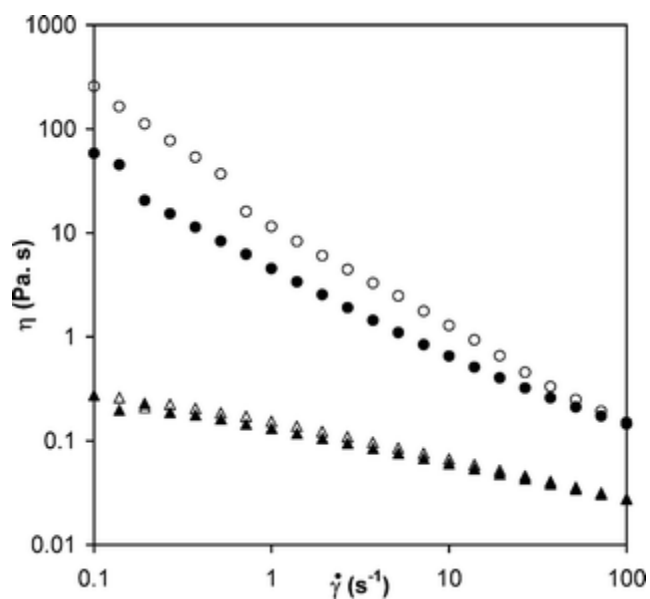
Figure 2.52 Viscosity η vs. increasing (open) and decreasing (closed) shear rates for 5wt% (ο) and 1.9 wt% (Δ) [69]

The authors observed thixotropic behaviour for HPTMAC-NCC suspensions through visual observations for a 4.9 wt% gel, which exhibited shear thinning on agitation. Oscillatory shear

tests on HPTMAC-NCC suspensions show that dynamic viscosity decreased with increasing angular frequency while the storage and elastic modulus increased with increasing concentration. Also on increasing concentration, the HPTMAC-NCC suspensions transforms from a viscous fluid to an elastic gel. Measuring viscosity as a function increasing and decreasing shear rates resulted in a thixotropic loop behaviour. This thixotropic hysteresis as shown in Figure 2.52 behaviour was attributed to the decrease in the magnitude of surface charge due to cationic functionalization of the NCC surface. [69]

According to Habibi et al. the sulphate ester groups introduced during sulphuric acid hydrolysis are labile and susceptible to removal under mildly alkaline conditions. Hence, they proposed to use TEMPO-mediated oxidation of NCC whiskers to introduce carboxylic functional groups which are not as labile as compared to the sulphate ester groups. Selective TEMPO-mediated oxidation was used on tunicate NCC whiskers so as to maintain the crystalline integrity of the whisker core. The reaction was conducted at room temperature at pH 10 using TEMPO/NaBr/NaOCl. Figure 2.53 shows a schematic of the NCC whiskers and how the surface hydroxyl groups get oxidized to carboxylic functional groups using TEMPO-mediated oxidation. Also the FTIR spectra of oxidized NCC whiskers show the characteristic C=O stretching peak at 1730 cm^{-1}. [70]
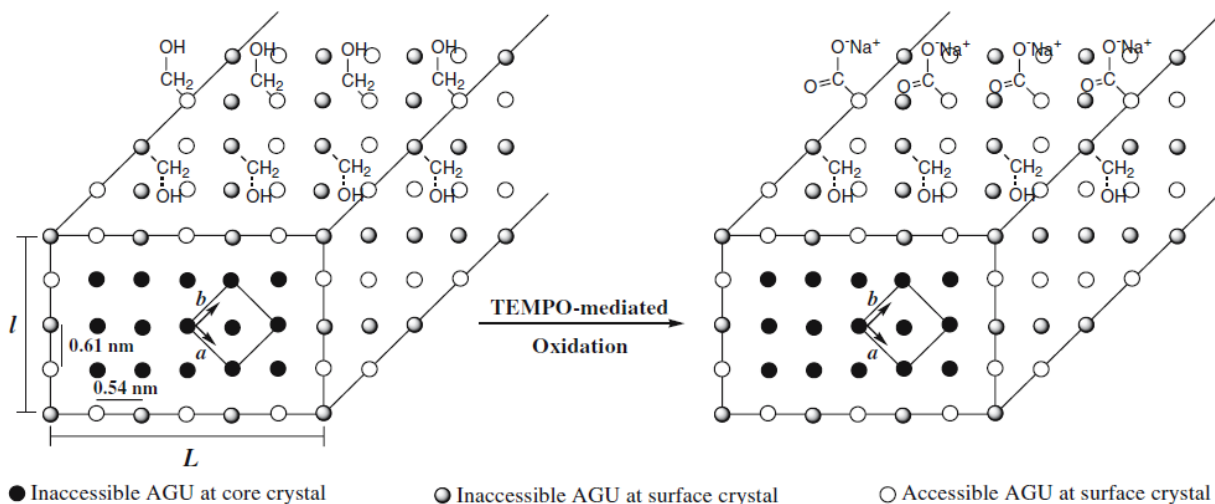
Figure 2.53 Schematic of the NCC whiskers before and after TEMPO-mediated oxidation [70]

Figure 2.54 shows the X-ray powder diffraction patterns before (a) and after (b) oxidation; both patterns exhibit the same sharpness and intensity of diffraction rings indicating that TEMPO-mediated oxidation did not induce any changes in the crystalline structure of the whisker cores. Figure 2.55 shows images of unoxidized (a) and oxidized (b) NCC whiskers observed under crossed polarizers. Where unoxidized NCC whiskers flocculate at 0.53% (w/v), oxidized NCC whiskers show shear birefringence at the same concentration without any flocculation or phase separation. From Figure 2.55b the authors deduce that even though birefringent domains are present but there is no further ordering into chiral nematic phase thus explaining the absence of characteristic fingerprint texture. Probable causes could be high viscosity of suspension or high PDI of tunicate whisker lengths. [70]
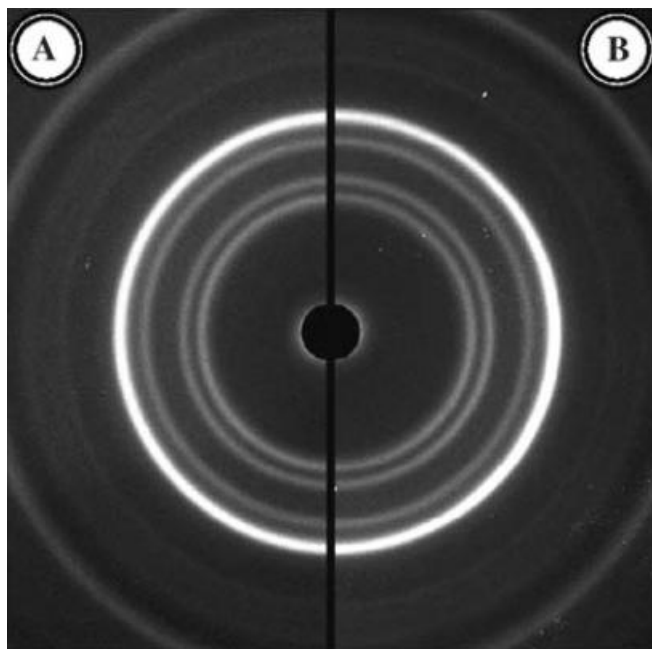
Figure 2.54 X-ray powder diffraction patterns before (a) and after (b) oxidation [70]
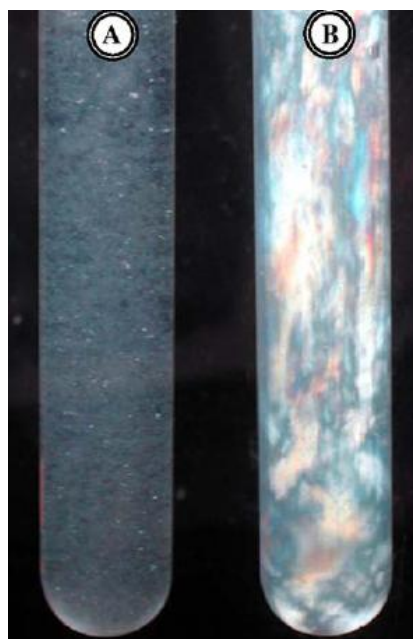
Figure 2.55 Images of unoxidized (a) and oxidized (b) NCC through crossed polarizers [70]

The first successful attempt at producing stable suspensions of NCC whiskers in non-polar solvents was undertaken by Heux et al.; NCC whiskers from cotton and tunicate were mixed with BNA surfactant (a phosphoric ester of polyoxyethylene nonylphenyl ether) at high pH and then freeze dried and redispersed in toluene and cyclohexane. Tunicate whiskers were produced at 0.3 wt% and cotton whiskers at 1 wt% for dilute solutions in cyclohexane and toluene. All the prepared solutions showed flow birefringence i.e. NCC whiskers acquire parallel orientation in the direction of flow indicating a quality of dispersion similar to NCC whiskers dispersed in water due to electrostatic repulsion. Next a higher concentration (36 wt%) was prepared in cyclohexane and observed between crossed polars. This concentrated solution showed an isotropic and an anisotropic phase and an optical micrograph of anisotropic phase showed the characteristic fingerprint pattern of chiral nematic phases. This observation made the authors conclude that the chiral nematic phases were formed in spite of a layer of surfactants around the NCC whiskers. They also proposed that this conclusion supports the idea proposed by Orts et al. [71] that chiral character is observed due to the shape of the NCC rods and not due to the chiral character of the cellulosic backbone. [72]

Apart from using surfactants to disperse NCC whiskers in organic solvents, Gousse et al. have utilized silylating agents to graft onto the NCC surface to produce less labile and chemically stable silylated NCC (see Figure 2.56). The authors observed experimentally that initially silylation was rapid but the reaction rate decreased thereafter reaching a constant after a few hours. Hence, the authors adopted a partial silylating methodology to maintain the structure integrity of the whisker core and redisperse the whiskers in low polarity organic solvents. TEM images of silylated whiskers (see Figure 2.57) show convoluted wavy contours indicating

aggregation in certain regions. Moreover, the partially silylated whiskers were found to be more swollen as compared to the needle-like images of unmodified whiskers, indicating slight silylation of the core as well. On complete silylation or using longer reaction times the structural morphology of the whiskers was completely destroyed. Figure 2.58 shows different X-ray powder diffraction patterns for untreated NCC and silylated NCC whiskers with increasing degree of substitution (DS) from (b) to (d); for the sample with highest degree of substitution (d) complete destruction of crystalline structure is observed. [73]
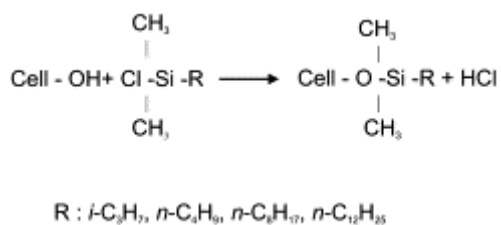
Figure 2.56 Silylation of NCC whiskers [73]
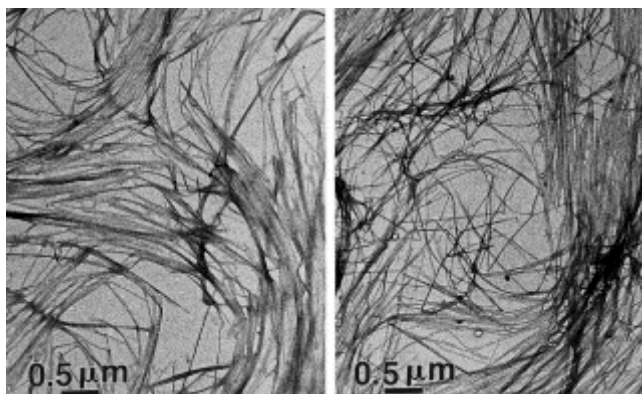
Figure 2.57 TEM image-Silylated NCC whiskers [73]
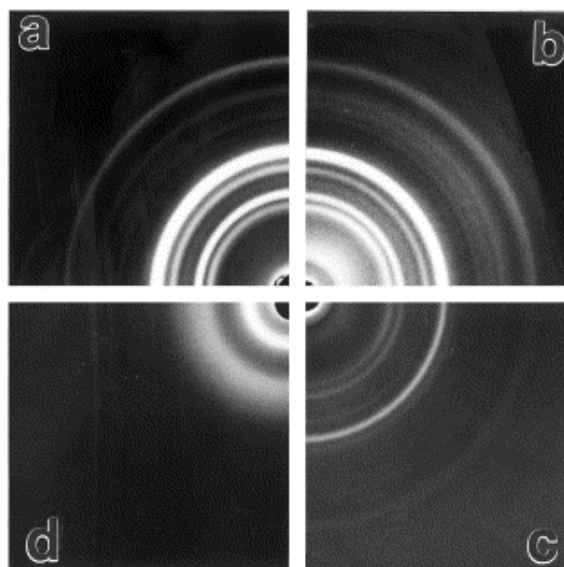
Figure 2.58 X-ray powder diffraction patterns for untreated NCC (a) and silylated NCC whiskers with increasing degree of substitution (b) DS=0.6 (c) DS=0.99 (c) DS =1.76 [73]

These partially silylated whiskers were readily redispersed in medium polarity organic solvents like acetone and THF but not in low polarity solvents like toluene and hexane. For e.g. in THF solvent, the suspension flocculated at DS =0.4 but formed a cloudy stable suspension at DS=0.6. Essentially four silylating agents were chosen and a model was developed to explain why the fibres lost their structural integrity on excessive silylation and why the partially/moderately silylated NCC whiskers dissolved in THF but not in solvents of lower polarity. Figure 2.59a shows NCC whisker with low DS but is still hydrophilic in nature as it keeps its structure integrity and flocculates in THF. Figure 2.59b shows NCC whisker with moderate DS rendering the surface hydrophobic. Here some chains are derivatized and some ends are soluble thus stabilizing the whiskers in organic solvents of low polarity. Figure 2.59c shows highly silylated whiskers such that the surface chains are solubilised in the reaction medium and the inner core is exposed to more silylation thereby compromising its structure integrity and crystalline nature. [73]
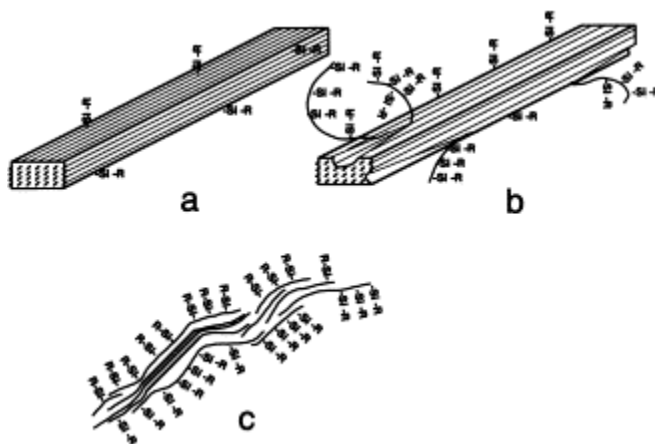
Figure 2.59 Schematic model explaining silylation of NCC whiskers [73]

Hydrophobically modified NCC whiskers were prepared by surface acylation using alkyenyl succinic anhydride (ASA). Two ASA agents were used: *iso*-octadecenyl succinic anhydride (*iso*-ODSA) and *n*-tetradecenyl succinic anhydride (*n*-TDSA) (see Figure 2.60 for structures). Aqueous dispersions of the ASA agents were formed in water and then mixed with NCC suspensions. Next the NCC whiskers were completely dried using freeze drying and then heating to 105°C to complete the acylation modification. TEM analysis showed that the acylated whiskers did not show any aggregation in 1,4-dioxane and X-ray diffraction patterns of the acylated whiskers did not exhibit any changes from the original whiskers, indicating that crystallinity of the NCC whiskers was unaffected by acylation. The acylated whiskers showed good dispersibility in low/medium polarity solvents. Table 2.2 summarizes some results of dispersibility tests conducted on acylated NCC whiskers. [74]
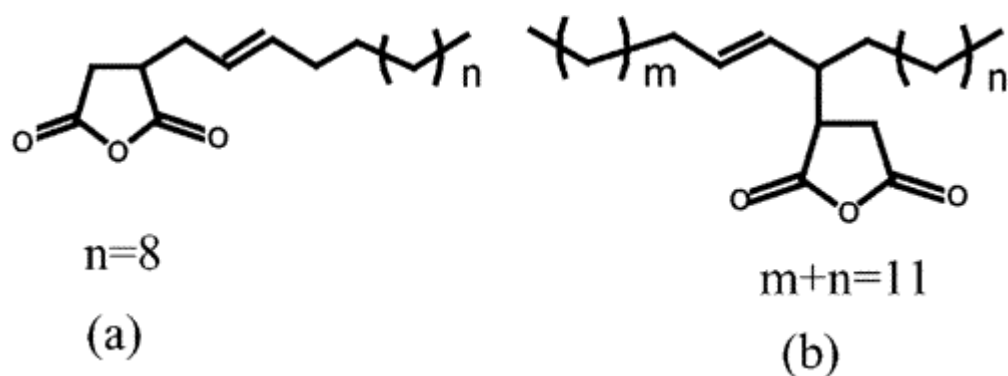
Figure 2.60 Structures of (a) iso-ODSA (b) n-TDSA [74]

solvent	relative permittivity (25 °C)	dispersion	
		original	iso-ODSA modified
water	78.54	a	c
formic acid	58.5 (16 °C)	a	c
dimethyl sulfoxide	46.45	a	b
N,N-dimethylacetamide	37.78	a	a
methanol	32.66	b	a
ethanol	24.55	c	a
acetone	20.56	c	a
1-butanol	17.51	d	a
dichloroethane	10.37	d	a
dichloromathane	8.93	d	a
tetrahydrofuran	7.58	d	a
chloroform	4.806 (20 °C)	d	a
toluene	2.37	d	a
1,4-dioxane	2.209	d	a
cyclohexane	2.02	d	b
hexane	1.8799	d	c

[a] Good dispersion. [b] Incomplete dispersion. [c] No dispersion. [d] Not tested.

Table 2.2 Dispersibility tests on acylated whiskers [74]

Surface acetylation of NCC whiskers (obtained from MCC) was undertaken by reacting it with vinyl acetate in the presence of potassium carbonate as catalyst. By progressively increasing

reaction times, it was observed that crystalline structure of the NCC whiskers was destroyed.

Figure 2.61 shows WAXD spectra of acetylated samples with different reaction times. Clearly the peaks at $2\theta=22°$ decrease in intensity suggesting that as the reaction time increased, the degree of acetylation increased and the inner crystalline structure of NCC whiskers was disrupted. 1 wt% acetylated whiskers dispersed easily in THF and were stable for more than 8 hours (see Figure 2.62). However, this was true for only acetylated whiskers with reaction time greater than 2 hours since reaction times lower than 2 hours resulted in partial acetylation of the NCC whisker surface. [75]
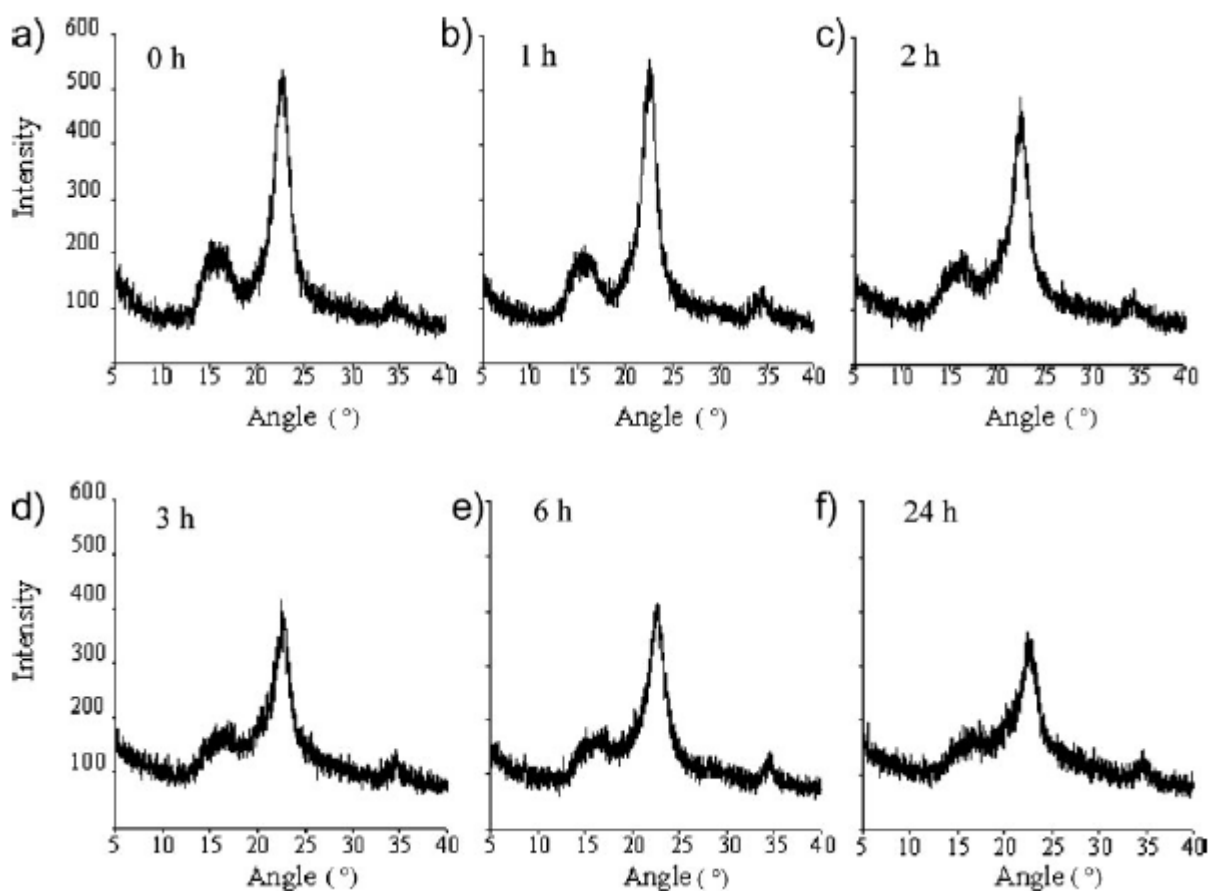
Figure 2.61 WAXD spectra of acetylated samples with different reaction times [75]
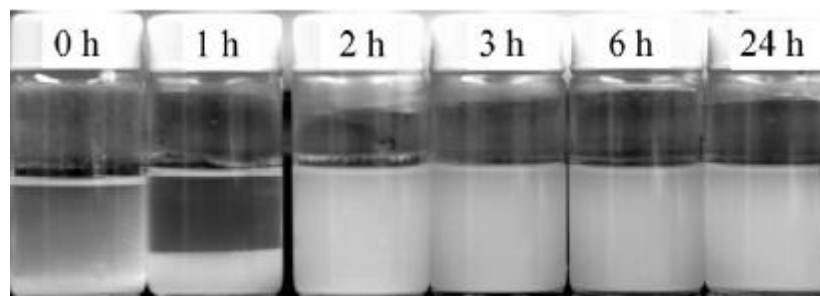
Figure 2.62 1wt% acetylated whiskers in THF [75]

Recently, Siqueira et al. grafted long chain isocyanate on NCC whiskers by using two new novel methods of in situ solvent exchange in order to prevent dispersion problems in the reaction medium. [76]
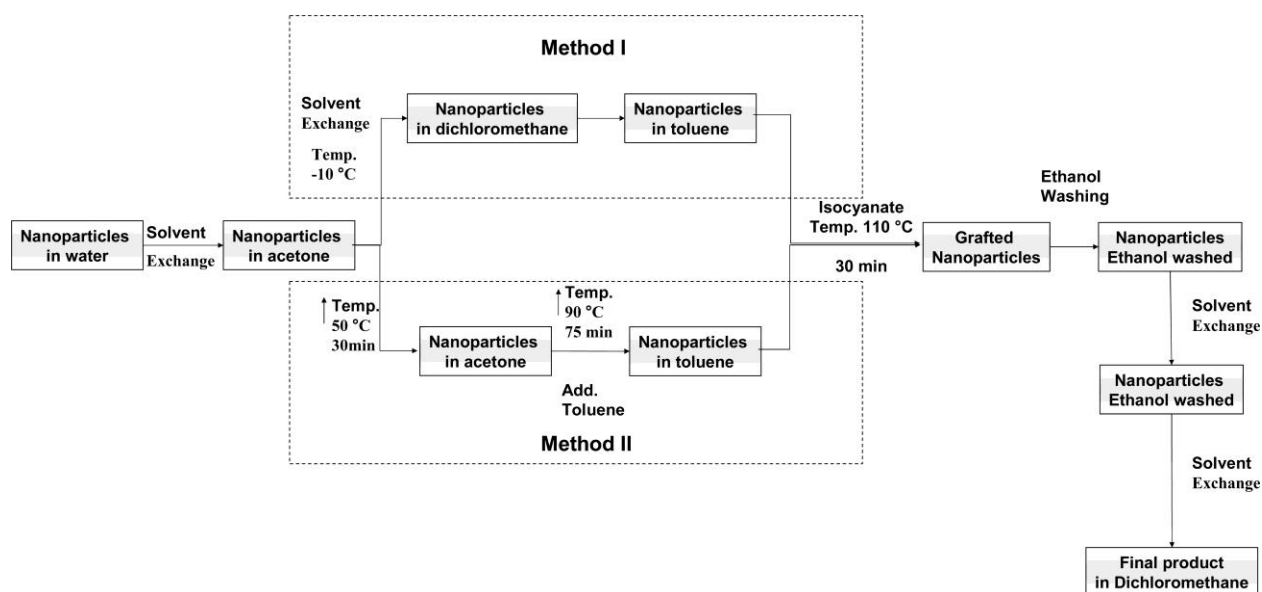
Figure 2.63 In situ solvent exchange process for grafting isocyanate on NCC whiskers [76]

Most techniques for surface modification of NCC whiskers involve the *grafting to* approach where a polymer chain is grafted onto the NCC surface. Recently, *grafting from* approach using

93

ATRP has been used to grow polymer chains from the NCC surface. ATRP stands for atom transfer radical polymerization which gives very precise control over grafting and produces well defined monodisperse particles. Surface initiated ATRP was used to graft polystyrene chains on the NCC surface. It was observed experimentally that polystyrene chains increased the absorption/adsorption of NCC-g-PS towards 1,2,4-Trichlorobenzene, an environmental organic pollutant. [77] Similar to their work, Xu et al. have synthesized NCC whiskers grafted with azobenzene polymers producing a novel amphotropic hairy rod system. This amphotropic system exhibited thermotropic and lyotropic liquid crystalline properties. Figure 2.64 shows a schematic for synthesis of NCC whisker grafted with Poly{6-[4-(4-methoxyphenylazo)phenoxy] hexyl methacrylate}(PMMAZO), a side chain liquid crystalline polymer. A direct evidence of successful grafting was formation of homogeneous dispersions in organic solvents like THF and other solvents for PMMAZO. Interestingly, the hairy rods form a lyotropic nematic phase in chlorobenzene above a critical concentration of 5.1 wt%; different LC transitions are also observed at different temperatures: smectic-to-nematic at 95°C, nematic-to-isotropic at 135°C and analogous lyotropic phase above 135°C. [78]
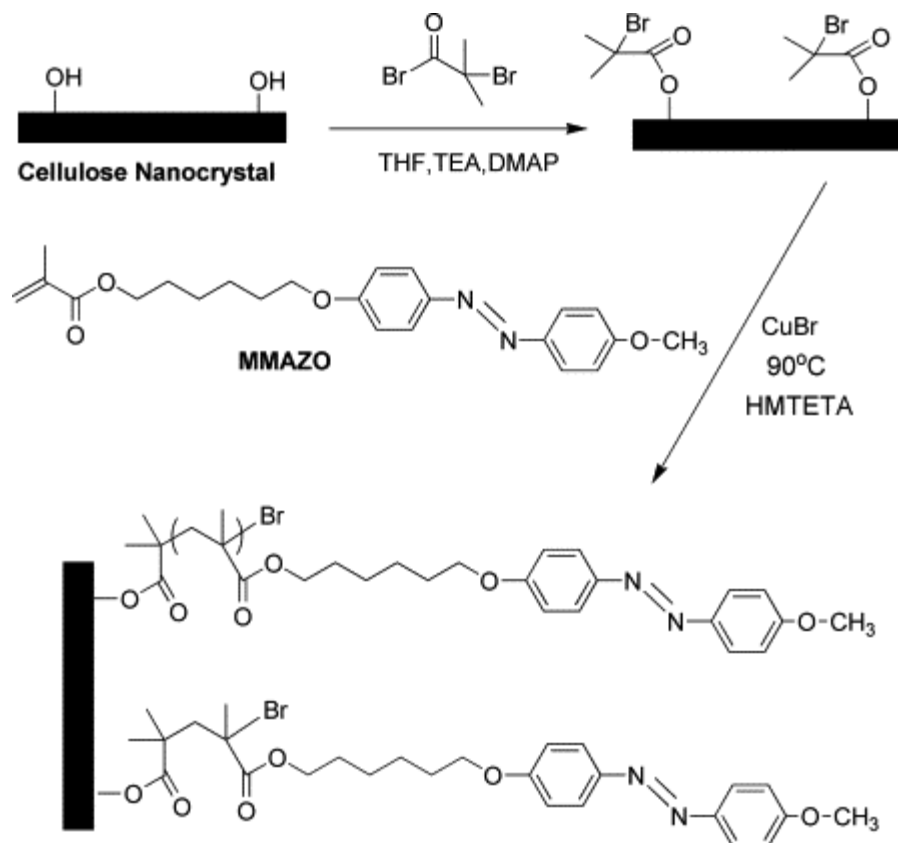
Figure 2.64 Synthesis of NCC whisker grafted with PMMAZO [78]

In an attempt to avoid complex surface functionalization routes, recently Braun et al. have combined the synthesis and functionalization of NCC in a single step (Figure 2.65). By utilizing a mixture of acetic acid, HCl and organic acids, NCC whiskers were synthesized and functionalized using Fischer esterification. Presence of acetate and butyrate groups affects the hydrophilicity of the NCC whiskers making their aqueous solutions unstable but exhibiting better dispersibility in ethyl acetate and toluene. [79]
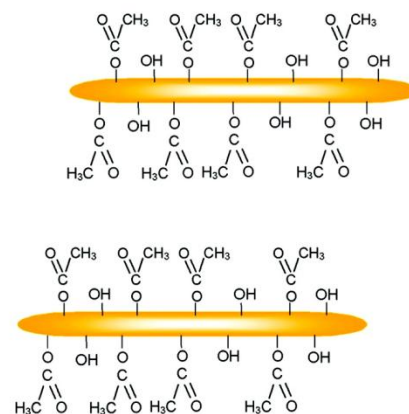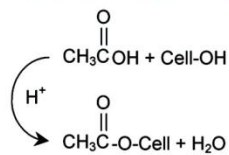
Figure 2.65 Single step process for cellulose hydrolysis and functionalization of NCC [79]

CHAPTER 3

CHARACTERIZATION TECHNIQUES

3.1 ZETA POTENTIAL MEASUREMENTS

As shown in Figure 3.1, for a charged particle suspended in an aqueous medium zeta potential is *not* the charge at the particle surface but it's the charge present at the slipping plane. For measuring zeta potential, the aqueous samples are subjected to an electric field making the charged particles move towards an oppositely charged electrode. The velocity with which the charged particles move is directly proportional to the amount of charge on the particle. The movement of charged particles towards an oppositely charged electrode causes a phase/frequency shift in the incoming laser beam. This effect is known as Laser Doppler Electrophoresis (LDE). The velocity of charged particles is determined as mobility; the particle mobility in turn is converted into zeta potential value using Smoluchowski and Huckel theories.

3.2 SURFACE TENSIOMETRY

Surface tension measurements were conducted in Dynamic Contact Angle Tensiometer (DCAT) shown in Figure 3.2. The DCAT software can take a single surface tension measurement or forward/reverse CMC measurements. The software also calculates the excess concentration and the surface area occupied per molecule at the interface. Surface tension measurements can be made using either the du Nouy ring method or the Wilhelmy plate method.
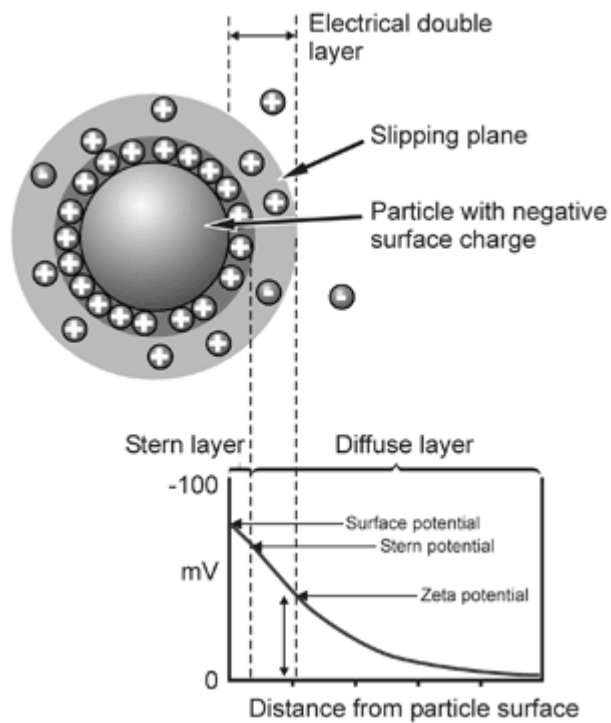
Figure 3.1 Schematic of zeta potential on a charged particle [122]

Figure 3.2 DCAT equipment for surface tension measurements [123]

3.3 FTIR

Fourier Transform Infra Red spectroscopy (FTIR) is used to determine the composition of unknown samples. When an unknown sample is irradiated with IR, the resulting FTIR spectra consists of absorbance and transmittance peaks. These characteristic peaks correspond to specific bonds within the unknown sample. An optical device called an interferometer allows FTIR machines to simultaneously measure all IR frequencies. Figure 3.3 shows the arrangement of sample and instrumentation in an FTIR machine.
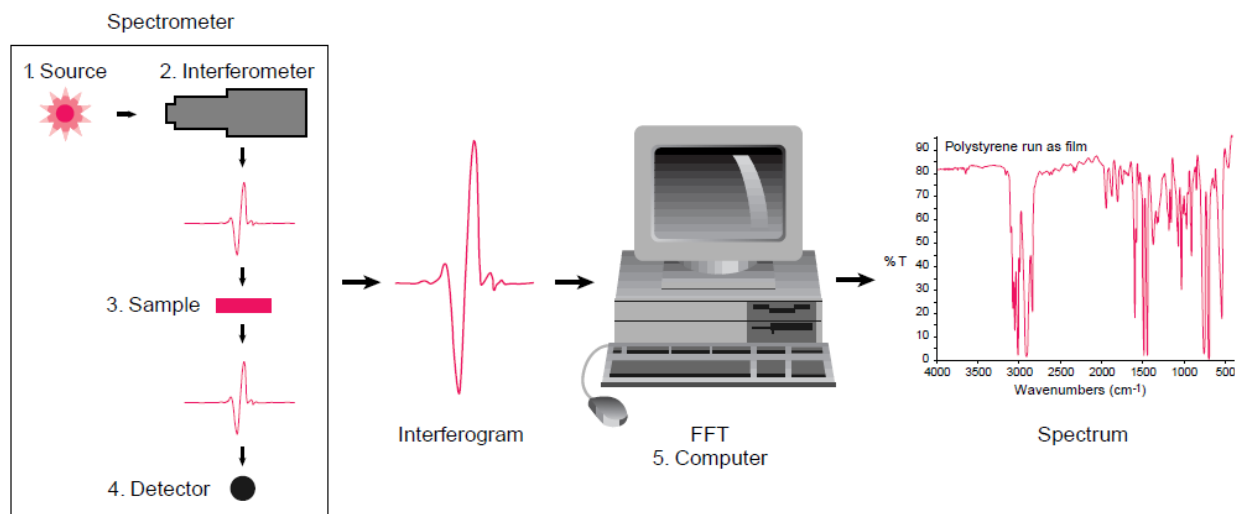
Figure 3.3 Basic FTIR set-up [124]

3.4 DLS

DLS stands for dynamic light scattering and is also commonly known as Photon Correlation spectroscopy (PCS) or Quasi-Elastic Light Scattering. DLS works on the principle of Brownian motion which is correlated to the size of the particles. Larger particles undergo lesser Brownian

motion as compared to smaller molecules which can diffuse faster. Stokes-Einstein equation is used to determine the size of the particles since this equation directly relates the hydrodynamic diameter of the particle with its diffusion coefficient. [125]

$$d(H) = kT / 3\pi\eta D \quad \text{(Stokes-Einstein equation)}$$

Equation 3.1 Stokes-Einstein equation for determination of hydrodynamic diameter

d(H): hydrodynamic diameter

D: translational diffusion coefficient

k: Boltzmann's constant

T: absolute temperature

η: viscosity

3.5 ITC

Isothermal Titration Calorimetry (ITC) is used to measure very minute heat changes when precise quantities of reactants are mixed together. As shown in Figure 3.4, the ligand is filled up in the syringe while the sample cell is filled with the polymer solutions. When the ligand is titrated into the sample cell, heat is either evolved (exothermic reaction) or absorbed (endothermic reaction). The amount of heat evolved or absorbed is directly proportional to the degree of binding between the ligand and the sample. The temperature difference between the sample cell and the reference cell is measured and converted into units of power; this physical temperature difference is called differential power (DP) and is defined as the power required to

maintain the sample and reference cells at the same temperature. Integrating the DP peaks with respect to time yields the ΔH value for the interactions.
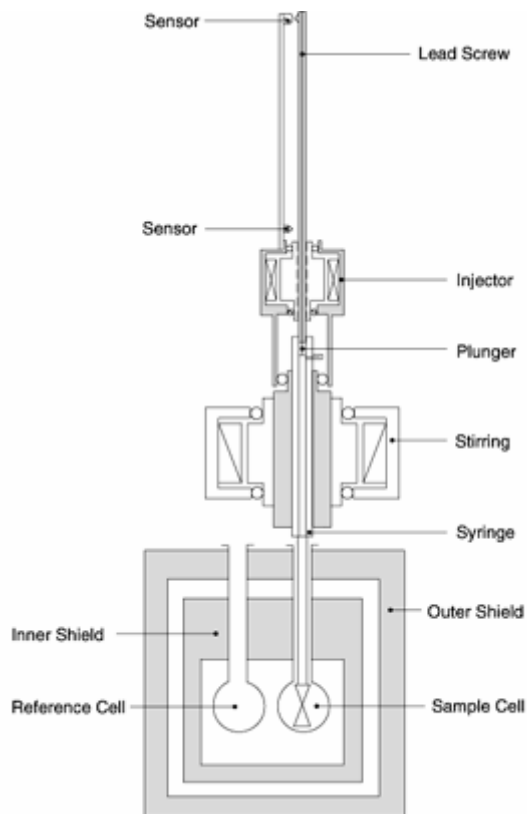
Figure 3.4 Basic set-up in a microcalorimeter [126]

3.6 DSC

Differential scanning calorimetry (DSC) can precisely measure exothermic or endothermic heat changes in the sample cell. In this sensitive technique, the sample to be studied is placed in the sample cell and then it is subjected to either a heating or a cooling cycle. Similar to ITC, the heat changes in the sample cell are correlated to the temperature difference between the sample and the reference cell, which is then calibrated to differential power (DP). [127]

CHAPTER 4

BIODEGRADABLE AND BIOCOMPATIBLE POLYAMPHOLYTE MICROGELS FROM CHITOSAN, CARBOXYMETHYL CELLULOSE AND MODIFIED METHYL CELLULOSE

4.1 Introduction

As mentioned in section 1.3.2, combination of the properties of *'polyampholyte'* and *'microgel'* results in the formation of *'polyampholyte microgels'* which are crosslinked polymer particles such that the constituent polymers possess positive and negative charges on their backbones.

The primary reason for synthesizing polyampholyte microgels is that their pH responsive behaviour will be attractive for drug and protein delivery applications. Ho et al. have synthesized polyampholyte microgels using poly(methacrylic acid) (PMAA) and poly(2-(dimethylamino)ethyl methacrylate) (PDMA). [6] Inverse microemulsion polymerization technique was used to polymerize MAA and DMA in the presence of a cross-linker (allyl methacrylate) to produce an amphoteric microgel system. The microgels exhibited swelling at low and high pH while they deswelled at neutral pH. Figure 4.1 shows the pH-responsive behaviour of polyampholyte microgels composed of PMAA and PDEA polymers. At low and high pH, the microgel particles acquire positive and negative charges respectively and the particles begin to swell due to the repulsion from like charges within the microgel particles. This allows counterions to enter the porous microgels resulting in increased swelling.

Conversely, as the solution approaches a neutral pH, equal number of positive and negative charges on the microgel particles results in a smaller hydrodynamic radii as the counterions leave the microgel particles causing them to deswell. Due to the overall charge neutralization on the surface of the microgel, the particles tend to flocculate at neutral pH ranges; the pH at which this phenomenon occurs is called the isoelectric point (IEP). In order to prevent flocculation of microgel particles at neutral pH ranges, a steric stabilizer such as poly (ethylene glycol) methacrylate (PEGMA) is grafted on the microgels. [6]
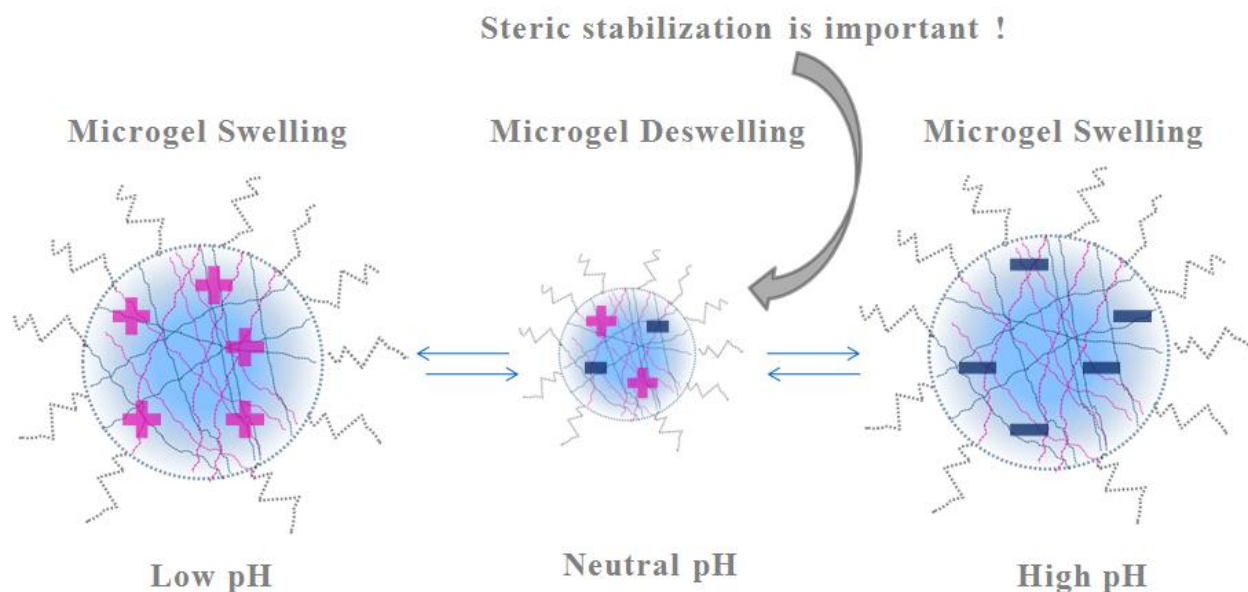
Figure 4.1 pH responsiveness of polyampholyte microgels (adapted from reference) [7]

Recently, many different polyampholyte microgel systems have also been explored. [80-83] Due to their potential applications and stimuli responsive characteristics of polyampholyte microgel systems, this project was aimed at synthesizing polyampholyte microgels using biopolymers as starting materials, instead of using synthetic monomers and initiators. Water soluble polymers are dispersed in a continuous organic phase together with a water soluble crosslinker, such as 1-

ethyl-3-(3-dimethylaminopropyl) carbodiimide (EDC) to produce crosslinked microgels. Simple EDC carbodiimide chemistry is used to crosslink the amino and carboxylic acid groups through amide linkages. [84]

Two different polyampholytic systems were synthesized: chitosan-carboxymethyl cellulose (CS-CMC) and chitosan-modified methyl cellulose (CS-ModMC). For the first system, chitosan and carboxymethyl cellulose were chosen since they would provide amine and carboxylic acid functionalities to the microgels. As a further extension of the CS-CMC system, we have also synthesized chitosan-modified methyl cellulose system where the methyl cellulose was modified by carboxymethylation [9] to incorporate carboxylic acid functionality to the microgels. Methyl cellulose contains methoxide groups which induce hydrophobic interaction between the methyl cellulose chains causing them to aggregate at the lower critical solution temperature (LCST). [15]Thus, by combining the pH responsive characteristics of chitosan and the thermo-responsive behaviour of methyl cellulose, we have synthesized a dual responsive system from biodegradable and biocompatible polymers.

The advantages of using these biodegradable polymers in place of synthetic monomers for microgel synthesis are as follows:

- The polymers are biodegradable and biocompatible [11] [8] [12]

- They are non toxic and non allergenic [2]

- They are readily available as they are obtained from natural sources, hence they are recyclable and cost effective [2]

- Using polymers as starting material instead of using synthetic monomers would ensure that no toxic initiators are present after the microgels are synthesized, making them suitable for biomedical and pharmacological applications [13] [14]

4.2 Experimental Section

4.2.1 Materials

Chitosan (M.W. 50000-190000, D.S ~75% - 80%) was purchased from Aldrich. Sodium salt of carboxymethyl cellulose (CMC-Na M.W. 250000, D.S - 1.2) was purchased from Acros Organics. Methyl cellulose (water soluble gum) was purchased from Fischer Scientific. Monochloroacetic acid (solid flakes, 99%) was purchased from Acros and used for carboxymethylation of methyl cellulose. Crosslinkers EDC (1-ethyl-3-(3-dimethylaminopropyl) carbodiimide, commercial grade) and NHS (*N*-Hydroxysuccinimide, 98%+) were purchased from Sigma and Acros Organics respectively. MES (2-(*N*-morpholino) ethanesulfonic acid, $\geq$99%) was used as buffer for the EDC crosslinking reaction and was purchased from Aldrich. Non-ionic surfactants Brij 92V and Brij 96V were purchased from Aldrich and Fluka respectively and were used as received. For steric stabilization, poly (ethylene glycol) methacrylate (PEGMA M.W. 300, inhibitors removed using basic alumina) was purchased from Sigma and tert-butyl hydroperoxide initiator (TBHP, 70% solution in water, N_2 flushed) was purchased from Acros Organics. Millipore deionized water was used for all experiments and sample preparations.

4.2.2 Synthesis of chitosan-carboxymethyl cellulose microgels

Inverse microemulsions are thermodynamically stable water-in-oil (W/O) emulsions formed on the addition of large amounts of surfactants. [25] Inverse microemulsion technique is especially useful for water soluble polymers which tend to polymerize in the bulk aqueous phase. [6] The water droplets in a W/O inverse microemulsion, act as nanoreactors and water soluble polymers can be easily encapsulated and crosslinked in the water droplets. For instance, Ho et al. have synthesized polyampholyte microgels from MAA and DMA monomers using inverse microemulsion technique. [6]

Non-ionic surfactants are necessary for producing inverse microemulsions because of their unique phase-inversion property. Non-ionic surfactants can transform an oil-in-water (O/W) emulsion at room temperature to water-in-oil (W/O) emulsion at higher temperatures. The temperature, at which phase-inversion occurs from O/W emulsion to W/O emulsion, is called the phase inversion temperature (PIT). Furthermore, non-ionic surfactants exhibit a unique hydrophile-lipophile balance (HLB) value. HLB gives the ratio of hydrophilic (water-loving) to lipophilic (oil-loving) segments on a surfactant. Mixing two non-ionic surfactants with different HLB values produces a desired HLB value for the surfactant system. Experiments have also shown that the HLB values for a mixture of non-ionic surfactants can change the phase inversion temperature. [29] Therefore, by mixing two non-ionic surfactants in a certain ratio produces an HLB value which corresponds to a desired phase inversion temperature.

For the synthesis of CS-CMC microgels, first a surfactant mixture was prepared by mixing 30 ml of hexane with 0.552 g of Brij 96 (HLB ~ 12.4) and 1.848g of Brij 92 (HLB ~ 4.9) surfactants. The combined HLB of this system was ~ 6.625 corresponding to a phase inversion temperature of around 70°C. [6] This surfactant mixture was added to a 100 ml (three necked) round bottomed reaction vessel and the temperature was raised to 70°C. 0.05g chitosan was dissolved in 10 ml of 1% acetic acid solution and 0.03g of CMC-Na (sodium salt of carboxymethyl cellulose) was dissolved in 10 ml of DI water. The pH of both polymer solutions were adjusted to around pH 5 since EDC crosslinker works effectively in the pH range of 4-6. [84] 0.1 wt% MES buffer was added to each polymer solution to maintain the pH at a constant value. 0.016g of EDC and 0.01g of NHS was added to the chitosan solution. The EDC/NHS loaded chitosan solution and CMC-Na solution were added simultaneously to the surfactant mixture in the reaction vessel. As soon as the polymers were added to the reaction vessel, the solution turned turbid. The reaction was allowed to proceed for another four hours. Free radical grafting method was used to graft steric stabilizers on the surface of the microgels. 0.1 ml of 1% TBHP solution and 0.2g of PEGMA-300 was added to the reaction vessel under N_2 purge. The grafting reaction was allowed to continue for another hour. In order to remove the hexane, the hot reaction mixture was poured into a rotary evaporator and hexane was removed under vacuum. The resulting thick microgel sample was diluted with DI water and dialyzed (M.W cut off: 10,000 Da) for about a week to remove the surfactants, initiator, unreacted polymers and any homopolymers of PEGMA which may have formed during the grafting reaction. We observed that the microgels were not stable over time and flocculated after approximately one week as shown in Figure 4.2a. However, after ultrasonicating for 5 minutes, the microgels seemed to form a stable dispersion again as shown in

Figure 4.2b. This may be due to the M.W. of PEGMA used for steric stabilization. Using PEGMA with 2000 M.W. might produce a more stable microgel sample.

Flocculation after standing for about a week

(a)

(b)

Stable dispersion formed after sonication
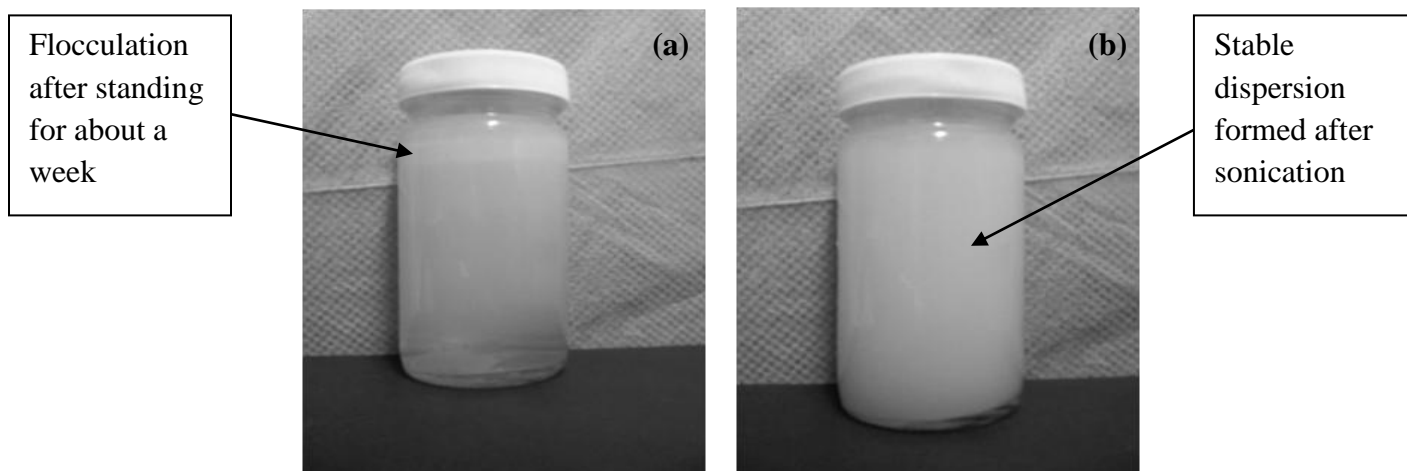
Figure 4.2 Reaction mixture of CS-CMC microgel system

4.2.3 Modification of methyl cellulose

In order to incorporate carboxylic acid groups on the methyl cellulose chains (Figure 4.3), carboxymethylation was used for chemical modification. Carboxymethylation of methyl cellulose was carried out using a standard slurry process. [85] 0.5g of methyl cellulose powder was suspended in 15 ml of isopropanol through vigorous stirring. 1.33 ml of 15% (w/v) NaOH solution was added drop wise into the suspension. The stirring was continued for another hour before adding 0.6g of monochloroacetic acid. The reaction mixture was heated to 55°C for about 1.5 hours. The reaction time was controlled to prevent depolymerisation of the starting methyl cellulose polymer. The product was recovered from the suspension, using acetone as the non-

solvent. The powder-like product was washed with acetone and 80% (v/v) ethanol solution several times and then dried at vacuum at 60°C.
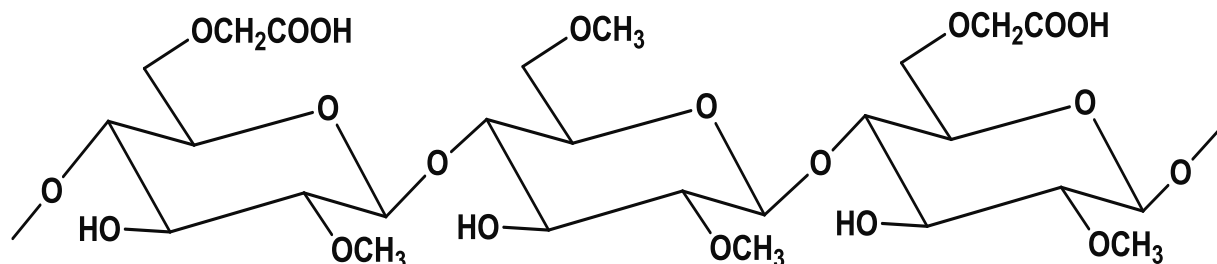
Figure 4.3 Structure of modified methyl cellulose

4.2.4 Synthesis of chitosan-modified methyl cellulose microgels

As described in section 4.2.2, the same experimental procedure was used to synthesize the CS-ModMC microgels, incorporating modified methyl cellulose instead of carboxymethyl cellulose. It was also observed that the modified methyl cellulose powder dissolved easily in DI water at room temperature. This is an evidence of successful carboxymethylation since unmodified methyl cellulose does not dissolve easily in water at room temperature. It must be dissolved in hot water first and then subsequently cooled so that it becomes completely soluble in water.

4.2.5 Characterization techniques

Potentiometric and Conductometric Titration

Simultaneous measurements of pH and conductivity were performed using the Metrohm 809 Titrando autotitrator. It is equipped with Tiamo software capable of dosing microlitre quantities of any titrant. All measurements were conducted in a closed jacketed vessel at 25°C with medium stirring. Initially, the pH of the microgel sample (0.1 wt%) was increased to pH 11 by addition of NaOH. The sample was then titrated with 0.1 N HCl and pH and conductivity were measured simultaneously till the pH of the sample approached 2. pH and conductivity values were plotted against concentration of HCl (in mM). The pH and conductivity curves showed different transition points confirming the presence of $-OCH_2COOH$ and $-NH_2$ functional groups on the synthesized microgels.

Zeta Potential Measurements

Zeta Potential measurements for microgel samples at different pH values were measured using Brookhaven ZetaPALS Analyzer. PALS stands for Phase Analysis Light Scattering which allows measurement of zeta potential as well as electrophoretic mobility. Concentration of the samples was maintained around ~ 0.1 wt% and the experiment was conducted at 25°C.

Dynamic Light Scattering

Dynamic Light scattering measurements were conducted at 25°C using BI-200SM goniometer for scattering detection at multiple angles. It is also equipped with BI9000AT digital correlator and BI-DNDC for static light scattering measurements as well. Laser with a wavelength of 636 nm was used. Microgel samples at different pH values were used for measurement of hydrodynamic radii and concentration of the samples was maintained around 0.1 wt%. In order to eliminate the effect of dust particles a 0.45 μm filter was used to filter the samples before measurement.

Surface Tension Measurements

Unmodified methyl cellulose (MC) and modified MC samples seemed to show some surface activity when the solutions were shaken or stirred. Hence, surface tension measurements were conducted for unmodified methyl cellulose and modified methyl cellulose samples. Since modified MC samples consist of carboxylic acid groups, it was expected that the surface activity of the modified samples would be affected by pH. So, surface tension measurements for modified MC samples were conducted at different pH values. Measurements were conducted in DCAT 11 (Dataphysics) at 25°C. It is equipped with a state-of-art software package and two liquid dispensing units (LDU) capable of dosing microlitre volumes of titrant. Wilhelmy plate method was used to measure dynamic surface tension values of the samples. Concentration of methyl cellulose and modified methyl cellulose samples were fixed at 2 g/L and the polymers were titrated into 50 ml of DI water in 30 volumetric increments.

Differential scanning calorimetry

Microcal VP-DSC instrument was used to determine the thermoresponsive properties of unmodified and modified methyl cellulose samples. Degassed 0.5 wt% samples were used in the sample cell along with DI water as the reference liquid. The experiments were conducted at constant pressure of ~ 27 psi. All upscan runs (from low to high temperature) were recorded. However, the downscan runs (high to low temperatures) were noisy hence, they have not been reported.

FTIR

Bio-Rad (Excalibur series) FTIR spectrometer was used to analyze the modified and unmodified methyl cellulose samples. The wavelength range considered is 400-4000 cm^{-1}. KBr powder was mixed with the powder samples to make thin FTIR films by compressing them between steel platens.

4.3 Results and Discussion

4.3.1 Chitosan-Carboxymethyl Cellulose microgels (CS-CMC)

Figure 4.4 shows the potentiometric and conductometric titration curve for 0.1 wt% CS-CMC microgel solution. At the start of the experiment, the sample was adjusted to pH 11 and then titrated with 0.1 N HCl. Different transition points on the pH and conductivity curves confirmed the presence of amino and carboxylic acid groups on the microgels. Transition points at the

conductivity curve were determined by the change in slope (inflexion points) and the intersection of vertical dashed lines with the pH curve is described as a transition point on the pH curve. For this system, the transition points on the pH curve were observed at pH of 9.4, 4.2 and 3.2. The titration curve exhibits four distinct regions: the first region (starting from left) corresponds to the neutralization of excess base. The second region (pH 9.4 to 4.2) corresponds to the protonation of $-OCH_2COO^-$ groups on the carboxymethyl cellulose (CMC) chains on the microgels. The third region (pH 4.2 to 3.2) corresponds to the protonation of $-NH_2$ groups on the chitosan (CS) chains in the microgels and finally the fourth region corresponds to excess acid present in the solution.

In terms of transition points on the pH curve, the first transition point at pH of 9.4 represents the start of protonation of $-OCH_2COO^-$ groups to $-OCH_2COOH$. This protonation ends at second transition point, pH of 4.2. This point also corresponds to the start of protonation of $-NH_2$ groups to $-NH_3^+$. At the third transition point, pH of 3.2, the protonation of $-NH_2$ groups is complete. By measuring the moles of HCl reacted for each functional group (second and third transition regions), the amount of $-OCH_2COOH$ and $-NH_2$ groups was determined as 1.5 and 1.1 meq/g of microgel.
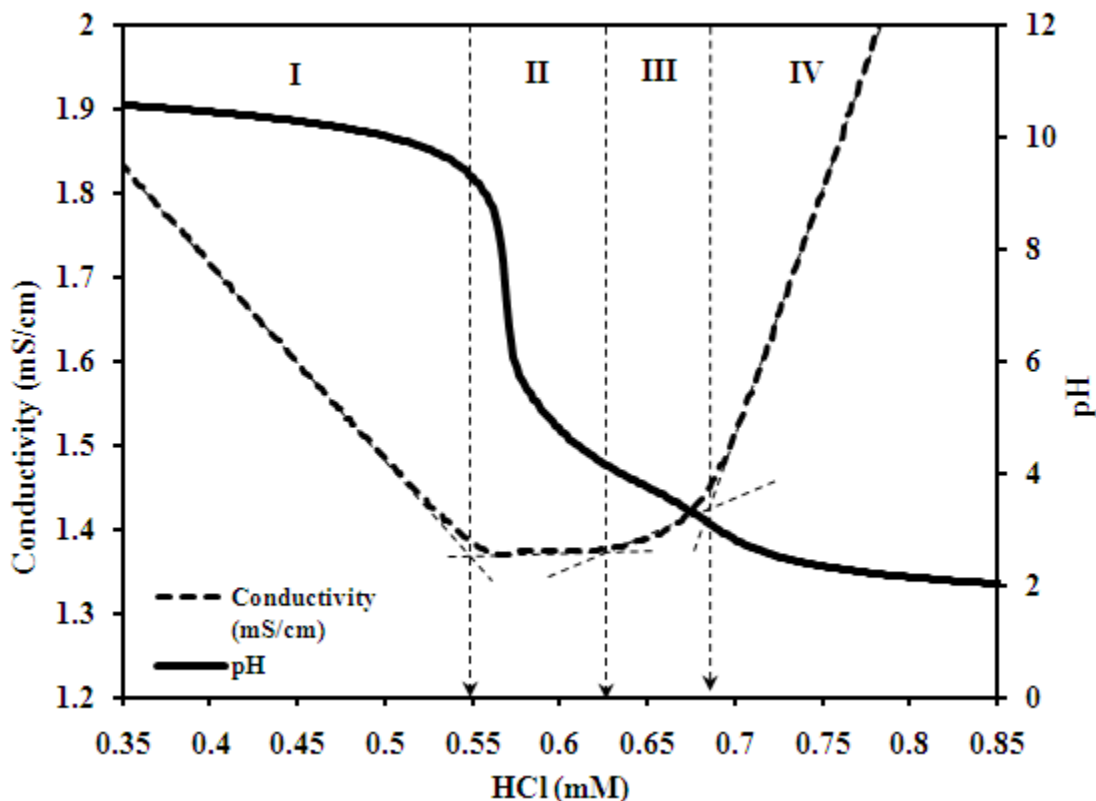
Figure 4.4 pH and conductivity titration curve for 0.1 wt% CS-CMC microgels

Figure 4.5a, 4.5b and 4.5c show the hydrodynamic radius and zeta potential values measured for 0.1 wt% microgel samples at different pH values. As shown in Figure 4.5a, for intermediate pH ranges between pH 4 to 9, a typical U-shaped profile was obtained for the hydrodynamic radius curve. At low pH, the -NH$_2$ groups on CS chains in the microgel are positively charged due to protonation of the amine groups. Because of repulsion between -NH$_3^+$ groups on CS chains, the microgel swells, and increases in size. Similarly, at high pH, the -OCH$_2$COOH groups on CMC chains are negatively charged due to deprotonation of the carboxylic groups. Therefore, the repulsion between -OCH$_2$COO$^-$ groups on CMC chains induces the swelling of the microgel. At

neutral pH, the microgel exhibits an overall neutral charge and the microgel deswells and shrinks in size.
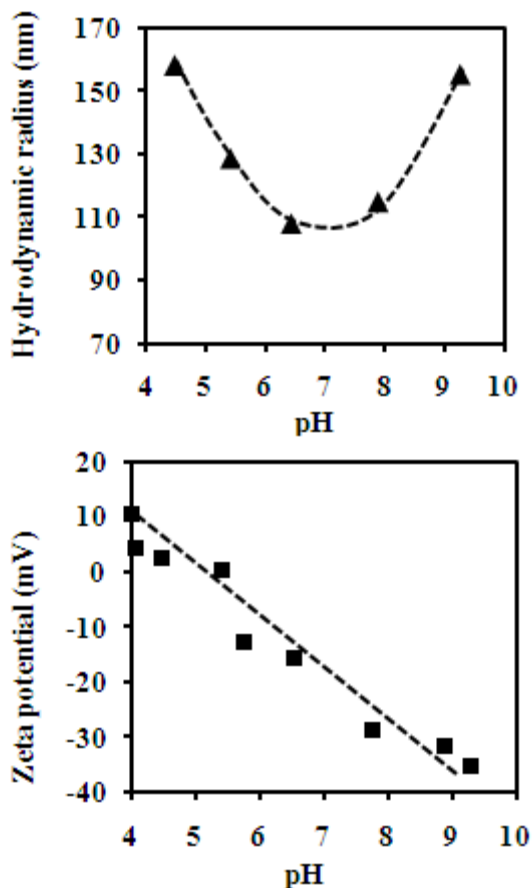
Figure 4.5a Hydrodynamic radius and Zeta potential vs. intermediate pH range (4-9) for 0.1 wt% CS-CMC microgel sample

As shown in Figure 4.5b and c, at extreme pH values (pH < 4 and pH > 10), the size of the microgels shows an appreciable reduction; so this observation cannot be attributed to charge shielding alone. One possible explanation could be the acid and base catalyzed hydrolysis of amide linkages within the microgel. Once the amide crosslinks are hydrolyzed at extreme pH values, the CS and CMC chains are expelled from the microgels, hence the microgel size

reduces. Several papers have reported the hydrolysis of an amide bond under acidic, basic and neutral conditions; [86] [87] [88] it was observed that the rate of amide hydrolysis was higher at extreme pH values (i.e. pH < 4 and pH > 10) than in a neutral pH range, where the amide hydrolysis was slower.

The zeta potential values (Figure 4.5c) also corroborate the above results. In the pH range of 4 to 9, the surface charge on the particles decreases from +10 mV to -40 mV as the microgels possess $-NH_3^+$ and $-OCH_2COO^-$ groups at low and high pH respectively. However, at pH < 4 and pH > 10, the charge on the microgel particle reduces, suggesting the expulsion of CS and CMC chains due to acid and base catalyzed amide bond hydrolysis.

Another important observation was made from zeta potential values in Figure 4.5c. While the maximum negative charge on the microgels is -40 mV, the maximum positive charge on the microgels is only +10 mV. This might seem contradictory since the amount of $-NH_2$ groups in the microgels (1.1meq/g) is comparable to the amount of $-OCH_2COOH$ groups in the microgels (1.5meq/g). Zeta potential analyzer measures only the surface charge on a particle and some of the surface $-NH_2$ groups are involved in PEGMA grafting; thereby lower positive zeta potential values are observed in experiments. Conversely, Figure 4.5b shows equivalent swelling in acidic and basic regions which can be explained from the fact that the number of $-OCH_2COOH$ and $-NH_2$ groups in the microgel are comparable. Furthermore, Figure 4.5b shows an iso-electric point (IEP) around pH 6 (where lowest hydrodynamic radius is observed) while Figure 4.5c shows an IEP around pH 5.5 (where zero zeta potential is observed). This may be attributed to experimental error during light scattering and zeta potential measurements.
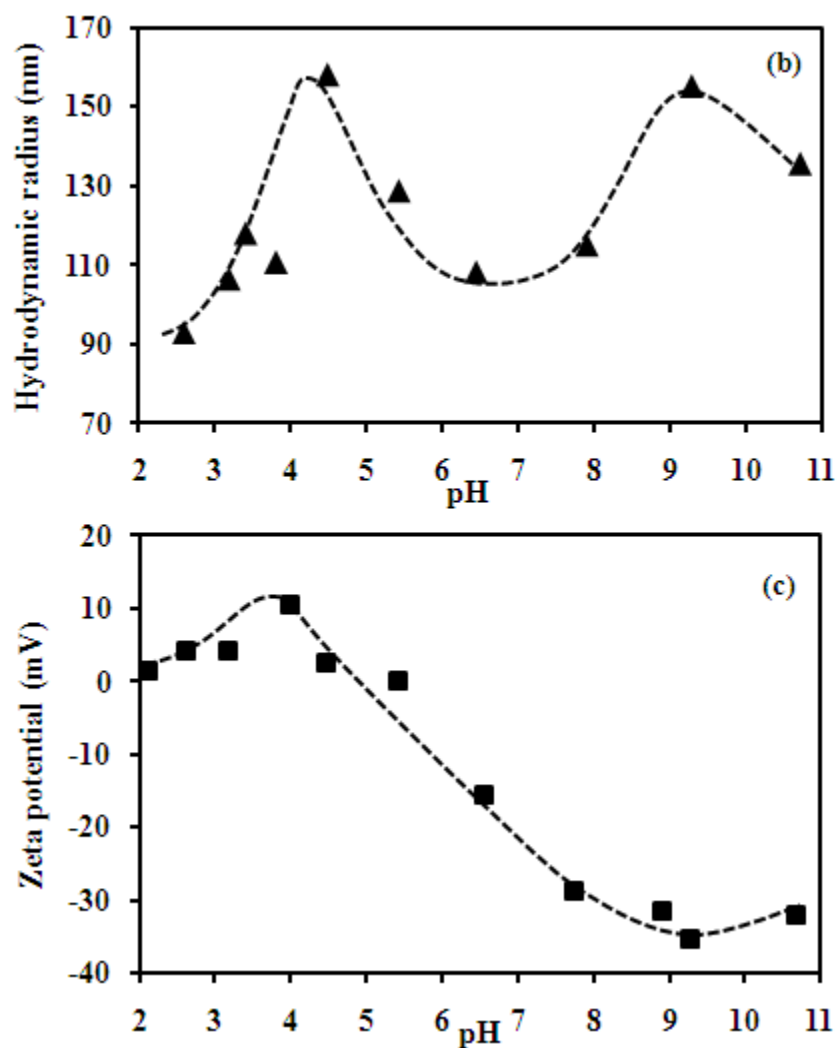
Figure 4.5 b and c Hydrodynamic radius & Zeta potential vs. pH for

0.1 wt% CS-CMC microgels

4.3.2 Modified Methyl Cellulose (Mod-MC)

Figure 4.6 shows the FTIR spectra of unmodified (a) and modified methyl cellulose (b). The spectra for modified MC shows the characteristic C=O frequency at 1750 cm^{-1} confirming the presence of carboxymethyl groups on the MC chains.
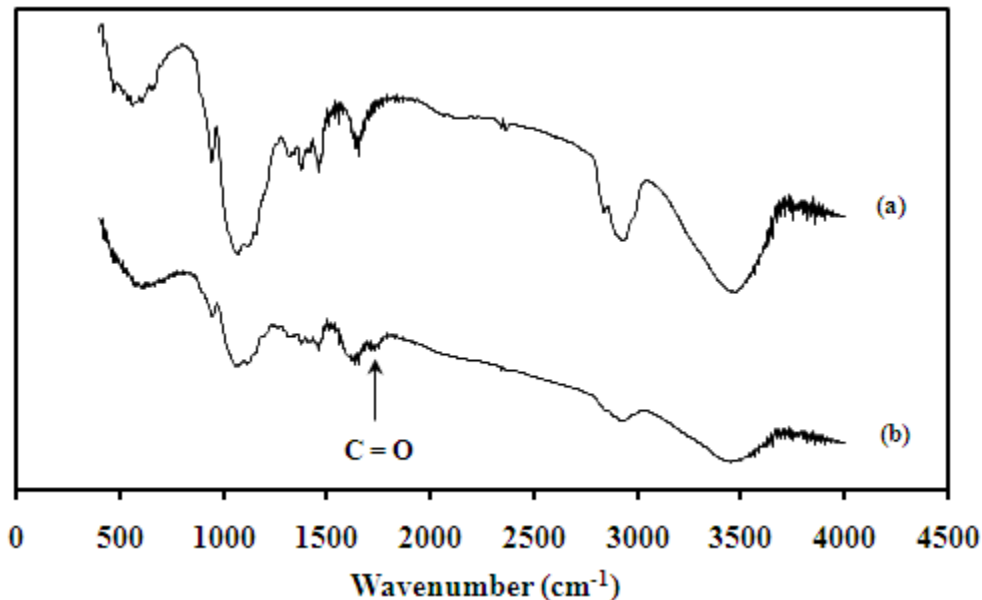
Figure 4.6 FTIR of unmodified methyl cellulose (a) and modified methyl cellulose (b)

Figure 4.7 shows the zeta potential results for modified MC samples at different pH values. As expected, the zeta potential values become more negative at higher pH values due to the deprotonation of carboxymethyl groups on the modified MC chains. Figure 4.8 shows the potentiometric and conductometric titration curve for 0.1 wt% modified MC sample. Intersection of vertical dashed lines with the pH curve is described as a transition point on the pH curve. The first region (starting from left) corresponds to excess OH$^-$ ions in the sample. The second region corresponds to the protonation of -OCH$_2$COO$^-$ groups to -OCH$_2$COOH (pH 9 to 3). The third region corresponds to the excess acid in the solution. By measuring the moles of HCl reacted in the second transition region, the no. of -OCH$_2$COOH groups was determined to be 2.6 meq/g of the sample.

118
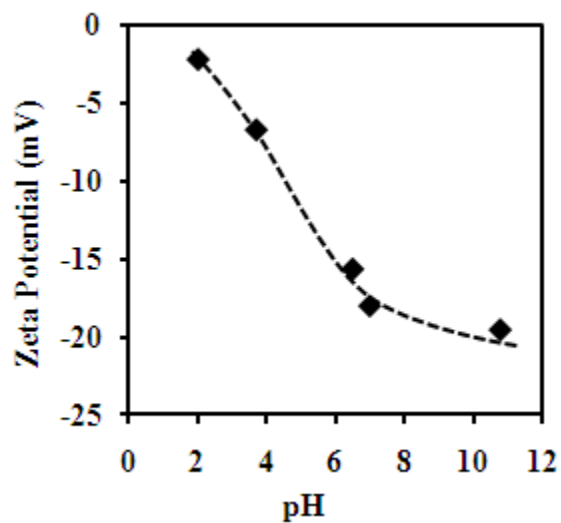
Figure 4.7 Zeta potential vs. pH for modified MC sample
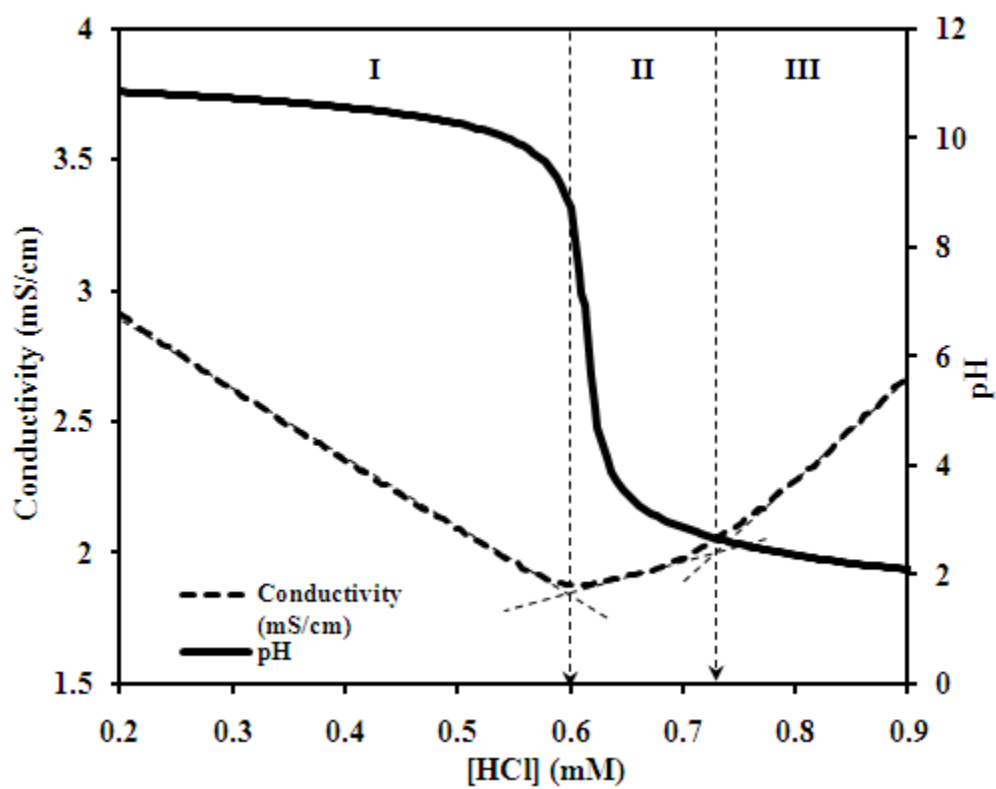
Figure 4.8 pH and conductivity vs. [HCl] for 0.1 wt % modified MC sample

119

We observed that unmodified and modified MC solutions exhibited surface activity when they were subjected to stirring/shaking. Figure 4.9a shows the surface tension results for unmodified MC and modified MC samples. The inset shows a magnification of the higher concentration region of surface tension of modified MC samples.
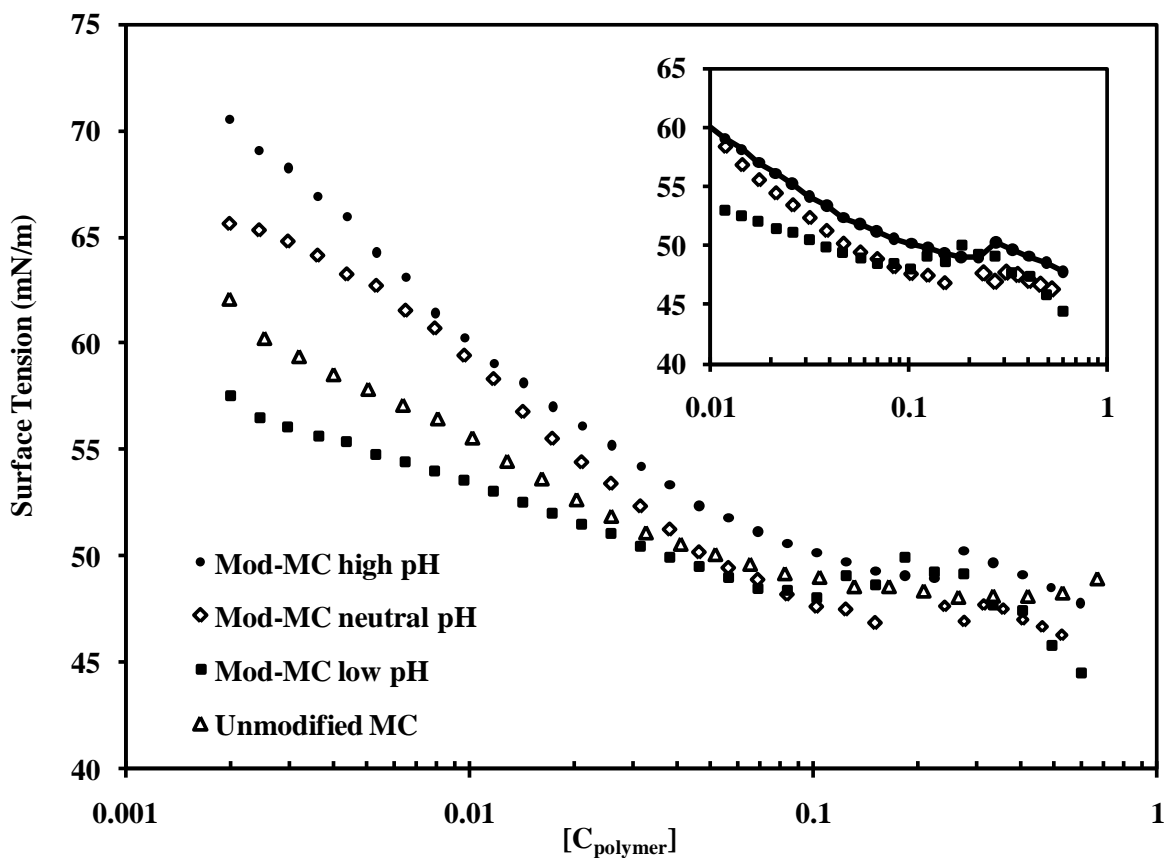
Figure 4.9a Surface tension curves for unmodified MC & modified MC at low,

neutral pH & high pH

According to Figure 4.9a, the surface tension of unmodified MC sample decreased as the concentration of the polymer was increased suggesting that the unmodified MC samples are

surface active. We hypothesize that unmodified MC chains conform at the at air-water interface in a manner such that the hydrophobic methoxide groups preferentially orient themselves into the non-aqueous air phase. Figure 4.9b shows a schematic of orientation of hydrophobic methoxide groups at the air-water interface. When the polymer concentration was increased, a higher proportion of hydrophobic methoxide groups induced the aggregation of MC chains at the interface causing the surface tension values to decrease further. Unmodified MC sample contains significantly high proportion of hydrophobic methoxide groups ($-OCH_3$) such that they preferentially partition to the air-water interface making unmodified MC surface active in nature. Since, unmodified MC shows surface activity similar to a surfactant, we expected to observe a CMC (critical micelle concentration), which is the concentration at which the surface tension values become constant. However, no CMC point was observed for unmodified MC sample i.e. no steady/constant value of surface tension was observed. Therefore, while unmodified MC is surface active like a surfactant, it does not possess other properties of a surfactant such as a CMC.

ORIENTATION OF -OCH$_3$ GROUPS INTO THE AIR PHASE
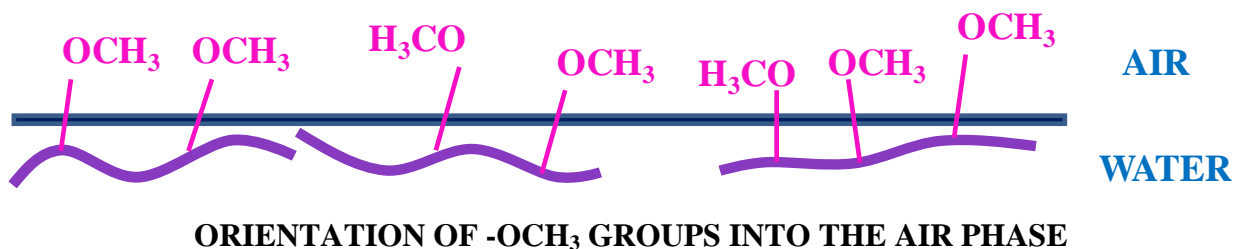
Figure 4.9b Unmodified MC chains at air-water interface

While unmodified MC chains are unresponsive to varying pH of the solution, the presence of carboxymethyl groups in modified MC chains makes them pH responsive; varying the pH affects

the degree of deprotonation of $-OCH_2COOH$ groups on modified MC chains. This effect is clearly seen in Figure 4.9a, where the surface tension curves for modified MC samples at different pH values show similar trends but their absolute values are different. For all modified MC samples at different pH values, the surface tension values decreased with increasing polymer concentrations indicating that the modified MC samples show surface activity at low, neutral and high pH.

For modified MC sample at low pH, the surface tension values are lower than those of unmodified MC sample suggesting that the modified sample at low pH is more surface active than unmodified MC. At low pH, the carboxymethyl groups in modified MC are protonated to $-OCH_2COOH$. Both the hydrophobic methoxide groups ($-OCH_3$) and the $-OCH_2COOH$ groups preferentially partition to the air-water interface (see Figure 4.9c) thereby decreasing surface tension of the solution. The partitioning of $-COOH$ groups of the linear polyelectrolytes to the air-liquid interface was also suggested by Okubo and Kobayashi. [89] Due to partitioning of -OCH_2COOH groups in addition to the partitioning of $-OCH_3$ groups, modified MC sample at low pH show greater partitioning to the air-water interface as compared to the unmodified MC sample. Thus, modified MC sample at low pH is more surface active as compared to unmodified MC sample.
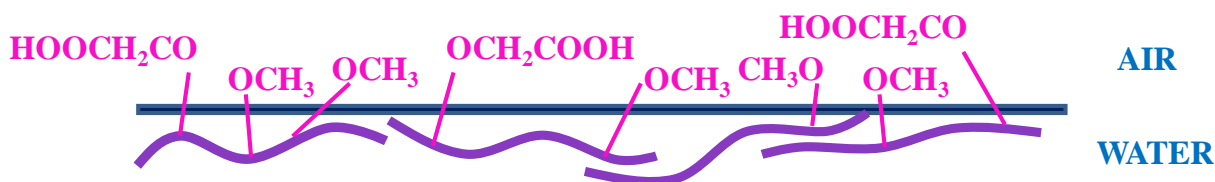
ORIENTATION OF -OCH₃ & -OCH₂COOH GROUPS INTO THE AIR PHASE

Figure 4.9c Modified MC chains (low pH) at air-water interface

At neutral pH, modified MC sample shows higher surface tension values as compared to the unmodified MC sample suggesting that the surface activity is lowered for modified MC sample. At neutral pH, a fraction of the carboxymethyl groups are deprotonated as -OCH_2COO^- and these charged groups tend to remain in the aqueous phase instead of the air phase (see Figure 4.9d). Thus, it becomes harder for the hydrophobic methoxide groups on modified MC chains to partition to the air-water interface, thereby reducing the surface activity in this case.
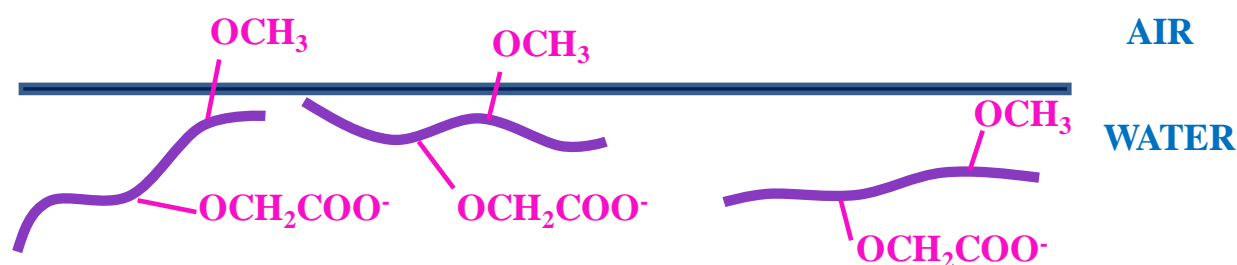
ORIENTATION OF -OCH_2COO^- GROUPS INTO THE WATER PHASE

Figure 4.9d Modified MC chains (neutral pH) at air-water interface

Similarly at high pH, most carboxymethyl groups on modified MC chains are deprotonated as -OCH_2COO^- which preferentially orient into the bulk aqueous solution. Hence, the surface activity of modified MC is further decreased at high pH in comparison to the unmodified MC sample. Like the unmodified MC sample, the modified MC samples did not show any CMC transition point for low, neutral and high pH.

4.3.3 Chitosan-Modified Methyl Cellulose microgels (CS-ModMC)

Figure 4.10 shows the potentiometric and titration curve for CS-ModMC microgel system. The intersection of vertical dashed lines with the pH curve is described as a transition point on the pH curve. As explained earlier for the CS-CMC system, the titration curve shows three transitions points at pH of 9.5, 5.5 and 3.8. Region I shows the presence of excess base in the sample. The second region (pH 9.5 to 5.5) corresponds to the start of the protonation of $-OCH_2COO^-$ groups to $-CH_2COOH$ on the modified MC chains in the microgel. The third region (pH 5.5 to 3.8) corresponds to the end of protonation of $-OCH_2COO^-$ groups and the start of protonation of $-NH_2$ groups to $-NH_3^+$. The fourth region corresponds to the end of protonation of $-NH_2$ groups on the CS chains and the presence of excess acid in the sample. By measuring the moles of HCl reacted for each functional group (second and third transition regions), the amount of $-OCH_2COOH$ and $-NH_2$ groups were determined as 0.8 and 0.6 meq/g of the microgel, respectively.
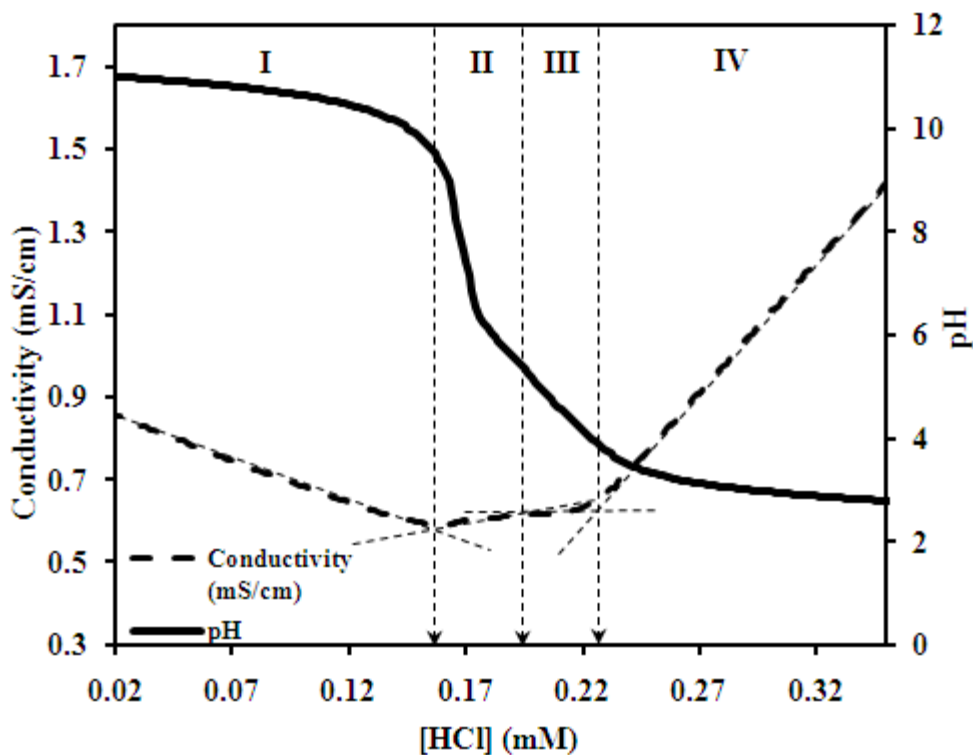
Figure 4.10 pH and conductivity titration curve for 0.1 wt% CS-ModMC microgels

Figs. 4.11a and b show the hydrodynamic radius and the zeta potential results for CS-ModMC microgel samples at different pH values. As explained for the CS-CMC system, in the pH range of 4 to 9, the microgels exhibit swelling at low and high pH and deswelling at neutral pH. However, for pH < 4 and pH > 10, the microgel size reduces drastically probably due to acid and base catalyzed hydrolysis of amide bonds. The zeta potential values also corroborate the above results since the surface charge on the microgels is lowered at the extreme pH values. The isoelectric point (IEP) from Figure 4.11a is ~ 7 while the IEP from Figure 4.11b is ~ 6.4.
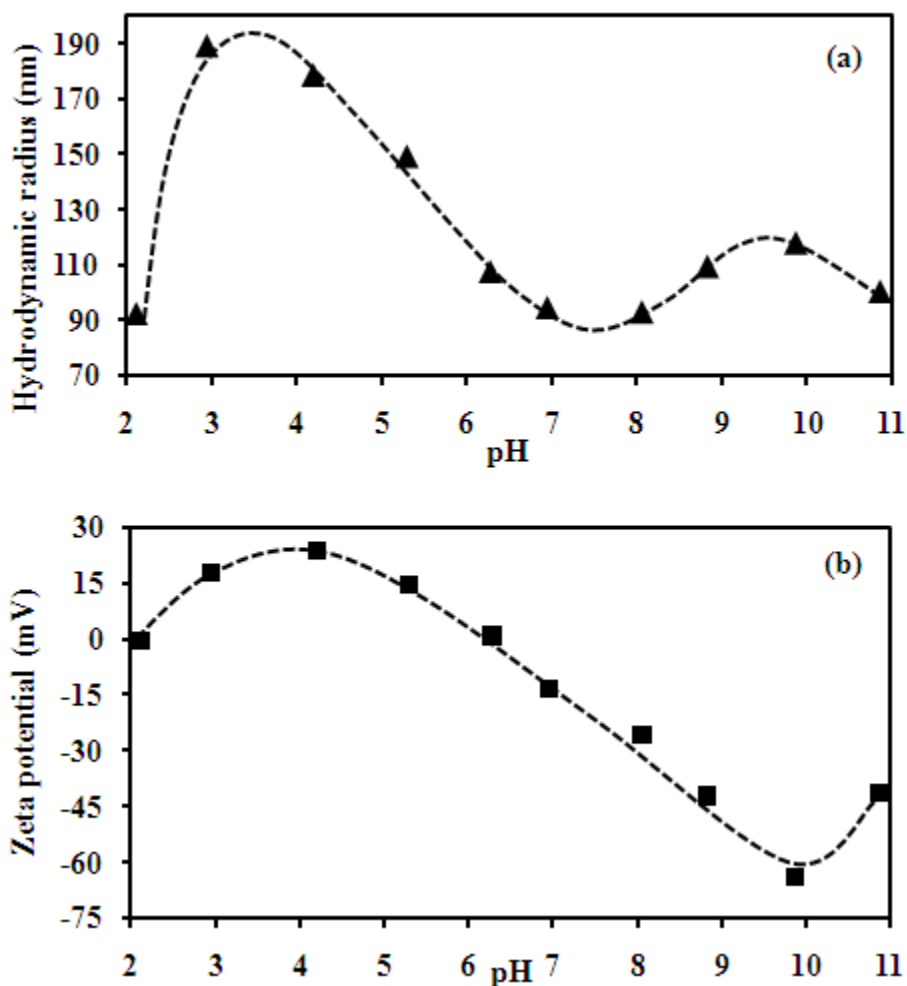
Figure 4.11a and b Hydrodynamic radius and Zeta potential vs. pH for CS-ModMC microgels

Thermoresponsive behaviour of CS-ModMC microgels

When aqueous methyl cellulose solutions were heated above a certain critical temperature called the lower critical solution temperature (LCST), the methoxide groups (-OCH$_3$) in methyl cellulose associate hydrophobically and produce a sol-to-gel transition in aqueous solutions. Thus, unmodified methyl cellulose solutions exhibit thermoresponsive behaviour at LCST. [15]

Since CS-ModMC microgels contain methoxide groups (-OCH$_3$) from modified MC chains, the microgels were expected to exhibit thermo-responsive character as well. In order to study the thermoresponsive behaviour of CS-ModMC microgels, the LCST of modified MC samples was determined using microcalorimetry (see Figure 4.12) and a characteristic LCST peak was observed at around 65°C. The hydrodynamic radii (R$_h$) vs. pH measurements were repeated for CS-ModMC microgels at the LCST of 65°C. By comparing the R$_h$ vs. pH behaviours at 25°C and 65°C (see Figure 4.13), the thermoresponsive character of CS-ModMC microgels was established.

Figure 4.12 shows the upscan results for unmodified and modified MC samples determined using a micro-calorimeter. Modified MC samples were studied at different pH values to analyze the effect of carboxymethyl groups on the hydrophobic association between modified MC chains. For unmodified MC sample, the LCST peak occurred at around 65°C. For the modified MC sample at low pH, a similar LCST peak at 65°C was observed. However, the peak for modified MC sample at low pH is larger (area wise) in comparison to the peak for unmodified MC sample. At low pH values, protonation of carboxymethyl groups to -OCH$_2$COOH groups facilitates hydrogen bonding between -OCH$_2$COOH and -OCH$_3$ groups while weakening the hydrophobic interactions between -OCH$_3$ groups. Therefore, a larger amount of energy is required to induce hydrophobic interactions between the modified MC chains at low pH; so the LCST peak for the modified MC sample is larger in comparison to that of unmodified MC sample. For modified MC sample at neutral pH, LCST peak was again observed around 65°C. At neutral pH, deprotonation of -CH$_2$COOH groups to -CH$_2$COO$^-$ reduces the hydrogen bonding between -CH$_2$COOH and -OCH$_3$ groups and facilitates the hydrophobic interactions between -OCH$_3$

groups. Hence, lesser energy is required to induce hydrophobic interactions between the modified MC chains at neutral pH making the LCST peak smaller in comparison to that of the unmodified MC sample. Similarly, at high pH, most of the carboxymethyl groups on modified MC chains are deprotonated as $-CH_2COO^-$. So, the hydrogen bonding between $-CH_2COOH$ and $-OCH_3$ groups is further weakened and the hydrophobic interactions between $-OCH_3$ groups are further strengthened. At high pH, we see a broad LCST peak ~ 55°C probably due to the enhanced hydrophobic interactions and gelling phenomena in the modified MC sample.
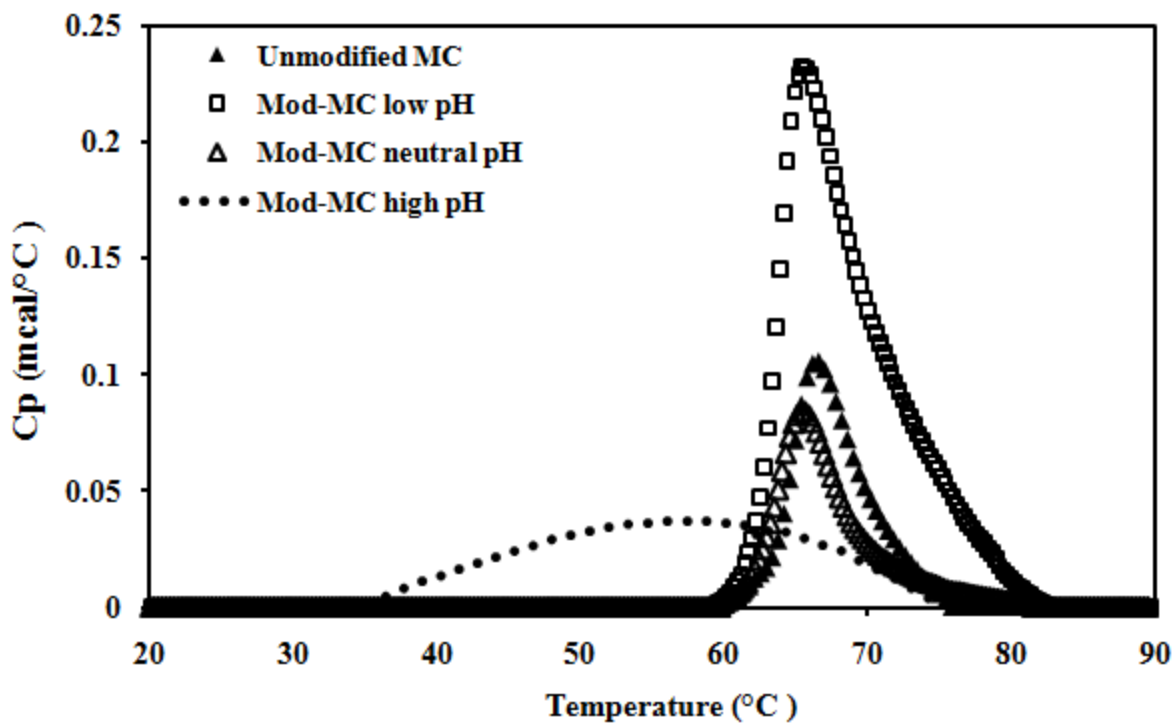
Figure 4.12 Upscan DSC curves for unmodified and modified MC samples
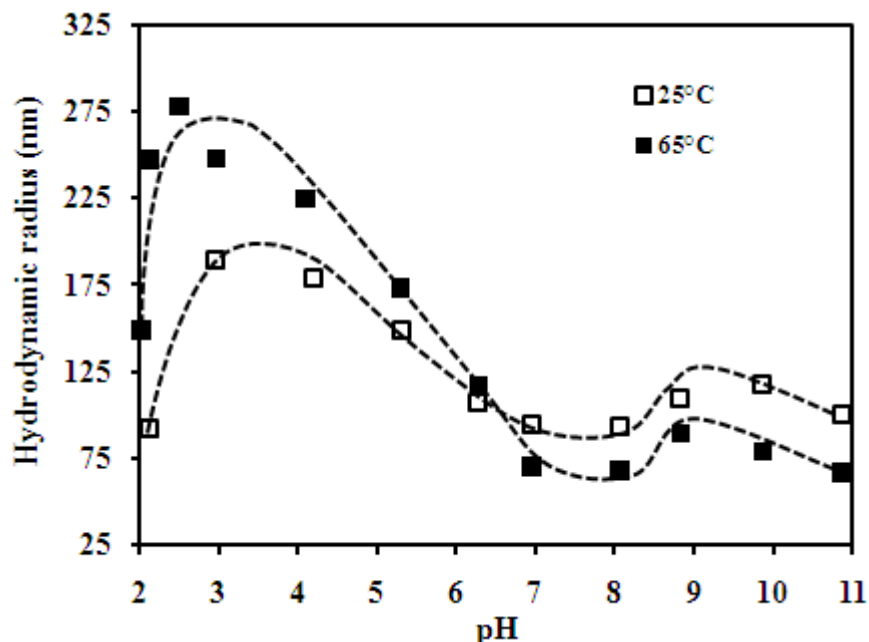
Figure 4.13 Hydrodynamic radii vs. pH at 25°C and 65°C for CS-ModMC microgels

Figure 4.13 shows a comparison of hydrodynamic radii vs. pH measurements obtained at two different temperatures; one at room temperature (25°C) and the other at the LCST (65°C). As shown in Figure 4.13, the CS-ModMC microgels are polyampholytic and possess pH-responsive behaviour at both temperatures. While the response profiles are similar at both temperatures, we observe a difference in the values of hydrodynamic radii (R_h) obtained at the two temperatures. At low pH values (pH < 6.5), the R_h values at 65°C are higher in comparison to those at 25°C. At higher pH values (pH > 6.5), the R_h values at 65°C are lower in comparison to those at 25°C. Similar to micro-DSC results for modified MC samples, this behaviour may be explained by the degree of deprotonation of modified MC chains in the microgel. At low pH, the hydrogen bonding between -CH_2COOH and -OCH_3 groups prevents the hydrophobic interactions between -OCH_3 groups. So, a large number of water molecules are partitioned to the porous microgel and surround the -OCH_3 groups. Thus, the microgel particles at 65°C swell more and show larger

129

hydrodynamic radii in comparison to the microgels at 25°C. Conversely at high pH, due to deprotonation of -CH$_2$COOH groups to -OCH$_2$COO$^-$, the hydrogen bonding between -CH$_2$COOH and -OCH$_3$ groups is weakened while the hydrophobic interaction between -OCH$_3$ groups is enhanced. Water molecules are no longer able to surround the -OCH$_3$ groups in the CS-ModMC microgel and are excluded from the microgel. Therefore, microgel particles at 65°C have smaller hydrodynamic radii in comparison to the microgels at 25°C.

Figure 4.14 shows the CS-ModMC microgel samples at three different pH values. The microgels show lower turbidity at low and high pH values while a more opaque solution is obtained at neutral pH. This is a visual proof that the microgels are swollen at low and high pH values and deswollen around the IEP. Similar visual results were obtained for CS-CMC microgel samples.

Figure 4.14 CS-ModMC microgel samples at low, neutral and high pH

4.4 Summary

This chapter explores the pH-responsive behaviour of two biocompatible and biodegradable polyampholyte microgels, which were prepared using inverse microemulsion technique: chitosan-carboxymethyl cellulose (CS-CMC) and chitosan-modified methyl cellulose (CS-ModMC). As an extension to the chitosan and CMC system, methyl cellulose was used in CS-ModMC microgels to develop a microgel with both pH and thermo responsive property. Carboxymethylation was used to modify methyl cellulose in order to introduce carboxylic acid functionality necessary for the crosslinking of the polymeric chains. The pH-responsive behaviour of the two microgels was confirmed by dynamic light scattering, zeta potential and potentiometric-conductometric measurements. Furthermore, surface active behaviour of unmodified and modified methyl cellulose was studied using surface tensiometry. For CS-CMC, the no. of $-OCH_2COOH$ and $-NH_2$ groups were determined to be 1.5 and 1.1 meq/g of the microgel sample, respectively. In pH range of 4-9, the zeta potential values varied from +10 mV to -40 mV, while the hydrodynamic radius varied from 160 nm in the swollen state (acidic and basic pH) to 110 nm in the "collapse" state (neutral pH). For CS-ModMC, the no. of $-OCH_2COOH$ and $-NH_2$ groups were determined to be 0.8 and 0.6 meq/g of the microgel sample, respectively. In pH range of 4-9, surface charge on the microgels varied from +25 mV to -60mV, and the hydrodynamic radii were 190 nm at low pH, 80nm at neutral pH, to 120 nm at a high pH.

CHAPTER 5

INTERACTION OF NANOCRYSTALLINE CELLULOSE WITH AN OPPOSITELY CHARGED SURFACTANT IN AN AQUEOUS MEDIUM

5.1 Introduction

NCC is derived from native cellulose (wood, cotton or plant fibres) and it possesses a number of advantages, such as biodegradability, recyclability, non-toxicity and high functionality due to presence of hydroxyl groups. [2] Because of its polyelectrolyte nature, NCC can be used in personal care applications, e.g. hair conditioners and shampoos. Personal care applications often employ surfactant formulations and understanding the effect of surfactants on NCC dispersions is vital for the adoption of NCC in these applications. It has been observed that NCC suspensions become unstable and phase separate in the presence of an oppositely charged surfactant. In order to understand the polymer-surfactant interactions between NCC and an oppositely charged surfactant, a cationic surfactant, tetradecyl trimethyl ammonium bromide (TTAB) was used.

Polymer-surfactant interaction is an important phenomenon that has attracted significant research interest because it is commonly observed in many systems. Numerous systems have been explored to elucidate the interaction between a charged polymer and an oppositely charged surfactant. [90-96] Interestingly, in addition to the commonly used techniques such as light scattering, SANS, microcalorimetry and surface tensiometry, McLachlan and co-workers

reported the use of 1D and 2D NMR technique to investigate the interactions between oppositely charged polymer-surfactant systems. [97]

In 2002, Wang and Tam, identified three kinds of interactions between negatively charged poly(acrylic acid) (PAA) and dodecyltrimethylammonium bromide (DTAB), a cationic surfactant. Initially they observed an electrostatic attraction between PAA and DTAB. After reaching a critical concentration, DTAB micellization on PAA chains was observed. They also observed that addition of salt screened the electrostatic interaction between PAA and DTAB and facilitated the free micellization of DTAB in bulk. [98]

Liu and Guo studied the interactions between casein and DTAB. According to their experimental results, they observed three different interactions on adding DTAB to 2 mg/ml casein solutions:

(i) Electrostatic attraction was observed between negatively charged amino acid groups and DTAB surfactant;

(ii) further addition of DTAB led to the formation of DTAB micelles on casein chains producing insoluble complexes;

(iii) further addition of DTAB produced free DTAB micelles and resolubilized the DTAB/casein complexes due to an overall positive charge on the complex. [99]

Wang and Tam also studied the interaction of methacrylic acid/ethyl acrylate copolymers (HASE) with DTAB surfactant and summarized the typical polymer-surfactant interactions observed in systems with opposite charges: electrostatic binding, micellization of the electrostatically bound micelles and resolubilization/gelation. [100]

Researchers have also studied the interaction of cationic chitosan with negatively charged sodium dodecyl sulphate (SDS). Onésippe and Lagerge showed that grafting alkyl chains makes the chitosan more hydrophobic and the alkylated chitosan exhibits amphiphilic behaviour at pH 4. The authors also concluded that alkyl chains facilitate the formation of chitosan complexes with SDS. [101] Mata et al. studied the interaction between carboxymethyl cellulose (CMC) and a number of cationic surfactants with varying hydrophobic chain lengths. The critical aggregation concentration (CAC) corresponding to the onset for the formation of polymer-surfactant complex is generally lower than the CMC. The authors observed that increasing the alkyl chain length of the surfactants decrease the CAC values. Longer surfactant chain length and larger surfactant head groups produce rapid complexation between CMC and surfactants. [102]

Chakraborty et al. reported that the polymer-surfactant interaction simultaneously leads to interfacial-adsorption and bulk complexation, where smaller surfactant aggregates are formed on the polymer chains. Formation of electrostatically driven polymer-surfactant complexes increases the hydrophobicity of the system leading to coacervation or phase separation. In a number of polymer-surfactant systems, three critical concentrations have been identified: (i) CAC corresponding to the onset of electrostatic interactions, (ii) C_s representing the saturation of polymer chains with surfactant molecules and (iii) C_m^* corresponding to the formation of free surfactant micelles. Chakraborty and co-workers observed that the CAC and C_s values from tensiometric and conductometric experiments were not identical and they attributed this apparent discrepancy due to different physiochemical changes which may occur in tensiometric and conductometric experiments. In conductometric experiments, the CAC corresponds to the completion of surfactant adsorption whereas in tensiometric experiments, the CAC corresponds

to the onset of interfacial adsorption of polymer surfactant complexes. In conductometric experiments C_s represents the onset of wrapping of polymer chains on the surfactant aggregates while in tensiometric experiments, C_s corresponds to the collapse of polymer-surfactant complexes from the air-water interface. [103] Oppositely charged polymer-surfactant complexation in bulk and at the interface has also been thoroughly investigated by Bain and co-workers. The authors proposed that different types of associations may be present in oppositely charged polymer-surfactant systems (such as interfacial layers, bulk complexation and precipitated phases), and a delicate balance of electrostatic and hydrophobic interactions is present for each kind of association. [104]

This chapter examines the forces involved in NCC-TTAB interactions and the underlying binding mechanism between NCC and TTAB molecules. Several physical techniques, such as surface tensiometry, isothermal titration calorimetry, conductivity measurements and phase separation measurements were used for this study. Since the system involves charged species, the effect of electrolyte (NaCl) on the polymer-surfactant interaction was also examined.

5.2 Experimental Methods

5.2.1 Materials

Freeze dried nanocrystalline cellulose (NCC) sample was supplied by FP Innovations. Tetradecyl trimethyl ammonium bromide (TTAB) (99% approx.) was purchased from Sigma. Sodium chloride (99%) was purchased from EMD chemicals. Deionized Millipore water was used for all sample preparations.

5.2.2 Characterization techniques

Isothermal Titration Calorimetry

The Microcal VP-ITC instrument was used to study the NCC-TTAB interactions. The titrations were conducted at constant temperature of 25°C. The volume of titrant (TTAB) was ~ 282 µL and 1.4551 mL of NCC sample was loaded in the sample cell. The titrant was injected at different volumes i.e. 2, 5 and 10 µL increments. The ΔH values for the dynamic interactions are reported as kJ/mol of injectant and were plotted against the concentration of titrant in the cell. For most measurements, the concentrations of TTAB and NCC were fixed at 10 g/L and 0.655 g/L. A TTAB concentration of 10 g/L was chosen to allow the investigation of the entire range of NCC-TTAB interactions. NCC concentration was fixed at 0.655 g/L as this concentration clearly showed all the four regions of interactions when TTAB was titrated to NCC in the sample cell.

Surface Tensiometry

Surface tension measurements were conducted in DCAT 11 (Dataphysics) at 25°C. It is equipped with a state-of-art software package and a liquid dispensing unit (LDU) capable of dosing microlitre volumes of titrant. The Wilhelmy plate method was used to measure dynamic surface tension values at the air-water interface. TTAB surfactant was titrated into 50 ml of NCC solution in all tensiometric measurements. The concentration of surfactant in LDU was fixed at 10 g/L and the concentration of all NCC solutions was fixed at 0.655g/L.

Conductivity Measurements

Conductivity measurements were conducted using the Metrohm 809 Titrando. It is equipped with Tiamo software capable of dosing microlitre quantities of any titrant. All measurements were conducted in a jacketed vessel at 25°C with medium stirring. The NCC sample (0.655 g/L) was titrated with 10 g/L TTAB solution and the conductivity of the NCC sample was measured using a conductivity electrode until a discernible CMC point for TTAB was observed.

Phase separation measurements

It is known that the electrostatically driven polymer-surfactant complexes may lead to coacervation and phase separation. This project also explored the phase separation behavior of NCC solutions in the presence of different TTAB concentrations. Five NCC solutions were prepared at a concentration of 0.655 g/L. TTAB was added to each NCC solution such that the resulting concentration of TTAB in the NCC solutions would be 0.1, 0.2, 0.5, 0.8 and 1.1 g/L. The height of the NCC flocs was quantified as a function of time, where the white turbid region at the bottom of the tube corresponded to the phase separated NCC.

Zeta potential measurements

Zeta Potential measurements for NCC-TTAB samples at different TTAB concentrations were measured using Brookhaven ZetaPALS Analyzer. These measurements were performed to determine the overall surface charge on the NCC samples in the presence of different

concentrations of TTAB. The concentration of the NCC in the samples was maintained at 0.655g/L and the experiment was conducted at 25°C.

5.3 Results and Discussion

5.3.1 Isothermal Titration Calorimetry

NCC-TTAB binding in bulk

Figure 5.1a shows the ITC curve for the NCC-TTAB interaction and clearly shows four distinct regions of interactions. Region I indicates the electrostatic interaction between the negatively charged NCC and the cationic surfactant TTAB. As previously reported, [98] [100] [105] the appearance of an endothermic peak in the ITC curves corresponds to an electrostatic interaction between the polymer and the surfactant. The initial upward slope represents electrostatic interactions, while the highest point of the peak corresponds to the optimum condition for the electrostatic binding of surfactant molecules to the opposite charges on the polymeric chains. The reason we did not observe such a peak in Figure 5.1a is because at the first injection (2 μL) of 10 g/L TTAB, the electrostatic interactions exceeded the maximum point. However, when a lower surfactant concentration (1 g/L) was used, we observed the maximum peak for electrostatic interactions (see Figure 5.1b) which is similar to that reported previously. Region II corresponds to the rearrangement of surfactant molecules on the NCC surface induced by hydrophobic interactions of the surfactant alkyl chains. In region III, the adsorption of surfactant on the charged NCC surface increases the local concentration of surfactant molecules that

promotes the formation of micelles on the surface of NCC. Such phenomenon is commonly referred to as polymer induced micellization and occurs at a lower concentration than the critical micelle concentration (CMC) for the formation of surfactant micelles in bulk solution. Region III is also attributed to the aggregation and bridging of NCC bound micelles to form larger aggregates containing several NCC nanorods. This phenomenon is favourable since NCC is a rigid rod-like nanocrystal, so NCC rods are unable to wrap around the TTAB micelles. Therefore, it is energetically favourable for two or more NCC rods to come together and share the TTAB surfactant micelles. This phenomenon is similar to a common behaviour at specific surfactant concentration exceeding the CAC, where the polymeric chains would wrap around the surfactant micelles and if the polymer concentration is sufficiently high, bridging and inter-molecular aggregation will occur. [100] When the concentration of TTAB surfactant was further increased, free surfactant micelles begin to form in the bulk; this onset is indicated by region IV. The entire binding mechanism is shown schematically in Figure 5.2. As previously discussed by Lapitsky et al. [105], one can conclude that non-cooperative binding occurs at very low TTAB concentrations and cooperative binding starts at the very first injection of 10 g/L TTAB. The ITC curve in Figure5.1a also indicates three important concentrations:

C_1: Onset of reorganization of adsorbed TTAB molecules

C_2: Onset of polymer induced micellization and aggregation of nanorods

C_3: Onset of free TTAB micellization
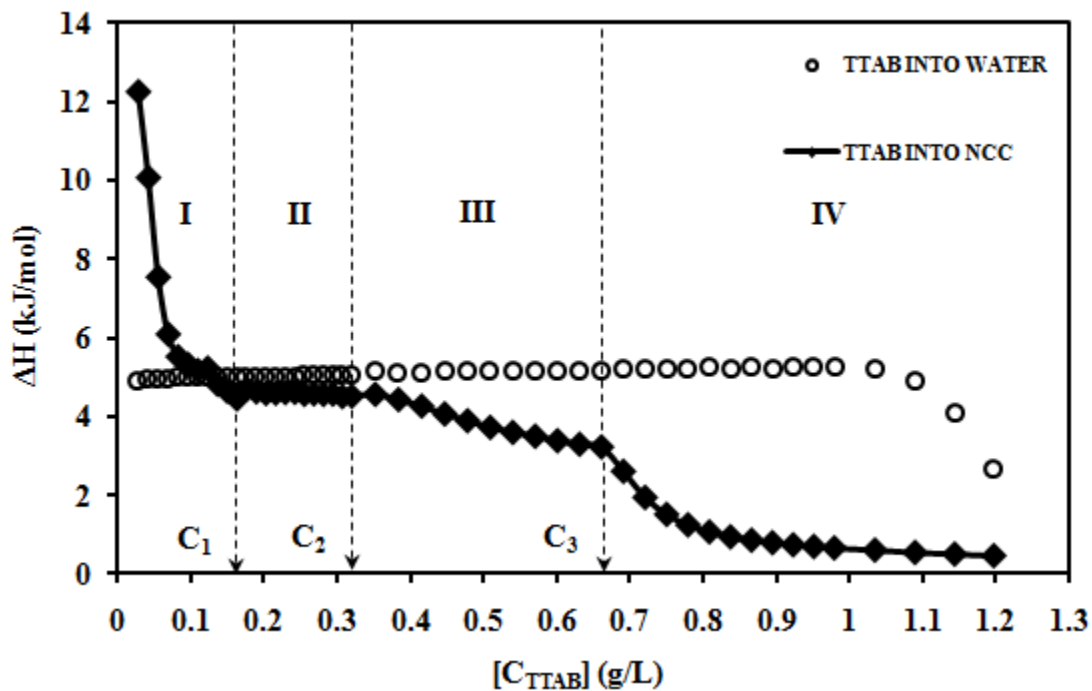
Figure 5.1a ITC curve for titration of 10g/L TTAB into water (o) and 0.655 g/L (NCC) (♦)
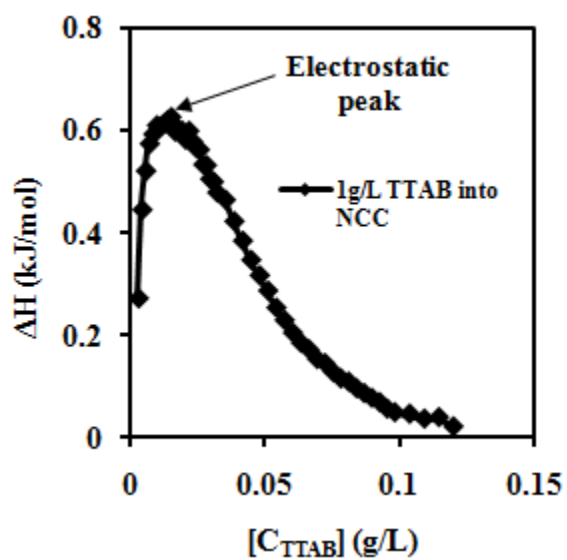
Figure 5.1b ITC curve for titration of 1 g/L TTAB into 0.655 g/L (NCC) (♦)
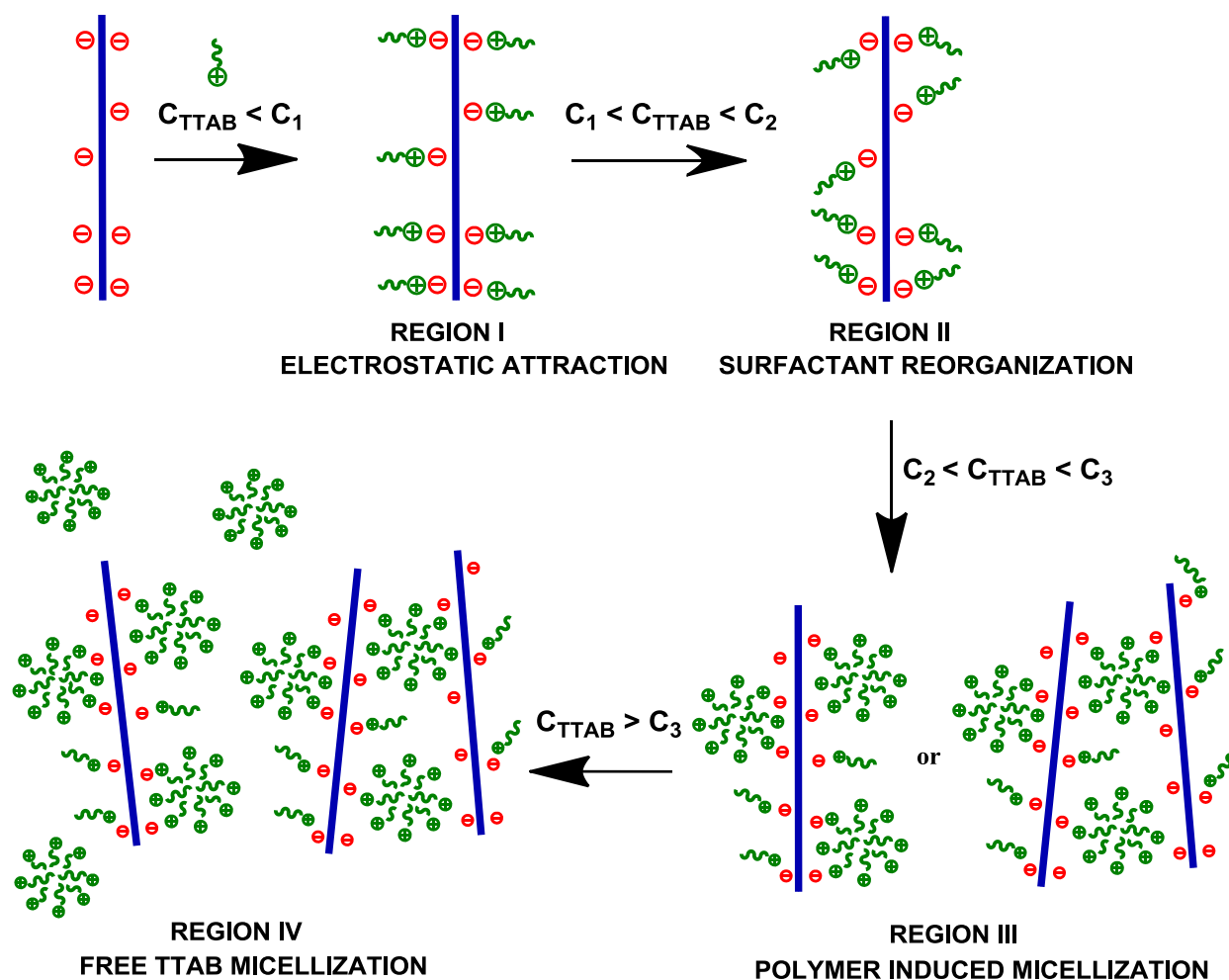
Figure 5.2 Mechanism of NCC-TTAB binding based on ITC experiments

Effect of polymer concentration

In order to study the effect of NCC concentration on NCC-TTAB binding, ITC experiments were conducted with different NCC concentrations in the cell, while keeping the concentration of TTAB surfactant constant at 10 g/L. The concentrations of NCC were chosen as: 0.0655 g/L, 0.3275 g/L and 0.4912 g/L. Figure 5.3a shows the ITC curve for NCC concentration of 0.0655 g/L. We observed that the titration curve for NCC is identical to the TTAB dilution curve. This result suggests that when the NCC concentration is very low there is no appreciable interaction

between TTAB and NCC. Hence, the ITC curve for 0.0655 g/L NCC follows the TTAB dilution curve and shows the CMC point for free TTAB micellization (C_m = 1.1 g/L).
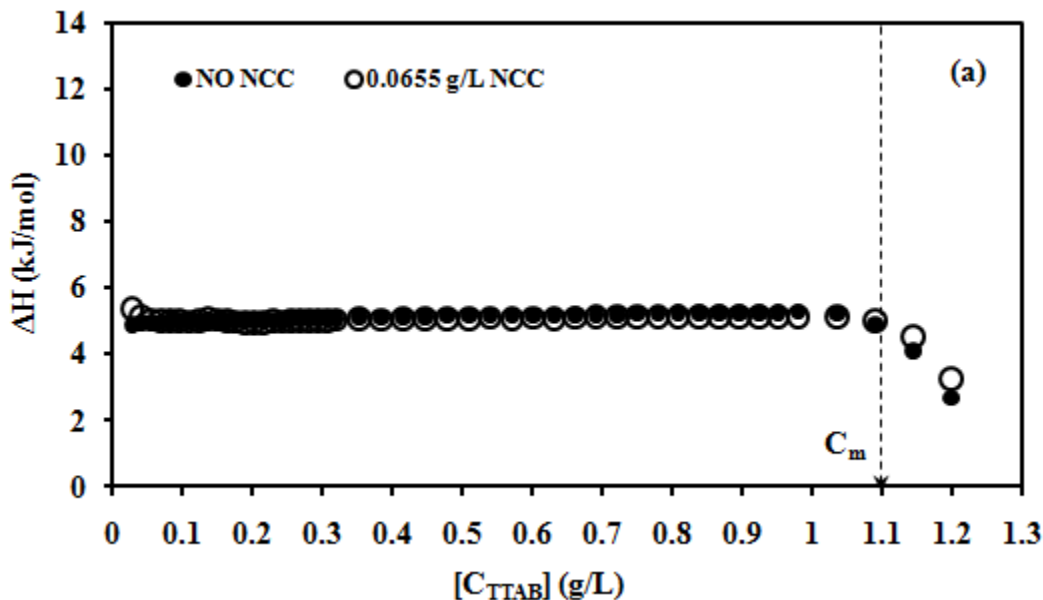
Figure 5.3a ITC curves for TTAB titration into water and 0.0655 g/L NCC concentration

When the NCC concentration was increased to 0.3275 g/L, subtle changes appeared in the ITC curve (Figure 5.3b). The ITC curve for 0.3275 g/L NCC displayed three regions of interactions: region I corresponding to electrostatic interactions between NCC and TTAB, region II corresponding to reorganization of adsorbed TTAB surfactant on NCC rods and region IV representing the onset of free TTAB micellization. This result suggests that an NCC concentration of 0.3275 g/L is high enough to observe electrostatic interactions between NCC and TTAB; however, it is not sufficiently high to observe region III corresponding to polymer induced micellization and aggregation of surfactant bound NCC rods, as was the case for 0.655 g/L sample. When the NCC concentration was further increased to 0.4912 g/L (see Figure 5.3c), we observed all four regions of interactions as previously observed in

0.655 g/L NCC. The observed variations in the ITC curves of the three samples with different concentrations suggest that NCC concentration is important for the occurrence of polymer induced micellization and aggregation of surfactant bound NCC rods.
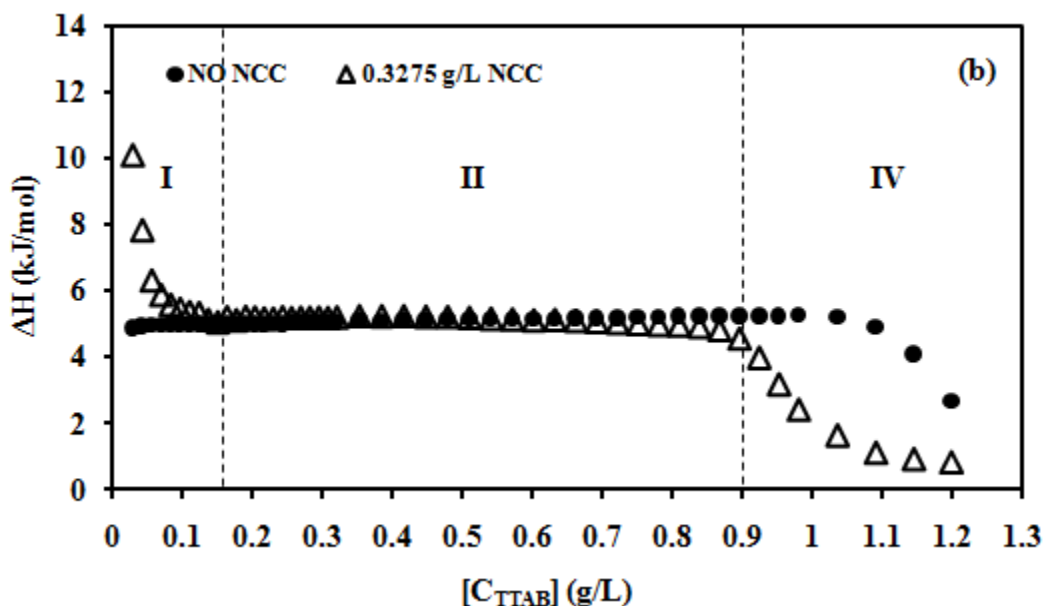
Figure 5.3b ITC curves for TTAB titration into water and 0.3275 g/L NCC concentration
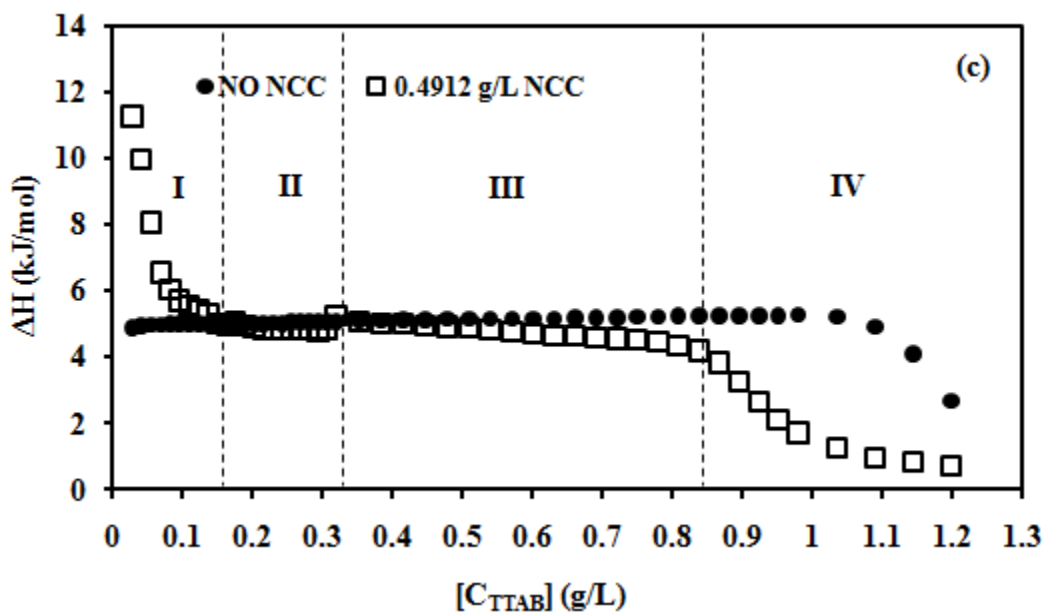
Figure 5.3c ITC curves for TTAB titration into water and 0.4912 g/L NCC concentration

Effect of salt

Since the primary interaction between NCC and TTAB is electrostatic in nature, it was expected that the addition of an electrolyte such as NaCl would shield/screen the negative charges on the NCC surface thereby weakening the NCC-TTAB electrostatic interaction and facilitating free micellization of TTAB molecules. Figs. 5.4a to 5.4d show the effect of addition of different salt concentrations on the NCC-TTAB interactions. For 0.001 M NaCl (Figure 5.4a), while all the four regions of interactions were observed, reduced electrostatic interaction in region I was observed due to the charge shielding effect of salt. Similarly at 0.005 M NaCl (Figure 5.4b), all four regions of interactions were present in the ITC curve. However an electrostatic peak was observed in region I; by screening out the negative charge on NCC, salt prevents the electrostatic interactions to exceed the maximum limit at the first dosing of 10 g/L TTAB. Figure 5.4c shows that the ITC curves for 0.005 M NaCl and 0.01 M NaCl were similar. At even higher salt concentrations of 0.05 M and 0.1 M (Figure 5.4d), while a low electrostatic peak was evident the regions II and III (from Figure 5.1a) were absent. The high concentration of salt probably allowed minimal electrostatic interaction between NCC and TTAB resulting in the low peaks; it also inhibited polymer induced micellization since the number of TTAB molecules bound to NCC is insufficient to produce micelles, resulting in the absence of Regions II and III from the ITC curves. Furthermore, the points A and B in Figure 5.4d, denote the CMC of free TTAB micelles and are determined as 0.55 g/L and 0.35 g/L respectively. The CMC values from points A and B are one order of magnitude less than the CMC of pure TTAB (~1.1 g/L). Based on the observed behaviour of NCC-TTAB interactions in presence of different salt concentration, one can infer that salt weakens the NCC-TTAB binding and facilitates free TTAB micellization.

Thevenot and co-workers have also reported the reduction in CMC values and an increase in micelle aggregation numbers in the presence of salt. The authors explain that addition of salt reduces the electrostatic repulsion between polar head groups of the surfactant thereby facilitating formation of micelles. [106]
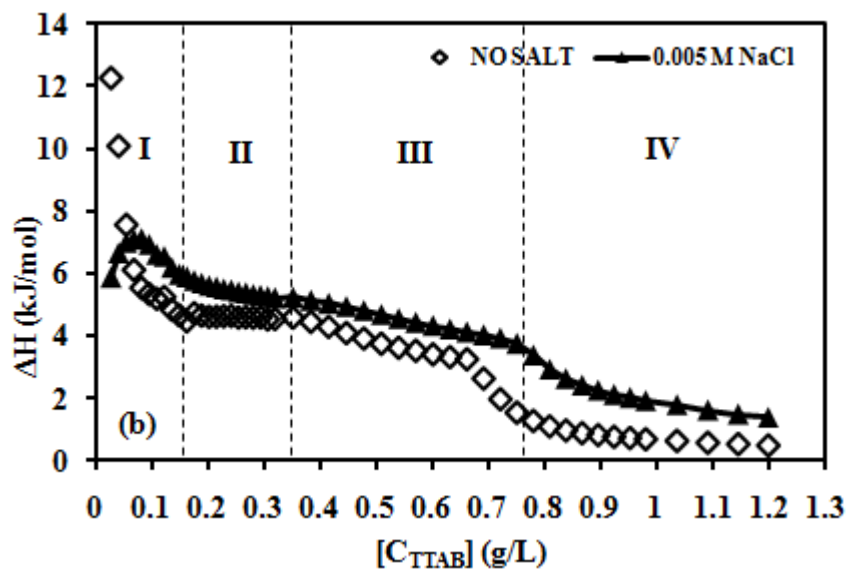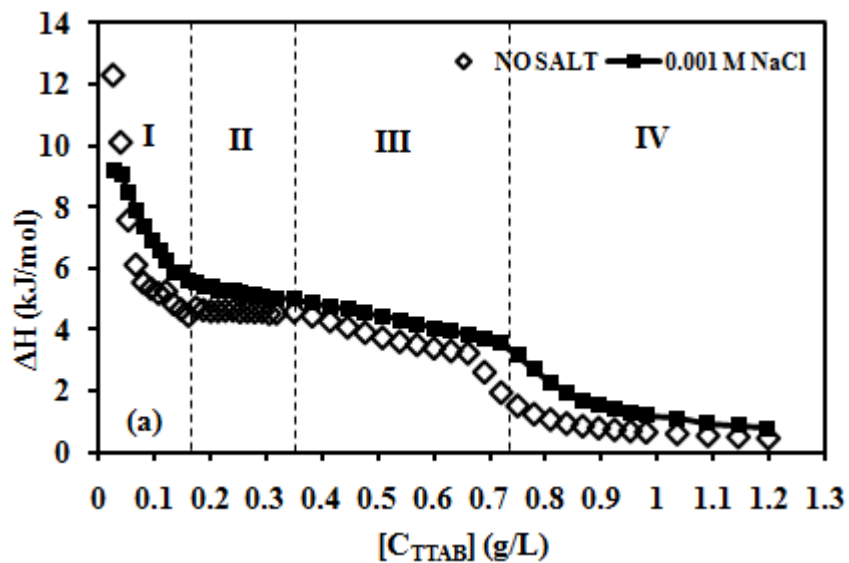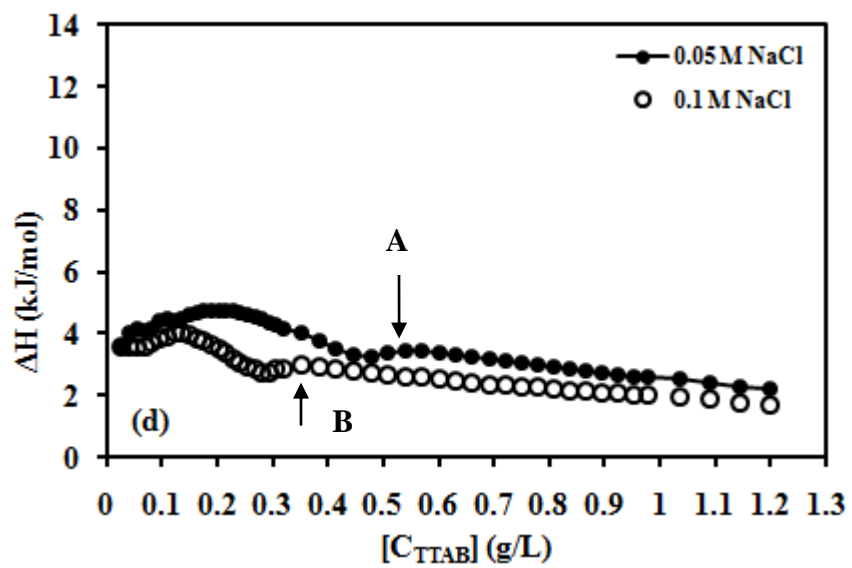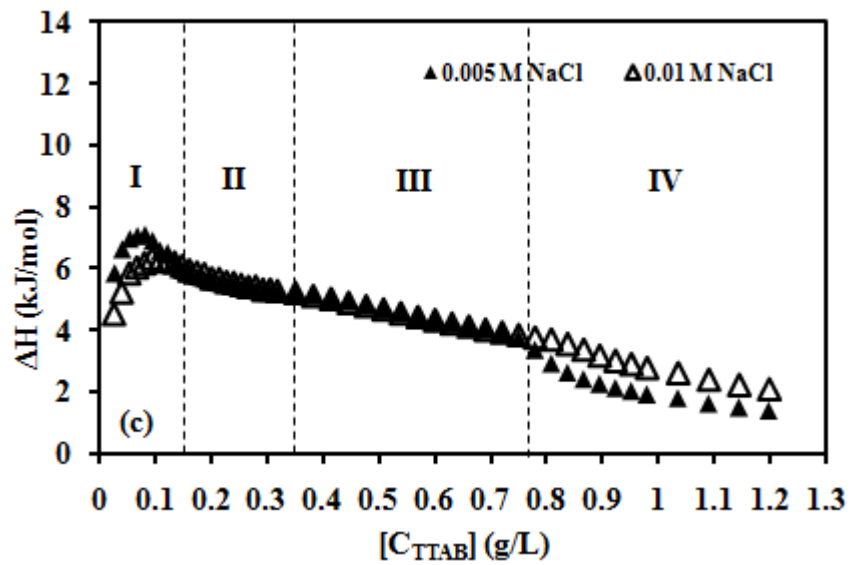
Figure 5.4 ITC curve for NCC-TTAB with different salt concentrations

5.3.2 Surface Tensiometry

NCC-TTAB binding at the air-water interface

On comparing the surface tension curves for TTAB titrated into NCC and the surface tension curve for TTAB dilution, we noticed that there was a reduction in surface tension in the presence of NCC (see Figure 5.5a). This may be attributed to the formation of surface active NCC-TTAB complexes (formed due to electrostatic attraction) which populate the air-water interface and reduce the surface tension in the presence of NCC as compared to the TTAB dilution alone. This drop in surface tension in the presence of a polymer has been observed by other researchers as well. [107] [108] The critical micelle concentration (CMC) of TTAB was identified as C_m and we observed that the CMC of TTAB in the presence of NCC (C_m^*) was higher. C_m^* was determined by the point where the TTAB-NCC curve merged with the TTAB dilution curve. In the presence of NCC, TTAB interacts electrostatically with the NCC and micellizes on the surface of NCC crystallites; thus more amount of surfactant is required for the formation of free micelles in an NCC solution making C_m^* greater than C_m as shown in Figure 5.5a.

Figure 5.5b shows different regions of NCC-TTAB interaction at the air-water interface. The curve clearly showed three distinct regions. The first region (I) represents a reduction in the surface tension at the interface due to aggregation of surfactant molecules at the air-water interface. This aggregation of surfactant was facilitated by the presence of oppositely charged NCC rods which increased the aggregation of surfactants at the interface. A sudden drop in surface tension was observed before onset of the second region (II). This sudden drop in surface

tension suggests saturation of the air-water interface with NCC-TTAB complexes. In the bulk aqueous phase, TTAB bound NCC rods lose their hydrophilic character and become more hydrophobic thereby necessitating the partitioning (expulsion) of TTAB hydrophobic chains at the air-water interface. Hence, TTAB bound NCC rods formed in the bulk solution begin to migrate and saturate the interface. Once NCC-TTAB complexes flood the entire air-water interface, the surface tension shows a drastic drop due to coverage of NCC-TTAB aggregates at the interface. At C_s^*, the   air-water interface becomes completely saturated and region II shows this interfacial saturation concentration (C_s^*). Region II also represents the onset of TTAB micellization on the NCC rods present at the interface and in the bulk. The appearance of C_m^* in region III indicates the CMC of TTAB in the presence of NCC and represents the onset of free TTAB micellization in the bulk aqueous phase.

Figure 5.6 shows the NCC-TTAB binding mechanism at the air-water interface & in the bulk. Region I shows the presence of NCC-TTAB electrostatic complexes at the air-water interface. Region II shows the interfacial saturation point (C_s^*) when NCC-TTAB complexes formed in the bulk migrate to the interface and form a complete coverage. Region III shows a saturated interface and free TTAB micellization in the bulk. It is important to note that desorption of NCC-TTAB complexes from the interface is not shown in region III. Since the surface tension curve for TTAB titration into NCC does not show any appreciable change in the slope after interfacial saturation (C_s^*), it is concluded that the NCC-TTAB complexes at the interface remain intact and don't get desorbed from the interface even as free TTAB micelles are formed in the bulk. [109] [94]
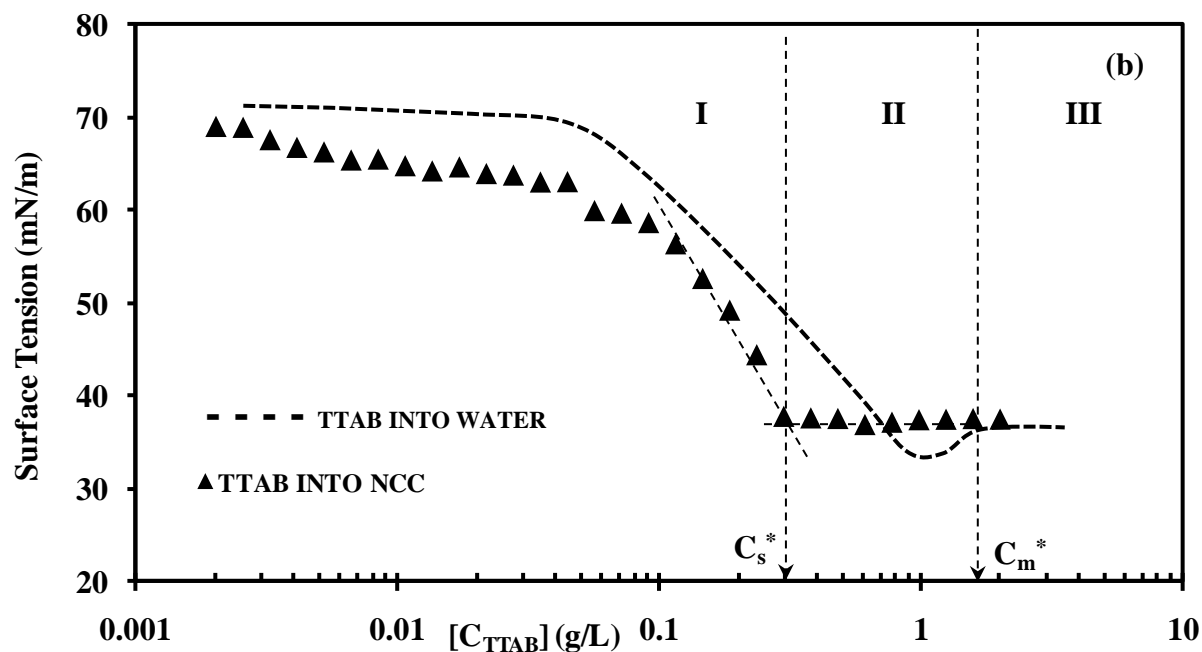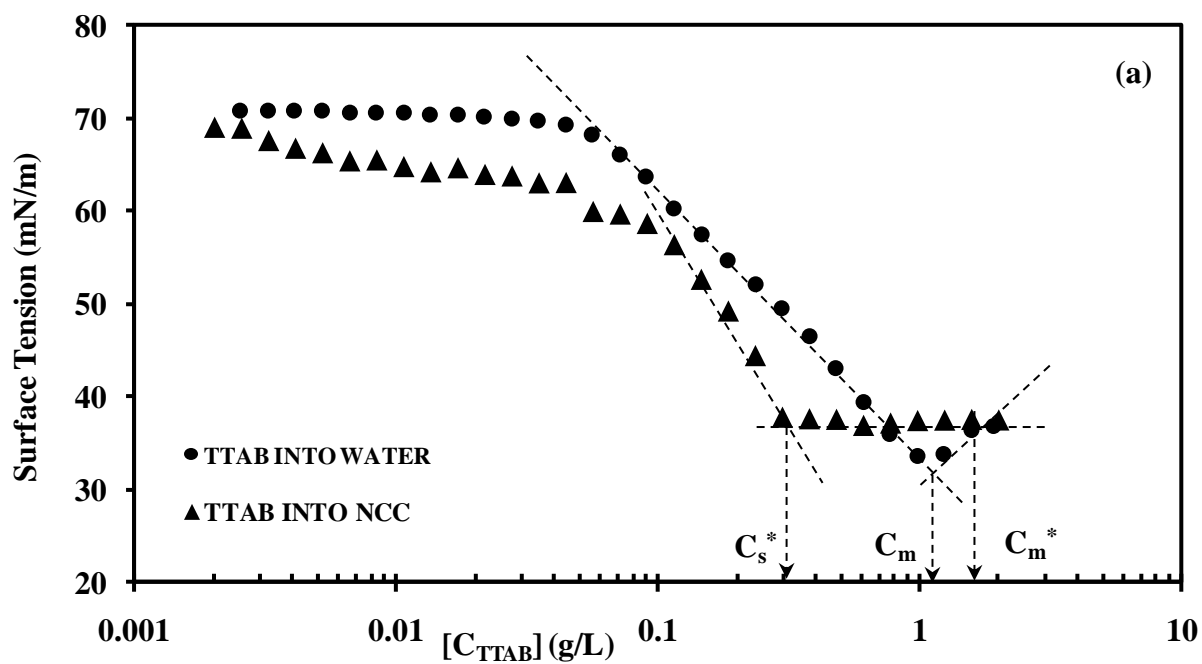
Figure 5.5 Surface tension curves of TTAB dilution and TTAB titrated into 0.655 g/L NCC
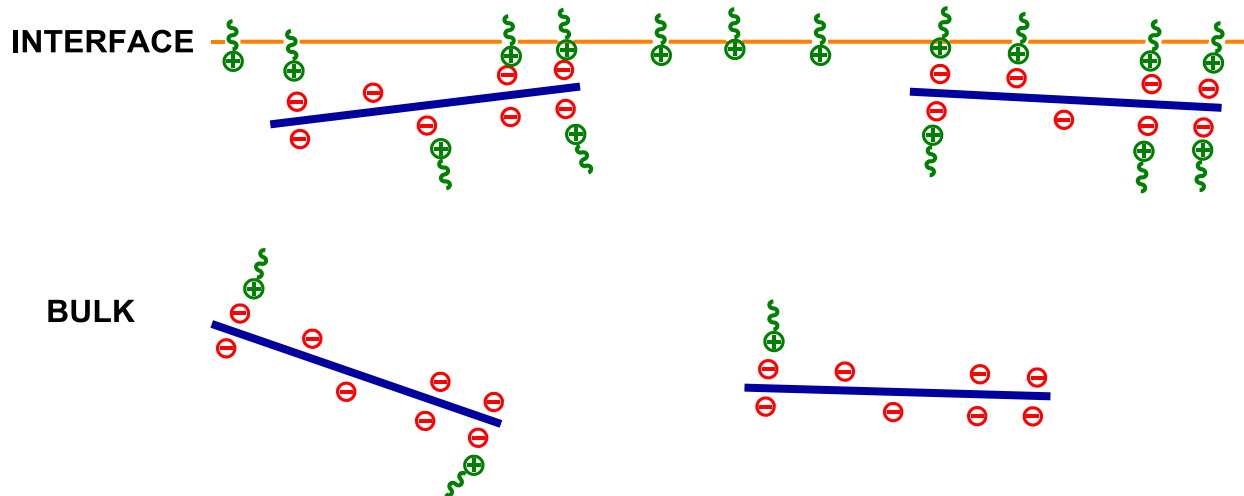
INTERFACE

BULK

REGION I

NCC-TTAB COMPLEXES FORMED AT THE INTERFACE
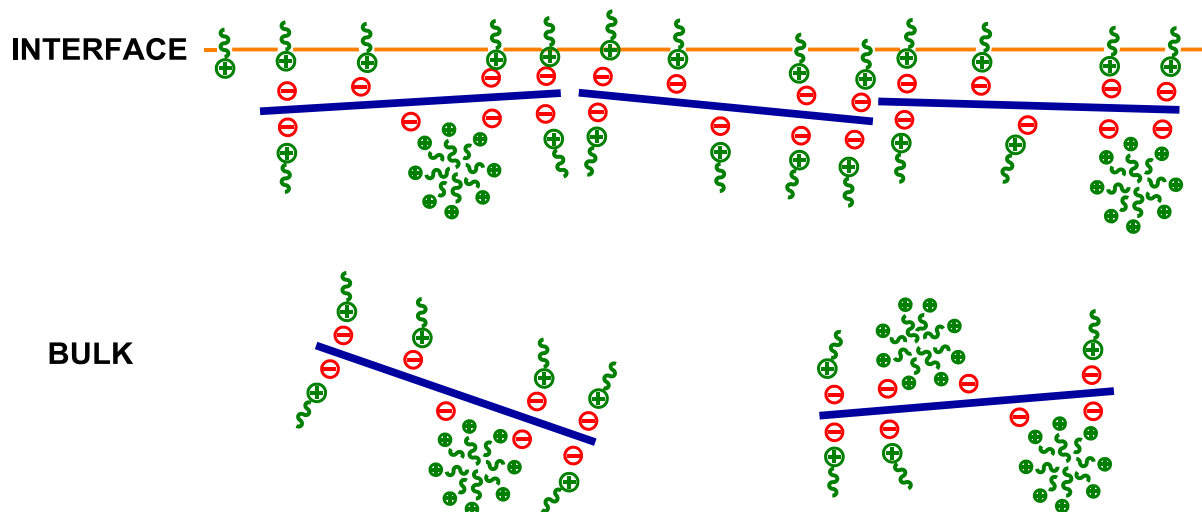
INTERFACE

BULK

REGION II

INTERFACE SATURATION BY NCC-TTAB COMPLEXES FORMED IN THE BULK

150
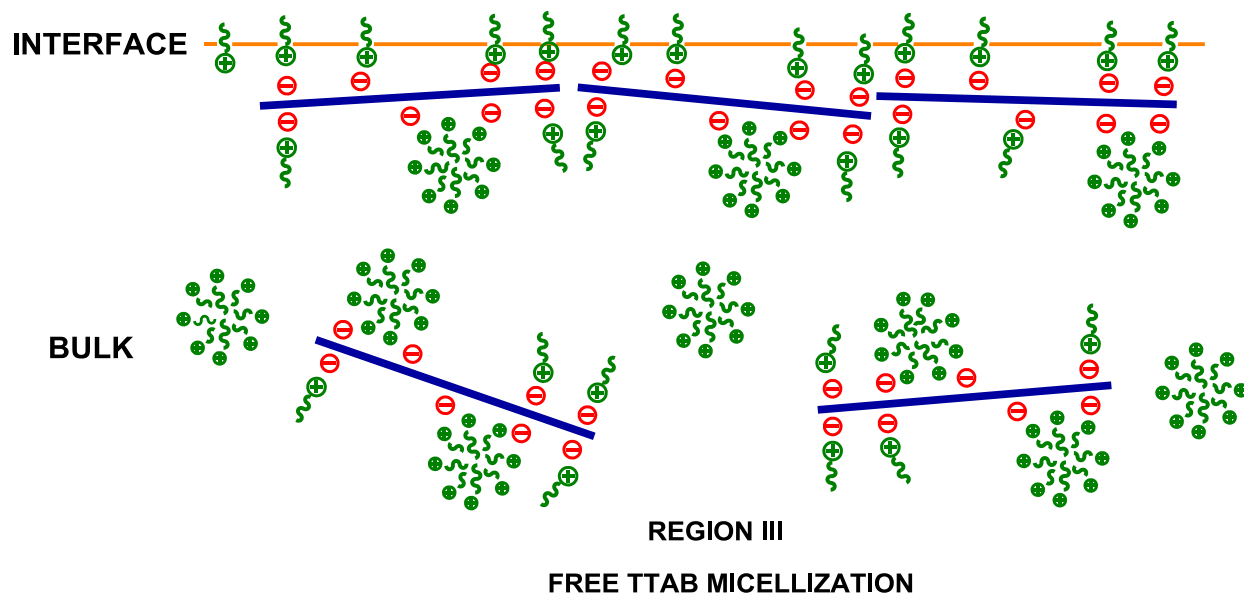
Figure 5.6 NCC-TTAB binding mechanism at the air-water interface and in the bulk

Effect of salt

As previously observed with the ITC results, it was expected that addition of an electrolyte like NaCl would affect the surface tension results as well. Since salt shields the charges on NCC surface, the NCC-TTAB electrostatic interactions are weakened and formation of NCC-TTAB complexes is also lowered. Lower NCC-TTAB interactions in turn facilitate the formation of free TTAB micelles. Therefore, it was anticipated that the CMC of TTAB in the presence of NCC (C_m^*) would be lowered. Figure 5.7 shows the surface tension curves for TTAB dilution and TTAB titration into NCC for different mediums: (a) water, (b) 0.005 M NaCl and (c) 0.05 M NaCl.

As shown in Figs. 5.7 a, b and c, the TTAB dilution curves were affected by the presence of salt. C_m values corresponding to CMC_{TTAB} were shifted to lower concentrations at 0.005 M and 0.05 M. This lowering of CMC of a surfactant in presence of salt [106] has been previously reported. As expected, Figs. 5.7b and c show that the CMC of TTAB in the presence of NCC (C_m^*) also decreased due to salt screening effect, which facilitates the formation of free TTAB micelles. Furthermore, in the presence of salt, the surface tension drop corresponding to interfacial saturation (with NCC-TTAB complexes) became less discernible in Figs. 5.7b and c. As there is a decreased formation of NCC-TTAB complexes in the bulk due to the salt shielding the negative charges on the NCC surface, interfacial saturation is not very pronounced in salt solutions. Hence the corresponding surface tension drop is less discernible and not very pronounced in salt solutions.
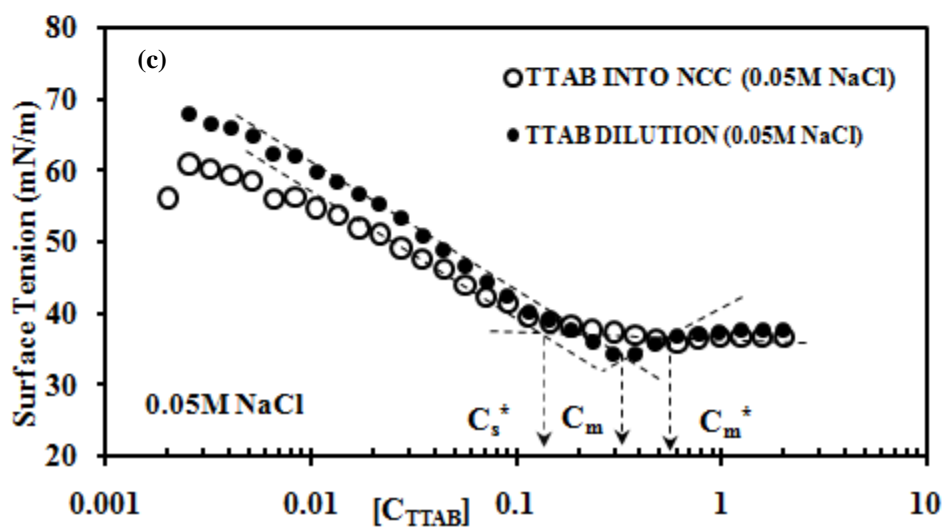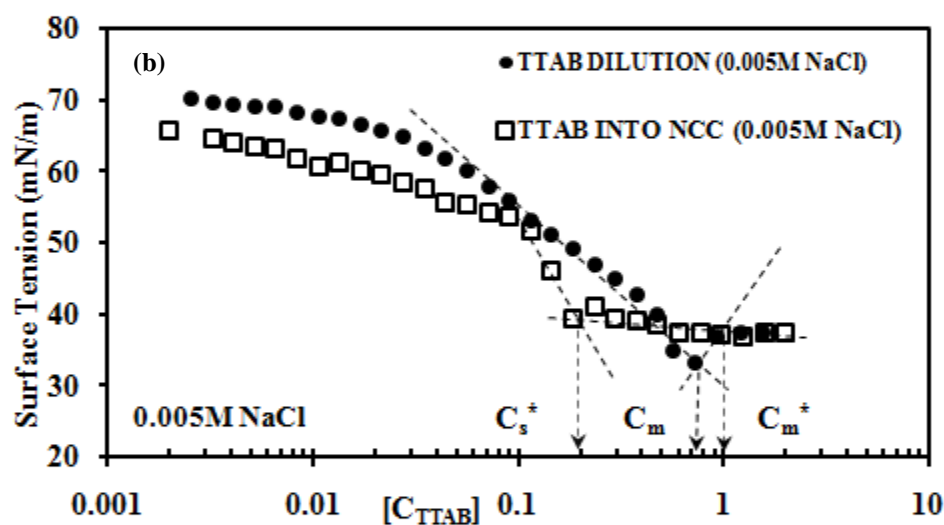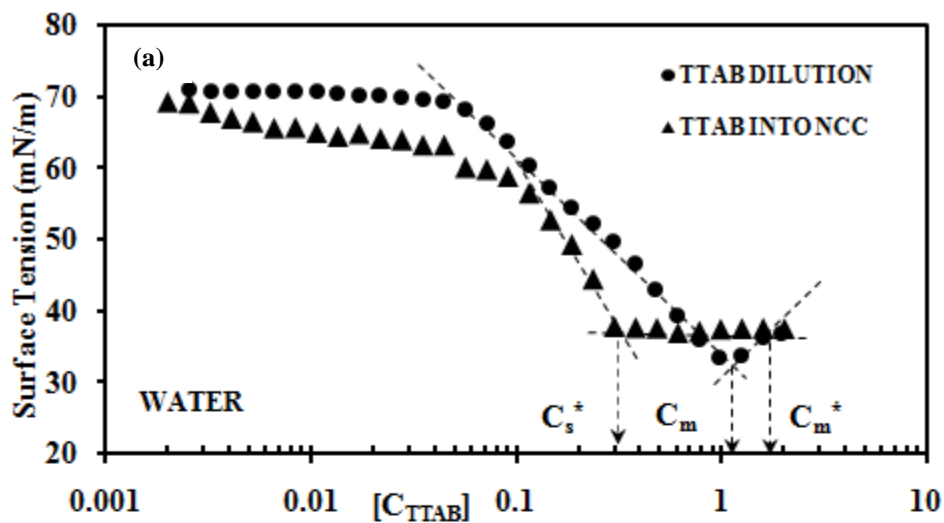
Figure 5.7 Surface tension curves at different salt concentrations

153

5.3.3 Conductivity Measurements

Conductivity measurements are very useful in observing polymer-surfactant interactions. A change in slope of the conductivity curve indicates the formation of free TTAB micelles in the bulk. Figs. 5.8a and b show the conductivity curves of TTAB titrated into water and into 0.655 g/L NCC solution respectively. The TTAB dilution curve showed one inflexion point indicating CMC of the surfactant (C_m). The conductivity curve of TTAB into NCC shows two inflexion points: the first inflexion point at 0.65 g/L TTAB concentration where the two curves seem to bifurcate (see Figure 5.8c) and the second inflexion point (see Figure 5.8b) represents the saturation of TTAB-NCC interaction and formation of TTAB micelles in bulk (i.e. C_m^*). As expected, $C_m^* > C_m$ (from Figure 5.8a and b, $C_m^* \sim 1.3$ g/L $C_m \sim 1.1$ g/L), which is similar to the surface tensiometry results. Similar conductivity results showing an increase in CMC of surfactant in presence of a polymer are reported elsewhere as well. [110]
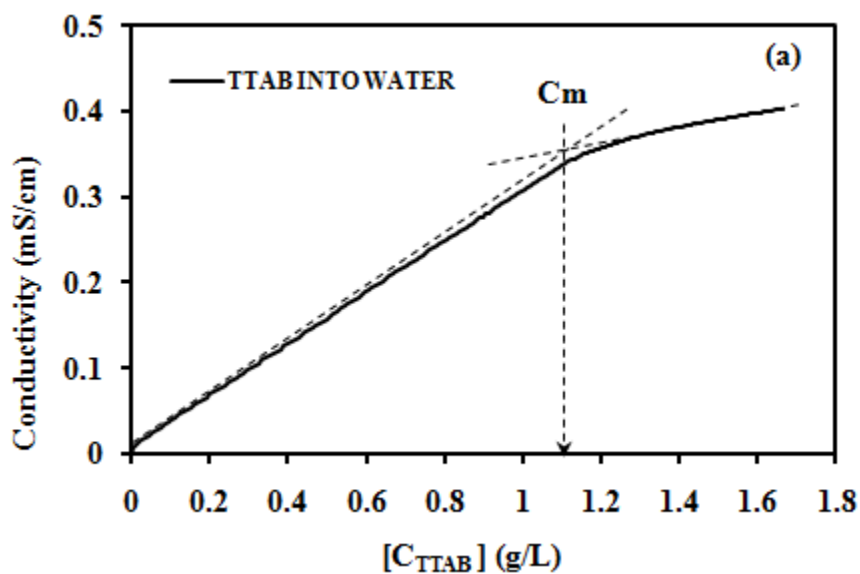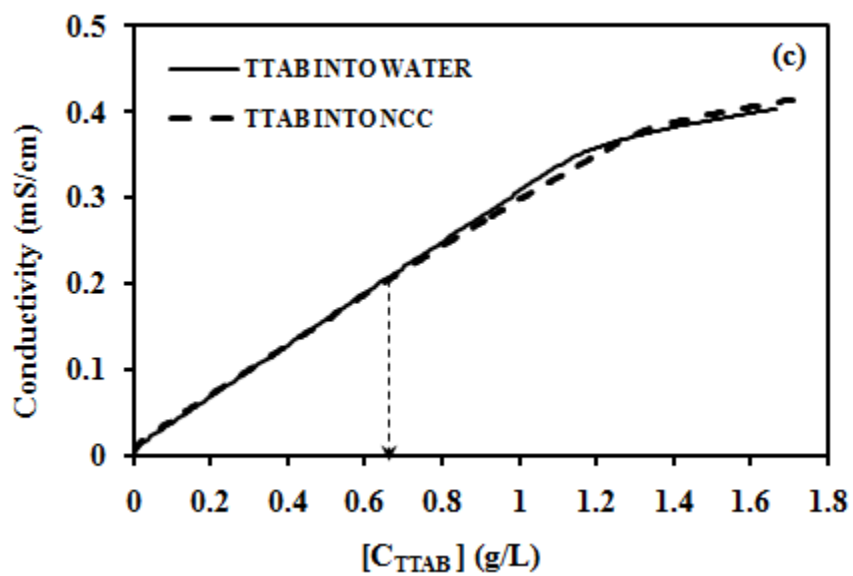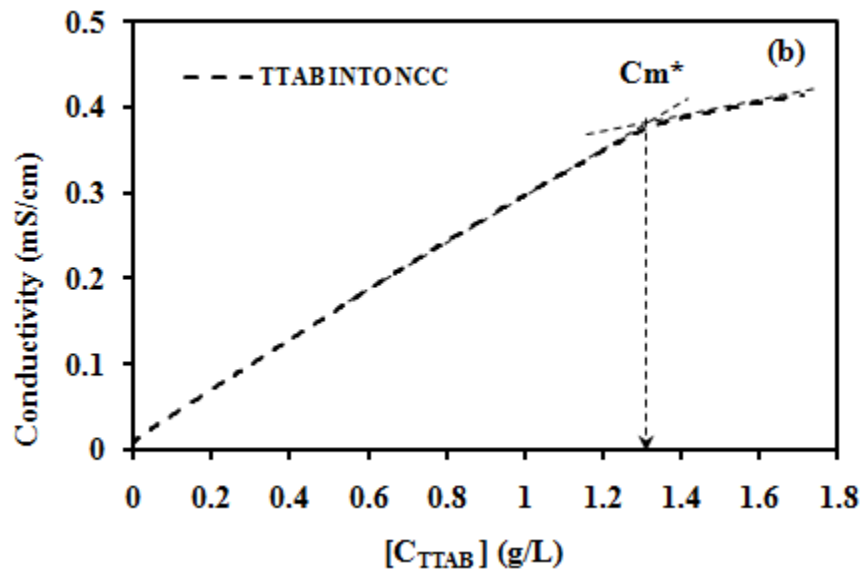
Figure 5.8 Conductivity curves for TTAB dilution and TTAB titrated into 0.655 g/L NCC

5.3.4 Phase separation measurements

NCC solutions in water are fine suspensions which are stable for long intervals of time. The negatively charged surface of NCC provides electrostatic repulsion thereby preventing agglomeration and settling of aqueous NCC suspensions. In the presence of an oppositely charged surfactant, such as TTAB, the NCC solutions tend to phase separate into a clear phase and an insoluble turbid phase (see Figure 5.9). Figure 5.11 shows the mechanism of phase separation in NCC-TTAB solutions. Initially NCC and TTAB interact electrostatically after which the TTAB molecules adsorbed on the NCC surface interact hydrophobically with other TTAB molecules from adjacent NCC rods. These hydrophobic interactions bring together all the surfactant bound NCC rods to form large particulates or hydrophobic flocs. With time, these hydrophobic flocs settle down due to gravity and phase separate as seen in Figure 5.9. Additionally, at higher concentrations, the flocs may be less dense and fewer in number as the NCC-TTAB complexes resolubilize in presence of large amount of surfactants [107] and there is a greater tendency to form free TTAB micelles in the bulk.

In phase separation experiments, the normalized phase separation height was measured with time. Figure 5.10a shows that the phase separation profiles were similar for lower TTAB concentrations of 0.1, 0.2 and 0.5 g/L. As expected, Figure 5.10b shows that the degree of phase separation decreased with increased TTAB concentration, especially at 1.1 g/L which is around the CMC of TTAB. As a general trend, it was observed that at lower TTAB concentrations, more phase separation was observed as compared to higher concentrations. As explained earlier, at higher TTAB concentrations, there is resolubilization of NCC-TTAB complexes and a greater

tendency by the surfactant molecules to form free TTAB micelles. Figure 5.10c shows the effect of salt on degree of phase separation. Due to the shielding/screening effect of NaCl, a lower degree of phase separation was observed in presence of salt in comparison to aqueous NCC solutions. The screening out of negative charges on NCC weakens the NCC-TTAB interactions thus lowering the formation of NCC-TTAB hydrophobic flocs and facilitating free TTAB micellization.
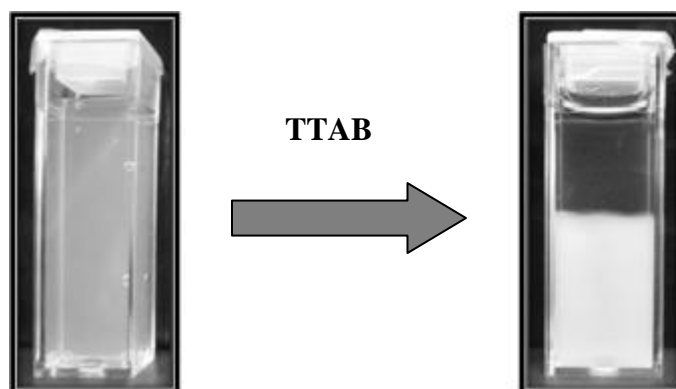
Figure 5.9 Phase separation of NCC aqueous suspensions in the presence of TTAB
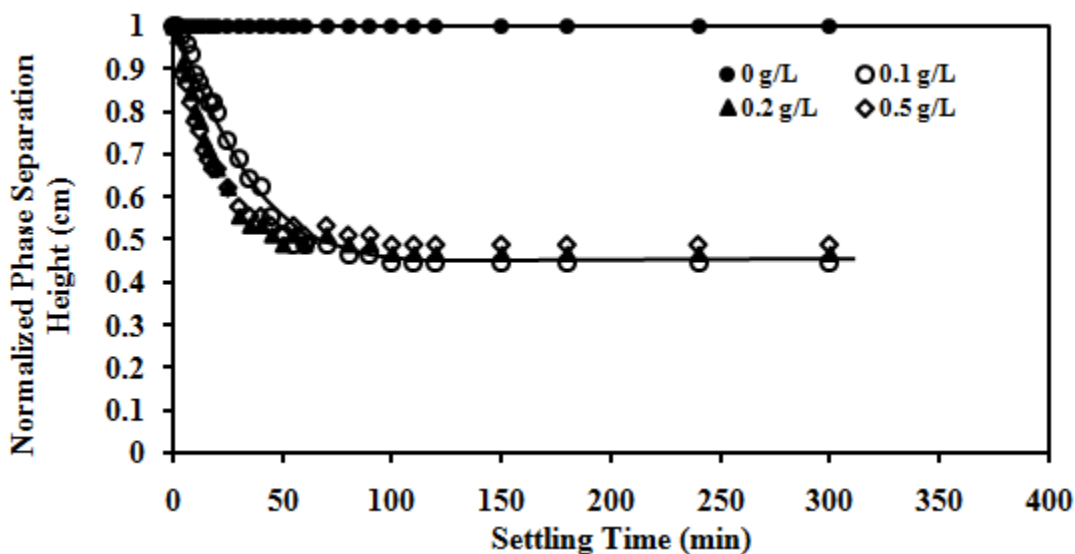
Figure 5.10a Phase separation heights in different TTAB conc. (0.1, 0.2 & 0.5 g/L TTAB)
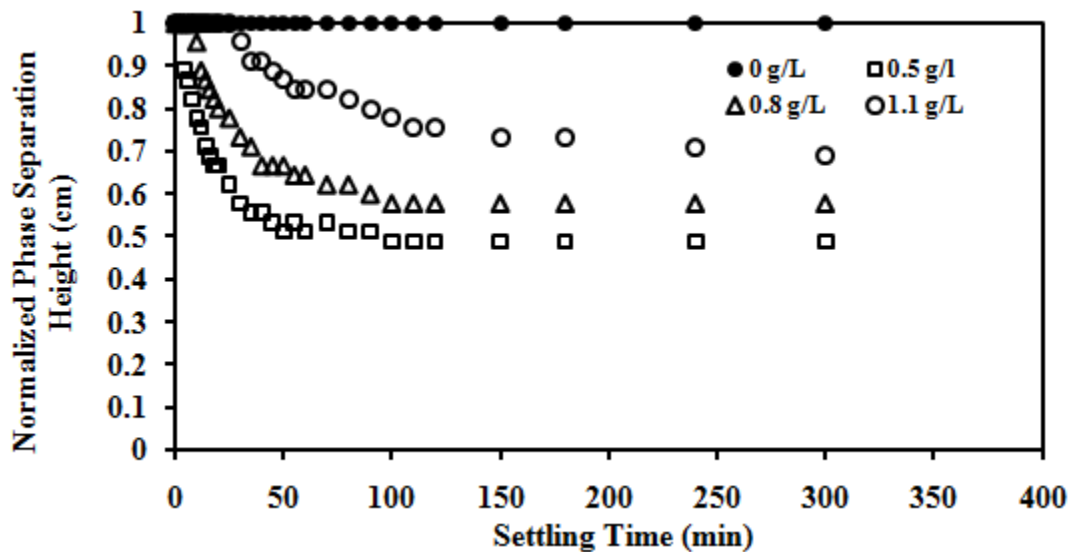
Figure 5.10b Phase separation heights in different TTAB conc (0.5, 0.8 & 1.1 g/L TTAB)
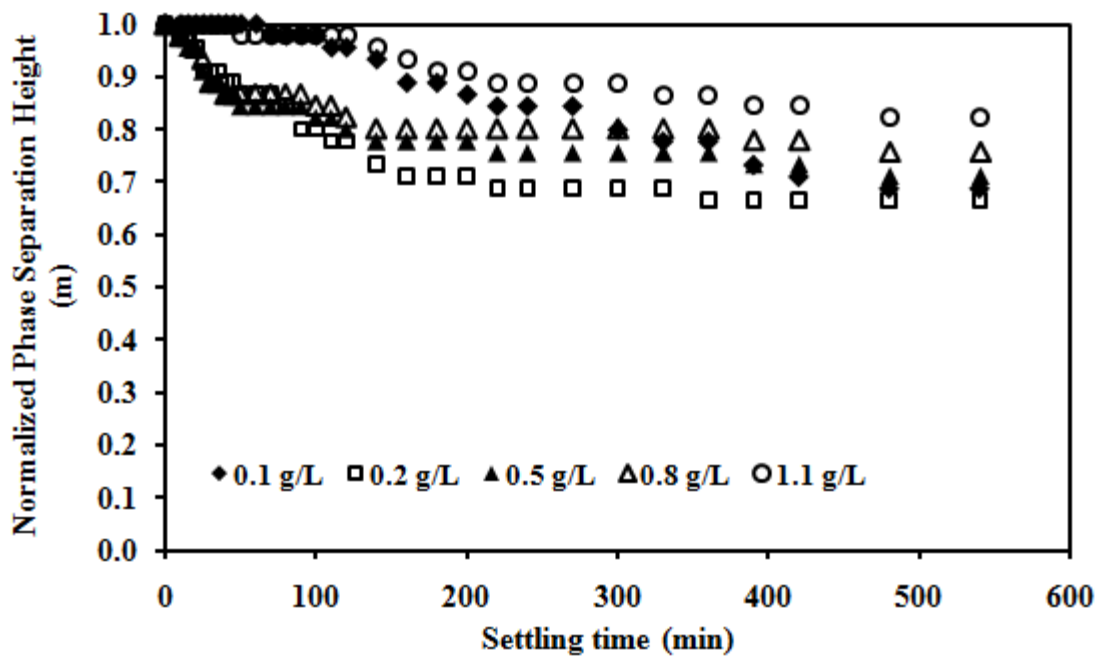
Figure 5.10c Phase separation heights in different TTAB concentrations in 0.005M salt

158
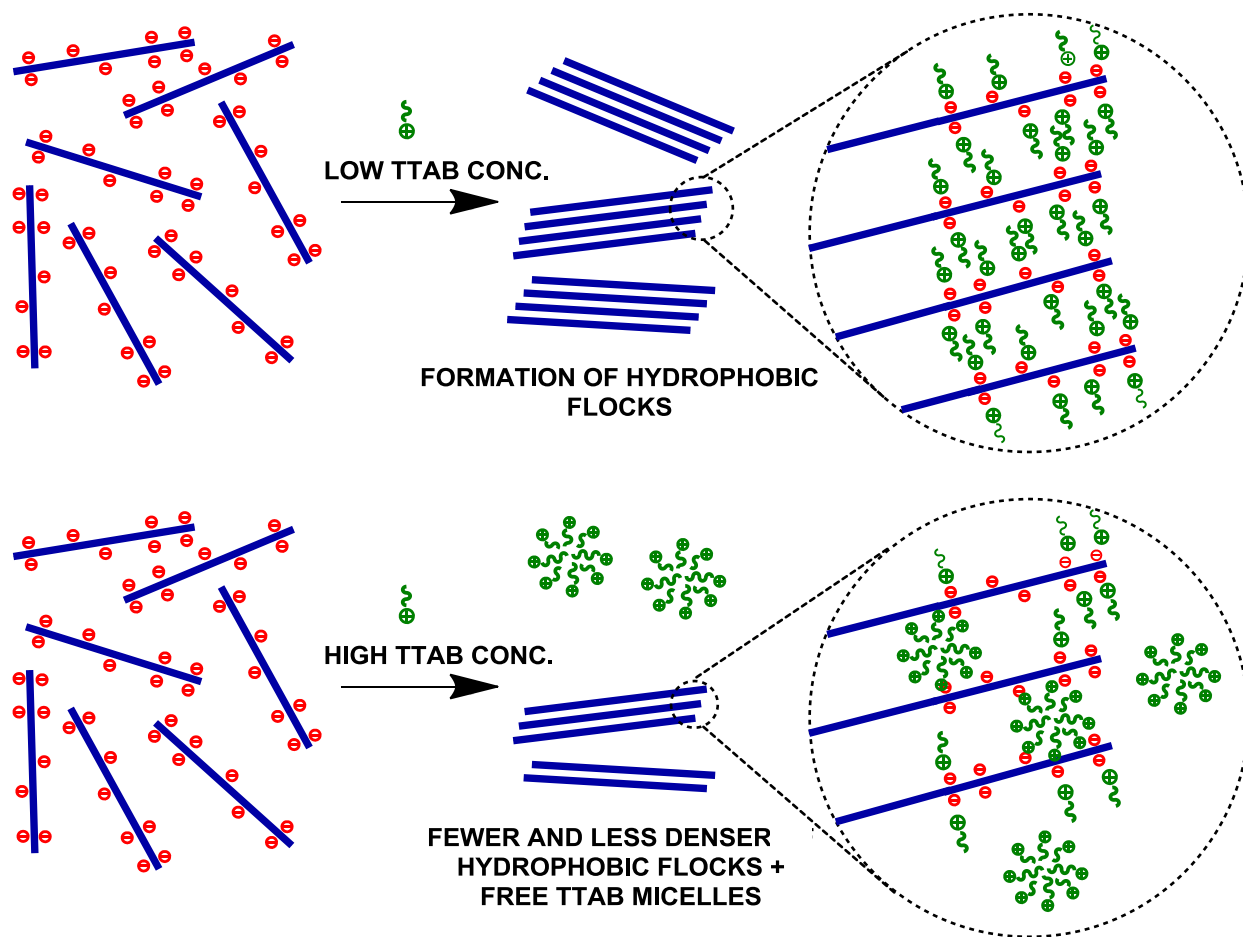
Figure 5.11 Mechanism of phase separation at low and high TTAB concentrations

5.3.5 Zeta potential results

Zeta potential measurements (Figure 5.12) were conducted with NCC-TTAB solutions containing different amounts of TTAB: 0.1, 0.2, 0.5, 0.8 and 1.1 g/L. While 0.1 and 0.2 g/L TTAB concentrations showed negative zeta potential values, 0.5, 0.8 and 1.1 g/L TTAB concentrations showed progressively positive values which levelled off at 1.1 g/L. It is hypothesized that at 0.1 and 0.2 g/L, the TTAB molecules are adsorbed on the NCC surface but do not form a complete coverage. Thereafter, TTAB micelles completely cover the NCC surface

and two or more NCC rods may come together producing higher zeta potential values at 0.5, 0.8 and 1.1 g/L. The zeta potential curve levels of around 1.1 g/L which is around the CMC of pure TTAB surfactant. At this point, no more polymer induced micellization is observed and free TTAB micellization occurs. This reversal of the surface charge on NCC-TTAB complexes was expected and similar results have been reported elsewhere as well. [111] [108]
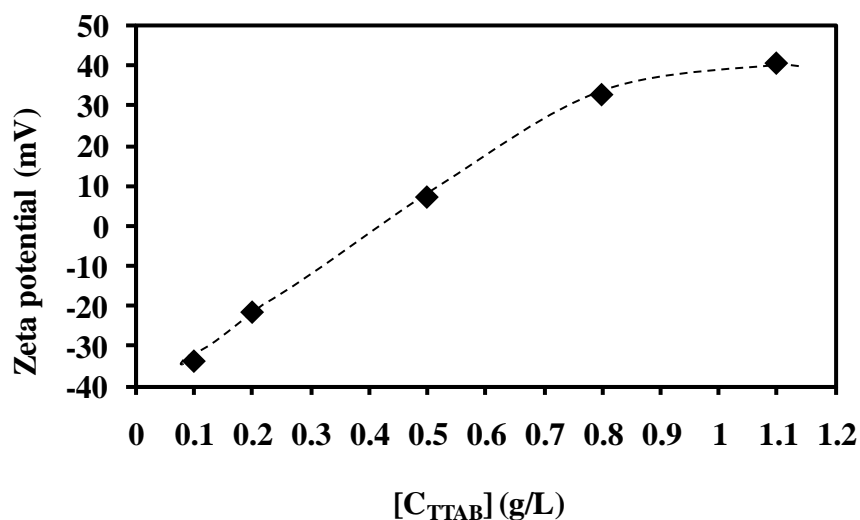
Figure 5.12 Zeta potential of 0.655 g/L NCC solutions at different TTAB concentrations

5.3.6 Comparison of ITC, Surface tensiometry and Zeta potential results

Figure 5.13 shows a comparison of ITC and Zeta potential results. The figure is divided into four regions corresponding to the four regions of interaction in the ITC curve. Region I in the ITC curve represents the electrostatic interactions between NCC and TTAB. The corresponding zeta potential value in region I show that the NCC-TTAB complexes are negative charged. This observation suggests that the TTAB molecules do not completely cover the NCC rods as some surface charges may not be accessible to TTAB molecules. Region II in the ITC curve represents

the reorganization of bound surfactants on the NCC rods. The corresponding zeta potential value in region II becomes less negative as compared to the value in region I; this is because TTAB concentration in the solution has now increased leading to increased NCC-TTAB interaction thereby neutralizing more negative charges on NCC. Region III in the ITC curve represents the polymer induced micellization of TTAB on NCC rods and the aggregation of surfactant bound NCC rods. Due to formation of TTAB micelles on the NCC rods, the corresponding zeta potential value in region III is positive. Finally, region IV in the ITC curve represents free TTAB micellization in bulk. This result is corroborated by the zeta potential values in region IV which become progressively positive and reach steady state around CMC_{TTAB} (i.e. 1.1 g/L).

Figure 5.14 shows the surface tension curve for titration of TTAB into NCC solution. The concentrations shown were correlated with the different regions of interaction in the ITC curve in Figure 5.1a. We observe that up to the TTAB concentration of 0.06 g/L, the surface tension steadily dropped due to the presence of NCC-TTAB complexes at the air-water interface. This concentration corresponds to region I in the ITC curve when NCC-TTAB complexes are being formed electrostatically in the bulk. Thereafter, a sharp drop in surface tension is observed corresponding to the interfacial saturation by NCC-TTAB complexes. This drop continues until a TTAB concentration of 0.3 g/L is reached. This concentration range of 0.06-0.3 g/L, corresponds to region I and II in the ITC curve. This observation suggests that while the interface is being saturated, the hydrophobic interactions and reorganization of adsorbed TTAB molecules occurs in the bulk. Interfacial saturation is observed to be complete at $C_s^* \sim$ 0.3 g/L and thereafter TTAB micellization on NCC begins. This region on surface tension curve corresponds to region III in the ITC curve ($C_2 \sim$ 0.32 g/L) and represents polymer induced micellization of TTAB molecules

on NCC. $C_m{}^*$ observed in Figure 5.14 also corresponds to the transition into region IV of the ITC curve representing formation of free TTAB micelles in bulk.
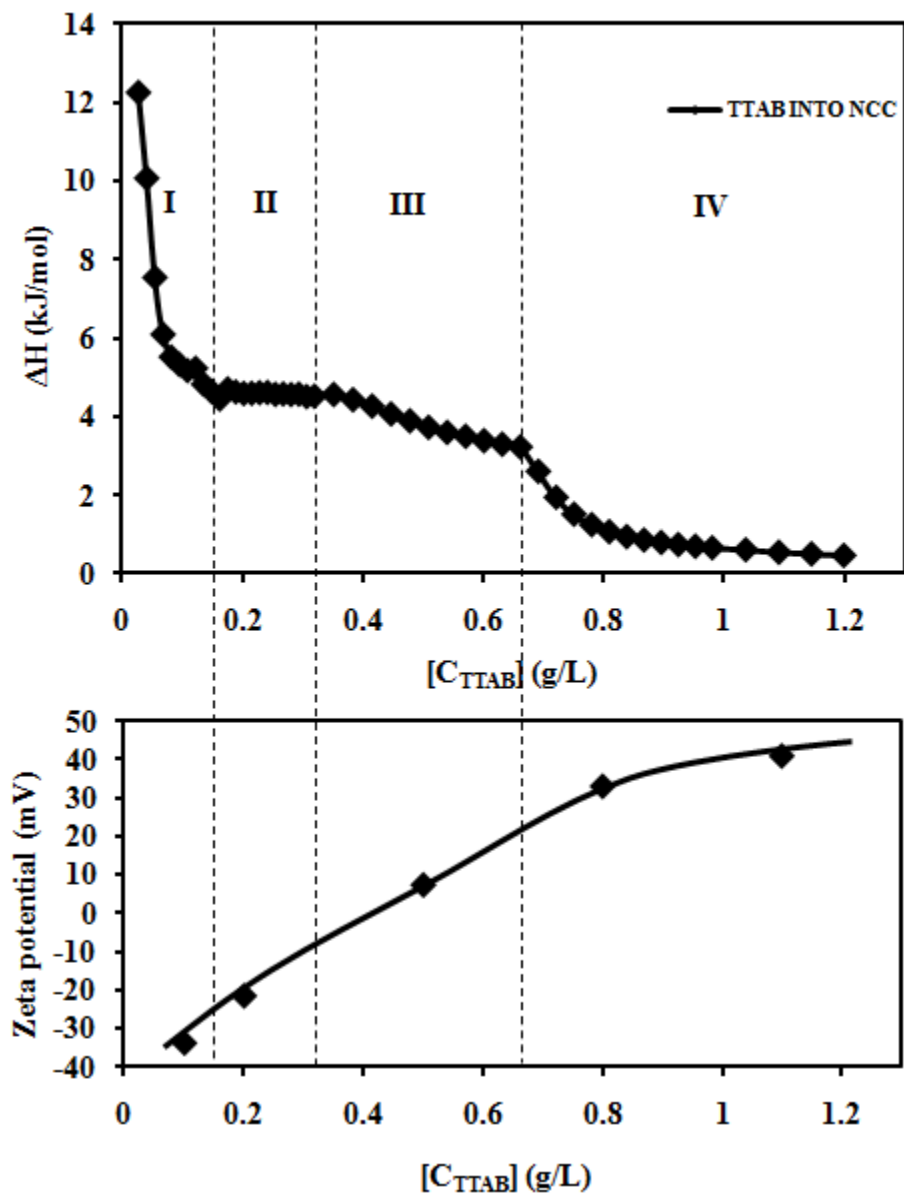
Figure 5.13 Comparison of ITC and zeta potential results
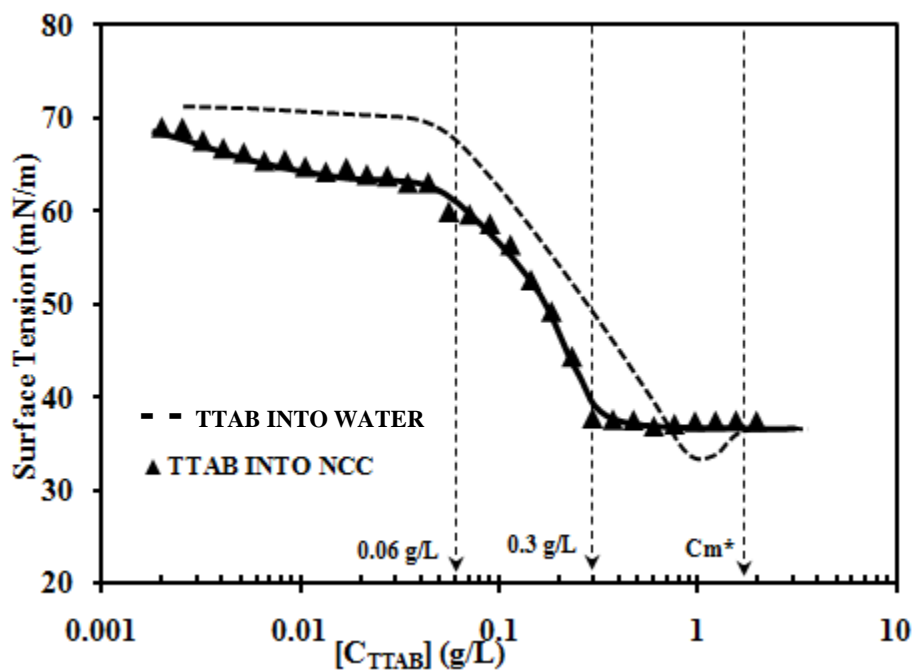
Figure 5.14 Surface tension results analyzed in comparison with ITC results

5.4 Summary

The interaction between negatively charged nanocrystalline cellulose (NCC) and a cationic surfactant, tetradecyl trimethyl ammonium bromide (TTAB) was examined by isothermal titration calorimetry (ITC), conductometric and potentiometric titrations and surface tensiometry. The interactions are controlled by two major forces, namely electrostatic and hydrophobic interactions. ITC and surface tension results confirmed two phenomena: (i) formation of *electrostatically driven* NCC-TTAB complexes in the bulk and at the interface (ii) *hydrophobically driven* polymer induced micellization of TTAB on NCC rods. Conductivity and surface tension results confirmed that the CMC of TTAB shifted from 1.1 g/L to 1.3 g/L in the presence of 0.655 g/L NCC. The settling and phase separation characteristics were quantified

163

by determining the height of the NCC flocs as a function of time, where the stability of the NCC in the presence of TTAB was correlated. Zeta potential results revealed a charge reversal from negative to positive charge on the NCC with increasing TTAB concentration, confirming the formation of NCC-TTAB complexes in aqueous solutions. The effect of electrolyte in shielding the negative charge on NCC was confirmed by ITC, surface tensiometry and phase separation experiments. Based on the corroborated data obtained from various experimental techniques, a physical mechanism for the interaction of NCC and TTAB is proposed. Furthermore, it was observed that using either electrolyte or high amount of TTAB, reduced the degree of phase separation in NCC suspensions; however, this is not a very feasible solution for using NCC along with surfactant formulations. Hence, steric stabilization of NCC by grafting poly (ethylene glycol) methacrylate (PEGMA) could be explored as a viable alternative in order to prevent the destabilization of NCC suspensions in the presence of a cationic surfactant.

CHAPTER 6

STERIC STABILIZATION OF NANOCRYSTALLINE CELLULOSE IN THE PRESENCE OF AN OPPOSITELY CHARGED SURFACTANT

6.1 Introduction

Due to its polyelectrolyte nature, NCC can be used in personal care applications, such as conditioners that employ polyelectrolytes in their formulations. Personal care applications often employ surfactant formulations and studying the effect of surfactants on NCC suspensions is imperative if NCC is to be adopted for use in personal care applications. In the previous chapter, we observed that aqueous NCC suspensions become destabilized and phase separate in the presence of an oppositely charged surfactant, tetradecyl trimethyl ammonium bromide (TTAB). The main forces involved in NCC-TTAB binding were identified as: (i) *electrostatic interactions* between NCC and TTAB (ii) *hydrophobic interactions* between the adsorbed TTAB molecules (iii) intermolecular hydrophobic interactions between surfactant bound NCC rods inducing bridging and aggregation of NCC rods. It was hypothesized that steric stabilization of NCC rods would reduce the electrostatic and hydrophobic interactions between NCC and TTAB. Hence, grafted poly (ethylene glycol) methacrylate (PEGMA) was grafted on the NCC rods using free radical *grafting to* approach. The structure of PEGMA is shown in Figure 6.1.
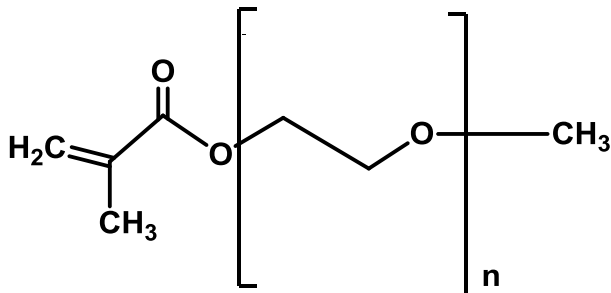
Figure 6.1 Structure of PEGMA

In their review on cellulose grafting and modification, Roy and co-workers [112] explain that there are three approaches to polymer grafting:

1. *Grafting-to* approach: In this method, a polymer with a functional end group is reacted with the functional groups on the cellulosic backbone.

2. *Grafting-from* approach: In this method, polymeric chains are grown from the cellulosic backbone itself.

3. *Grafting-through* approach: In this method, a vinyl macromonomer is combined with a low molecular weight co-monomer through co-polymerization.

The authors explain that the *Grafting-to* approach is limited by crowding of polymeric chains at the cellulosic backbone that prevents the diffusion of other reactive chain ends to the substrates thereby affecting the final grafting efficiency. Different methods of polymer grafting have been extensively reviewed by Bhattacharya and Misra. [113] A number of   papers [114-120] have also reported the grafting of cellulosic polymers using the conventional free radical approach. The mechanism of grafting using free radical approach is shown in Figure 6.2.

166

$$S_2O_8{}^{2-} \longrightarrow 2\ SO_4{}^{-}\cdot$$

$$Cellulose\text{-}OH\ +\ S_2O_8{}^{2-} \longrightarrow Cellulose\text{-}O\cdot\ +\ HSO_4{}^{-}\ +\ SO_4{}^{-}\cdot$$

$$Cellulose\text{-}O\cdot\ +\ Monomer \longrightarrow Graft\ Polymer$$

$$SO_4{}^{-}\cdot\ \ +\ Monomer \longrightarrow Homopolymer$$
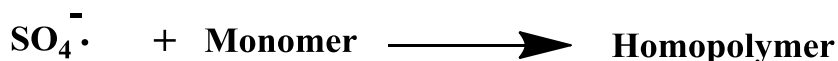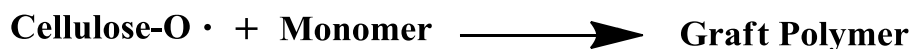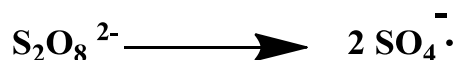
Figure 6.2 Schematic showing free-radical grafting approach [112]

In recent years, a number of papers have reported on the modification of NCC by the grafting approach. These papers have been discussed thoroughly in the NCC modification section in chapter 2.

6.2 Experimental Methods

6.2.1 Materials

Freeze dried nanocrystalline cellulose (NCC) sample was supplied by FP Innovations. Tetradecyl trimethyl ammonium bromide (TTAB) cationic surfactant (99% approx.) was purchased from Sigma. For steric stabilization, poly (ethylene glycol) methacrylate (PEGMA M.W. 300 Da, inhibitors removed using basic alumina) was purchased from Sigma. PEGMA 2000 (50 wt % in water) was purchased from Aldrich and used as received. Sodium persulphate initiator (98% +) was purchased from Acros. Millipore deionized water was used for all the sample preparations.

6.2.2 Synthesis of NCC-g-PEGMA samples

20 g/L of unmodified NCC solution was purged with N_2 for half hour in order to purge dissolved oxygen which might react with the free radicals of the initiator and affect the grafting reaction. The initiator was also purged with N_2 to remove any dissolved oxygen and the desired amount of sodium persulphate initiator was added to the NCC solution. The temperature of the reaction mixture was then increased to 70°C in order to produce the free radicals. Finally the desired amount of PEGMA was added and the reaction was allowed to continue for 4 hours. The reaction mixture was dialyzed for a week in regenerated-cellulose tubing (with 12000-14000 as M.W. cutoff). The M.W. cutoff was sufficient to remove the unreacted PEGMA, initiator and PEGMA homopolymers.

Depending on the ratio of PEGMA to NCC used for the grafting reaction, different NCC-g-PEGMA samples were synthesized. The ***grafting ratio*** (PEGMA : NCC) is defined as the amount of PEGMA used with respect to 20 g/L of the NCC sample. Furthermore, two different molecular weights of PEGMA were used: PEGMA-300 and PEGMA-2000. Keeping these two parameters in mind, the grafting ratio and the M.W. were added as a suffix to the sample names. Hence, the samples were designated as NCC-PEGMA-300(x2), NCC-PEGMA-300(x6), NCC-PEGMA-300(x10) & NCC-PEGMA-300(x14) for 300 M.W. series and NCC-PEGMA-2000(x2), NCC-PEGMA-2000(x6), NCC-PEGMA-2000(x10) and NCC-PEGMA-2000(x14) for 2000 M.W. series. The numeral in the brackets represents the grafting ratio used for the grafting reaction i.e. 2:1, 6:1, 10:1 and 14:1. For instance, for the 2:1

sample, the amount of PEGMA used was twice the amount of NCC and for the 6:1 sample the amount of PEGMA used was six times the amount of NCC used for grafting.

6.2.3 Characterization techniques

Isothermal Titration Calorimetry

Microcal VP-ITC instrument was used to study the interaction between NCC-g-PEGMA samples and TTAB surfactant at a constant temperature of 25°C. The volume of titrant (TTAB) was ~ 282 μL and 1.4551 mL of NCC-g-PEGMA sample was loaded into the sample cell. The titrant was injected at different volumes i.e. 2, 5 and 10 μL increments. The ΔH values for the dynamic interactions were reported as kJ/mol of injectant and were plotted against the concentration of titrant in the cell. For most measurements, the concentrations of TTAB and NCC-g-PEGMA samples were fixed at 10 g/L and 0.655 g/L respectively. A TTAB concentration of 10 g/L was chosen to allow investigation of the entire range of NCC-g-PEGMA and TTAB interactions. NCC-g-PEGMA concentration was fixed at 0.655 g/L as this concentration clearly showed all the regions of interactions when TTAB was titrated into it.

Phase separation measurements

It is known that the electrostatically driven polymer-surfactant complexes may lead to coacervation and phase separation. We have studied the phase separation behaviour of NCC-g-PEGMA solutions in the presence of different TTAB concentrations. NCC-g-PEGMA solutions at a concentration of 0.655 g/L were prepared and TTAB was added to the solutions

such that the resulting concentration of TTAB in the NCC-g-PEGMA solutions would be 0.1, 0.1, 0.5, 0.8 and 1.1 g/L. The solutions were allowed to stand and the phase separation height was measured with time, where the white turbid region at the bottom of the tube was considered as phase separated NCC.

FTIR

Bio-Rad (Excalibur series) FTIR spectrometer was used to analyze the PEGMA modified NCC samples. The wavelength range considered is 400-4000 cm^{-1}. KBr powder was mixed with unmodified NCC and freeze dried NCC-g-PEGMA samples to make thin FTIR films by compressing them between steel platens.

6.3 Results and Discussion

6.3.1 FTIR analysis of NCC-g-PEGMA samples

The grafting of PEGMA on NCC was confirmed by the presence of C=O group in the FTIR spectra of NCC-g-PEGMA samples. Figure 6.3a shows the carbonyl (C=O) group on PEGMA determined from FTIR analysis. Figure 6.3b shows the FTIR spectrum of NCC-PEGMA-300(x2) sample. The spectrum clearly shows the characteristic C=O frequency at 1750 cm^{-1}, confirming the grafting of PEGMA-300 on NCC. Similar peaks at 1750 cm^{-1} were obtained for all other NCC-PEGMA-300 samples. Figure 6.3c shows the FTIR spectrum of NCC-PEGMA-2000(x14) sample indicating the characteristic C=O frequency at 1750 cm^{-1} confirming the grafting of

PEGMA-2000 on NCC. Similarly, all other NCC-PEGMA-2000 samples showed the characteristic C=O peak at 1750 cm^{-1}.
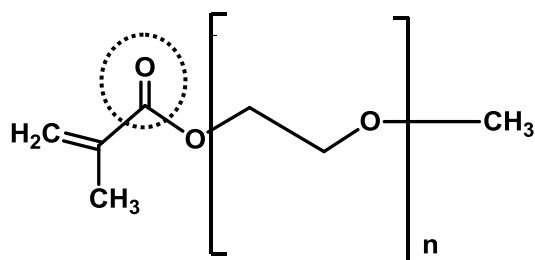
Figure 6.3a Carbonyl group on PEGMA used for FTIR analysis
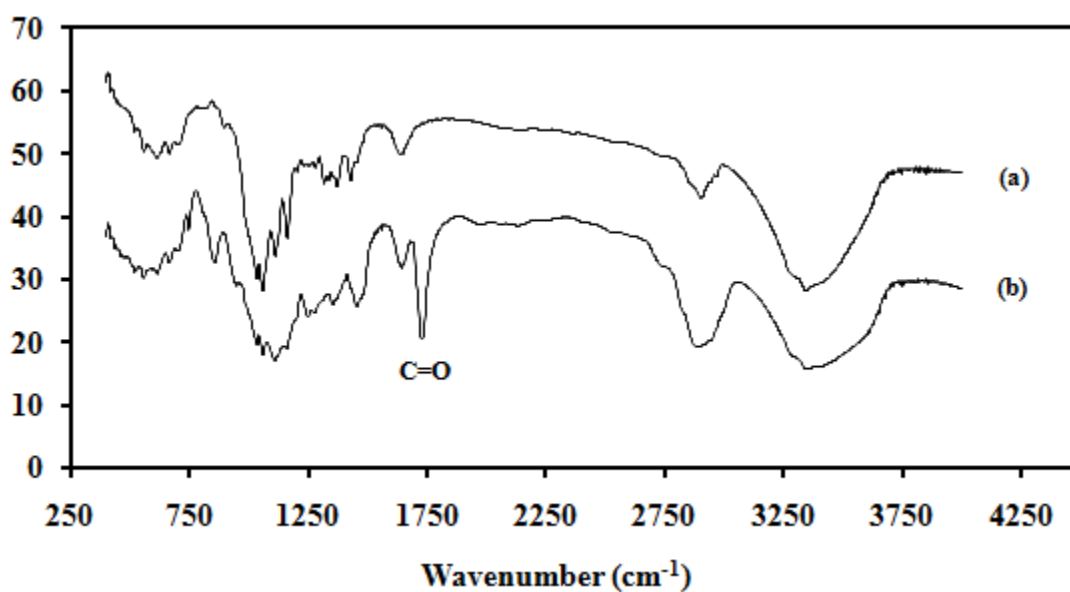
Figure 6.3b FTIR spectra of unmodified NCC (a) and NCC-PEGMA-300(x2) (b)
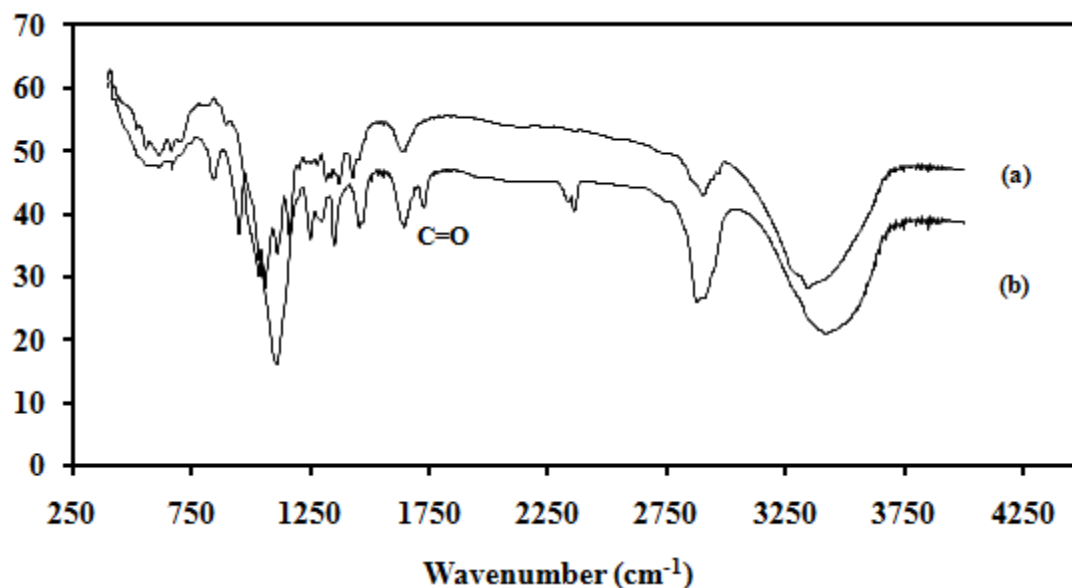
Figure 6.3c FTIR spectra of unmodified NCC (a) and NCC-PEGMA-2000(x14) (b)

6.3.2 Isothermal Titration Calorimetry (ITC) results

ITC results for unmodified NCC

The ITC results for TTAB titration into unmodified NCC sample has been discussed previously in chapter 5 (section 5.3.1). To summarize, the major interactions were identified as: electrostatic attraction, hydrophobic interactions and polymer induced micellization. The important concentrations C_1, C_2 and C_3 (from Figure 5.1a) were determined as:

C_1: onset of reorganization of adsorbed TTAB molecules;

C_2: onset of polymer induced micellization and aggregation of nanorods;

C_3: onset of free TTAB micellization in bulk.

ITC results for NCC-PEGMA-300 samples

Figure 6.4 shows the ITC curve for the titration of TTAB into NCC-PEGMA-300(x2) sample. The titration curves for TTAB/water and TTAB/unmodified NCC are also shown for reference. Similar to the trend shown by the NCC-TTAB curve, the NCC-PEGMA-300(x2) curve also shows four distinct regions of interaction. Region I corresponds to the electrostatic attraction between NCC-PEGMA-300(x2) and TTAB. A reduction in electrostatic interaction was observed for the NCC-PEGMA-300(x2) sample as compared to the NCC sample. This is because the PEGMA-300 chains provide steric hindrance and decreased the interaction of TTAB molecules and the negative charges on the NCC. Region II corresponds to the reorganization of adsorbed TTAB molecules to promote the formation of micelles on the NCC. However, the presence of PEGMA-300 chains also reduced the degree of reorganization compared to unmodified NCC. Region III corresponds to the formation of TTAB micelles on individual NCC rods similar to the third region in unmodified NCC sample; however, aggregation of surfactant bound NCC rods was prevented. It was hypothesized that the presence of PEGMA-300 chains provides adequate steric repulsion to prevent the surfactant bound NCC rods to bridge together and aggregate. This is may be the reason why region III closely follows the TTAB dilution curve as surfactant bound NCC rods repel each other sterically and facilitate the formation of free TTAB micelles in the bulk. Region IV corresponds to free micellization of TTAB in bulk. Since PEGMA-300 chains weaken the NCC-TTAB interaction, we observed that the onset for NCC-PEGMA-300(x2) sample ($C_1^{'}$, $C_2^{'}$ and $C_3^{'}$) are shifted to higher concentrations as compared to those for NCC (C_1, C_2 and C_3). Table 6.1 shows the values of $C_1^{'}$, $C_2^{'}$ and $C_3^{'}$ observed for NCC-PEGMA-300(x2) sample (from Figure 6.4) in comparison with C_1, C_2 and C_3 for NCC sample

(from Figure 5.1a). Clearly, the critical transitions for NCC-PEGMA-300(x2) sample are shifted to higher concentrations suggesting that greater amount of TTAB surfactant was needed to promote the various interactions defined by the critical transitions.
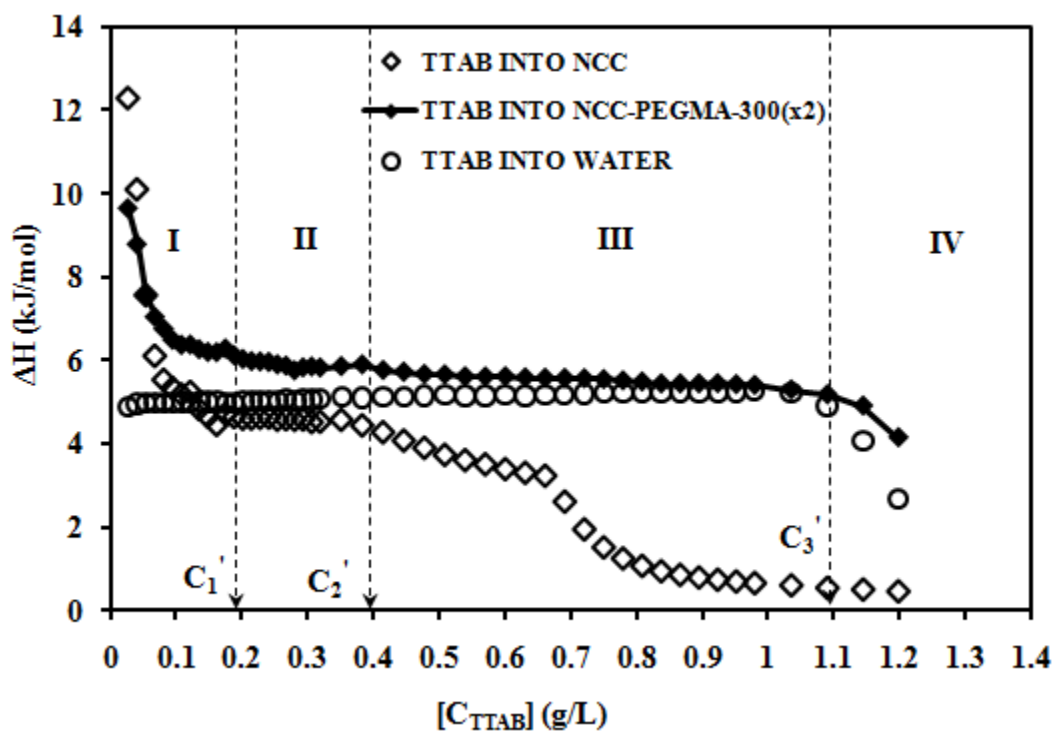
Figure 6.4 ITC curve-titration of TTAB into water (o), NCC (◊) & NCC-PEGMA-300(x2) (♦)

Sample	Onset of Reorganization(II)	Onset of Polymer induced micellization(III)	Onset of free TTAB micellization(IV)
NCC	$C_1 \sim 0.17$ g/L	$C_2 \sim 0.32$ g/L	$C_3 \sim 0.67$ g/L
NCC-PEGMA-300(x2)	$C_1' \sim 0.20$ g/L	$C_2' \sim 0.39$ g/L	$C_3' \sim 1.1$ g/L
NCC-PEGMA-300(x6)	$C_1'' \sim 0.32$ g/L	C_2'' not observed	$C_3'' \sim 1.15$ g/L
NCC-PEGMA-300(x10)	Same as (x6)	C_2'' not observed	Same as (x6)
NCC-PEGMA-300(x14)	Same as (x6)	C_2'' not observed	Same as (x6)

Table 6.1 ITC result table for NCC-PEGMA-300 samples

174

Figure 6.5 shows the detailed binding mechanism of NCC-PEGMA-300(x2) and TTAB. Regions I and II show the reduced electrostatic attraction and reduced surfactant reorganization due to presence of PEGMA-300 chains. Region III shows polymer induced micellization of TTAB molecules on the NCC rods; however, aggregation and shared micellization are inhibited due to steric repulsion from PEGMA-300 chains grafted on the NCC. This in turn facilitates the formation of free TTAB micelles in region IV.
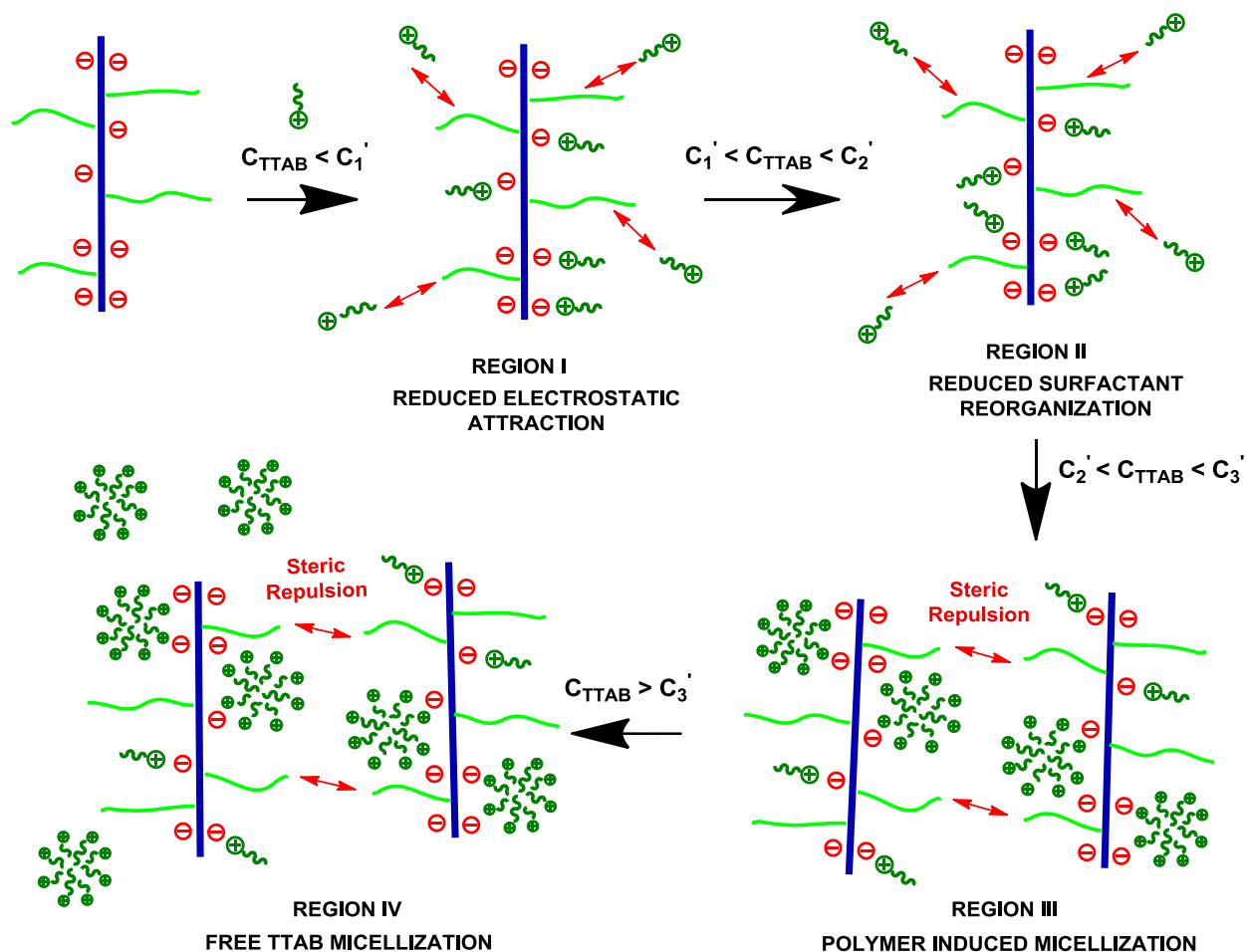
Figure 6.5 Mechanism of TTAB binding with NCC-PEGMA-300(x2)

Figure 6.6 shows the ITC curve for the titration of TTAB into NCC-PEGMA-300(x6) sample. The numeral in the bracket indicates that the amount of PEGMA-300 used for grafting is three times greater than the amount used for NCC-PEGMA-300(x2) sample. When higher amount of PEGMA-300 was used for grafting, the graft density on NCC increased; thus, the NCC-TTAB interaction was further weakened as steric repulsive forces are further strengthened with increased graft density on the NCC. From the ITC curve, we observed three regions of interactions instead of the usual four. Clearly region III corresponding to polymer induced micellization and aggregation of NCC rods was absent in the NCC-PEGMA-300(x6) sample.

Region I corresponds to the electrostatic interaction between NCC-PEGMA-300(x6) and TTAB. The electrostatic interactions were further lowered compared to the unmodified NCC and the transition point for reorganization $(C_1^{''})$ was shifted to an even higher concentration as compared to NCC and NCC-PEGMA-300(x2) samples (see Table 6.1). This is because the NCC-PEGMA-300(x6) sample has more grafted chains than NCC-PEGMA-300(x2) sample; so greater amount of steric hindrance repels the TTAB molecules and hinders their interaction with NCC rods. This hindrance would necessitate the need for more amount of TTAB to completely saturate all NCC-TTAB electrostatic interactions. Region II corresponds to the reorganization of adsorbed TTAB molecules on NCC. Since region II shows no change in slope uptil $C_3^{''}$, it was inferred that region III, which represents polymer induced micellization and aggregation, is absent. Greater graft density of NCC-PEGMA-300(x6) sample prevents the polymer induced micellization and aggregation of NCC rods. Therefore, in the absence of region III, region II eventually transits into region IV corresponding to free TTAB micellization in bulk. This is the reason why $C_2^{''}$ was not indicated for NCC-PEGMA-300(x6) sample. As expected, the onset of

free TTAB micellization ($C_3^{''}$) also shifted to an even higher concentration compared to NCC and NCC-PEGMA-300(x2) samples due its higher graft density (see Table 6.1).
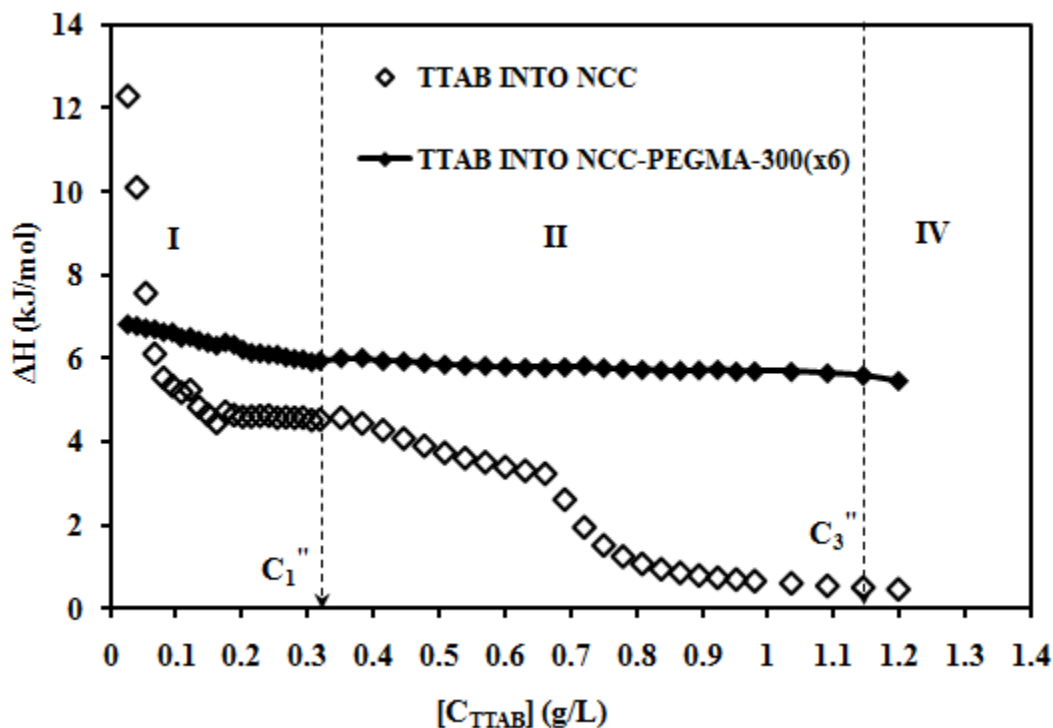
Figure 6.6 ITC curve for titration of TTAB into NCC (◊) and NCC-PEGMA-300(x6) (♦)

Figure 6.7 shows a schematic of TTAB interaction with NCC-PEGMA-300(x6) sample. As explained above, regions I and II indicate that the NCC-TTAB interactions were further weakened compared to NCC and NCC-PEGMA-300(x2) samples. Region III was absent since NCC-PEGMA-300(x6) sample possessed a higher graft density and steric repulsion forces were further enhanced compared to NCC and NCC-PEGMA-300(x2) samples. Thus, for NCC-PEGMA-300(x6) sample, polymer induced micellization and aggregation of nanorods was completely prevented. Region IV shows free TTAB micellization and sterically-stabilized surfactant bound NCC rods.
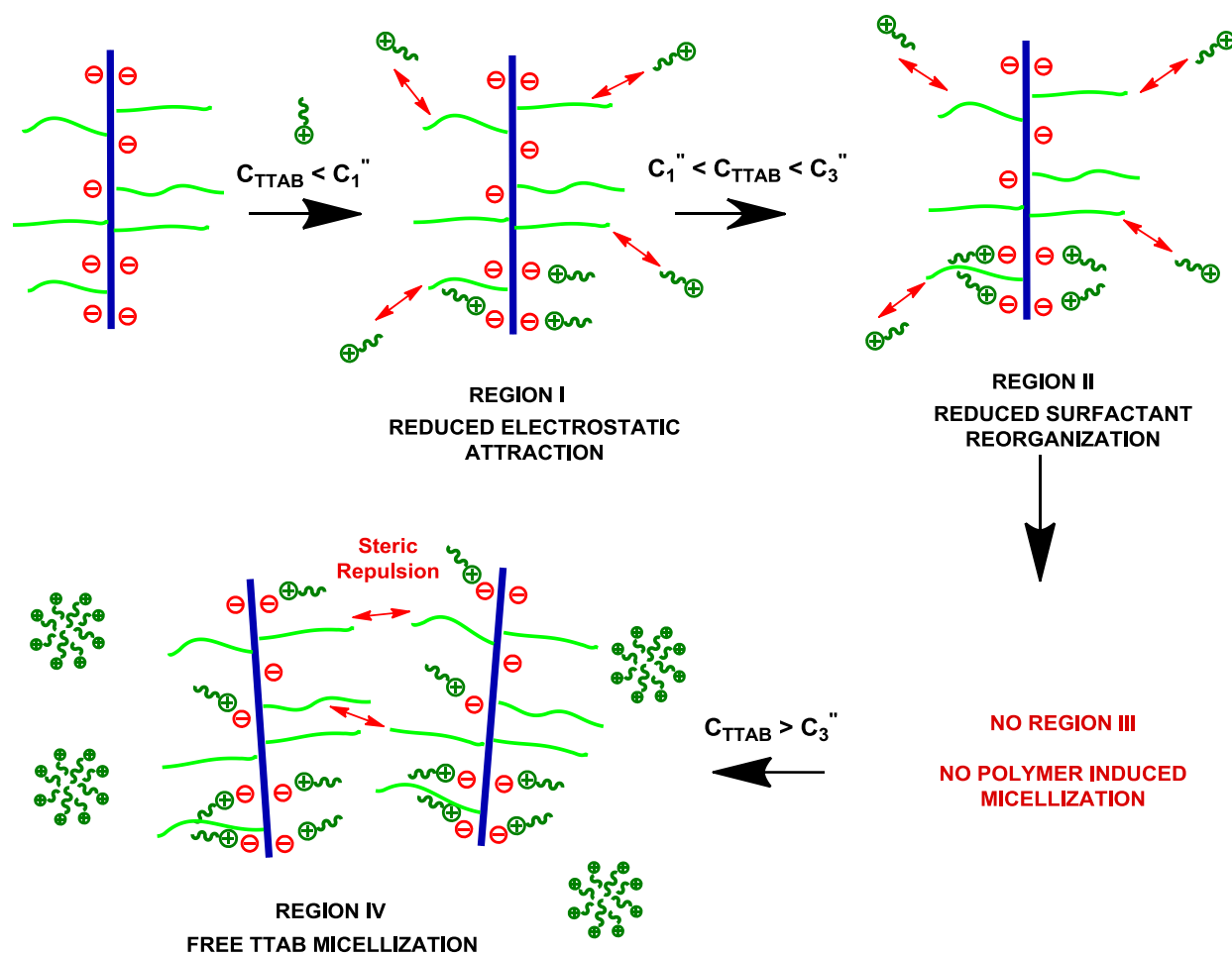
Figure 6.7 Mechanism of TTAB binding with NCC-PEGMA-300(x6)

Figure 6.8 shows the ITC titration curves for TTAB titration into NCC-PEGMA-300(x6), (x10) and (x14) samples. The curves have been magnified for visual clarity otherwise they overlap one another and discerning them visually becomes very difficult. The overlapping of ITC curves for (x6), (x10) and (x14) samples indicated that once an optimum grafting ratio was used for grafting, increasing the amount PEGMA-300 beyond the optimum value did not increase the number of grafted chains on NCC. Hence, the ITC curves did not show any appreciable change after the optimum grafting ratio was attained. The grafting ratio of 6:1

(for NCC-PEGMA-300(x6) sample) was probably the optimum ratio for grafting because increasing the grafting ratio beyond 6:1, like for (x10) and (x14) samples, did not produce any appreciable changes in the ITC curve. This was because increasing the amount of PEGMA-300 beyond a ratio of 6:1 did not increase the grafting density on the NCC itself. One probable explanation could be that 6:1 grafting ratio produced an optimum amount of grafting density on the NCC such that the grafted chains sterically repelled additional PEGMA-300 chains. So even when the amount of PEGMA-300 was increased further, i.e. for (x10) and (x14) samples, no additional grafting would occur; hence, no noticeable change in the ITC curves was observed for (x10) and (x14) samples compared to the (x6) sample. Thus, the amount of grafting on NCC and the degree of steric stabilization were comparable for NCC-PEGMA-300(x6), (x10) and (x14) samples.
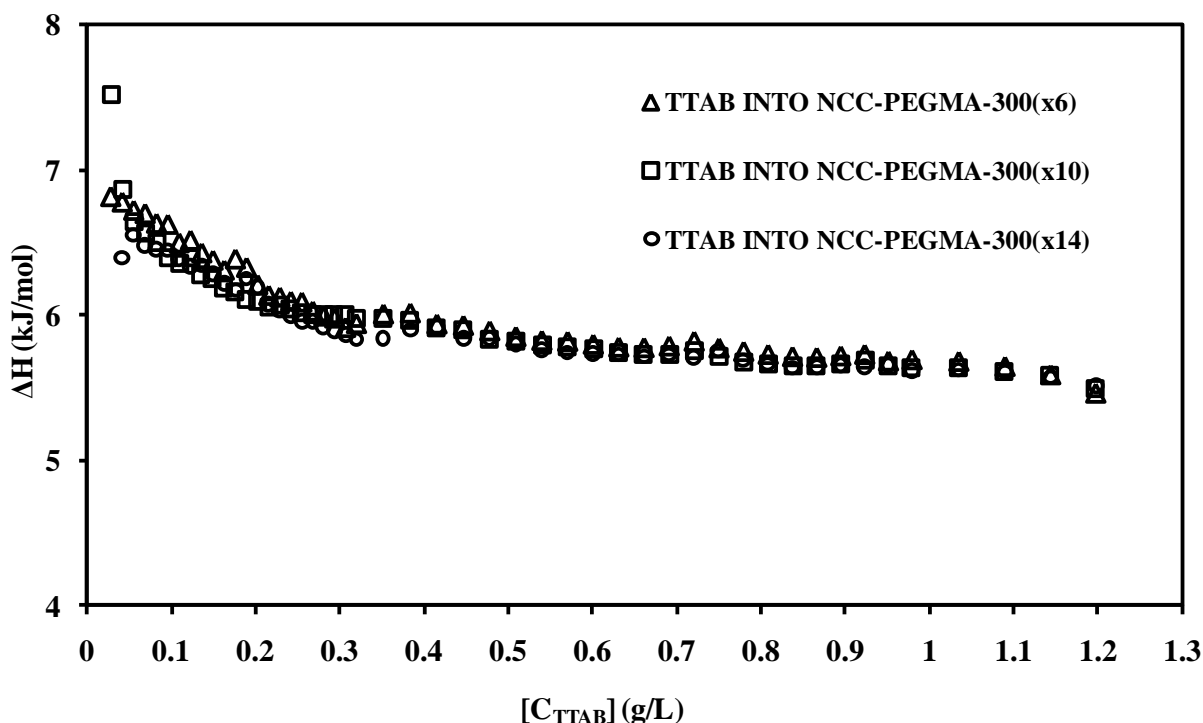
Figure 6.8 ITC curve for titration of TTAB into NCC-PEGMA-300(x6), (x10) and (x14) samples

By analyzing the ITC curves for all the NCC-PEGMA-300 samples, it was concluded that grafting PEGMA-300 chains on NCC surface was successful in reducing the electrostatic and hydrophobic interactions observed in NCC-TTAB system. NCC-PEGMA-300(x2) sample showed a lower electrostatic interaction (region I) and a lower tendency to aggregate surfactant bound NCC rods (region III). NCC-PEGMA-300(x6) sample not only showed a reduced electrostatic interaction (region I), but it also limited the polymer induced micellization and aggregation of NCC rods due to the steric repulsion (indicated by absence of region III). NCC-PEGMA-300(x10) and NCC-PEGMA-300(x14) samples exhibited an identical ITC trend to NCC-PEGMA-300(x6) sample. This suggests that increasing the grafting ratio beyond 6:1 did not necessarily weaken or completely eliminate the NCC-TTAB interaction. Therefore, we can conclude that NCC-PEGMA-300(x6) sample represents the optimum grafting ratio to weaken the NCC-TTAB interactions.

ITC results for NCC-PEGMA-2000 samples

Figure 6.9 shows the ITC curve for titration of TTAB to unmodified NCC and NCC-PEGMA-2000(x2) sample. Similar to the NCC-PEGMA-300(x2) sample, four regions of interactions were observed. Region I shows electrostatic interactions between NCC-PEGMA-2000(x2) and TTAB. However, the electrostatic interactions were lower in comparison to the NCC-TTAB system because of steric repulsion from PEGMA-2000 chains grafted on the NCC. Region II shows the reorganization of adsorbed TTAB molecules on the NCC surface. Region III shows polymer induced micellization and aggregation of surfactant bound NCC rods. Unlike the NCC-PEGMA-300(x2) sample, where region III in the ITC curve

followed the TTAB dilution curve (see Figure 6.4), the region III of the NCC-PEGMA-2000(x2) sample did not follow the of TTAB/water curve. Hence, the aggregation of surfactant bound NCC rods was not completely prevented. Region IV shows free TTAB micellization in the bulk. As discussed in the previous section, the $C_1^{'}$, $C_2^{'}$ and $C_3^{'}$ for NCC-PEGMA-300(x2) sample were shifted to higher concentrations compared to C_1, C_2 and C_3 for NCC sample. This was explained on the basis of steric hindrance which induces a delay in the different transition points on the ITC curve. As expected, for NCC-PEGMA-2000(x2) sample, $C_2^{'}$ and $C_3^{'}$ (from Figure 6.9) shifted to higher concentration values compared to C_2 and C_3 for NCC-TTAB system (from Figure 5.1a). These values are tabulated in Table 6.2. However, $C_1^{'}$ for NCC-PEGMA-2000(x2) sample did not show an appreciable change compared to C_1. This may be because of the M.W. of PEGMA. PEGMA-2000 possessed a longer chain length compared to PEGMA-300. PEGMA-2000 chains grafted on NCC could sterically repel other PEGMA-2000 chains resulting in lower grafting on the NCC surface. Therefore, it was hypothesized that NCC-PEGMA-2000(x2) sample possess less grafting compared to NCC-PEGMA-300(x2) sample. This difference in grafting density could probably explain why we do not observe such large shifts in $C_1^{'}$, $C_2^{'}$ and $C_3^{'}$ for NCC-PEGMA-2000(x2) sample compared to NCC-PEGMA-300(x2) sample. For e.g. region III in NCC-PEGMA-2000(x2) sample showed some aggregation of NCC rods compared to NCC-PEGMA-300(x2) system.
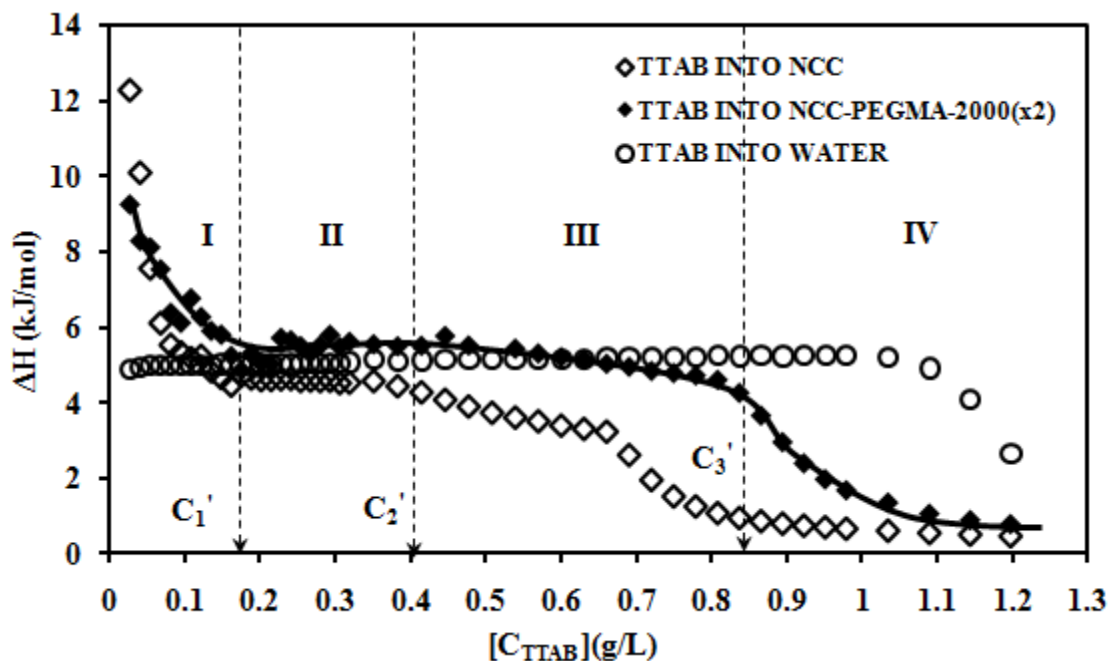
Figure 6.9 ITC curve - titration of TTAB into water (o), NCC (◊) & NCC-PEGMA-2000(x2) (♦)

Sample	Onset of Reorganization(I)	Onset of Polymer induced micellization(II)	Onset of free TTAB micellization(III)
NCC	$C_1 \sim 0.17$ g/L	$C_2 \sim 0.32$ g/L	$C_3 \sim 0.67$ g/L
NCC-PEGMA-2000(x2)	$C_1^{'} \sim 0.18$ g/L	$C_2' \sim 0.40$ g/L	$C_3^{'} \sim 0.84$ g/L
NCC-PEGMA-2000(x6)	$C_1^{''} \sim 0.18$ g/L	C_2'' not observed	$C_3^{''} \sim 1.04$ g/L
NCC-PEGMA-2000(x10)	Same as (x6)	C_2'' not observed	Same as (x6)
NCC-PEGMA-2000(x14)	$C^* \sim 0.07$ g/L	Not observed	$C_m = C_m^* \sim 1.05$ g/L

Table 6.2 ITC result table for NCC-PEGMA-2000 samples
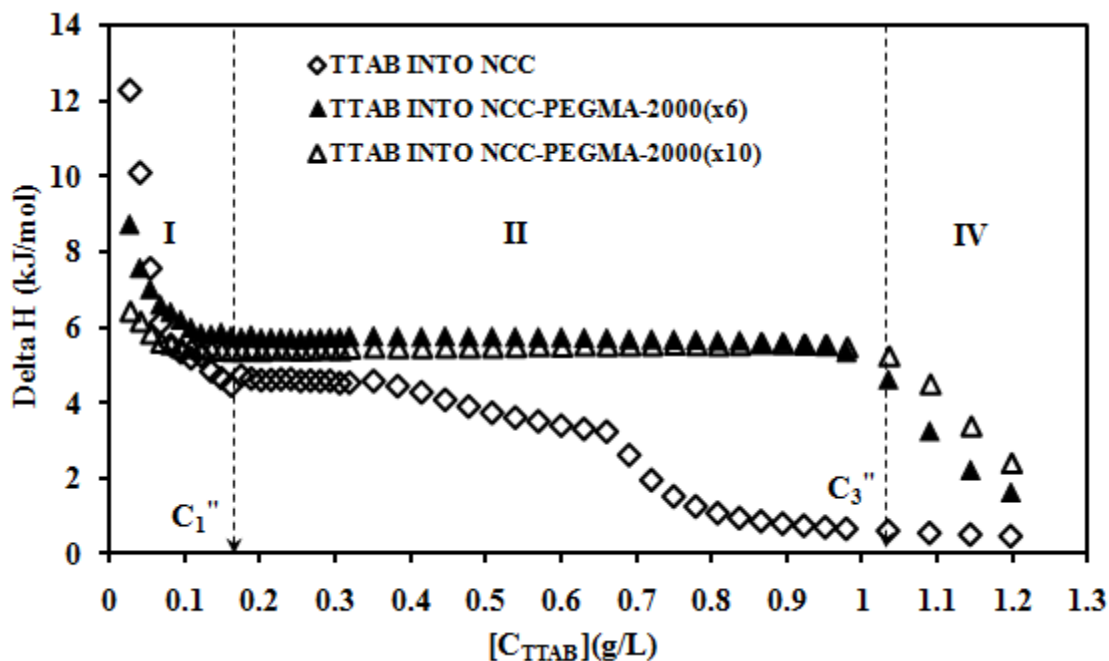
Figure 6.10 ITC curve for titration of TTAB into NCC (◊), NCC-PEGMA-2000(x6) (▲) and

NCC-PEGMA-2000(x10) (Δ)

Figure 6.10 above shows the titration of TTAB into NCC-PEGMA-2000(x6) and

NCC-PEGMA-2000(x10) samples. Similar to TTAB titration into NCC-PEGMA-300(x6), the

curve only showed three regions of interactions. Regions I and II correspond to electrostatic

interaction and reorganization of adsorbed TTAB molecules, respectively. Since the slope in

region II did not change, it was hypothesized that region II transits into free TTAB micellization

(region IV) without observing any polymer induced micellization or aggregation of surfactant

bound NCC rods. Again, this could be explained due to the steric repulsion from grafted

PEGMA-2000 chains on the NCC rods. Moreover, NCC-PEGMA-2000(x6) sample has more

graft density than NCC-PEGMA-2000(x2) sample; hence, region III is observed for the latter but

not the former sample. Due to the absence of region III for NCC-PEGMA-2000(x6) sample, the

183

onset of polymer induced micellization, represented by $C_2^{''}$, was not indicated in the ITC curve. Moreover, the ITC curves for NCC-PEGMA-2000(x6) and NCC-PEGMA-2000(x10) samples exhibited the same shape and transitions points. From this observation, it was concluded that after reaching an optimum grafting ratio of 6:1 for the NCC-PEGMA-2000(x6) sample, further increase in grafting ratio to 10:1 did not significantly increase the grafting density on the NCC surface. So, the amount of grafting on NCC and the degree of steric stabilization are comparable for NCC-PEGMA-2000(x6) and NCC-PEGMA-2000(x10) samples.

Through visual observations, it was observed that the reaction mixtures for all NCC-PEGMA samples were stable over long periods of time with the exception of NCC-PEGMA-2000(x14) sample, which phase separated into two layers: a denser turbid phase and a lighter clear liquid phase. This observation may be attributed to presence of excess amount of PEGMA during the synthesis of NCC-PEGMA-2000(x14) sample that may produce comb like grafted structures on the NCC surface (Figure 6.11a).
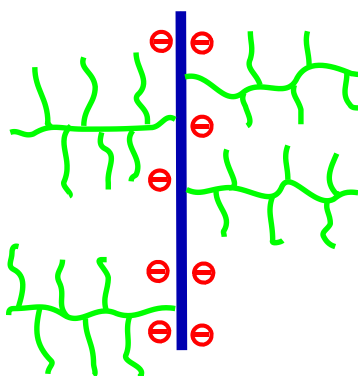
Figure 6.11a Comb like graft structures in NCC-PEGMA-2000(x14) sample

Due to their comb-like structures, the grafted PEGMA chains can interact hydrophobically instead of providing steric repulsion between the NCC rods. Hydrophobic interactions between

the comb-like structures may cause bridging and aggregation of the grafted NCC rods (see Figure 6.11b). This mechanism could possibly explain the phase separation of NCC-PEGMA-2000(x14) sample after dialyzing the reaction mixture.
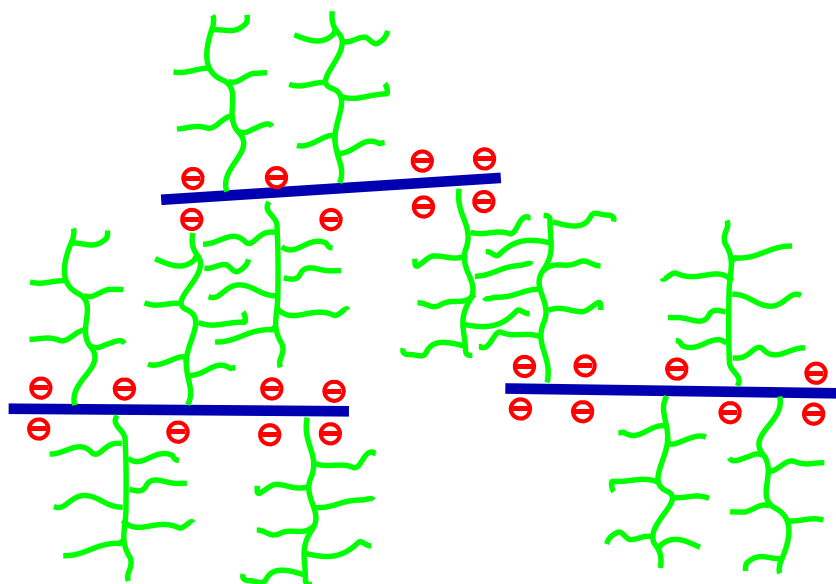
Figure 6.11b Hydrophobically induced aggregation of comb-like structures subsequently causing phase separation in NCC-PEGMA-2000(x14) sample

Figure 6.12 shows the ITC curve for titration of TTAB into NCC-PEGMA-2000(x14) sample, where electrostatic interaction seemed to be absent. However, a completely reversed trend was observed that corresponded to the hydrophobic interactions of TTAB hydrophobic segments with the hydrophobic comb-like PEGMA structures shown in Figure 6.11a. Beyond a critical TTAB concentration, C^*, the ITC curve followed exactly the TTAB/water curve suggesting that TTAB molecules no longer interacted with the comb-like PEGMA structures and were free to micellize in bulk. This is the reason why the CMC of pure TTAB (C_m) is equal to the CMC of TTAB in the presence of NCC-PEGMA-2000(x14) sample (C_m^*).
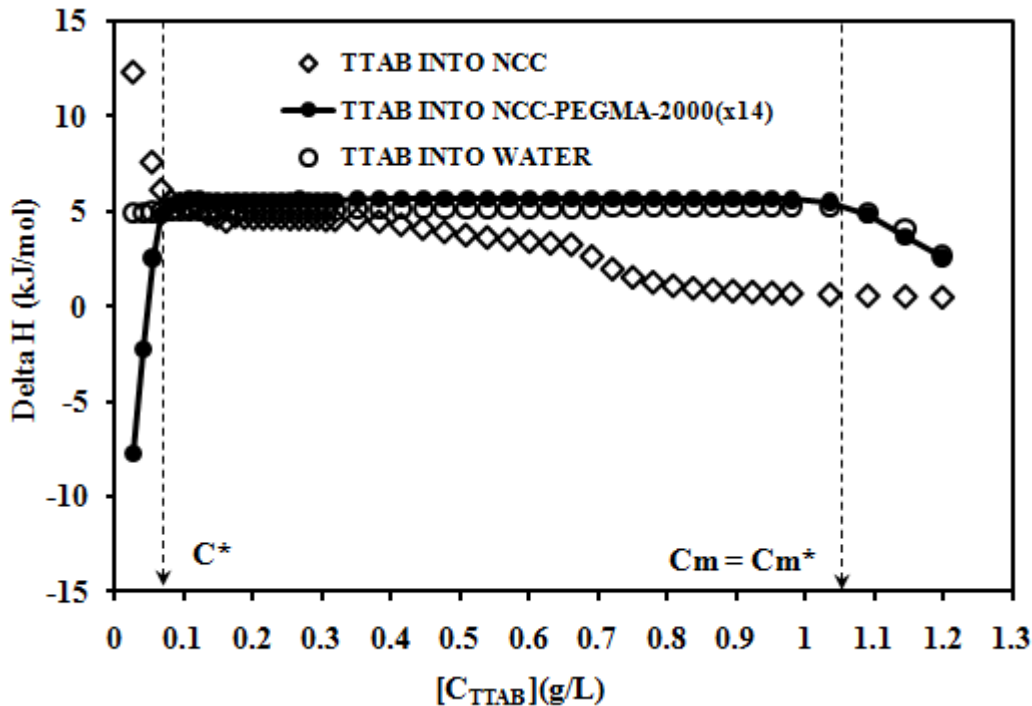
Figure 6.12 ITC curve-titration of TTAB into water (o), NCC (◊) &

NCC-PEGMA-2000(x14) sample (•)

Analysis of ITC results for all the NCC-PEGMA-2000 samples revealed that grafting NCC with PEGMA-2000 chains reduced the NCC-TTAB interactions due to steric repulsion forces. NCC-PEGMA-2000(x2) sample showed a lower electrostatic interaction in region I compared to unmodified NCC sample. NCC-PEGMA-2000(x6) and NCC-PEGMA-2000(x10) samples showed a reduced electrostatic interaction in region I and also prevented the polymer induced micellization and aggregation of NCC rods (indicated by absence of region III). Moreover NCC-PEGMA-2000(x6) and NCC-PEGMA-2000(x10) samples exhibited identical ITC trends, suggesting that increasing the grafting ratio beyond 6:1 did not necessarily weaken or eliminate the NCC-TTAB interaction. Therefore, the grafting ratio of 6:1 for NCC-PEGMA-2000(x6)

sample was considered optimum to reduce the interactions in NCC-TTAB system. On increasing the grafting ratio to 14:1 for NCC-PEGMA-2000(x14) sample, comb-like graft structures were probably formed which induced hydrophobic aggregation of the grafted NCC rods instead of sterically stabilizing the NCC system.

6.3.3 Phase separation results

Phase separation results for unmodified NCC

In the previous chapter (section 5.3.4), it was reported that in the presence of TTAB, the NCC solutions tend to phase separate into a clear phase and an insoluble turbid phase. Summary of the interactions is explained as follows: firstly, NCC and TTAB interact electrostatically. Next, the adsorbed TTAB molecules interact hydrophobically with other TTAB molecules from adjacent NCC rods. Hydrophobic interactions induce the aggregation and bridging of surfactant bound NCC rods to form larger aggregates or flocs. Eventually, these hydrophobic flocs settle down due to gravity and phase separate as a function of time.

Phase separation results for NCC-PEGMA-300 samples

The main purpose of grafting PEGMA on NCC was to introduce steric repulsion between NCC rods thereby preventing the phase separation phenomenon observed in the presence of TTAB. Phase separation experiments were conducted with TTAB and NCC-PEGMA-300 samples to confirm the effectiveness of steric hindrance in preventing phase separation. TTAB

187

concentrations were fixed at 0.1 and 1.1 g/L and the phase separation profiles were compared for different NCC-PEGMA-300 samples. NCC-PEGMA-300(x14) samples phase separated immediately when TTAB was added. Hence, their phase separation profiles could not be determined. This behavior may be attributed to enhanced hydrophobic interactions between the PEGMA chains (on NCC-PEGMA-300(x14) sample) and the hydrophobic segments of TTAB.
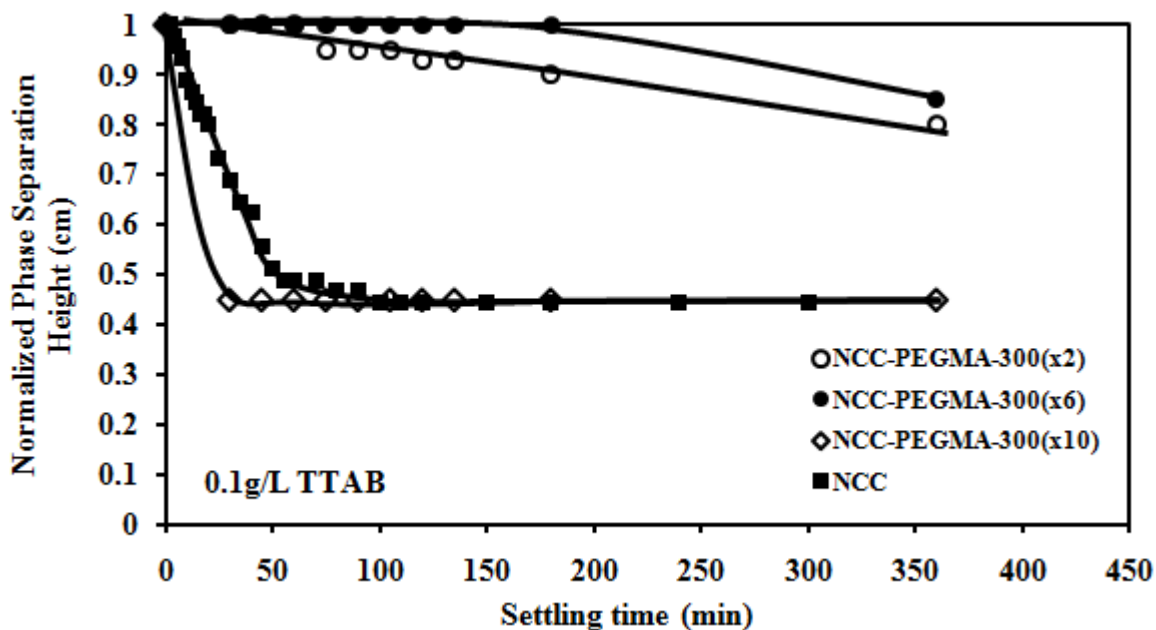
Figure 6.13a Phase separation heights for different NCC-PEGMA-300 samples at 0.1 g/L TTAB

Figure 6.13a shows the phase separation results for different NCC-PEGMA-300 samples at a constant TTAB concentration of 0.1 g/L. It was observed that NCC-PEGMA-300(x2) and NCC-PEGMA-300(x6) samples were less likely to phase separate while the NCC-PEGMA-300(x10) sample showed maximum phase separation compared to the unmodified NCC sample. Furthermore, NCC-PEGMA-300(x6) sample showed the lowest degree of phase separation compared to all other samples indicating that the grafting ratio of 6:1

was optimum for preventing phase separation. This result clearly indicates that grafting of PEGMA-300 chains weakened the NCC-TTAB interaction especially for NCC-PEGMA-300(x2) and NCC-PEGMA-300(x6) samples. However, the NCC-PEGMA-300(x10) sample showed maximum phase separation probably due to enhanced hydrophobic interactions between grafted PEGMA chains and the hydrophobic tails of TTAB molecules.
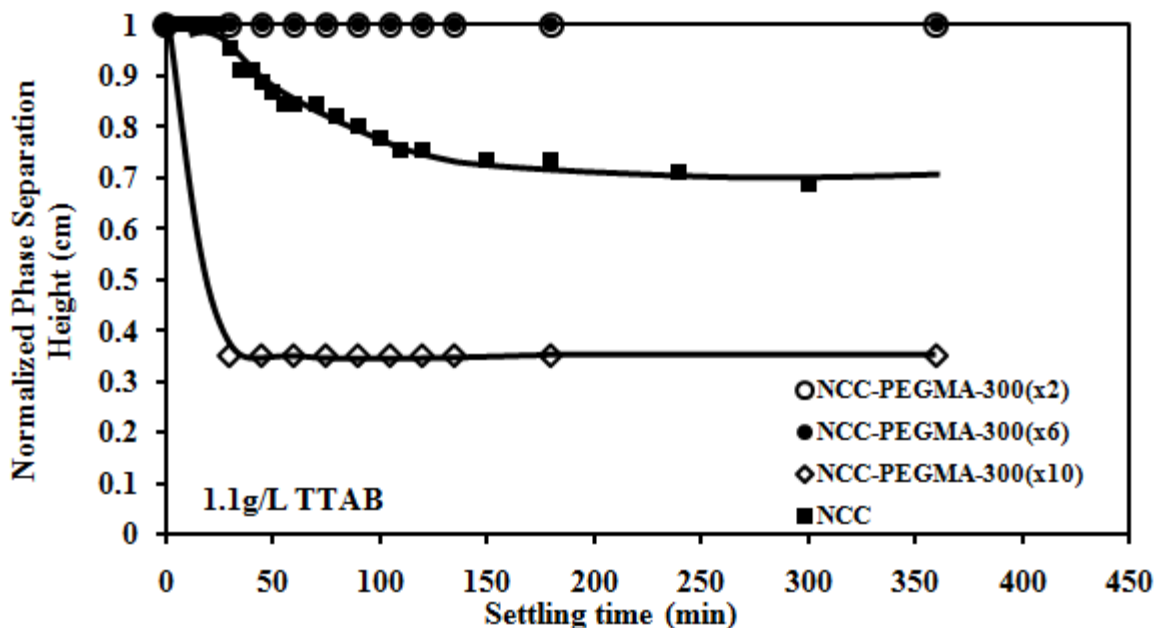
Figure 6.13b Phase separation heights for different NCC-PEGMA-300 samples at 1.1 g/L TTAB

For a higher TTAB concentration of 1.1 g/L (Figure 6.13b), a lower degree of phase separation was expected for all samples. This is because the NCC-g-PEGMA and TTAB complexes resolubilize at higher concentrations and TTAB has a greater tendency to form free micelles in bulk. NCC-PEGMA-300(x2) and NCC-PEGMA-300(x6) samples showed no phase separation up to 7 hours and showed negligible phase separation after 24 hours. Again, NCC-PEGMA-300(x10) sample showed maximum phase separation. At both low and high

concentrations of TTAB, NCC-PEGMA-300(x2) and NCC-PEGMA-300(x6) samples showed a lower phase separation tendency as compared to unmodified NCC sample. Moreover, the NCC-PEGMA-300(x6) sample seemed to be most stable as it exhibited the lowest phase separation values at both low and high TTAB concentrations.

Phase separation results for NCC-PEGMA-2000 samples

Phase separation experiments were conducted with TTAB and NCC-PEGMA-2000 samples. TTAB concentrations used were 0.1 and 1.1 g/L and the phase separation profiles were compared for different NCC-PEGMA-2000 samples. NCC-PEGMA-2000(x14) samples phase separated immediately when TTAB was added; hence, their phase separation profiles could not be determined. Again, this behaviour may be attributed to enhanced hydrophobic interactions between the PEGMA chains and the hydrophobic segments of TTAB. Figure 6.14a shows the phase separation profiles for different NCC-PEGMA-2000 samples at 0.1 g/L TTAB concentration. While all NCC-PEGMA-2000 samples showed better resistance to phase separation as compared to the NCC sample; the NCC-PEGMA-2000(x10) sample showed no phase separation in 0.1 g/L TTAB. This result might suggest that the NCC-PEGMA-2000(x10) is the most stable sample; however, at 1.1 g/L TTAB concentration, NCC-PEGMA-2000(x10) sample showed maximum phase separation (see Figure 6.14b). Furthermore, NCC-PEGMA-2000(x6) sample showed the lowest degree of phase separation at 1.1 g/L TTAB concentration. These observations suggested that NCC-PEGMA-2000(x6) sample is the most stable sample at both low and high concentrations of TTAB, which could be attributed to the

optimum grafting ratio of 6:1 that provided optimum steric hindrance to stabilize the NCC system in presence of TTAB.
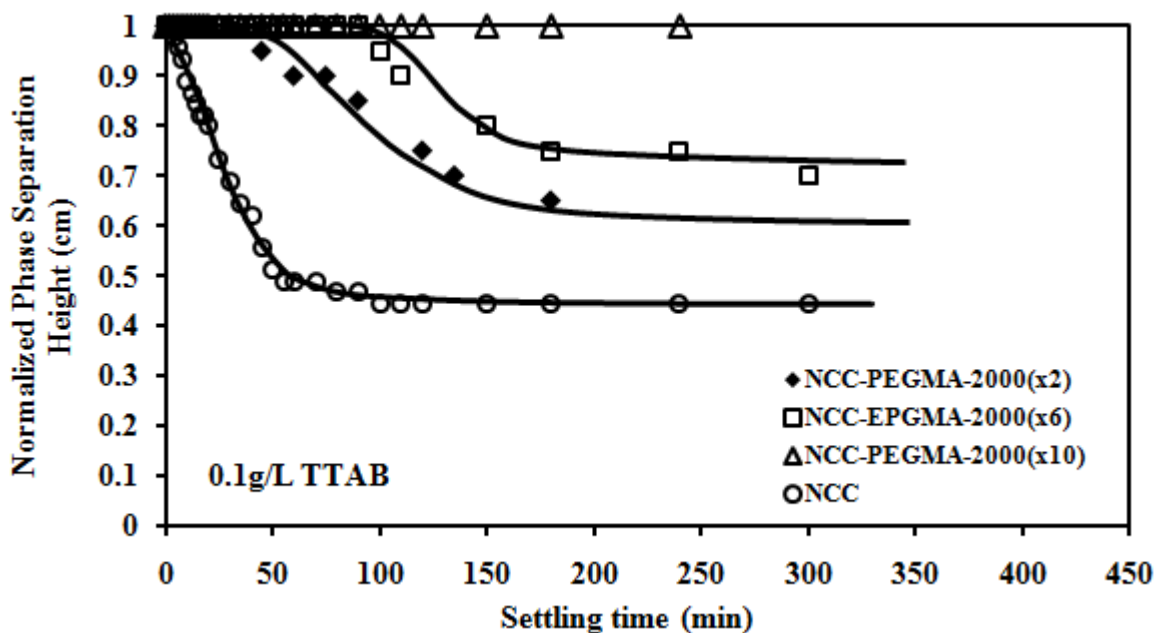
Figure 6.14a Phase separation ht. for different NCC-PEGMA-2000 samples at 0.1 g/L TTAB
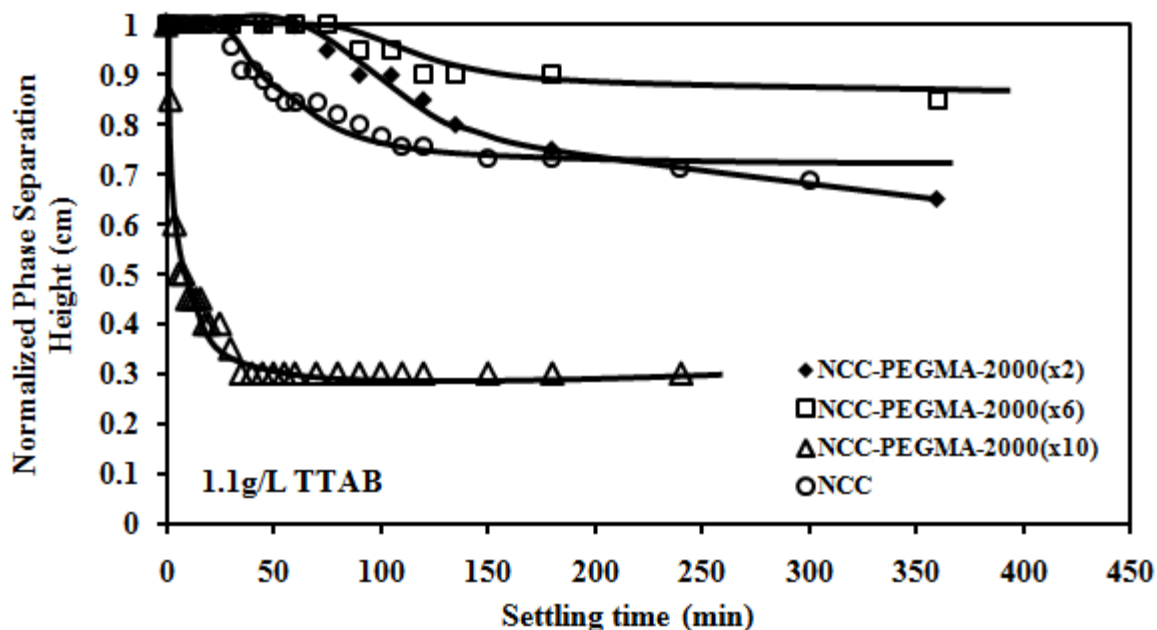
Figure 6.14b Phase separation ht. for different NCC-PEGMA-2000 samples at 1.1 g/L TTAB

6.4 Comparison of NCC-PEGMA-300 and NCC-PEGMA-2000 samples

The ITC results for all grafted samples showed a slightly different trend compared to the unmodified NCC sample. NCC-PEGMA-300(x2) and NCC-PEGMA-2000(x2) samples (with a grafting ratio of 2:1) weakened the NCC-TTAB interactions somewhat. More importantly, NCC-PEGMA-300(x6) and NCC-PEGMA-2000(x6) samples (with a grafting ratio of 6:1) further weakened the NCC-TTAB interactions. Thereafter, increasing the grafting ratio to 10:1 and 14:1 did not result in further weakening of NCC-TTAB interactions. Thus, for both NCC-PEGMA-300 and NCC-PEGMA-2000 samples, optimum grafting ratio was determined as 6:1. Similar inferences were drawn from phase separation experiments. NCC-PEGMA-300(x2) and NCC-PEGMA-2000(x2) samples showed a lower degree of phase separation compared to NCC sample, both at low and high TTAB concentrations. However, NCC-PEGMA-300(x6) and NCC-PEGMA-2000(x6) samples showed the lowest degree of phase separation compared to all other samples, both at low and high TTAB concentrations.

Considering the effect of M.W., both PEGMA-300 and PEGMA-2000 chains were capable of providing steric hindrance in the NCC system. As discussed previously, it was hypothesized that NCC-PEGMA-300 samples possessed a slightly higher grafting density on NCC compared to NCC-PEGMA-2000 samples. Therefore, PEGMA-300 is a better choice for grafting compared to PEGMA-2000.

6.5 Summary

Nanocrystalline cellulose (NCC) is a rod-like crystalline polymer with negative surface charges. In the presence of a positively charged surfactant, tetradecyl trimethyl ammonium bromide (TTAB), aqueous suspensions of NCC destabilize and phase separate into a clear phase and a white turbid phase. In order to prevent this destabilization in the presence of TTAB surfactant, poly (ethylene glycol) methacrylate (PEGMA) was grafted on the NCC surface to provide steric stabilization to the NCC rods. PEGMA chains were grafted on NCC via the free radical polymerization to produce NCC-g-PEGMA systems; PEGMA grafting was conducted with two different molecular weights of PEGMA (300 and 2000 Da) and different grafting ratios (ratio of PEGMA to NCC). PEGMA grafting was confirmed by FTIR. Isothermal titration calorimetry (ITC) and phase separation measurements were used to study the stability of NCC-g-PEGMA systems in the presence of TTAB. Both experiments confirmed that improved stability of NCC-g-PEGMA suspensions was achieved in the presence of TTAB surfactant. According to both ITC and phase separation results, NCC-PEGMA-300(x6) and NCC-PEGMA-2000(x6) samples were considered the most stable samples in the presence of TTAB. Furthermore, the grafting ratio of 6:1 was determined as the optimum ratio for the PEGMA grafting reaction. Increasing grafting ratio beyond 6:1 produced hydrophobic association of grafted chains instead of sterically stabilizing the NCC system.

CHAPTER 7

CONCLUSIONS AND FUTURE RECOMMENDATIONS

7.1 PROJECT 1: POLYAMPHOLYTE MICROGELS

Due to the benefits of cellulose based systems (biocompatibility and biodegradability), this project was aimed at developing novel cellulosic nanoparticles with potential pharmaceutical and personal care applications. Chitosan (CS), carboxymethyl cellulose (CMC) and modified methyl cellulose (ModMC) were used to synthesize biocompatible and biodegradable microgel systems. These crosslinked microgel systems were prepared using inverse microemulsion technique. Polyampholytic and pH-responsive behaviour was observed in CS-CMC microgel system. The microgels swelled at low and high pH values and deswelled at neutral pH values. The microgels also exhibited positive charges at low pH, negative charges at high pH and neutral charges at neutral pH. Furthermore, methyl cellulose was modified using carboxymethylation to incorporate them in the form of a microgel along with chitosan. pH & temperature responsive behaviours were observed in CS-ModMC microgel system. Therefore, both microgel systems could be used as potential drug carriers since they are composed of biocompatible and non-toxic polymers and are pH-responsive as well. pH-responsive properties could be used for drug delivery to either the tumour cells where the pH of the surrounding medium is acidic or the GI (gastrointestinal) tract where the pH of the surrounding medium is basic. Hence, for both polyampholytic systems, future work would involve the study of loading and unloading of model drugs. Changing the ratio of starting polymers and increasing the amount of crosslinker may also be explored to

improve synthesis procedures for the microgels. Also, microcalorimetric studies of CS-ModMC microgel system will be examined to further characterize their temperate responsive properties.

7.2 PROJECT 2: NANOCRYSTALLINE CELLULOSE

Recently, proposals to use NCC suspensions in personal care applications (like shampoos, conditioners etc.) have emerged. However, such applications also consist of surfactant formulation; this limits the number of applications since NCC suspensions have been observed to become unstable and phase separate in the presence of an oppositely charged surfactant. Isothermal titration calorimetry (ITC), surface tensiometry, conductivity measurements, phase separation measurements and zeta potential measurements were used to investigate the interactions between negatively charged nanocrystalline cellulose (NCC) and a cationic surfactant TTAB. The major interactions identified were: (i) electrostatic interactions between NCC and TTAB, (ii) micellization of TTAB on NCC rods (also called polymer induced micellization) and (iii) hydrophobic interactions between the surfactant bound NCC rods leading to aggregation and coacervation. Electrolyte (NaCl) addition significantly weakened the NCC-TTAB electrostatic interaction due to charge shielding. Further studies using light scattering and binding isotherms (using a surfactant selective electrode) may be done in the future to help understand the morphology and structure of NCC-TTAB complexes.

In order to improve the stability of NCC suspensions in the presence of an oppositely charged surfactant (TTAB), PEGMA chains were grafted on the NCC surface to produce steric stabilization. Free radical method was used to synthesize NCC-g-PEGMA samples. PEGMA-300

and PEGMA-2000 were used for the grafting reaction. ITC and phase separation experiments showed that PEGMA grafting introduced steric hindrance and prevented the electrostatic and hydrophobic interactions in the NCC-TTAB system; NCC-PEGMA-300(x6) and NCC-PEGMA-2000(x6) samples were considered the most stable samples in the presence of TTAB. The grafting ratio of 6:1 was determined as the optimum ratio for the PEGMA grafting reaction and PEGMA-300 was proposed as the better option for PEGMA grafting. Increasing the grafting ratio beyond 6:1 induced hydrophobic association of grafted chains instead of sterically stabilizing the NCC system. The properties of NCC-g-PEGMA samples can be further explored using light scattering studies to measure the R_g/R_h ratios for each of the grafted samples. The variation of R_g/R_h with increasing grafting ratio would help in understanding the morphology and structure of grafted NCC rods as a function of grafting ratio. Poly(propylene glycol) (PPG) with different molecular weights (and different LCSTs) could also be grafted on the NCC rods to produce a temperature responsive NCC-g-PPG system.

REFERENCES

[1]   Klemm D, Heublein B, Fink HP, Bohn A. Cellulose: Fascinating biopolymer and sustainable raw material. Angewandte Chemie-International Edition 2005;44:3358-93.

[2]   Samir MASA, Alloin F, Dufresne A. Review of recent research into cellulosic whiskers, their properties and their application in nanocomposite field. Biomacromolecules 2005;6:612-26.

[3]   Neyret S, Vincent B. The properties of polyampholyte microgel particles prepared by microemulsion polymerization. Polymer 1997;38:6129-34.

[4]   Das M, Kumacheva E. From polyelectrolyte to polyampholyte microgels: comparison of swelling properties. Colloid Polym Sci 2006;284:1073-84.

[5]   Tan BH, Tam KC. Review on the dynamics and micro-structure of pH-responsive nano-colloidal systems. Adv Colloid Interface Sci 2008;136:25-44.

[6]   Ho BS, Tan BH, Tan JPK, Tam KC. Inverse microemulsion polymerization of sterically stabilized polyampholyte microgels. Langmuir 2008;24:7698-703.

[7]   Tan BH, Ravi P, Tan LN, Tam KC. Synthesis and aqueous solution properties of sterically stabilized pH-responsive polyampholyte microgels. J Colloid Interface Sci 2007;309:453-63.

[8]   Rinaudo M. Main properties and current applications of some polysaccharides as biomaterials. Polym Int 2008;57:397-430.

[9]   Heinze T, Koschella A. Carboxymethyl ethers of cellulose and starch - A review. Macromolecular Symposia 2005;223:13-39.

[10]   Mansour OY, Nagaty A, Elzawawy WK. Variables Affecting the Methylation Reactions of Cellulose. J Appl Polym Sci 1994;54:519-24.

[11]   Yoon DS, Cho YK, Oh KW, Kim S, Kim YA, Han JI, Lim G. A microfluidic gel valve device using reversible sol-gel transition of methyl cellulose for biomedical application. Microsystem Technologies-Micro-and Nanosystems-Information Storage and Processing Systems 2006;12:238-46.

[12]   Chen H, Fan M. Novel thermally sensitive pH-dependent chitosan/carboxymethyl cellulose hydrogels. J Bioact Compatible Polym 2008;23:38-48.

[13]   Kamel S, Ali N, Jahangir K, Shah SM, El-Gendy AA. Pharmaceutical significance of cellulose: A review. Express Polymer Letters 2008;2:758-78.

[14]   Agnihotri SA, Mallikarjuna NN, Aminabhavi TM. Recent advances on chitosan-based micro- and nanoparticles in drug delivery. J Controlled Release 2004;100:5-28.

[15]   Chevillard C, Axelos MAV. Phase separation of aqueous solution of methylcellulose. Colloid Polym Sci 1997;275:537-45.

[16]   Elazzouzi-Hafraoui S, Nishiyama Y, Putaux J, Heux L, Dubreuil F, Rochas C. The shape and size distribution of crystalline nanoparticles prepared by acid hydrolysis of native cellulose. Biomacromolecules 2008;9:57-65.

[17]   Lima MMD, Borsali R. Rodlike cellulose microcrystals: Structure, properties, and applications. Macromolecular Rapid Communications 2004;25:771-87.

[18]   Rinaudo M. Chitin and chitosan: Properties and applications. Progress in Polymer Science 2006;31:603-32.

[19]   Khor E, Lim LY. Implantable applications of chitin and chitosan. Biomaterials 2003;24:2339-49.

[20]   Eyler RW, Klug ED, Diephuis F. Determination of Degree of Substitution of Sodium Carboxymethylcellulose. Anal Chem 1947;19:24-7.

[21]   Zhang LM. New water-soluble cellulosic polymers: A review. Macromolecular Materials and Engineering 2001;286:267-75.

[22]   Li L, Wang QQ, Xu YR. Thermoreversible association and gelation of methylcellulose in aqueous solutions. Nihon Reoroji Gakkaishi 2003;31:287-96.

[23]   Mansour OY, Nagaty A, Elzawawy WK. Variables Affecting the Methylation Reactions of Cellulose. J Appl Polym Sci 1994;54:519-24.

[24]   Wang QQ, Li L. Effects of molecular weight on thermoreversible gelation and gel elasticity of methylcellulose in aqueous solution. Carbohydr Polym 2005;62:232-8.

[25]   Oh JK, Drumright R, Siegwart DJ, Matyjaszewski K. The development of microgels/nanogels for drug delivery applications. Progress in Polymer Science 2008;33:448-77.

[26] Rolland JP, Maynor BW, Euliss LE, Exner AE, Denison GM, DeSimone JM. Direct fabrication and harvesting of monodisperse, shape-specific nanobiomaterials. J Am Chem Soc 2005;127:10096-100.

[27] Zhang H, Tumarkin E, Sullan RMA, Walker GC, Kumacheva E. Exploring microfluidic routes to microgels of biological polymers. Macromolecular Rapid Communications 2007;28:527-38.

[28] Wang L, Gu Y, Zhou Q, Ma G, Wan Y, Su Z. Preparation and characterization of uniform-sized chitosan microspheres containing insulin by membrane emulsification and a two-step solidification process. Colloids and Surfaces B-Biointerfaces 2006;50:126-35.

[29] Lehnert S, Tarabishi H, Leuenberger H. Investigation of Thermal Phase Inversion in Emulsions. Colloids and Surfaces A-Physicochemical and Engineering Aspects 1994;91:227-35.

[30] Zhang L, Jin Y, Liu HQ, Du YM. Structure and control release of chitosan/carboxymethyl cellulose microcapsules. J Appl Polym Sci 2001;82:584-92.

[31] Ichikawa S, Iwamoto S, Watanabe J. Formation of biocompatible nanoparticles by self-assembly of enzymatic hydrolysates of chitosan and carboxymethyl cellulose. Bioscience Biotechnology and Biochemistry 2005;69:1637-42.

[32] Watanabe J, Iwamoto S, Ichikawa S. Entrapment of some compounds into biocompatible nano-sized particles and their releasing properties. Colloids and Surfaces B-Biointerfaces 2005;42:141-6.

[33] Ioshchenko YP, Kablov VF, Zaikov GE. Polymeric complexes of chitosan with proteins and hydroxyl-containing polymers. Russian Journal of Applied Chemistry 2008;81:1434-40.

[34] Lagaron JM, Fendler A. High Water Barrier Nanobiocomposites of Methyl Cellulose and Chitosan for Film and Coating Applications. Journal of Plastic Film & Sheeting 2009;25:47-59.

[35] Beck-Candanedo S, Roman M, Gray DG. Effect of reaction conditions on the properties and behavior of wood cellulose nanocrystal suspensions. Biomacromolecules 2005;6:1048-54.

[36] Roman M, Winter WT. Effect of sulfate groups from sulfuric acid hydrolysis on the thermal degradation behavior of bacterial cellulose. Biomacromolecules 2004;5:1671-7.

[37] Filson PB, Dawson-Andoh BE, Schwegler-Berry D. Enzymatic-mediated production of cellulose nanocrystals from recycled pulp. Green Chem 2009;11:1808-14.

[38] Capadona JR, Shanmuganathan K, Triftschuh S, Seidel S, Rowan SJ, Weder C. Polymer Nanocomposites with Nanowhiskers Isolated from Microcrystalline Cellulose. Biomacromolecules 2009;10:712-6.

[39] Bondeson D, Mathew A, Oksman K. Optimization of the isolation of nanocrystals from microcrystalline cellulose by acid hydrolysis. Cellulose 2006;13:171-80.

[40] Bai W, Holbery J, Li K. A technique for production of nanocrystalline cellulose with a narrow size distribution. Cellulose 2009;16:455-65.

[41] Hirota M, Tamura N, Saito T, Isogai A. Water dispersion of cellulose II nanocrystals prepared by TEMPO-mediated oxidation of mercerized cellulose at pH 4.8. Cellulose 2010;17:279-88.

[42] Yun YS, Cho SY, Jin H. Flow-Induced Liquid Crystalline Solutions Prepared from Aspect Ratio-Controlled Bacterial Cellulose Nanowhiskers. Molecular Crystals and Liquid Crystals 2010;519:141-8.

[43] Li R, Fei J, Cai Y, Li Y, Feng J, Yao J. Cellulose whiskers extracted from mulberry: A novel biomass production. Carbohydr Polym 2009;76:94-9.

[44] Siqueira G, Abdillahi H, Bras J, Dufresne A. High reinforcing capability cellulose nanocrystals extracted from Syngonanthus nitens (Capim Dourado). Cellulose 2010;17:289-98.

[45] Rosa MF, Medeiros ES, Malmonge JA, Gregorski KS, Wood DF, Mattoso LHC, Glenn G, Orts WJ, Imam SH. Cellulose nanowhiskers from coconut husk fibers: Effect of preparation conditions on their thermal and morphological behavior. Carbohydr Polym 2010;81:83-92.

[46] van den Berg O, Capadona JR, Weder C. Preparation of homogeneous dispersions of tunicate cellulose whiskers in organic solvents. Biomacromolecules 2007;8:1353-7.

[47] Viet D, Beck-Candanedo S, Gray DG. Dispersion of cellulose nanocrystals in polar organic solvents. Cellulose 2007;14:109-13.

[48] Dong XM, Kimura T, Revol JF, Gray DG. Effects of ionic strength on the isotropic-chiral nematic phase transition of suspensions of cellulose crystallites. Langmuir 1996;12:2076-82.

[49] Dong XM, Gray DG. Effect of counterions on ordered phase formation in suspensions of charged rodlike cellulose crystallites. Langmuir 1997;13:2404-9.

[50] Revol JF, Godbout L, Dong XM, Gray DG, Chanzy H, Maret G. Chiral Nematic Suspensions of Cellulose Crystallites - Phase-Separation and Magnetic-Field Orientation. Liquid Crystals 1994;16:127-34.

[51] Pan J, Hamad W, Straus SK. Parameters Affecting the Chiral Nematic Phase of Nanocrystalline Cellulose Films. Macromolecules 2010;43:3851-8.

[52] Habibi Y, Heim T, Douillard R. AC electric field-assisted assembly and alignment of cellulose nanocrystals. Journal of Polymer Science Part B-Polymer Physics 2008;46:1430-6.

[53] Orts WJ, Godbout L, Marchessault RH, Revol JF. Shear-Induced Alignment of Liquid-Cystalline Suspensions of Cellulose Microfibrils. Flow-Induced Structure in Polymers 1995;597:335-48.

[54] Bercea M, Navard P. Shear dynamics of aqueous suspensions of cellulose whiskeys. Macromolecules 2000;33:6011-6.

[55] Ebeling T, Paillet M, Borsali R, Diat O, Dufresne A, Cavaille JY, Chanzy H. Shear-induced orientation phenomena in suspensions of cellulose microcrystals, revealed by small angle X-ray scattering. Langmuir 1999;15:6123-6.

[56] Edgar CD, Gray DG. Influence of Dextran on the Phase Behavior of Suspensions of Cellulose Nanocrystals. Macromolecules 2002;35:7406.

[57] Beck-Candanedo S, Viet D, Gray DG. Induced phase separation in cellulose nanocrystal suspensions containing ionic dye species. Cellulose 2006;13:629-35.

[58] Beck-Candanedo S, Viet D, Gray DG. Induced phase separation in low-ionic-strength cellulose nanocrystal suspensions containing high-molecular-weight blue dextrans. Langmuir 2006;22:8690-5.

[59]   Beck-Candanedo S, Viet D, Gray DG. Partitioning of charged and neutral dextran-dye derivatives in biphasic cellulose nanocrystal suspensions. Canadian Journal of Chemistry-Revue Canadienne De Chimie 2008;86:503-11.

[60]   Beck-Candanedo S, Viet D, Gray DG. Triphase equilibria in cellulose nanocrystal suspensions containing neutral and charged macromolecules. Macromolecules 2007;40:3429-36.

[61]   Kvien I, Tanem BS, Oksman K. Characterization of cellulose whiskers and their nanocomposites by atomic force and electron microscopy. Biomacromolecules 2005;6:3160-5.

[62]   Lahiji RR, Xu X, Reifenberger R, Raman A, Rudie A, Moon RJ. Atomic Force Microscopy Characterization of Cellulose Nanocrystals. Langmuir 2010;26:4480-8.

[63]   Rusli R, Eichhorn SJ. Determination of the stiffness of cellulose nanowhiskers and the fiber-matrix interface in a nanocomposite using Raman spectroscopy. Appl Phys Lett 2008;93:033111.

[64]   Terech P, Chazeau L, Cavaille JY. A small-angle scattering study of cellulose whiskers in aqueous suspensions. Macromolecules 1999; 32 1872-1875.

[65]   Bonini C, Heux L, Cavaille JY, Lindner P, Dewhurst C, Terech P. Rodlike cellulose whiskers coated with surfactant: A small-angle neutron scattering characterization. Langmuir 2002;18:3311-4.

[66]   Lima MMD, Borsali R. Static and dynamic light scattering from polyelectrolyte microcrystal cellulose. Langmuir 2002;18:992-6.

[67]   Lima AMD, Wong JT, Paillet M, Borsali R, Pecora R. Translational and rotational dynamics of rodlike cellulose whiskers. Langmuir 2003;19:24-9.

[68]   Araki J, Wada M, Kuga S. Steric stabilization of a cellulose microcrystal suspension by poly(ethylene glycol) grafting. Langmuir 2001;17:21-7.

[69]   Hasani M, Cranston ED, Westman G, Gray DG. Cationic surface functionalization of cellulose nanocrystals. Soft Matter 2008;4:2238-44.

[70]   Habibi Y, Chanzy H, Vignon MR. TEMPO-mediated surface oxidation of cellulose whiskers. Cellulose 2006;13:679-87.

[71]   Orts WJ, Godbout L, Marchessault RH, Revol JF. Enhanced ordering of liquid crystalline suspensions of cellulose microfibrils: A small angle neutron scattering study. Macromolecules 1998;31:5717-25.

[72]   Heux L, Chauve G, Bonini C. Nonflocculating and chiral-nematic self-ordering of cellulose microcrystals suspensions in nonpolar solvents. Langmuir 2000;16:8210-2.

[73]   Gousse C, Chanzy H, Excoffier G, Soubeyrand L, Fleury E. Stable suspensions of partially silylated cellulose whiskers dispersed in organic solvents. Polymer 2002;43:2645-51.

[74]   Yuan HH, Nishiyama Y, Wada M, Kuga S. Surface acylation of cellulose whiskers by drying aqueous emulsion. Biomacromolecules 2006;7:696-700.

[75]   Cetin NS, Tingaut P, Oezmen N, Henry N, Harper D, Dadmun M, Sebe G. Acetylation of Cellulose Nanowhiskers with Vinyl Acetate under Moderate Conditions. Macromolecular Bioscience 2009;9:997-1003.

[76]   Siqueira G, Bras J, Dufresne A. New Process of Chemical Grafting of Cellulose Nanoparticles with a Long Chain Isocyanate. Langmuir 2010;26:402-11.

[77]   Morandi G, Heath L, Thielemans W. Cellulose Nanocrystals Grafted with Polystyrene Chains through Surface-Initiated Atom Transfer Radical Polymerization (SI-ATRP). Langmuir 2009;25:8280-6.

[78]   Xu Q, Yi J, Zhang X, Zhang H. A novel amphotropic polymer based on cellulose nanocrystals grafted with azo polymers. European Polymer Journal 2008;44:2830-7.

[79]   Braun B, Dorgan JR. Single-Step Method for the Isolation and Surface Functionalization of Cellulosic Nanowhiskers. Biomacromolecules 2009;10:334-41.

[80]   Wang X, Zhang L, Wang L, Sun J, Shen J. Layer-by-Layer Assembled Polyampholyte Microgel Films for Simultaneous Release of Anionic and Cationic Molecules. Langmuir 2010;26:8187-94.

[81]   Schachschal S, Balaceanu A, Melian C, Demco DE, Eckert T, Richtering W, Pich A. Polyampholyte Microgels with Anionic Core and Cationic Shell. Macromolecules 2010;43:4331-9.

[82]   Christodoulakis KE, Vamvakaki M. Amphoteric Core-Shell Microgels: Contraphilic Two-Compartment Colloidal Particles. Langmuir 2010;26:639-47.

[83]   Xu K, Tan Y, Chen Q, An H, Li W, Dong L, Wang P. A novel multi-responsive polyampholyte composite hydrogel with excellent mechanical strength and rapid shrinking rate. J Colloid Interface Sci 2010;345:360-8.

[84]   Nakajima N, Ikada Y. Mechanism of Amide Formation by Carbodiimide for Bioconjugation in Aqueous-Media. Bioconjug Chem 1995;6:123-30.

[85]   Heinze T, Pfeiffer K. Studies on the synthesis and characterization of carboxymethylcellulose. Angewandte Makromolekulare Chemie 1999;266:37-45.

[86]   Kahne D, Still WC. Hydrolysis of a Peptide-Bond in Neutral Water. J Am Chem Soc 1988;110:7529-34.

[87]   Smith RM, Hansen DE. The pH-rate profile for the hydrolysis of a peptide bond. J Am Chem Soc 1998;120:8910-3.

[88]   Zahn D. On the role of water in amide hydrolysis. European Journal of Organic Chemistry 2004:4020-3.

[89]   Okubo T, Kobayashi K. Surface tension of biological polyelectrolyte solutions. J Colloid Interface Sci 1998;205:433-42.

[90]   Courtois J, Berret J-. Probing Oppositely Charged Surfactant and Copolymer Interactions by Isothermal Titration Microcalorimetry. Langmuir 2010;26:11750-8.

[91]   Kogej K. Association and structure formation in oppositely charged polyelectrolyte-surfactant mixtures. Adv Colloid Interface Sci 2010;158:68-83.

[92]   Nystrom B, Kjoniksen A, Beheshti N, Maleki A, Zhu K, Knudsen KD, Pamies R, Hernandez Cifre JG, Garcia de la Torre J. Characterization of polyelectrolyte features in polysaccharide systems and mucin. Adv Colloid Interface Sci 2010;158:108-18.

[93]   Fechner M, Kosmella S, Koetz J. pH-dependent polyampholyte SDS interactions. J Colloid Interface Sci 2010;345:384-91.

[94]   Bain CD, Claesson PM, Langevin D, Meszaros R, Nylander T, Stubenrauch C, Titmuss S, von Klitzing R. Complexes of surfactants with oppositely charged polymers at surfaces and in bulk. Adv Colloid Interface Sci 2010;155:32-49.

[95]   Pacios IE, Lindman B, Thuresson K. Polyelectrolyte-surfactant complexes with long range order. J Colloid Interface Sci 2008;319:330-7.

[96] Cui Y, Pelton R, Cosgrove T, Richardson R, Dai S, Prescott S, Grillo I, Ketelson H, Meadows D. Not All Anionic Polyelectrolytes Complex with DTAB. Langmuir 2009;25:13712-7.

[97] McLachlan AA, Marangoni DG. 1D and 2D NMR investigations of the interaction between oppositely charged polymers and surfactants. Canadian Journal of Chemistry-Revue Canadienne De Chimie 2010;88:124-34.

[98] Wang C, Tam KC. New insights on the interaction mechanism within oppositely charged polymer/surfactant systems. Langmuir 2002;18:6484-90.

[99] Liu Y, Guo R. Interaction between casein and the oppositely charged surfactant. Biomacromolecules 2007;8:2902-8.

[100] Wang C, Tam KC, Jenkins RD, Tan CB. Interactions between methacrylic acid/ethyl acrylate copolymers and dodecyltrimethylammonium bromide. J Phys Chem B 2003;107:4667-75.

[101] Onesippe C, Lagerge S. Studies of the association of chitosan and alkylated chitosan with oppositely charged sodium dodecyl sulfate. Colloids and Surfaces A-Physicochemical and Engineering Aspects 2008;330:201-6.

[102] Mata J, Patel J, Jain N, Ghosh G, Bahadur P. Interaction of cationic surfactants with carboxymethylcellulose in aqueous media. J Colloid Interface Sci 2006;297:797-804.

[103] Chakraborty T, Chakraborty I, Ghosh S. Sodium carboxymethylcellulose-CTAB interaction: A detailed thermodynamic study of polymer-surfactant interaction with opposite charges. Langmuir 2006;22:9905-13.

[104] Bain CD, Claesson PM, Langevin D, Meszaros R, Nylander T, Stubenrauch C, Titmuss S, von Klitzing R. Complexes of surfactants with oppositely charged polymers at surfaces and in bulk. Adv Colloid Interface Sci 2010;155:32-49.

[105] Lapitsky Y, Parikh M, Kaler EW. Calorimetric determination of surfactant/polyelectrolyte binding isotherms. J Phys Chem B 2007;111:8379-87.

[106] Thevenot C, Grassl B, Bastiat G, Binana W. Aggregation number and critical micellar concentration of surfactant determined by time-dependent static light scattering (TDSLS) and conductivity. Colloids and Surfaces A-Physicochemical and Engineering Aspects 2005;252:105-11.

[107] Taylor DJF, Thomas RK, Penfold J. Polymer/surfactant interactions at the air/water interface. Adv Colloid Interface Sci 2007;132:69-110.

[108] Vincekovic M, Bujan M, Smit I, Filipovic-Vincekovic N. Phase behavior in mixtures of cationic surfactant and anionic polyelectrolytes. Colloids and Surfaces A-Physicochemical and Engineering Aspects 2005;255:181-91.

[109] Bell CG, Breward CJW, Howell PD, Penfold J, Thomas RK. Macroscopic Modeling of the Surface Tension of Polymerâˆ'Surfactant Systems. Langmuir 2007; 2007;23:6042-52.

[110] Bakshi MS, Sachar S. Surfactant polymer interactions between strongly interacting cationic surfactants and anionic polyelectrolytes from conductivity and turbidity measurements. Colloid Polym Sci 2004;282:993-9.

[111] Onesippe C, Lagerge S. Study of the complex formation between sodium dodecyl sulfate and chitosan. Colloids and Surfaces A-Physicochemical and Engineering Aspects 2008;317:100-8.

[112] Roy D, Semsarilar M, Guthrie JT, Perrier S. Cellulose modification by polymer grafting: a review. Chem Soc Rev 2009;38:2046-64.

[113] Bhattacharya A, Misra BN. Grafting: a versatile means to modify polymers - Techniques, factors and applications. Progress in Polymer Science 2004;29:767-814.

[114] Toledano-Thompson T, Loria-Bastarrachea MI, Aguilar-Vega MJ. Characterization of henequen cellulose microfibers treated with an epoxide and grafted with poly(acrylic acid). Carbohydr Polym 2005;62:67-73.

[115] Shukla SR, Athalye AR. Graft-Copolymerization of Glycidyl Methacrylate Onto Cotton Cellulose. J Appl Polym Sci 1994;54:279-88.

[116] Ghosh P, Das D. Modification of cotton by acrylic acid (AA) in the presence of NaH2PO4 and K2S2O8 as catalysts under thermal treatment. European Polymer Journal 2000;36:2505-11.

[117] Suo A, Qian J, Yao Y, Zhang W. Synthesis and properties of carboxymethyl cellulose-graft-poly(acrylic acid-co-acrylamide) as a novel cellulose-based superabsorbent. J Appl Polym Sci 2007;103:1382-8.

[118]   Aliouche D, Sid B, Ait-Amar H. Graft-copolymerization of acrylic monomers onto cellulose. Influence on fibre swelling and absorbency. Annales De Chimie-Science Des Materiaux 2006;31:527-40.

[119]   Sabaa MW, Mokhtar SM. Chemically induced graft copolymerization of itaconic acid onto cellulose fibers. Polym Test 2002;21:337-43.

[120]   Pulat M, Isakoca C. Chemically induced graft copolymerization of vinyl monomers onto cotton fibers. J Appl Polym Sci 2006;100:2343-7.

[121]   Figure1.5 - Image from
http://forestproducts.orst.edu/faculty/simonsen/Nanocomposites.pdf

[122]   Malvern Instruments ltd, Retrieved 27 July 2010, from
http://www.malvern.com/LabEng/technology/zeta_potential/zeta_potential_LDE.htm

[123]   Dataphysics Instruments, Retrieved 20 July 2010, from Image from
http://www.laborexport.hu/pdf/DPI_Products_Overview_E.pdf

[124]   Figure 3.3 - Image from http://mmrc.caltech.edu/FTIR/FTIRintro.pdf

[125]   Malvern Instruments ltd, Retrieved 1 August 2010, from
http://www.malvern.com/common/downloads/campaign/MRK656-01.pdf

[126]   VP-ITC Microcalorimeter user's manual, Retrieved 5 June 2010, from
http://www.med.yale.edu/wmkeck/biophysics/VP_ITC_MANUAL_11_20_02a.pdf

[127]   VP-DSC Microcalorimeter user's manual, Retrieved 2 August 2010,
fromhttp://www.uic.edu/orgs/ctrstbio/manuals/vpdsc_manual.pdf